Transactions of the ASME®

Technical Editor
ARTHUR J. WENNERSTROM
Senior Associate Technical Editor
G. K. SEROVY
Associate Technical Editors
Advanced Energy Systems
M. J. MORAN
Environmental Control
H. E. HESKETH
Fuels and Combustion Technologies
R. E. BARRETT
Gas Turbine
T. H. OKIISHI
Internal Combustion Engine
J. A. CATON
Nuclear Engineering
S. M. CHO
Power
R. W. PORTER

BOARD ON COMMUNICATIONS
Chairman and Vice-President
R. NICKELL

Members-at-Large
J. LLOYD
R. REDER
F. SCHMIDT
M. FRANKE
M. KUTZ
T. MIN
F. LANDIS
R. ROCKE
W. WINER
R. GENTILE
R. MATES

President, E. L. DAMAN
Executive Director,
D. L. BELDEN
Treasurer, ROBERT A. BENNETT

PUBLISHING STAFF
Mng. Dir., Publ., JOS. SANSONE
Managing Editor,
CORNELIA MONAHAN
Sr. Production Editor,
VALERIE WINTERS
Editorial Prod. Asst.,
MARISOL ANDINO

Transactions of the ASME, Journal of Turbomachinery (ISSN 0889-504X) is published quarterly (Jan., Apr., July, Oct.) for $95 per year by The American Society of Mechanical Engineers, 345 East 47th Street, New York, NY 10017. Second-class postage paid at New York, NY and additional mailing offices. POSTMASTER: Send address change to The Journal of Turbomachinery, c/o The AMERICAN SOCIETY OF MECHANICAL ENGINEERS, 22 Law Drive, Box 2300, Fairfield, NJ 07007-2300."

CHANGES OF ADDRESS must be received at Society headquarters seven weeks before they are to be effective. Please send old label and new address.

PRICES: To members, $27.00, annually; to nonmembers, $95.00. Add $12.00 for postage to countries outside the United States and Canada.

STATEMENT from By-Laws. The Society shall not be responsible for statements or opinions advanced in papers or ... printed in its publications (B 7.1, para. 3).

INDEXED by Applied Mechanics Reviews and Engineering Information, Inc.

Journal of Turbomachinery

Published Quarterly by The American Society of Mechanical Engineers

VOLUME 110 • NUMBER 3 • JULY 1988

TECHNICAL PAPERS

TECHNICAL BRIEFS

ANNOUNCEMENTS

Development, Testing, and Performance Prediction of Radial Compressor Stages for Multistage Industrial Compressors

P. Dalbert
Research and Development Engineer.

M. V. Casey
Aerodynamic Development Manager.

Turbocompressor Department,
Sulzer Escher Wyss Ltd.,
Zurich, Switzerland

E. Schurter
Research Engineer,
Fluid Dynamics Laboratory,
Sulzer Brothers,
Winterthur, Switzerland

A review of some theoretical and experimental techniques currently in use for the aerodynamic development of standard stages for industrial centrifugal compressors is presented. Design methods for standardized families of radial compressor stages are summarized. The closed-loop test stands used for performance measurements are described and methods of test data analysis for identifying component performance and improving component matching are discussed. Test data obtained from standardized families of stages are analyzed using elementary dimensional analysis. This allows a simple structure for the interpolation of the large amounts of test data to be formulated. Correction formulae for secondary effects (such as changes in gas properties, Reynolds number, and small deviations from geometric similarity) are also derived from measurements. The data are incorporated into a stage-stacking calculation method for performance prediction of multistage compressors.

Introduction

Multistage and single-stage centrifugal compressors are used extensively for the compression of gases in many industries. The large field of applications necessitates a wide variety of compressor types and frame sizes. The different pressure levels of the various applications—from vacuum blowers to barrel compressors with discharge pressures up to 500 bar—and the provision for external or internal intercoolers and sidestream flows lead to many different casing designs. The wide range of suction volumes gives rise to a large range of machine sizes using different impeller diameters and the many pressure ratios and variety of gases to be compressed require different rotational speeds and numbers of stages.

In addition to the large variation in size and mechanical design there are also different operating requirements for each application. In some cases, a machine with minimum power consumption at a single operating point is specified, whereas in other applications several different operating points, perhaps even with different gases, have to be guaranteed. In all cases the machines have to be reliable, robust, as small and inexpensive as possible, and still meet the customer's specifications.

To cover this wide field of applications in an economical way it is usually necessary for the manufacturer to custom-tailor the compressor design using pre-engineered and pretested components. In some cases only relatively minor changes from an existing design are needed (e.g., scaling to a larger impeller diameter, variation of the impeller outlet widths, or modification of bladed diffusers). In others, it may be necessary to use different stage types or to change the number of stages. The reliability of this type of design is very much increased when an effective standardization of stage types and components is adopted and when the standardized stages are fully developed and tested before they are applied in machine design. This greatly simplifies the thermodynamic design of multistage compressors as the performance of the compressor can then be accurately determined from the cumulative performance of the individual stages (so called "stage stacking"). It also has obvious advantages for the mechanical and rotordynamic design as the machine is made up of modular components that have all previously been tried and tested. Standardized components are also ideally suitable for automatic drafting in CAD systems and for CAM.

It is the purpose of this paper to describe some techniques that are currently in use in an industrial environment for the aerodynamic development, performance testing, and evaluation of standardized compressor stages. The use of numerical methods for the geometry definition and design of standardized families of radial compressor stages is summarized. The closed-loop test stands used for performance measurements are described. This testing serves to confirm that the performance objectives have been met, to ensure the optimum matching between components and to generate the database needed for performance prediction. A simple method of test data analysis, which separates the performance of the impeller and diffuser, is explained, and its use to optimize the matching between an impeller and a bladed diffuser is demonstrated.

The data obtained from the measurements of single stages at different aerodynamic conditions form the basis of a

Contributed by the International Gas Turbine Institute and presented at the 33rd International Gas Turbine and Aeroengine Congress and Exhibition, Amsterdam, The Netherlands, June 5–9, 1988. Manuscript received by the International Gas Turbine Institute September 18, 1987. Paper No. 88-GT-34.

practical and accurate performance prediction method for multistage compressors. The use of standardized families of stages and elementary dimensional analysis allows a simple structure for the interpolation of the large amounts of test data to be formulated. Correction formulae for secondary effects (such as changes in gas properties, Reynolds number, and small deviations from geometric similarity) are also derived from appropriate measurements.

Examples of the prediction accuracy of the stage-stacking calculation method for multistage compressors at design and off-design operating points are given.

Design and Standardization Procedure

The requirements of a new stage are specified as values of flow coefficient, tip-speed Mach number, efficiency, polytropic head coefficient, and operating range. These nondimensional values are more convenient to the designer of industrial compressor stages than the values of flow capacity, pressure ratio, diameter, and tip speed. They are independent of the type of gas to be compressed and the size of the machine and allow a new stage to be compared directly with those already available. The flow coefficient Φ has been found more useful than a dimensionless specific speed, defined as $n_s = NV_1^{1/2}\Delta h_p^{-3/4}$ (Rodgers, 1980), or a specific diameter, $\delta_s = D_2\Delta h_p^{1/4}V_1^{-1/2}$ (Simon, 1987), to quantify the swallowing capacity of industrial stages. This is because the head rise coefficient of most practical stages varies only within a fairly small range, $0.45 < \Delta h_p/u_2^2 < 0.65$ while the flow capacity varies by a factor of 30 ($0.004 < \Phi < 0.13$). The tip-speed Mach number is used rather than the pressure ratio Π or a "$N/\sqrt{T}$"- speed parameter, as the large differences in the molecular weight of the gases to be compressed is then automatically taken into account. The relative importance of the design parameters depends on the planned application.

Figure 1 shows a diagram of the "Computer-Aided Engineering" design procedure used for radial compressor stages. In the first step a preliminary design is carried out, which takes into account some one-dimensional calculations, experience with similar stage types, and geometric and manufacturing constraints. It specifies the complete blade and channel geometry as an initial estimate. This information is then fed into a geometry definition program "LAYOUT," which has been described in detail by Casey (1983). "LAYOUT" provides a full description of the geometry of the blades and the flow passages of the stage as well as automatic interfaces to other available software for fluid dynamic analysis, mechanical analysis, and computer-aided manufacturing (CAM). It should be noted that the same program may be used for the design of all the flow channels and blades in a compressor stage (impeller, diffuser, and return channel) providing all the necessary drawings and diagrams

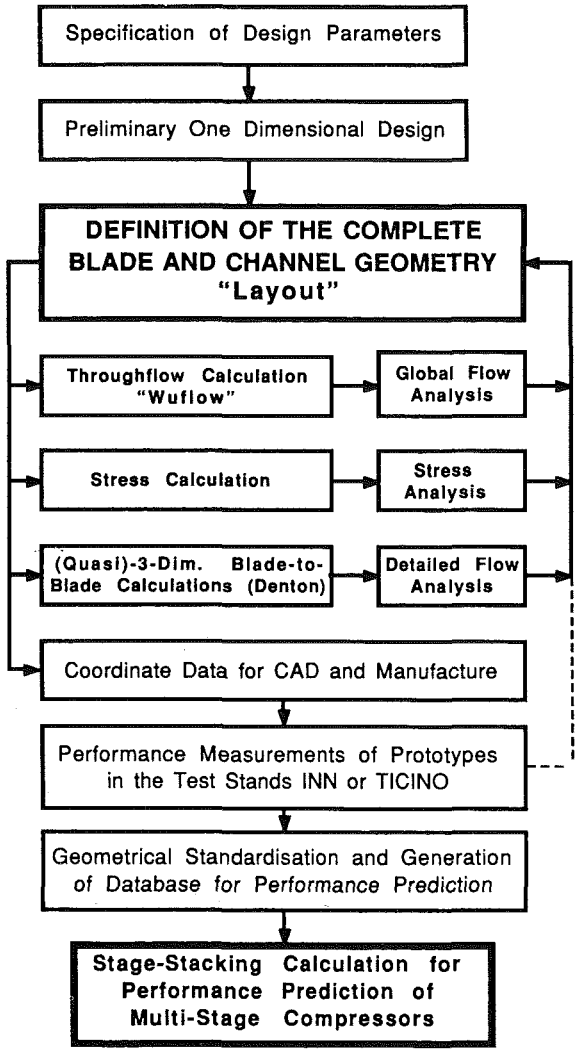

Fig. 1 Design procedure for radial stages

Nomenclature

b_2 = impeller outlet width
c = absolute velocity
D_2 = impeller tip outlet diameter
h = enthalpy
ln = natural logarithm
Mc = Mach number of absolute velocity
m = mass flow
Mu_2 = stage Mach number
n = polytropic exponent
N = rotational speed
P = power
p = pressure
R = gas constant
Re = Reynolds number
s = entropy
u = speed of the blade
V = volume flow
α = angle
β_2 = blade outlet angle
γ = ratio of specific heats
γ_0 = degree of reaction
Δ = difference
ζ = total pressure loss coefficient
η_D = diffuser efficiency
η_R = impeller efficiency
η_p = polytropic stage efficiency (total-total)
μ_0 = work coefficient
μ_p = polytropic head coefficient
μ_R = impeller work coefficient
ν = kinematic viscosity
Φ = flow coefficient

Subscripts

0 = stage inlet
1 = impeller inlet
2 = impeller outlet
3 = diffuser outlet
4 = stage outlet
C = correction value
D = diffuser
m = meridional
OPT = at optimum efficiency
p = polytropic process
ref = reference value
R = impeller
u = circumferential

Superscript

* = total conditions

Note: All angles are indicated with respect to the tangential direction.

for documentation of the design. In an iterative fashion the designer has now the possibility to optimize the impeller layout. He can use the coordinate data in the various output files of the "LAYOUT" program for a number of different purposes:

1 Streamline curvature throughflow program "WUFLOW" described by Casey and Roth (1984) for an overall flow analysis.

2 Stress calculation with a fully three-dimensional finite element model ANSYS (1983).

3 Fully three-dimensional or a quasi-three-dimensional blade-to-blade time marching program by Denton (1983) for detailed flow analysis.

4 Specification of the geometry for manufacture of the impeller and as input data for CAD.

Using the "LAYOUT" program as an impeller generator the designer repeatedly adjusts the shape of the blades and flow channels until he finds a suitable geometry that combines acceptable aerodynamic performance with low stress levels and is economical to manufacture. If he feels that an optimum design has been achieved, one or two prototype impellers are built and their performance is exhaustively tested in dedicated test stands (see Test Stands section). If the performance objectives are met the new stage can be standardized and the measured characteristic curves are used to calculate the performance of compressors which incorporate the new stage type. If the performance objectives have not been met, the test measurements can be used to suggest the most promising areas where a redesign may be worthwhile.

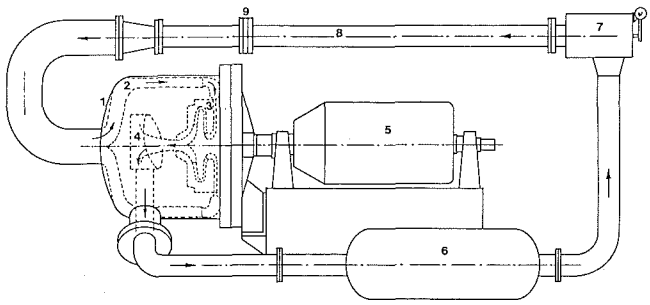

Fig. 2 Closed-loop of test stand INN: (1) pressure vessel; (2) inlet channel; (3) stage; (4) outlet collector; (5) 125 kW pendulum electromotor; (6) gas cooler; (7) throttle valve; (8) pipe for flow rate measurements; (9) flow nozzle (ASME standard)

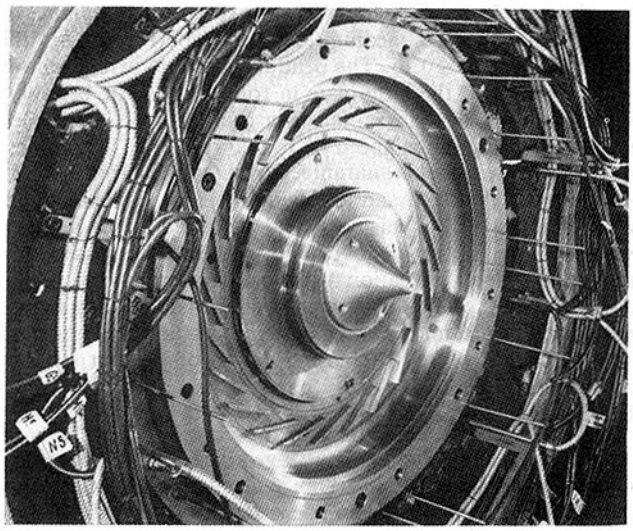

Fig. 3 Typical radial stage in test stand INN (view onto diffuser and hub disk of impeller)

The standardization procedure for compressor stages has been refined over many years based on experience with many different stages. The impeller geometry is standardized using the geometry definition program with the help of the throughflow calculations. Each impeller type is initially designed for a specific flow coefficient with a certain outlet width, but can be manufactured with the same blade shape over a range of outlet widths to adapt it to other flow coefficients. The width of the impeller outlet can be varied following the ISO standard R40 series (i.e., $^{40}\sqrt{10} \approx 1.06$) giving a very fine adjustment of the stage flow capacity. The flow channels within the impeller are modified such that the hub and shroud contours follow the path of the meridional streamlines determined by the throughflow calculation of the original design.

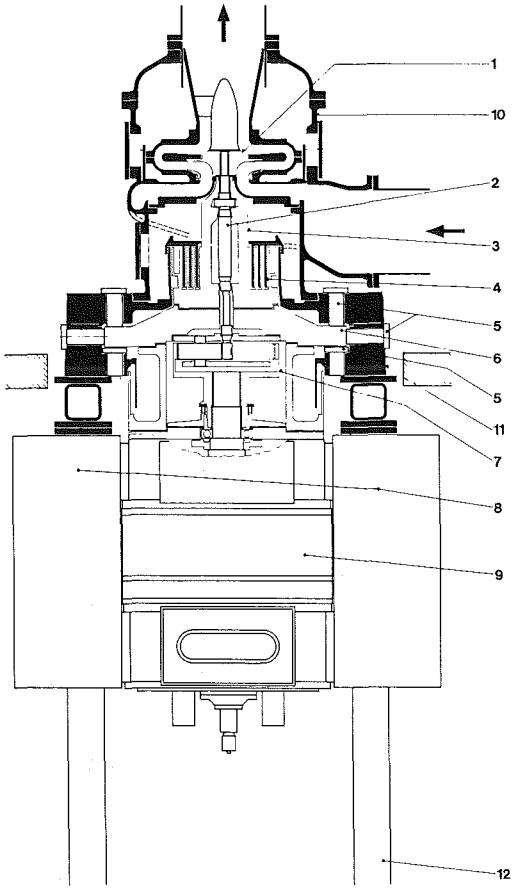

Fig. 4 Test stand TICINO: (1) impeller; (2) high speed shaft; (3) bearing case of high speed shaft; (4) mercury seal; (5) upper, radial and lower hydrostatic bearing; (6) pendulum base plate; (7) planetary gear; (8) motor coolers; (9) direct current motor; (10) compressor casing; (11) base frame; (12) pillars

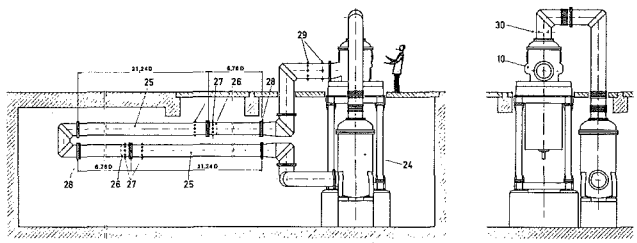

Fig. 5 Closed-loop of test stand TICINO: (10) compressor casing; (24) gas cooler with throttle valve; (25) pipes for flow rate measurements; (26) flow nozzles (ASME standard); (27) pressure taps for mass flow measurement; (28) thermometers for mass flow measurement; (29) pressure taps and thermometers at compressor inlet; (30) thermometers at compressor outlet

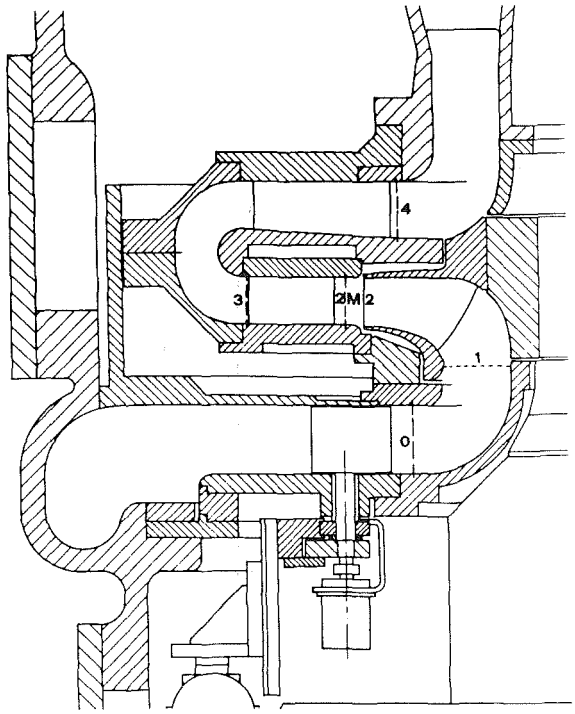

Fig. 6 Typical radial stage and measuring planes in the test stand: measuring planes: 0 = inlet; 2M = diffuser inlet; 3 = diffuser outlet; 4 = stage outlet; calculating planes: 1 = impeller inlet; 2 = impeller outlet

This leads to a similar flow field for each member of the impeller family (with similar blade inlet and outlet angles, incidence, blade loading and diffusion levels), and ensures that similar characteristic curves are obtained for each member of the family.

Other elements of the stage are also standardized. For example, the ratio of widths of the diffuser and return channels relative to the impeller outlet width is held constant for each member of a standardized stage family. A different diffuser and return channel width ratio can, however, be used for different families. The blade shape of vaned diffusers is standardized in such a way that various diffuser configurations with different radial extent and different throat areas can be obtained. The selection of the best diffuser configuration and optimum matching between impeller and diffuser is not possible using purely theoretical methods. Instead, the optimization of the diffuser is usually carried out by performance testing (see the next section).

Within this system of diffuser standardization there is an enormous number of different parameters that can be varied to achieve an optimum design. It is, of course, not economical to test all possible diffuser variants with each impeller. In practice, experience with previous stages can usually be called upon to provide a good estimate of the most promising diffuser configuration. The tests are then reduced to the variation of the most important diffuser parameters: the inlet throat area or blade inlet angle and the degree of diffuser pinch (ratio of diffuser width to impeller outlet width).

Test Stands, Testing, and Data Analysis

General. Measurements with prototype impellers are carried out in one of two single-stage closed-loop test stands (Figs. 2 to 6). The closed circuits have the advantage that different test gases at different pressure levels can be used. This means that is is possible to run performance tests with Freon-12 at higher tip-speed Mach numbers than would be possible using air as test gas at the maximum rotational speed of the motors. The use of Freon-12 (dichlorodifluoromethane) as a test medium is a common practice in experimental investigations of the aerodynamic characteristics of airfoils in wind tunnels as reported by Weller (1978). Due to the high molecular weight of Freon-12, its speed of sound is less than one-half that of air. Therefore the rotational speed of the impeller in a test stand for experiments with radial compressor stages is also less than half for the same blade tip-speed Mach number. The Reynolds number is controlled by the pressure level in the circuit. This advantage and the fact that the compressibility effects can be predicted with acceptable accuracy by a table of real gas properties makes Freon-12 a very useful test medium. The main complications are the need for a completely leak-proof test loop and a means of recovering the used Freon-12. It is, of course, also possible to use other gases as test medium, e.g., carbon dioxide (CO_2) or argon to test the effect of the isentropic exponent or Reynolds number on the performance of the stages.

A fundamental feature of the measurements carried out is the very close attention given to geometric similarity. The geometry of the wetted flow channels for the tests is chosen to correspond as closely as possible to the compressor stages that occur in actual compressors.

Test Stands. The two test stands differ essentially in their construction, maximum impeller size, and flow rate:

- The smaller test compressor, which is called "INN," is a horizontally mounted single-stage test stand as shown in Fig. 2. The closed loop comprises a pressure vessel with the test stage, a water-cooled heat exchanger in the high-pressure duct, a throttle valve for the flow rate control, and an ASME standard flow measuring device. It is driven by a 125 kW electromotor and designed for flow rates of $0.001 \leq \Phi \leq 0.04$ at a maximum circuit pressure level of 6 bar with a standard impeller diameter of 315 mm and maximum speed of 10,000 rpm. The stage with a radial inlet channel, a shrouded impeller, bladed (Fig. 3) or unbladed radial diffuser, return bend, and return channel is typical of most of the stages used in multistage process compressors. The test cell is designed such that many items can be exchanged, giving great flexibility in test procedure. For the analysis of exit volutes the return channel can be replaced by volutes of different geometries.
- The test stand "TICINO" (Fig. 4) is a vertically mounted test compressor with essentially the same stage geometry and shrouded impellers as INN. Since the stand has a power of 800 kW it is possible to carry out performance measurements of stages with impeller diameters up to 450 mm at blade tip speeds up to 350 m/s, leading to a tip-speed Mach number of unity with air as test medium. The flow coefficient is in the range of $0.03 \leq \Phi \leq 0.15$. The pendulum direct current motor, which is fixed at the base plate in four hydrostatic bearings, drives the impeller via a planetary gear and the high-speed shaft with a maximum speed of 15,000 rpm. The airtightness of the pressure vessel is guaranteed by a moment-free mercury seal between the fixed and the swinging parts. The maximum inlet pressure level of this test stand is limited by the mercury seal to approximately 2 bar absolute pressure. The closed-loop test stand with an indication of the main parts is shown in Fig. 5. The test cell of TICINO can also be converted into a stage with an axial inlet and preswirl vanes, an unshrouded impeller, and an outlet volute. The casing design of the test stand is again such that it uses parts that are similar to those used for standard machines.

Data Acquisition and Processing. The measurements are carried out with the help of an automatic data acquisition system, incorporating an on-line calculation and plot of the main test stand parameters. The inlet and outlet pressures (i.e., measuring planes 0 and 4, Fig. 6) as well as several inter-

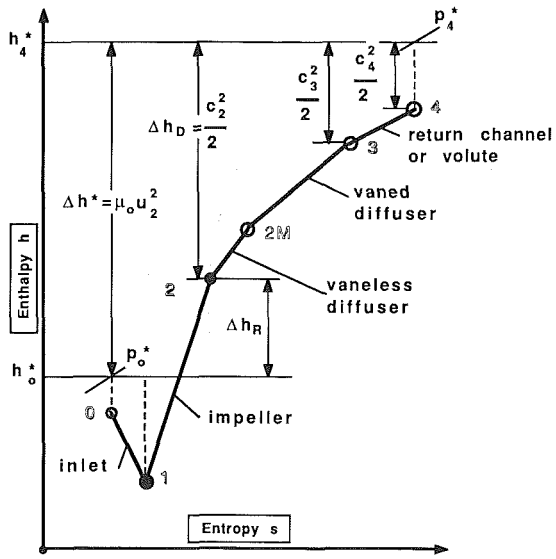

Fig. 7 Compression path in *h*-*s* diagram

nal pressures (planes 2 and 3), which will be discussed in detail below, are continuously measured by pressure transducers (accuracy $\Delta p/p \approx 0.1$ percent) at several points around the circumference of the stage. The inlet and outlet temperatures are measured by resistance thermometers (accuracy $\Delta T^*/T^* \approx 0.03$ percent). The flow rates are calculated from the calibration values of the ASME flow nozzles in the loop. The power absorbed by the impeller is measured directly by a load cell (accuracy ≈ 0.1 percent) taking the reaction of the torque of the pendulum motor.

Usually the standard characteristics are measured at constant rotational speed and constant suction conditions. The flow rate is controlled by the throttle valve in the circuit. The inlet temperature is held constant by the heat exchanger.

After adjusting the main parameters, such as rotational speed, circuit pressure level, and volume flow, the power input from the measurements of torque and mass flow through the stage is compared with the power calculated from total temperature rise in the completely insulated stage. Only if the difference between the two measurements is less than 1 percent (i.e., if the steady state of the compressor has been reached) can a measuring point of the stage characteristic be accepted. Immediately after scanning the data several times and calculating their mean values, a preliminary evaluation of stage efficiency, polytropic head, and work coefficient is made. By this means these values can be checked on line and the variations controlled to be within certain predetermined limits. In this way and by very high standards of accuracy in the calibration of the measuring instruments it is possible to ensure a maximum error in efficiency, work input, and flow capacity of less than ± 1 percent.

Data Analysis. The performance of a compressor stage depends essentially on its geometry, flow rate, inlet pressure, inlet temperature, the gas properties, and the rotational speed of the impeller. For a fixed geometry (Fig. 6) and a specific test medium the compression path in the *h*–*s* diagram may be sketched as in Fig. 7.

Stage Performance. For the description of the performance of the whole stage from plane 0 to plane 4 the corresponding pressures and temperatures, the rotational speed, the mass flow, and the mechanical power are known from measurement. With these data the most important nondimensional parameters that describe the thermodynamic behavior can be calculated:

• The flow coefficient, which is a nondimensional velocity ratio, is defined as

$$\Phi = m/(\rho_0^* u_2 D_2^2) \tag{1}$$

• The Reynolds number relates essentially the effect of gas friction and stage performance. The most useful definition is shown by Casey (1985a) to be

$$\mathrm{Re} = u_2 b_2/\nu_0^* \tag{2}$$

• The tip-speed Mach number or stage Mach number refers to the mechanical tip speed of the impeller and is defined as

$$\mathrm{Mu}_2 = u_2/\sqrt{\gamma R T_0^*} \tag{3}$$

• The work coefficient μ_0 describes the required input power to compress a unit mass of gas from the inlet to exit total pressure

$$\mu_0 = (P/m)/u_2^2 = (h_4^* - h_0^*)/u_2^2 = \Delta h^*/u_2^2 \tag{4}$$

• If the compression of the gas follows the pressure–volume relation of a polytropic process the integral of the polytropic head rise can be written as

$$\Delta h_p = {}_0{}^*\int^{4^*} dp/\rho$$

$$= RT_0^*\{n/(n-1)\}\{(p_4^*/p_0^*)^{(n-1)/n} - 1\} \tag{5}$$

Because of its proportionality to the square of the tip speed, its nondimensional parameter—the polytropic head coefficient μ_p—is defined as

$$\mu_p = \Delta h_p/u_2^2 \tag{6}$$

• Of the many possible definitions of the efficiency of a thermodynamic process, a suitable and consistent definition is the ratio of the useful work output to work input per unit mass flow. Thus the polytropic efficiency is

$$\eta_p = \Delta h_p/(P/m) = \Delta h_p/\Delta h^* = \mu_p/\mu_0$$

$$= (\gamma - 1)/\gamma \ln(p_4^*/p_0^*)/\ln(T_4^*/T_0^*) \tag{7}$$

Figure 8 shows an example of the measured characteristic curves as functions of the flow coefficient, at five different stage Mach numbers between 0.5 and 1.2 for a stage that is similar to the one sketched in Fig. 6. The diffuser blade inlet angle was set to 26 deg; the Reynolds number of each curve increases proportional to the blade tip speed {equation (2) with $\nu_0^* = \text{constant}$}. All variables are normalized with respect to the value at the peak efficiency point at $\mathrm{Mu}_2 = 1.0$. For clarity, the reference values of work and head coefficient have been multiplied by 1.25 and 1.5, respectively. Of interest in these curves is the large effect of tip-speed Mach number on performance. Increasing the Mach number leads to a shift in flow coefficient, an increase in work coefficient, and a reduction of operating range. In this example, which is a stage designed for $\mathrm{Mu}_2 = 0.9$, the efficiency increases up to $\mathrm{Mu}_2 = 0.8$, with only a very small drop to $\mathrm{Mu}_2 = 1.0$ (partly because the constant suction conditions lead to a higher Reynolds number with increase in tip speed) and then falls off at higher Mach numbers as the shock losses at impeller eye increase. It is clear from this diagram that measurements over a range of Mach numbers have to be carried out in order to obtain accurate data for the effect of compressibility.

Impeller and Diffuser Performance. One of the primary objectives of the test procedure is to identify and optimize the matching between an impeller and a bladed diffuser. Tests are carried out with different diffuser blade inlet angles and a theoretical method is used to separate the performance characteristics of the impeller and the diffuser. The principles of this separation go back to Meldahl (1941) and Hausenblas (1965). The method has been found extremely useful, not only

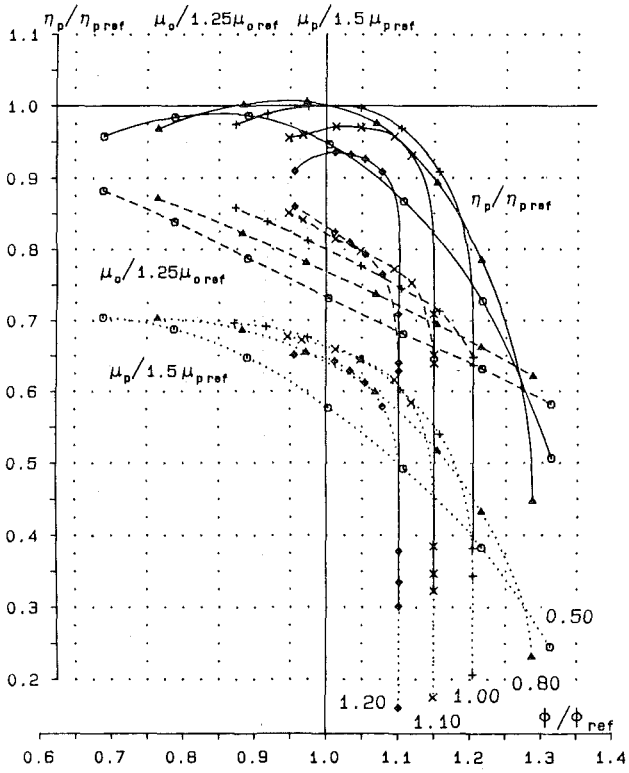

Fig. 8 Relative stage characteristics of TICINO measurements: impeller D9, vaned diffuser $\alpha_{2D} = 26$ deg, stage Mach number $Mu_2 = 0.5$, 0.8, 1.0, 1.1, and 1.2

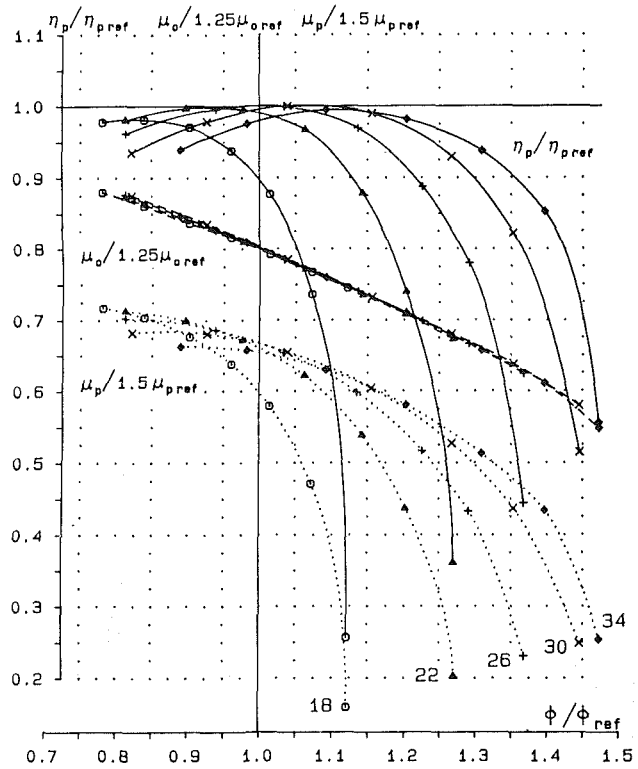

Fig. 9 Relative stage characteristics of TICINO measurements: impeller D9, stage Mach number $Mu_2 = 0.8$, diffuser angles $\alpha_{2D} = 18$, 22, 26, 30, and 34 deg

for analysis of compressors, but also for pumps (Ambühl and Bachmann, 1980). In order to use this technique an additional static pressure measurement at the impeller outlet is required. In fact, with shrouded impellers it is more convenient to place this measuring plane in the diffuser inlet measurement plane 2M (Fig. 6). The thermodynamic state in 2M has to be calculated from the known mean value of p_{2M}, the diffuser mass flow (not the same as the impeller mass flow because of the leakage flow over the cover disks), the impeller work input, and the stagnation temperature T_2^* (which is equal to T_4^* assuming that the change of state between 2 and 4 is adiabatic). With these data, the change of the moment of momentum in the impeller and the change of momentum flux

$$c_{u2M} r_{2M} = \gamma_f c_{u2} r_2 \tag{8}$$

between 2 and 2M, all the unknown one-dimensional mean values of thermodynamic data and the velocities in the separation plane 2 can be iteratively determined. The correction factor γ_f of the momentum flux contains an analytical model of the wall friction losses in the vaneless diffuser part (see Traupel, 1982, and Johnston and Dean, 1966).

With the definition of the following parameters the performance of the rotor and stator can be separated and the mean outlet velocity triangle determined.

- The degree of reaction indicates which part of the required power is necessary for the increase of the static pressure in the impeller:

$$\gamma_0 = \Delta h_R/\Delta h^* = \Delta h_R/(P/m) = 1 - (c_2^2/2)/\mu_0 u_2^2 \tag{9}$$

- The impeller total-to-static efficiency between planes 1 and 2 is defined as the ratio of the polytropic head rise to the input power less the kinetic energy at the impeller outlet

$$\eta_R^* = ({}_0{}^*\textstyle\int^{2^*} dp/\rho)/\Delta h_R = ({}_1{}^*\textstyle\int^2 dp/\rho)/\{\Delta h^* - (c_2^2/2)\} \tag{10}$$

The more commonly used definition of the impeller total-to-total efficiency where the polytropic rise of the total pressure is compared with the work input is easily determined with equations (9) and (10)

$$\eta_R^* = ({}_0{}^*\textstyle\int^{2^*} dp/\rho)/\Delta h^* = ({}_0{}^*\textstyle\int^2 dp/\rho + \Delta h_D)/\Delta h^* = \gamma_0\eta_R + (1-\gamma_0) \geq \eta_R \tag{11}$$

This definition of the impeller efficiency always leads to a higher value than equation (10).

- The diffuser static-to-total efficiency between planes 2 and 4 includes the return channel or the volute

$$\eta_D = ({}_2\textstyle\int^{4^*} dp/\rho)/\Delta h_D = ({}_2\textstyle\int^{4^*} dp/\rho)/(c_2^2/2) \tag{12}$$

- By comparing the paths of the polytropic compression in the two-stage parts, an approximation for the stage efficiency can be given

$$\eta_p \approx \gamma_0\eta_R + (1-\gamma_0)\eta_D \tag{13}$$

This equation is only exactly correct if the stage polytropic head rise Δh_p is equal to the sum of the polytropic head rise of the impeller $({}_0{}^*\textstyle\int^2 dp/\rho)$ and diffuser $({}_2\textstyle\int^{4^*} dp/\rho)$, which means that $\eta_R \equiv \eta_D \equiv \eta_p$.

- The angle of the absolute velocity c_2 at the impeller outlet is

$$\alpha_2 = \tan^{-1}\{c_{m2}/c_{u2}\} \tag{14}$$

and the Mach number of the absolute velocity c_2 is

$$Mc_2 = \{2(1-\gamma_0)\mu_0 Mu_2^2/[1+(\gamma-1)\gamma_0\mu_0 Mu_2^2]\}^{0.5} \tag{15}$$

Figure 9 shows the relative stage characteristics of the same stage as in Fig. 8 at the tip-speed Mach number $Mu_2 = 0.8$ with the variation of the diffuser blade angle α_{2D} from 18 to 34 deg. As reference the peak efficiency and the respective flow coefficient at a diffuser angle setting of $\alpha_{2D} = 26$ deg are used. Again as in Fig. 8 the curves of μ_0 and μ_p are shifted by using the factors 1.25 and 1.5. The diffuser blade has a circular arc centerline and constant thickness. The point of rotation of the

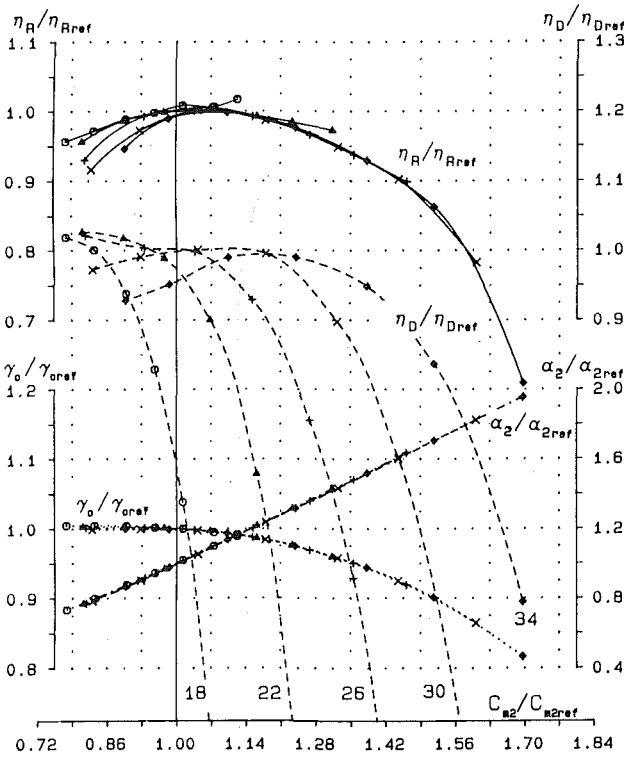

Fig. 10 Relative impeller and diffuser characteristics for the same measurements as in Fig. 9

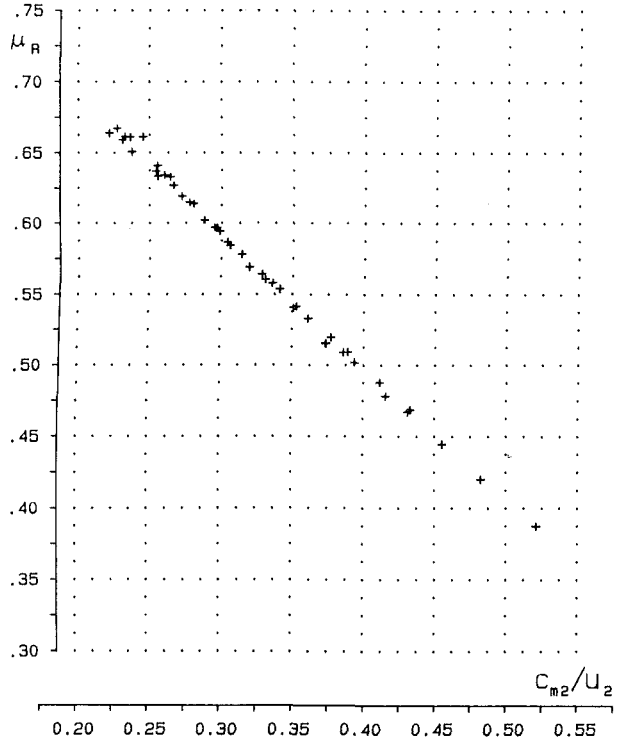

Fig. 11 Impeller work coefficient versus relative meridional velocity at impeller outlet: all measurements of Figs. 9 and 10 including measurements with an unbladed diffuser

blade is at the leading edge and consequently the blade outlet angle varies from approximately 36 to 46 deg. In Fig. 10 the corresponding curves of the impeller and the diffuser relative efficiencies, the degree of reaction $\gamma_0/\gamma_{0\ ref}$, and the outlet flow angle $\alpha_2/\alpha_{2\ ref}$ are plotted versus the impeller outlet meridional velocity $c_{m2}/c_{m2\ ref}$, where all reference values refer to the optimum point of Fig. 9. At this tip Mach number the best stage efficiency is obtained with a diffuser inlet blade angle between 22 and 26 deg. At other tip-speed Mach numbers a higher or a lower inlet angle of diffuser may give better matching.

This method of separating the stage performance into separate impeller and diffuser characteristics should, in order to be most useful, lead to the same impeller characteristic when the same impeller is tested with different diffusers. In fact, as can be seen in Fig. 10, this is not exactly the case. The largest differences (up to ± 3 percent) occur in the impeller total-to-static efficiency characteristic when the impeller is operating near stall or the diffuser near choke. Exactly the same applies for the impeller total-to-total efficiency because equation (11) just shifts η_R to some higher value depending on the magnitude of γ_0. The velocity triangle at impeller outlet, and parameters such as γ_0, α_2, and Mc_2 that are related to the velocity triangle, are not nearly as sensitive to the diffuser being used. This suggests that the changes in impeller efficiency are not related to an impeller–diffuser interaction, but rather due to the change in pressure field at impeller outlet as the incidence of the diffuser changes (see Inoue and Cumpsty, 1984).

The diffuser characteristics obtained by this method are usually similar for all members of a standardized impeller family, but can vary a great deal from one impeller family to another. This is probably due to the well-known fact that diffuser performance is largely determined by the flow structure at inlet (blockage, distortion, turbulence, etc.) and different impeller families give rise to different diffuser inlet flows.

In spite of all these restrictions the procedure determines a representative one-dimensional velocity triangle at the impeller outlet and a rotor efficiency as a function of the inlet flow coefficient ("single zone modeling," Japikse, 1987). It is clear that the use of mean one-dimensional values is a drastic simplification of a very complex flow field (unsteady, "jet-wake" distortion, turbulence, etc.). Nevertheless, these one-dimensional values provide an extremely useful database for correlations of slip factor, for assessing the effect of flow inlet angle on diffuser performance, and for the important engineering decisions to make an improvement of the stage.

Component Performance. With additional detailed evaluation it is moreover possible to calculate specific "separated" characteristics of the individual components. Of particular interest are the impeller work coefficient between planes 1 and 2 without disk friction losses on the hub and shroud disk, the diffuser pressure recovery between planes 2 and 3 and the return channel or volute losses between planes 3 and 4. Such coefficients allow the research engineer to review the results of impeller prototype or new stage measurements.

An important test of the quality of the measurements carried out with a single impeller and a series of diffusers is the plot of μ_R versus c_{m2}/u_2, where μ_R is the work coefficient μ_0 less the friction losses and the leakage flows over the hub and shroud disks of the impeller. The friction losses on the cover disks are determined from analytical models, and the leakage flows from the measured pressure drop across the labyrinth seals. Figure 11 shows this unique impeller work input characteristic for all the measured points of Figs. 9 and 10 at $Mu_2 = 0.8$.

As a second example, the results of an investigation of the effect of different volutes and return channels on the stage performance are demonstrated in Figs. 12 and 13. This series of measurements was carried out to provide a data set to study the influence of different downstream elements. In Fig. 12 relative characteristics at $Mu_2 = 0.8$ of a stage with the same impeller, an unbladed diffuser, and four different outlet

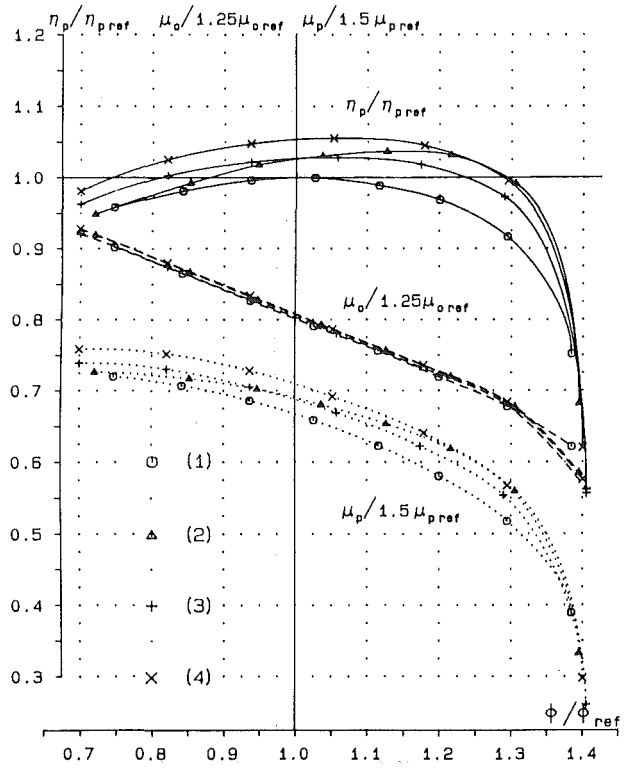

Fig. 12 Relative stage characteristics of INN measurements: impeller D4 with vaneless diffuser and different outlet geometries: return channels: VAR.I(1) and VAR.II (2); volutes: Type 2 (3) and Type 6 (4)

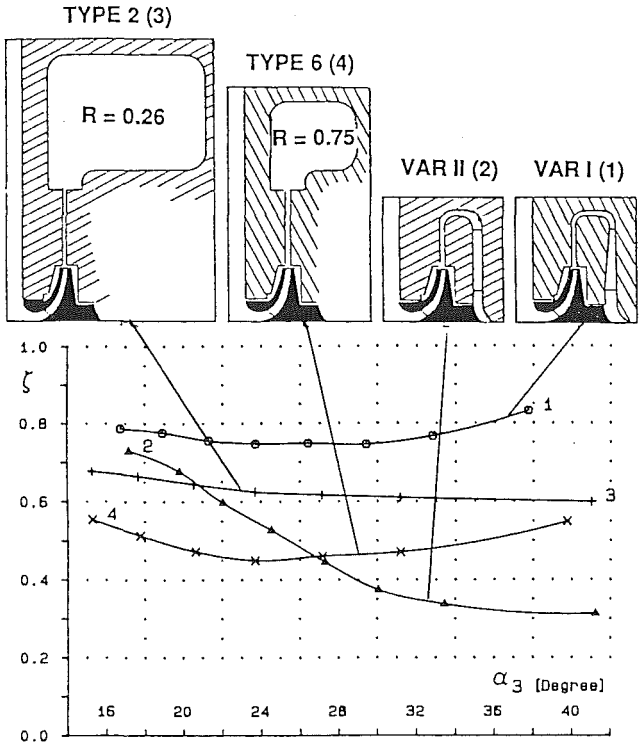

Fig. 13 Effect of flow angle on loss of different outlet geometries (same stage geometries as Fig. 12)

geometries are plotted. The reference values are those of the optimum point of the return channel Variant I (1). The corresponding loss characteristics of the return channels or the volutes, respectively, are shown in Fig. 13. The loss coefficient ζ between the diffuser outlet (plane 3) and the stage outlet (plane 4) is the ratio of the stagnation pressure difference to the kinetic energy at the diffuser outlet

$$\zeta = (p_4^* - p_3^*)/(p_3^* - p_3) \tag{16}$$

For the unbladed diffuser the flow angle α_3 is calculated using the theory given in equation (8), and varies from 15 deg at surge to 40 deg at choke conditions.

The starting point of these measurements is the return channel *Variant I* (see sketches in Fig. 13). *Variant II* has an improved deceleration ratio due to the increased inlet width and parallel walls. The two volutes differ essentially in their "degree of off-design" R, which is the ratio of the ideal outlet area of the volute needed to collect the volume flow of the stage without diffusion to the actual area of its volute (Casey, 1985b):

$$R = A_{4\,\text{ideal}}/A_4 \tag{17}$$

The very large volute *Type 2* has a degree of off-design of 0.26 whereas *Type 6* has $R = 0.75$.

The results of these measurements can be summarized as follows:

- The work coefficient is not strongly affected by the volute or return channel. This important result shows that the work input of the impeller is not changed by the different circumferential pressure distributions in the diffuser caused by the downstream geometries.
- The volute or return channel has only a small effect on the surge point. This result may only be valid, of course, for stages of this type with backward swept impellers giving a relatively steep pressure–volume characteristic.
- The only large effect of the volute or return channel is seen in the pressure rise and efficiency of the stage as a consequence of the different losses in the downstream elements. They can give rise to more than 5 percent of change in efficiency with unbladed diffusers.
- A comparison of the two Figs. 12 and 13 points out that the variation in stage efficiency correlates very well with the loss coefficients.

Multistage Compressor Performance Prediction

A practical method of predicting the performance of stages from standardized families, which takes into account experience from a large number of stage types, can be described as follows (Casey and Marty, 1986). The "base" characteristics are given as

$$\eta_{pB} = f_\eta(\Phi_B, \text{Mu}_2, b_2/D_2) \tag{18}$$

$$\mu_{0B} = f_\mu(\Phi_B, \text{Mu}_2, b_2/D_2) \tag{19}$$

where the functions f_η and f_μ represent the interpolation with respect to Φ_B, Mu_2, and b_2/D_2 of the measurements of those stages within the standardized family that have been tested. The use of a single geometric parameter to quantify the geometry of a stage is only possible for standardized stages where all geometric variations between members of the family are functions of this parameter. In the present case, all blade angles (impeller, diffuser, and return channel) are fixed in the design and standardization process, and the variation of the flow channel width through the stage is a unique function of the impeller outlet width ratio b_2/D_2. The actual values of the stage performance can then be calculated by

$$\Phi = \Phi_B \cdot (\Phi/\Phi_B)_{C1} \cdot (\Phi/\Phi_B)_{C2} \cdot \ldots + \Sigma\Delta\Phi_C \tag{20}$$

$$\eta_p = \eta_{pB} \cdot (\eta_p/\eta_{pB})_{C1} \cdot (\eta_p/\eta_{pB})_{C2} \cdot \ldots + \Sigma\Delta\eta_{pC} \tag{21}$$

$$\mu_0 = \mu_{0B} \cdot \{\mu_0/\mu_{0B})_{C1} \cdot (\mu_0/\mu_{0B})_{C2} \cdot \ldots + \Sigma\Delta\mu_{0C} \tag{22}$$

$$\mu_p = \mu_0 \cdot \eta_p \tag{23}$$

where the terms $(\Phi/\Phi_B)_{Ci}$, $(\eta_p/\eta_{pB})_{Ci}$, $(\mu_0/\mu_{0B})_{Ci}$, and $\Sigma\Delta\Phi_C$,

$\Sigma\Delta\eta_{pC}$, $\Sigma\Delta\mu_{0C}$ represent the multiplicative or additive corrections that may be necessary for the effects described below. These equations take into account the major importance of Φ_B, Mu_2, and b_2/D_2 on the performance while relegating secondary effects to the role of corrections of the basic interpolations.

Corrections. The use of the measurements on standardized families of stages as database for interpolation is only strictly valid where flow similarity and geometric similarity are maintained. The changes in gas and density between prototype and actual machines call for corrections for the deviation from flow similarity (Reynolds number and isentropic exponent). Exact geometric scaling of components is not always possible since certain dimensions cannot be scaled in proportion to the impeller outlet diameter. For example, there may be changes both in the relative roughness, Ra/D_2, of the wetted surfaces and in the clearance ratio, j/D_2, where j is either the clearance gap of the labyrinth seals of a shrouded impeller or the clearance between the impeller blades and casing of an open impeller. All deviations from geometric similarity are taken into account by correction formulae. Some of the most important corrections in the applications considered are summarized in the following.

Reynolds Number, Roughness, and Diameter. The field of application of centrifugal compressors includes extremely high pressures at low flow volumes where the Reynolds number of a stage may be more than 200 times the Reynolds number of the original prototype stage. The effect on the stage performance is very large as shown by Casey (1985a) and cannot be neglected. The correction of the efficiency $\Delta\eta_{p\ \mathrm{Re}}$ depends essentially on the change in friction factor of the equivalent pipe flow and an empirical factor which is a function of the impeller outlet width. The equivalent friction factor itself is also a function of size and roughness. It can be shown that a correction is also necessary for the flow rate $(\Phi/\Phi_B)_{\mathrm{Re}}$ and the work coefficient $(\mu_0/\mu_{0B})_{\mathrm{Re}}$.

Low Tip Mach Number. Machines operating on hydrogen gas or gas mixtures with very low molecular weight have low tip-speed Mach numbers. Measurements at very low Mu_2 with low volume flow and power input are usually insufficiently accurate. A simple one-dimensional analysis of the impeller outlet triangle points out that at constant flow coefficient the work coefficient decreases parabolically with decreasing tip Mach number lower than $Mu_2 \approx 0.5$. Measurements carried out at $Mu_2 = 0.5$ can therefore be extrapolated by using a correction $\Delta\mu_{0\ \mathrm{Mu}<0.5}$. A change in efficiency is automatically covered by the Reynolds correction.

Preswirl. The main purpose of inlet guide vane adjustments is the control of pressure rise of the impeller. The change of the work coefficient $(\mu_0/\mu_{0B})_\Psi$ where Ψ is the angle of the inlet guide vane, is accompanied by a change in efficiency $(\eta_p/\eta_{pB})_\Psi$ and in flow rate $(\Phi/\Phi_B)_\Psi$.

Inlet and Outlet. Different inlet or outlet geometries (volutes or return channels) lead to different loss coefficients than in prototype measurements (as shown in the section on Component Performance above). These affect essentially the stage efficiency and are corrected with

$$\Delta\eta_{p\ \mathrm{IN,OUT}} = -\Delta\zeta^*(c_{\mathrm{IN,OUT}}/u_2)^2/2\mu_0. \qquad (24)$$

Labyrinths. The construction and the clearance of the labyrinth seals on the shroud and hub disks of the impellers affect the leakage flow and hence volume flow and the pressure rise of the impeller. Additionally it can be shown that the change of the disk friction on hub and shroud has an influence on the work coefficient. Thus deviations from the standard labyrinth clearances of the prototype impellers are corrected by $\Delta\Phi_L$, $\Delta\eta_{pL}$, and $\Delta\mu_{0L}$. The prototype measurements are usually carried out with standard clearances in order to avoid the need for this correction, which could otherwise be quite large for low-flow coefficient stages.

Impeller Blade Cutback. The cutback of the blades at the outer diameter of impellers may be necessary in cases where certain intermediate pressures are specified (sidestreams) that cannot be reached with standard impeller diameters or certain limitations of the rotational speed are given (electromotor without gear). Although the effect of blade cutback is very dependent on the stage type used, above all with respect to stage efficiency, it is possible to specify a reasonable correction for the decreasing work coefficient. Within certain limitations $(\mu_0/\mu_{0B})_{\mathrm{cutback}}$ is proportional to the square of the blade outer diameter ratio D_2/D_{2B}. For exact data on the effect of blade cutback, measurements with the stage in question need to be carried out.

Swirl Brakes. Flow brakes in the axial gap between impeller shroud disk and casing are used to reduce axial thrust by changing the pressure distribution along the shroud or to reduce rotor instability due to the swirl velocity of the leakage flow in the labyrinth seal (Wyssman et al., 1984). These flow brakes, which can be installed anywhere between the outlet diameter of the impeller and just upstream of the labyrinth seal, can have a considerable effect on the stage characteristics at low flow coefficients. Measurements have shown essentially the following effects:

- When the brakes are installed at the outer diameter they lead to an increase of the work coefficient due to increasing friction losses on the impeller shroud. Moreover the pressure coefficient decreases due to increasing leakage flow and this results in a loss of efficiency.
- When installed just upstream of the labyrinth seal they have almost no effect on the leakage flow and a smaller decrease in efficiency and work coefficient that is mainly due to the increased friction losses.

The installation of a swirl flow brake leads to a correction of the characteristics in the form of $\Delta\mu_{0\ \mathrm{brake}}$ and $\Delta\eta_{p\ \mathrm{brake}}$.

Comparisons

The prediction technique described above provides a practical and accurate method of calculating the performance of a radial compressor stage at design and off-design conditions. Incorporated into a stage-stacking calculation program, this technique provides a very efficient method for the thermodynamic design and optimization of multistage compressors. Comparisons with the predicted and measured performance of complete units are shown in this section.

The first machine is an intercooled air compressor where the intercoolers form part of the compressor casing (a so-called "isotherm" compressor). The machine comprises five radial impellers each equipped with a vaned diffuser, as follows:

Stage	1	2	3	4	5
Φ	0.106	0.07	0.069	0.069	0.068
Mu_2	0.91	0.86	0.73	0.65	0.58
D_2, mm	560	530	450	400	375
b_2/D_2, percent	6.7	7.1	7.5	7.5	7.5
α_{2D}, deg	30	22	22	22	22

The intercoolers are between the first four stages; the first stage is fitted with variable inlet guide vanes. Figure 14 shows a comparison of the measured and predicted performance of the machine with different guide vane settings (positions from -3 to $+1$).

The second example is a barrel compressor operating on a mixture of hydrocarbon gases with an inlet pressure of 41 bar and an outlet pressure of 140 bar. Again the machine comprises five impellers:

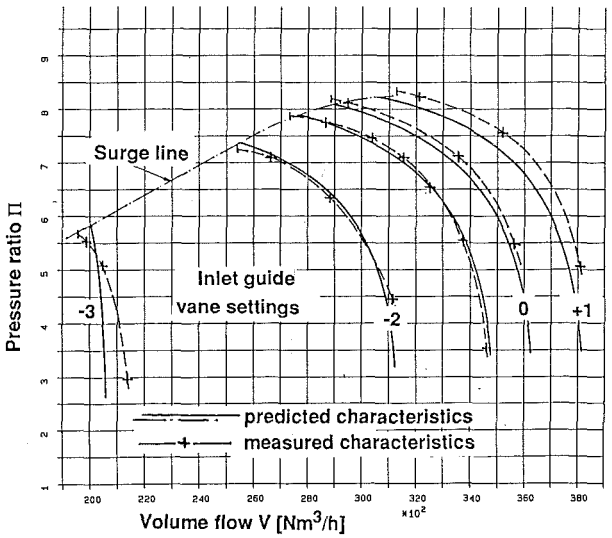

Fig. 14 Π-V characteristic of a five-stage air compressor with different inlet guide vane settings

Stage	1	2	3	4	5
Φ	0.065	0.055	0.045	0.032	0.031
Mu_2	0.65	0.63	0.60	0.63	0.55
D_2, mm	500	500	500	475	450
b_2/D_2, percent	8	6.3	5.3	4.25	4
α_{2D}, deg	vaneless	22	22	18	18

In this case the single external intercooler is between stages 3 and 4. The comparison of the measurement at 100 percent rotational speed and the prediction is shown in Fig. 15.

The good agreement shown in these two examples is typical of that normally achieved with the procedure outlined in this paper. It can be attributed to a number of factors. Firstly, the measurements carried out in the single-stage test stands are of very high quality. Secondly, the standardization procedure for new stages allows the performance of stages with intermediate outlet width ratios to be accurately predicted. Thirdly, due attention is given to flow similarity in the calculation procedure, with the important variation of performance with stage Mach number being included in the characteristic curves, and the secondary effect of Reynolds number included as a correction term. Finally, the standardization procedure and the close attention given to manufacturing tolerances on critical components means that the fundamental requirement of geometric similarity of shape between the stages used in machines and the prototype stages tested in the single-stage test stands is always assured.

Acknowledgments

The authors wish to thank Sulzer Escher Wyss, Ltd., for permission to publish this paper, and many engineers and colleagues for their assistance and useful discussions, which made this work possible.

References

Ambühl, H., and Bachmann, P., 1980, "Bestimmung der Verlustanteile einzelner Stufenkomponenten in ein- und mehrstufigen Pumpturbinen radialer Bauart," *Escher Wyss Mitteilungen*, Vol. 53, No. 1/2, pp. 82–91.

ANSYS, 1983, "Engineering Analysis System," Swanson Analysis Systems Inc., Houston, USA.

Casey, M. V., 1983, "A Computational Geometry for the Blades and Internal Flow Channels of Centrifugal Compressors," ASME *Journal of Engineering for Power*, Vol. 105, pp. 288–295.

Casey, M. V., and Roth, P., 1984, "A Streamline Curvature Throughflow Method for Radial Turbocompressors," *Computational Methods in Turbomachinery*, I. Mech. E. Conference Publications 1984-3, London, Paper No. C57/84.

Casey, M. V., 1985a, "The Effect of Reynolds Number on the Efficiency of Centrifugal Compressor Stages," ASME *Journal of Engineering for Gas Turbines and Power*, Vol. 107, pp. 541–548.

Casey, M. V., 1985b, "The Design and Performance of Radial Compressor Outlet Volutes," unpublished SEWZ Technical Report No. TK-0133.

Casey, M. V., and Marty, F., 1986, "Centrifugal Compressors—Performance at Design and Off-Design," *Proc. of the Institute of Refrigeration*, Vol. 82, 1985–86, pp. 71–80.

Denton, J. D., 1983, "An Improved Time Marching Method for Turbomachinery Flow Calculation," ASME *Journal of Engineering for Power*, Vol. 105, pp. 514–523.

Hausenblas, H., 1965, "Trennung der Lauf- und Leitradverluste bei der Auswertung von Versuchen an einstufigen Radialverdichtern," *Forsch. Ing.-Wes.*, Vol. 31, No. 1.

Inoue, M., and Cumpsty, N. A., 1984, "Experimental Study of Centrifugal Impeller Discharge Flow in Vaneless and Vaned Diffusers," ASME *Journal of Engineering for Gas Turbines and Power*, Vol. 106, pp. 455–467.

Japikse, D., 1987, "A Critical Evaluation of Three Centrifugal Compressors With Pedigree Data Sets: Part 5—Studies in Component Performance," ASME JOURNAL OF TURBOMACHINERY, Vol. 109, pp. 1–9.

Johnston, J. P., and Dean, R. C., 1966, "Losses in Vaneless Diffusers of Centrifugal Compressors and Pumps," ASME *Journal of Basic Engineering*, Vol. 88, pp. 49–62.

Meldahl, A., 1941, "Die Trennung der Rad- und Diffusorverluste bei Zentrifugalgebläsen," *Brown Boveri Mitt.*, Aug./Sept., pp. 203–206.

Rodgers, C., 1980, "Specific Speed and Efficiency of Centrifugal Impellers," *Proc. of the Symposium on Performance Prediction of Centrifugal Pumps and Compressors*, ASME, pp. 191–200.

Simon, H., 1987, "Design Concept and Performance of a Multistage Integrally Geared Centrifugal Compressor Series for Maximum Efficiencies and Operating Ranges," ASME Paper No. 87-GT-43.

Traupel, W., 1962, *Die Theorie der Strömung durch Radialmaschinen*, Verlag G. Braun, Karlsruhe, p. 113ff.

Weller, W., 1978, "Comparison of Aerodynamic Data Measured in Air and Freon-12 Wind-Tunnel Test Mediums," NASA TM 78671.

Wyssman, H. R., Pham, T. C., and Jenny, R. J., 1984, "Prediction of Stiffness and Damping Coefficients for Centrifugal Compressor Labyrinth Seals," ASME *Journal of Engineering for Gas Turbines and Power*, Vol. 106, pp. 920–926.

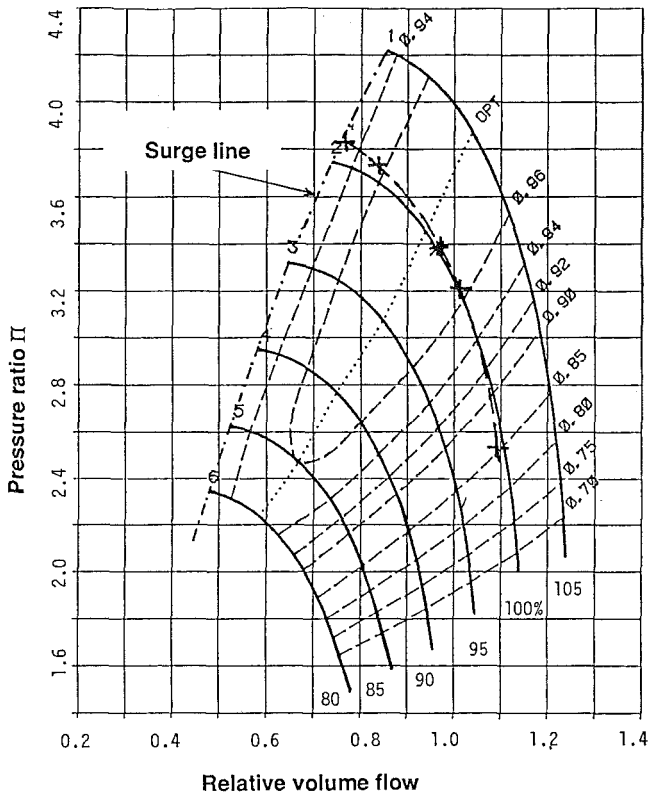

Fig. 15 Π-V_{ref} characteristic of a five-stage barrel compressor with variable speed N/N_{ref}

Unsteady Flow in a Centrifugal Compressor With Different Types of Vaned Diffusers

U. Haupt

U. Seidel

Institute of Turbomachinery,
University of Hannover,
Hannover, Federal Republic of Germany

A. N. Abdel-Hamid

The American University in Cairo,
Cairo, Egypt

M. Rautenberg

Institute of Turbomachinery,
University of Hannover,
Hannover, Federal Republic of Germany

Experiments were conducted to investigate the characteristics of self-excited flow oscillations in a high-performance centrifugal compressor system with a straight channel radial vaned diffuser. Fast response dynamic pressure transducers on the shroud wall and blade-mounted strain gages were used to identify the onset of the oscillations and their characteristics in space and time. In addition, flow characteristics near the shroud wall were visualized by an oil injection method, showing the extent of upstream directed reverse flow in the impeller range during significant unsteady flow compressor operation. Rotating nonuniform flow patterns were found in a wide range of operating speeds before the occurrence of surge. The number of lobes in the nonuniform flow patterns was dependent on the operating conditions and varied from two to four. Results of this experimental investigation were compared with those obtained from a previous investigation of the same compressor but with a cambered vane diffuser. Considerable similarity between the two configurations was found in the spatial distribution of the unsteady pressure field and in the frequencies of the fluctuations. The stability margin before the occurrence of surge and the operating regimes in which very intense pressure fluctuations were found were however different. In both cases, flow visualization techniques revealed the occurrence of reversed flow near the shroud wall of the impeller. Reverse flow extent up to the leading edge of the splitter blades systematically correlated with the occurrence of a nonuniform pressure pattern rotating with relatively high speed. Low rotational speed pressure patterns were observed when the extent of the reverse flow was up to the leading edge of the long blade. These different flow characteristics can be related to the occurrence of distinct rotating stall cell numbers. This result could be confirmed by unsteady pressure and blade vibration measurements.

Introduction

The impact of the flow diffusion system downstream of the impeller on performance and range of centrifugal compressors has been investigated extensively in the past. Based on these investigations design procedures have been established, which are now available in the open literature (Japikse, 1984).

At off-design conditions, however, the prediction of compressor performance becomes increasingly more difficult, especially in the regimes where flow oscillations in the compressor system are likely to occur. The spatial distribution of the flow variation during self-excited oscillations in compressors may extend over the entire compressor system, in which case the phenomenon is known as surge, or may be limited to some of the compressor components such as the impeller and the diffuser. In this paper only self-excited oscillations of the latter type are considered.

No valuable generally accepted physical model exists at present for the occurrence of rotating stall or other oscillating pressure patterns in centrifugal and axial compressors as well. For this reason today the prediction of the aerodynamic characteristics during compressor operation in the unsteady flow regime can only be accomplished mainly based on empirical data and experience. A number of research activities in the past dealt with the question of which component affects the flow stability most. Recently Haupt et al. (1988) and Chen et al. (1987, 1988) presented a theory for the inception of rotating stall on centrifugal compressors with vaned diffusers, which was based on the experimental detection of significant reverse flow phenomena in the impeller. The adopted physical model assumed Karman vortices in the impeller as the controlling mechanism for the inception of rotating stall for this configuration of compressor system.

At the Institute of Turbomachinery of the University of Hannover an extensive experimental program has been conducted to study the performance characteristics of vaneless and vaned radial diffusers, and the mechanism of interaction between impeller and diffuser. Diffferent diffuser configurations were installed in a centrifugal compression system with

Contributed by the International Gas Turbine Institute and presented at the 33rd International Gas Turbine and Aeroengine Congress and Exhibition, Amsterdam, The Netherlands, June 5-9, 1988. Manuscript received by the International Gas Turbine Institute September 15, 1987. Paper No. 88-GT-22.

the same impeller and collecting system. The earlier phases of the program dealt with many aspects of the steady flow characteristics in the various diffuser configurations. The results of these investigations have already been published in the open literature (Bammert et al., 1983; Kaemmer and Rautenberg, 1986; Stein and Rautenberg, 1987).

In the latter phases of the investigations attention was focused on the phenomena of self-excited flow oscillations. For each tested diffuser configuration, detailed static and dynamic pressure measurements were carried out to determine the zones of compressor map, in which self-excited flow oscillations existed, and the characteristics of the unsteady pressure patterns in space and time. The results for one vaneless and one vaned diffuser configuration were recently published (Haupt et al., 1986, 1988; Abdel-Hamid et al., 1987). The observed characteristics of the unsteady flow fields for these two configurations were very different.

Compressor Operaton With Vaneless Diffusers. For the case of compressor operation with a vaneless radial diffuser, self-excited oscillations of the rotating and of the nonrotating type as well were observed. In addition, the superposition of different unsteady flow patterns in a single operating point could be identified by a detailed analysis of the pressure and blade vibration data. Figure 1 shows an example of such a group of pressure patterns. Pressure fluctuations at 20.6 and 122.4 Hz are due to pressure patterns rotating in different directions, while those at 3.8 and 220 Hz are due to standing pressure patterns. The rotational speed of the two and three-lobe rotating patterns were 0.039 and 0.153 of the impeller speed, respectively. The largest shroud wall pressure oscillations were observed over the impeller at $x/s = 0.8$. The relative significance of the pressure oscillations associated with the different types of self-excited flow oscillations was dependent on the operating speed of the compressor although the nonrotating oscillation was dominant in many cases.

An example of the superposition of different unsteady flow phenomena in a single operating point is given in the graph in Fig. 1. Signals of a number of pressure tranducers at different peripheral locations in a plane near impeller inlet were analyzed, and results were plotted in six steps of one period of the different pressure oscillations. This graph represents clearly the occurrence of a low-frequency pressure oscillation, where conditions over the whole circumference are nearly in phase. Two different rotating stall patterns—one (122.4 Hz) rotating with and the other (20.6 Hz) opposite to the direction of the impeller—could be analyzed as well as an additional unsteady flow phenomenon at 220 Hz, showing a nonrotating nature, oscillating around a fixed axis represented in the graph by the dotted line.

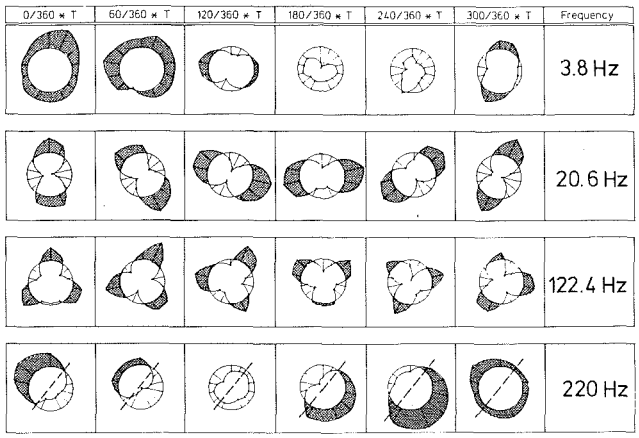

Fig. 1 Peripheral propagation of different rotating and nonrotating unsteady flow patterns during one cycle of oscillation occurring at a single operating point of the compressor with a vaneless diffuser: compressor operating point: $n_{red} = 16{,}000$ rpm, immediately before surge; measurement plane: $x/s = 0.2$

Measurements of self-excited flow oscillations in vaneless radial diffusers of different geometry and test facility, presented by Abdel-Hamid et al. (1979), Abdel-Hamid (1980), Van den Braembussche et al. (1980), Kinoshita and Senoo (1985), and Frigne and Van den Braembussche (1985) indicated the existence of rotating pressure patterns with lobe numbers ranging from 1 to 4. The direction of pattern rotation was always the same as that of the impeller. The phenomenon was shown to be dependent, among other things, on the boundary conditions at diffuser exit. Practical successful methods of controlling its occurrence were demonstrated by Abdel-Hamid (1981, 1987). The variance between results of the different authors cited above demonstrates the dependence of the oscillation characteristics on the system configuration, and on the dynamic interaction between the impeller and the diffuser.

Compressor Operation With Vaned Diffusers. For compressor operation with the cambered vane diffuser, as investigated by the present authors (Abdel-Hamid et al., 1987) the observed self-excited flow oscillations were always of the rotating type in a direction opposite to that of the impeller. The speed of pattern rotation was dependent on the lobe number of the patterns, and was in the range of 0.04 to 0.06 for a lobe number of 3, and 0.15 to 0.17 for a two-cell rotating stall. The amplitude of shroud wall pressure oscillations was the largest in the semivaneless space between the impeller exit

Nomenclature

b = diffuser width
f = frequency
m = lobe number
$\dot{m}$ = mass flow rate
n = rotational speed
p = pressure
r = radius
$r.s.$ = rotating stall
RS = rotating stall
s = blade length at tip
t = time
T = time period of oscillation
T = temperature
x = distance from inducer inlet at blade tip
z = axial distance
ϵ = blade strain
η = efficiency
λ = radius ratio $= r/r_2$
π = pressure ratio
① ② ③ ④ = number of rotating stall cells

Subscripts

bl = blade
K = inlet plenum conditions
N = design conditions
p = pressure oscillation
red = reduced to reference conditions: $T_K = 288.15$ K, $p_K = 1.01325$ bar
RS = rotating stall
s = shaft revolution
stat = static conditions
tot = stagnation conditions
1 = number of blade vibration mode
2 = impeller exit
4 = diffuser inlet
6 = diffuser outlet

Superscripts

$\hat{}$ = amplitude

and the throat of the vaned diffuser. The amplitudes of the oscillations were much higher for the patterns with two lobes than for the patterns with three cells. The two-lobe rotating patterns occurred at high operating speeds only, while the three-lobe patterns were observed at low operating speeds.

In this paper the detailed characteristics of self-excited flow oscillations of the compression system with a straight channel vaned diffuser are presented. The results are compared with those of previously tested diffuser configurations, to categorize the observed phenomena. The extent of variations of the flow properties at different points in the compression system during flow oscillations is given to establish a measure of the severity of oscillations, and to shed some light on the physical processes involved.

Compressor Test Facility

Unsteady flow characteristics on the compressor with a straight channel diffuser were determined experimentally by means of pressure and blade vibration measurements and oil injection experiments. This investigation was carried out on a single-stage centrifugal compressor test rig operated as an open loop. The test rig was described in detail by Bammert et al. (1974).

Compressor Test Rig. The compressor as shown in the sectional view in Fig. 2 is driven by a 1350 kW d-c motor coupled to a gear box. The maximum values of compressor pressure ratio and mass flow were $\pi \approx 5$ and $\dot{m}_{red} \approx 10$ kg/s, respectively. The flow enters in the axial direction through a short suction pipe from a settling chamber, and passes through the impeller and the long straight channel diffuser. The flow downstream is collected in an annular collecting chamber and then leaves the compressor by the outlet tube, which is tangential to the machine.

Operating conditions of the compressor in the experiments described below were obtained at different speed lines (constant reduced rotational speed) and various mass flow, which was controlled by a throttle valve located downstream of the compressor.

Impeller. The unshrouded impeller of the test compressor used for this investigation has characteristic thin blades of about 1 mm thickness at the inlet tip and 4 mm at the outlet. The blades respond very sensitively to unsteady flow phenomena. The impeller has an outer diameter of 400 mm and 28 radial ended blades with every second blade cut back at the inlet. The material is aluminum alloy.

Geometry of the Vaned Diffuser Used in the Present Investigation. A schematic diagram showing the geometry of the diffuser configuration with 19 straight wedge vanes is shown in Fig. 3. The vane leading edge is located at a radius ratio λ_4 of 1.15 and extends to a radius ratio of λ_6 of 1.95. The wedge angle is 9°57′ and is set such that the angle between the pressure side surface and the tangent to the leading edge circle is 17°48′. The diffuser width ratio b_4/r_2 is 0.119. The configuration is typical of industrial-type compression systems.

Signal Transmission System for Blade Vibration Data. In addition to the high-frequency response pressure transducers mounted in the compressor shroud wall, blade vibration characteristics are obtained from semiconductor strain gages on the blades. For the transmission of these signals an eight-channel FM-telemetry system was used, which has been described in detail by Haupt et al. (1982). The telemetry transmitter is situated in the bore of the hollow impeller shaft and is connected to the strain gages. The energy for this system is transmitted to the rotating shaft by an inductive power supply, consisting of a coil system located on the socket tube between the compressor and the gear box. In the telemetry receiver a reconversion process of a high-frequency signal is accomplished by separation of channels, demodulation, filtering, and amplifying. For the investigation described below only one blade vibration signal was selected for recording and analyzing with the pressure signals.

Measurement Procedure for the Unsteady Flow Phenomena

The measurement technique and procedures, which are suitable for unsteady flow, have already been presented in

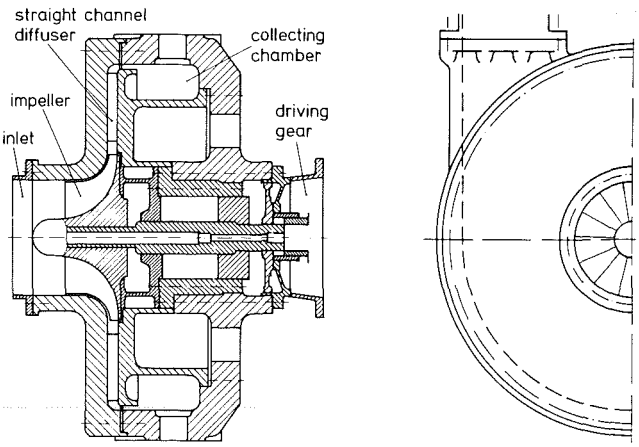

Fig. 2 Cross-sectional view of the test compressor with straight channel diffuser

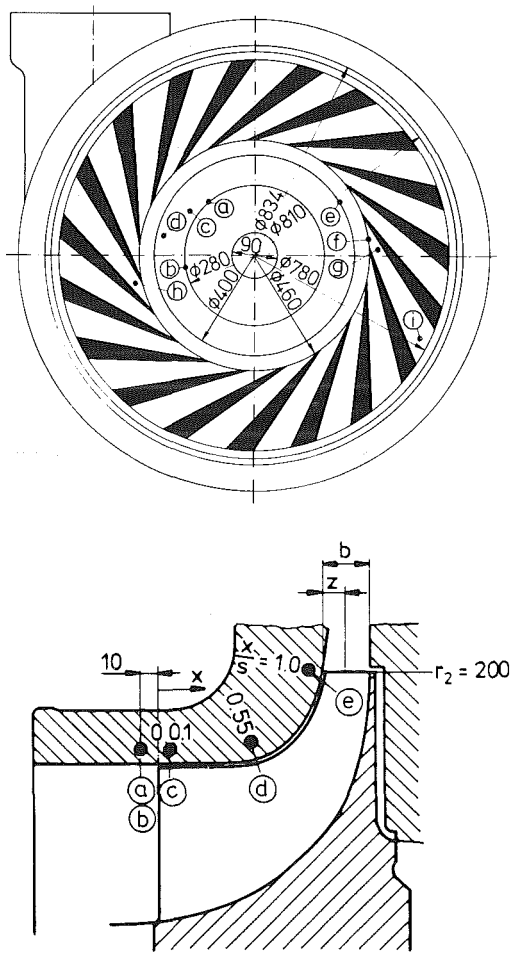

Fig. 3 Geometry and shape of straight channel diffuser with locations of pressure transducers (*a–i*) in the impeller and diffuser range

detail by Haupt et al. (1986). Dynamic pressure transducers were positioned at different locations along the flow path in the compressor, as shown in Fig. 3, to determine the variation of the flow properties in space and time. During the tests the signals from the pressure transducers were recorded on magnetic tape and were analyzed in detail at a later time.

Typically the compressor was operated along constant speed lines, covering a flow range from choking to surge, while observing the flow behavior. For the purpose of this investigation six complete data points, at successively lower mass flow rates, were collected before the occurrence of massive compressor surge.

Additional oil injection experiments were conducted to investigate the flow propagation behavior concerning flow direction in the impeller range near shroud. For this purpose an oil pattern flow visualization method has been developed. In such experiments, the compressor was operqated in the unsteady flow regime at conditions under which certain rotating stall configurations had been analyzed before by means of pressure and blade vibration measurements. Colored oil has been injected impulsively through a hole in the shroud wall into its boundary layer inside, at a location near impeller exit at $x/s = 0.8$.

The injected oil is transported by the flow, leading to traces on the shroud wall and the channels of the impeller. After the injection, the compressor was operated still five minutes approximately under the unsteady flow conditions, and then was stopped. The investigation of the oil traces on the shroud wall and the impeller was accomplished after disassembly of the compressor, especially by removing the shroud wall.

Results and Discussions

The range of compressor operating conditions investigated in this study is shown in Fig. 4. For each speed line several points were taken, before the onset and during the occurrence of self-excited flow oscillations. For each point at which oscillations were observed, the spatial and temporal characteristics of the oscillations were determined and plotted in the diagram of Fig. 4 by different symbols. The techniques used in the analysis to obtain these characteristics from the data have been previously discussed in detail by Haupt et al. (1986) and Abdel-Hamid et al. (1987). A summary of the variation of the oscillation characteristics with compressor operating conditions is given in Table 1.

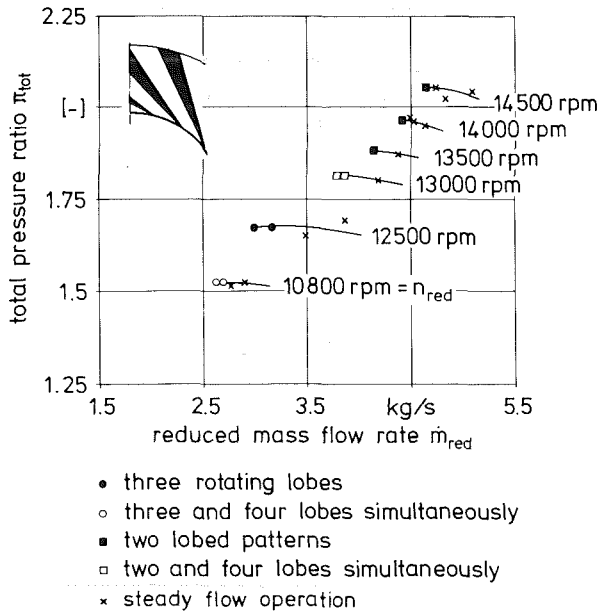

Fig. 4 Results of unsteady flow measurements in the compressor chart showing the characteristics of the rotating stall phenomena (see also Table 1)

Lobe Numbers and Rotational Speed of Cells. Three different types of self-excited flow oscillations were obtained in this investigation. Each type was characterized by a rotating pattern of nonuniform flow, but with different lobe numbers ranging from two to four. According to results given in Table 1, superimposed rotating patterns with three and four lobes were analyzed from signals recorded at 10,800 rpm. As the speed was increased to 12,500 rpm, flow fluctuations due to a three-cell rotating stall were very intensive, while the patterns with four lobes were not existent at this operating point. Further increase of compressor speed to 13,000 rpm resulted in elimination of the three-lobe patterns, the emergence again of the four-cell rotating stall, and the onset of a new rotating pattern with two lobes. At speeds higher than 13,000 rpm the four-lobe pattern was eliminated completely, and only the pattern with two lobes was obtained.

All the patterns observed were rotating against the direction of impeller rotation. The speed of rotation of the patterns varied with the number of lobes. The rotational speed of the two-lobe patterns was in the range of 0.157 to 0.214 of the impeller speed, while the speed ranges for the three and four-lobe patterns were 0.061–0.096 and 0.01–0.02 of the impeller speed, respectively. For a given lobe number, the pattern rotational speed decreased systematically, as the impeller rotational speed was increased. This interesting result will be discussed later, when data are compared for unsteady flow compressor operation with different types of vaned diffusers.

Pressure Oscillation Waveform and Phase Relationship. The flow oscillations at different points on the shroud wall were determined from the output of the dynamic pressure transducers. Figure 5 shows the typical pressure fluctuations at different locations for the three-cell rotating stall operating point at 12,500 rpm. As observed for conditions at all speed lines, the pressure fluctuations varied in intensity from impeller inlet to diffuser exit as shown in Table 1. The shroud pressure fluctuations were relatively large in general near the impeller exit and the diffuser semivaneless space. Low-pressure fluctuations existed at impeller inlet and diffuser channel exit. The pressure fluctuations at low operating speeds were much higher than those observed at higher speeds.

The waveform of the pressure fluctuations at impeller inlet ($x/s = 0.1$) in Fig. 5 also shows that the blade-to-blade pressure change in this region varied considerably during one cycle of

Table 1 Summary of results of unsteady flow measurements on a centrifugal compressor with a straight channel diffuser

reduced impeller speed n_{red} [min^{-1}]	reduced mass flow rate $\dot{m}_{red}$ [kg/s]	lobe number m	upstream of impeller	x/s = 0.1	x/s = 0.55	x/s = 1.0	diffuser inlet	diffuser throat	diffuser channel exit	pattern rotational speed ratio	comments
10800	2.69	-3 -4	• •	▫ •	▫ ▫	□ □	□ □	□ □	▫ •	0.089 0.016	intermittent occurrence of rotating stall
10800	2.62	-3 -4	• •	• ▫	▫ □	□ □	▫ □	▫ □	• ▫	0.087 0.021	intermittent occurrence of r. s.
12500	2.99	-3	□	□	□	□	□	□	□	0.06	intermittent occurrence of r. s.
13000	3.86	-2 -4	• •	• •	▫ ▫	▫ ▫	▫ ▫	▫ ▫	• •	0.212 0.012	
13000	3.79	-2 -4	• •	• ▫	▫ □	▫ □	▫ □	▫ □	• ▫	0.212 0.012	
13600	4.14	-2	•	•	▫	▫	▫	▫	•	0.198	
14200	4.42	-2	•	•	▫	▫	▫	▫	•	0.173	
14500	4.65	-2	•	•	▫	▫	▫	▫	•	0.156	

□ ≙ 1000 Pa

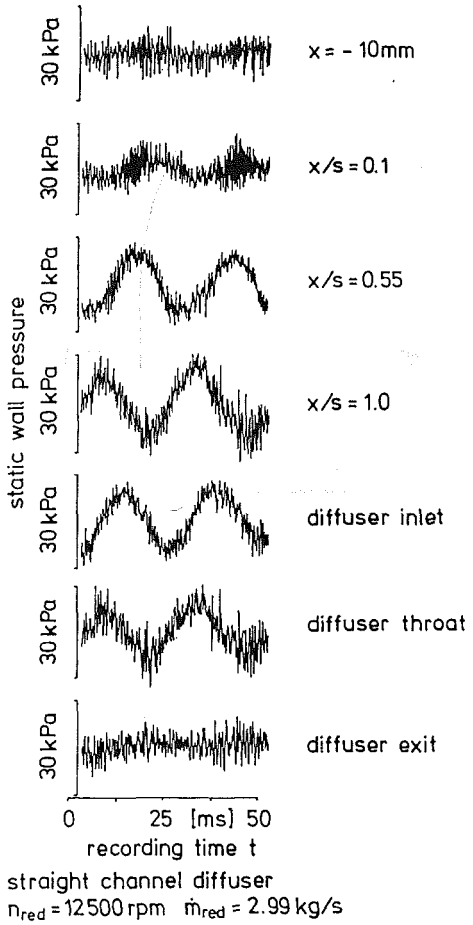

Fig. 5 Pressure signals in the time domain from transducers along the flow path in the compressor

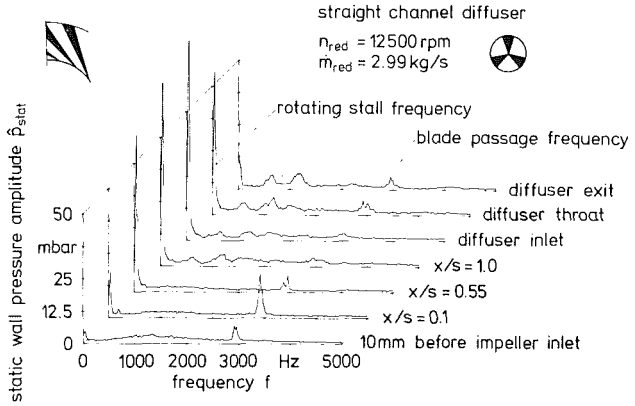

Fig. 6 Analysis of unsteady pressure data recorded at compressor operation during occurrence of the three-cell rotating stall; flow characteristics at different meridional locations along the flow path

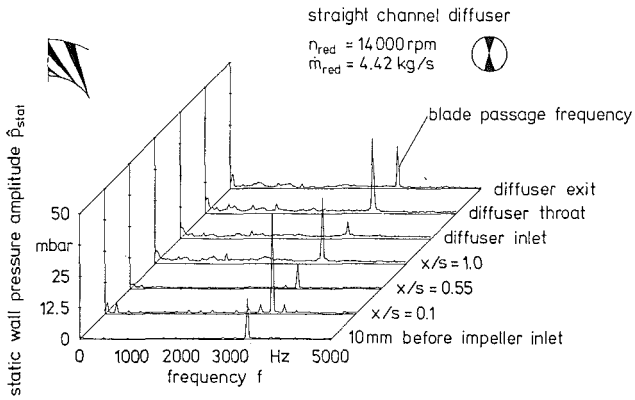

Fig. 7 Pressure spectra from signals along the flow path in the compressor at the *two-cell rotating stall* operating conditions

flow oscillations. This behavior shows great coincidence to corresponding conditions on the compressor with the cambered vane diffuser, as described by Haupt et al. (1988). It has been demonstrated by these data, and confirmed by means of other measurement techniques, that flow conditions in the impeller inlet near shroud change periodically from forward to reverse flow directions. Favorable conditions, characterized by high blade-to-blade pressure differences in the signal at $x/s = 0.1$, are obtained in the forward flow time period, resulting in a high level of downstream pressure level ($x/s = 0.55$). Low blade-to-blade pressure difference at $x/s = 0.1$ signifies reverse flow conditions near shroud, leading to a corresponding low level of pressure at $x/s = 0.55$.

In addition, time domain signals along the flow path in Fig. 5 show very significant phase shifts. As a surprising result it can be concluded that even in the impeller channel there is no in-phase behavior of the pressure oscillations as was expected. From the signal at impeller inlet in the downstream direction, the phases are shifting continuously to a maximum angle at diffuser inlet, before the phase difference decreases again toward the diffuser exit. Phase relationships in Fig. 5 for the three-cell rotating stall at 12,500 rpm are similar to those, obtained on the compressor with the cambered vane diffuser at 12,300 rpm, where also a three-lobe rotating stall was analyzed (see Abdel-Hamid et al., 1987, Fig. 10). It should be mentioned that phase relationships of the oscillating pressures as shown in Fig. 5 were nearly constant over the whole range of rotating stall occurrence.

Investigation of the Nature of Pressure Oscillations. Further insight into the flow characteristics during rotating stall compressor operation was obtained in plotting the frequency spectra of the different pressure signals from transducers along the flow path. In Figs. 6 and 7 those spectra are shown for two characteristic compressor operation conditions, representing the three and two-lobe rotating pattern occurrence at 12,500 and 14,000 rpm, respectively. Comparing these two diagrams, a typical broadband behavior, mainly in the frequency range 0–3000 Hz, can be observed in Fig. 6. Different from this characteristic, a minimum of pressure fluctuation amplitudes is obtained in the impeller zone in the whole considered frequency range (away from discrete oscillations) for the two-lobe-pattern operation at 14,000 rpm in Fig. 7. This broadband behavior of the pressure signals, as shown in Fig. 6, was investigated on the same compressor by Haupt et al. (1988), and could be analyzed as a reverse flow in the impeller zone near the shroud, directed from the impeller outlet toward the inlet close to the blade suction side. According to these results, pressure spectra in the impeller range in Fig. 6 give clear indication to reverse flow up to a location *before impeller inlet* regarding especially conditions at $x = -10$ mm. The lower significance of broadband signal behavior in Fig. 7 can be related to a much lower intensity of the reverse flow. On its way upstream from the impeller outlet it does obviously not affect the blade inlet zone, which responds sensitively to reverse flow excitation. The front of the reverse flow, where it mixes with the forward flow, seems to be located more downstream in the impeller inlet zone, compared to conditions in Fig. 6.

The corresponding blade vibration characteristics were analyzed and plotted in Figs. 8 and 9 to confirm the difference

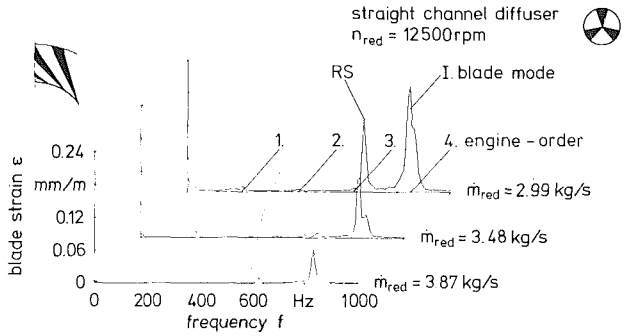

Fig. 8 Blade response to broadband pressure fluctuations shown in Fig. 6 for various mass flow rates

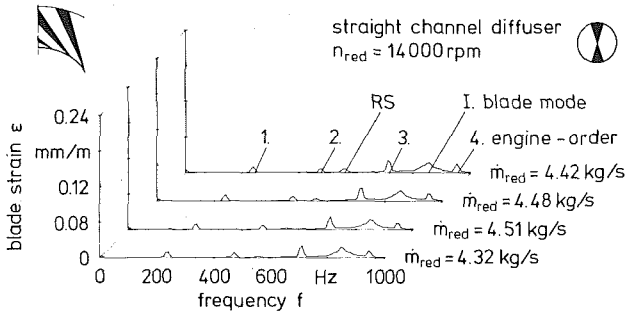

Fig. 9 Blade response to unsteady flow excitation (two cells) shown in Fig. 7 for various mass flow rates

between the amplitudes of the broadband pressure fluctuations. Significant broadband excitation can be observed in the blade spectra in Fig. 8 when the mass flow is decreased and when the blade responds to the three-lobe rotating pressure pattern occurring at $\dot{m}_{red} = 2.99$ kg/s. Corresponding blade strain for the two-cell rotating stall at 14,000 rpm is plotted in Fig. 9 in the same scale, demonstrating the absence of broadband pressure fluctuations in the impeller inlet zone by the constant value of first blade mode stress level ($f_1 \approx 800$ Hz) toward lower values of mass flow. It can be concluded from the results in these two diagrams that reverse flow up to the blade leading edge zone characterizes flow conditions of the three-cell rotating stall at 12,500 rpm, while the extent of upstream directed reverse flow is considerably smaller for the two-lobe rotating pressure pattern at 14,000 rpm.

An oil injection experiment was conducted to confirm results mentioned above. Oil was injected in the flow channel near the impeller exit ($x/s = 0.8$) through a hole in the shroud wall, when the compressor was operated at 12,500 rpm and during occurrence of the three-cell rotating stall. The result of this experiment is given in Fig. 10, showing the colored dye, which represents reverse flow conditions near the shroud. It is demonstrated by this experiment that the reverse flow extends up to a location before the impeller inlet, as shown in this figure in a view of the impeller, before the shroud wall was disassembled.

Comparison Between the Characteristics of Flow Oscillations With Two Types of Vaned Diffusers

Corresponding results, obtained from experiments on the compressor with the cambered vane diffuser, were used for a comparison with data collected for the configuration with the straight channel diffuser as given above. This comparison was accomplished, in order to study the differences of the influence of the two types of vaned diffusers on the characteristics of unsteady flow. Corresponding results for the compressor with the cambered vane diffuser have been published recently by Abdel-Hamid et al. (1987).

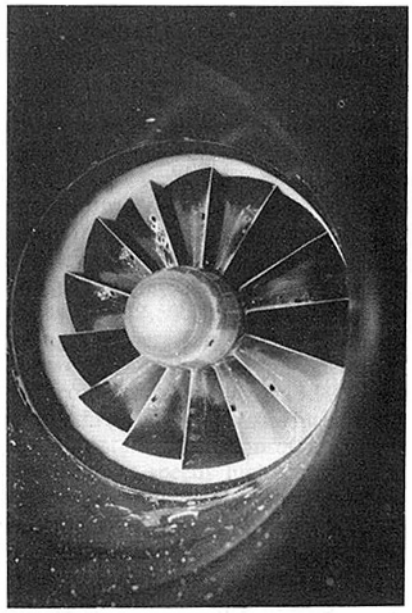

Fig. 10 Result of oil injection experiment at *three-cell rotating stall* compressor operation at 12,500 rpm and $\dot{m}_{red} = 2.99$ kg/s; for corresponding pressure and blade vibration analysis see Figs. 6 and 8, respectively; photo shows colored dye in the impeller zone after oil injection at $x/s = 0.8$

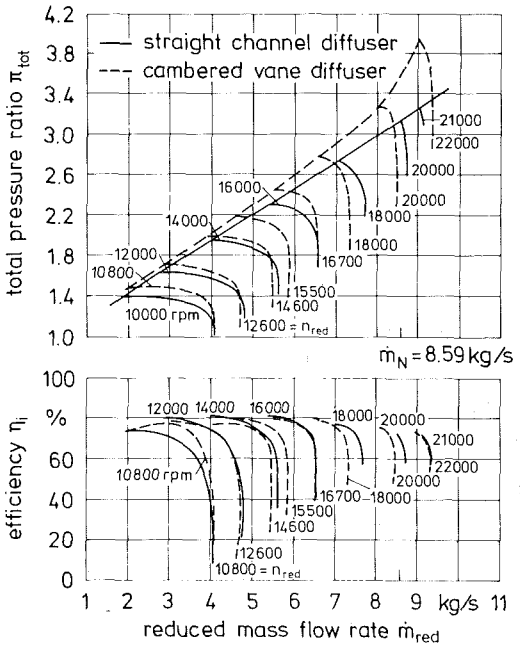

Fig. 11 Comparison of compressor characteristics

The use of the two different vaned diffusers interacting aerodynamically with the same impeller and collecting chamber results in differences in the compressor characteristics, as shown in Fig. 11. Concerning operating conditions in the unsteady flow regime, it is obvious that the surge line is shifted toward higher mass flow rates for the configuration with the straight channel diffuser, compared to the cambered vane type.

Table 2 Summary of results of unsteady flow measurements on a centrifugal compressor with a cambered vane diffuser

reduced impeller speed n_{red} (min^{-1})	reduced mass flow rate $\dot{m}_{red}$ (kg/s)	lobe number m	upstream of impeller	x/s = 0.1	x/s = 0.55	x/s = 1.0	diffuser throat	diffuser channel exit	pattern rotational speed ratio	comments
10800	–	–	–	–	–	–	–	–	–	
12300	3.19	-3	▪	▫	□	□	□	▫	0.06	intermittent occurrence of rotating stall
12300	3.04	-3	▪	▫	□	□	□	▫	0.05	steady rotating stall
13000	3.38	-3	·	▫	□	□	□	▫	0.04	strong intermittent occurrence of r. s.
13500	3.75	-2 -3	· ·	▪ ▪	▫ ▪	▪ ▪	▫ ▫	· ▫	0.194 0.04	
13500	3.69	-2 -3	· ·	▪ ▪	▫ ▫	▫ ▫	▫ ▫	▪ ▫	0.194 0.04	
14000	4.07	-2	·	▪	▫	▫	▫	▪	0.17	intermittent occurrence of r. s.
14000	3.94	-2	▫	▫	□	□	□	▫	0.17	intermittent occurrence of r. s.
14000	3.87	-2	▫	□	□	□	□	▫	0.17	steady r. s.
14500	4.3	-2	▫	□	□	□	□	▫	0.148	intermittent occurrence of r. s.
14500	4.07	-2	▫	□	□	□	□	□	0.148	steady r. s.

□ ≙ 1000 Pa

Comparison of Lobe Number and Intensity of Pressure Oscillations. In order to compare data with those given in Table 1 for the compressor with the straight channel diffuser, Table 2 shows the characteristics of flow oscillations analyzed from measurements on the compressor with the cambered vane diffuser. The pressure fluctuations in Table 2, associated with the two-lobe pattern observed at compressor speeds of 14,000 rpm and higher, were large in an absolute sense and were as much as four times larger than those observed at the lower speeds of 13,000 rpm and below in a relative sense. For the straight channel diffuser, the intensity of the pressure fluctuations was large in an absolute sense only at compressor speed of 12,500 rpm. At higher and lower speeds the intensities were reduced and were very low at compressor speeds of 13,500 rpm and higher.

In addition, comparison between the compressor maps with the two types of diffusers showed that the onset of flow oscillations for a given compressor speed occurs at a relatively higher mass flow rate for the straight channel diffuser than for the cambered vane diffuser, as also can be expected from the differences in the surge margin shown in Fig. 11.

Moreover, for the speed lines of 10,800 and 13,600 rpm, flow oscillations existed with the straight channel diffuser, and did not with the cambered vane diffuser prior to the occurrence of surge. The compression system with the cambered vane diffuser therefore is more stable than with the straight channel diffuser, although the pressure fluctuations associated with self-excited flow oscillations were more intense for the cambered vane diffuser than for the straight channel diffuser.

Comparison of Rotational Speed of Pressure Patterns. While differences in the variation of the pressure fluctuation intensity with the compressor operating speed were obtained for the two types of vaned diffusers, a surprising result was obtained when the corresponding speed ratios of the nonuniform flow patterns were compared. As shown in Fig. 12 the speed ratios for the two types of diffuser correlate quite well. According to this important diagram, high lobe numbers of rotating pressure patterns are associated with a low speed ratio of the patterns and vice versa. In addition, coincidence for both types of diffusers can not only be obtained for the general decrease of rotational pattern speed, when the impeller

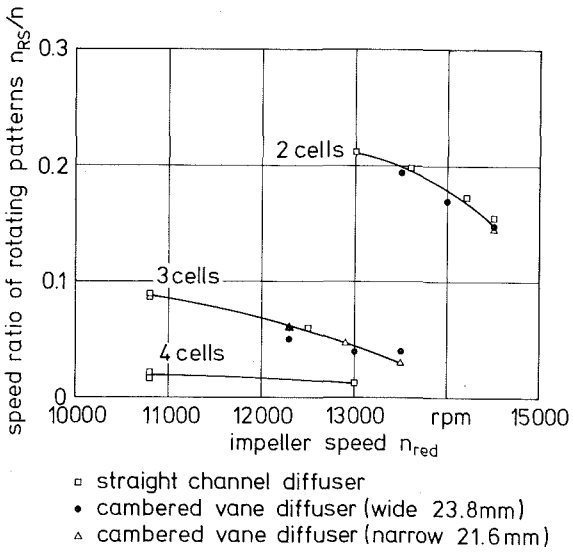

Fig. 12 Comparison of rotational speed of the different pressure patterns for three types of vaned diffusers

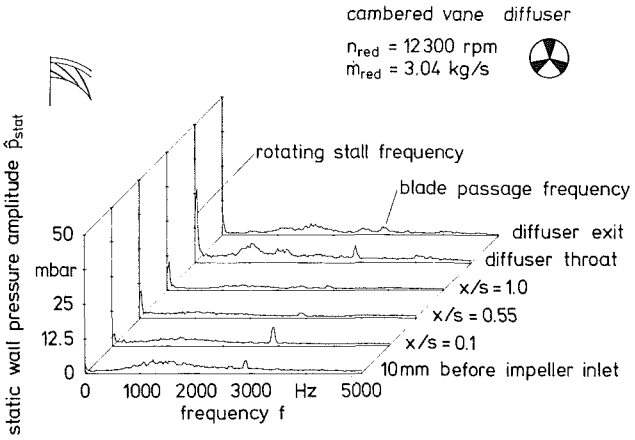

Fig. 13 Corresponding results of unsteady pressure measurements on the compressor with the cambered vane diffuser; *three-cell rotating stall* at n_{red} = 12,300 rpm

speed is increased, but also in the absolute values of the rotational speeds of the flow patterns, and the speed range of occurrence of distinct lobe numbers.

In order to generalize this information, corresponding data obtained on the same compressor with an additional type of diffuser are plotted in Fig. 12. This third diffuser has the same vane shape as the cambered vane one, but has a smaller width of 21.6 mm compared to 23.8 mm for the wide aerodynamic diffuser. All the data obtained for this diffuser also correlate well with the corresponding results of the two other configurations.

Comparison of the Characteristics of Rotating Flow Patterns. Results of an analysis of pressure signals recorded on the compressor with the cambered vane diffuser—corresponding to those in Figs. 6 and 7 for the straight channel diffuser—are plotted in Figs. 13 and 14. These results are presented for two different rotational speeds, 12,300 and 14,500 rpm, where a three and a two-cell rotating stall, respectively, could be analyzed (see Table 2). Similar to results for the straight channel diffuser in Figs. 6 and 7, characteristic broadband pressure fluctuations can be observed in Fig. 13 for the three-lobe pattern, while much lower pressure amplitude

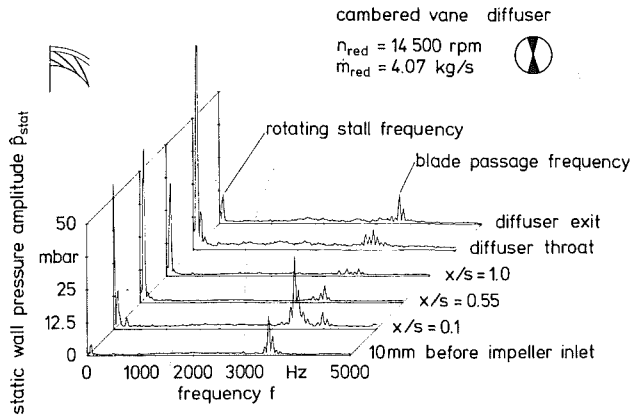

Fig. 14 Pressure spectra from signals along the flow path in the compressor with the cambered vane diffuser at the *two-cell rotating stall* operating conditions

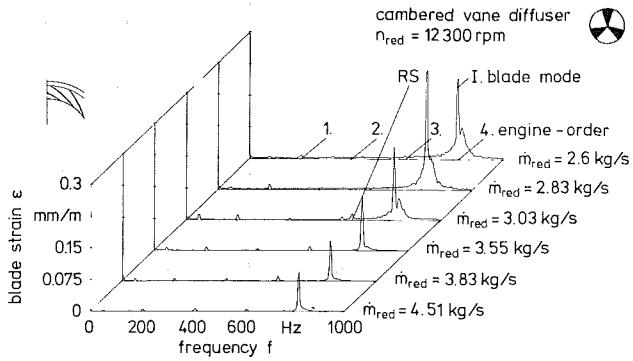

Fig. 15 Blade response to pressure conditions as shown in Fig. 13 for various mass flow rates

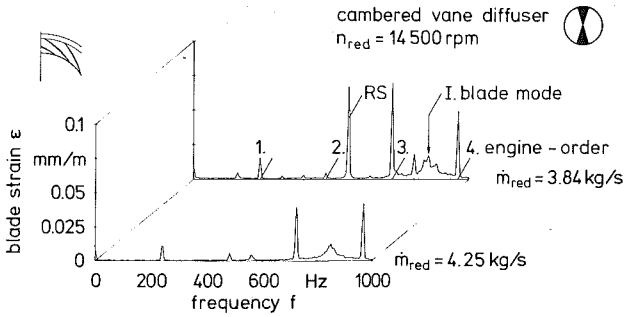

Fig. 16 Blade response to pressure conditions as shown in Fig. 14 for various mass flow rates

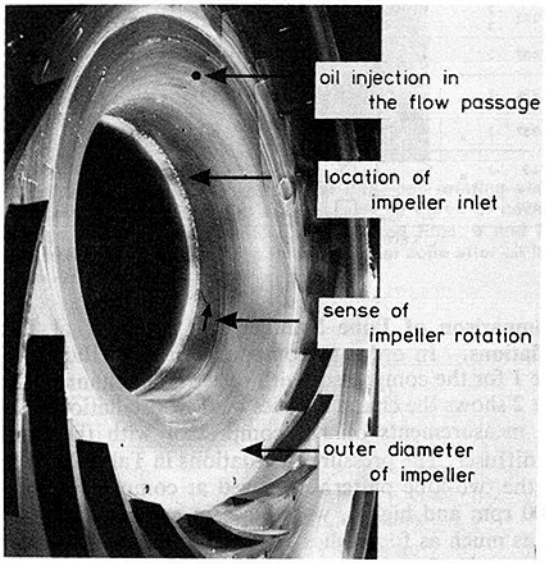

Fig. 17 Result of oil injection experiment on the compressor with the cambered vane diffuser; n = 12,300 rpm; $\dot{m}_{red}$ = 2.83 kg/s; *RS three cells*; oil injection at x/s = 0.8; for corresponding pressure and blade vibration analysis see Figs. 13 and 15

levels are obtained in the frequency range up to 3000 Hz for the two-cell rotating stall, although the absolute pressure oscillation amplitude of this unsteady flow pattern was found to be the highest.

Corresponding blade vibration spectra are given in Figs. 15 and 16, similar to results for the straight channel diffuser in Figs. 8 and 9. Spectra of signals in Fig. 15, recorded at different mass flow rate compressor operations, demonstrate again the increase of blade vibration amplitude toward lower mass flow due to the increasing broadband nature of the signal. This again can be associated with the occurrence of reverse flow ranging *up to a location at impeller inlet*. An oil injection experiment at this operating point with results as shown in Fig. 17 confirms this result.

Similarly to the blade vibration data in Fig. 9, the blade response to unsteady flow at $\dot{m}_{red} = 14{,}500$ rpm is shown in Fig. 16 for two operating conditions near surge.

The spectrum obtained at $\dot{m}_{red} = 4.25$ kg/s represents conditions on the verge of rotating stall, as can be identified by the weak response in the spectrum. Reducing the mass flow to $\dot{m}_{red} = 3.84$ kg/s, the blade response to the two-lobe rotating stall, directed opposite to the impeller rotation, increases significantly. According to Abdel-Hamid et al. (1987), the blade frequency due to rotating stall excitation f_{bl} is equal to $m \cdot f_s \pm f_p$, where m signifies the lobe number, f_s the shaft rotation frequency, and f_p the pressure oscillation frequency, recorded from a fixed transducer. In this equation "+" and "−" represent the rotational direction of the traveling cell against or with the impeller, respectively. In the present case in Fig. 16, the blade frequency excited due to rotating stall occurrence is

$$f_{bl} = (2 \times 244) + 76 = 564 \text{ Hz}$$

In this equation, the "actual" rotational speed of the impeller had to be used, which was slightly different from the reduced value.

The essential result in Fig. 16 can be obtained by observing the I. mode behavior of the blade. The intensity of the first mode excitation in the range of $f_I \approx 800$ Hz remains nearly constant at a low absolute value of blade stress level and demonstrates the absence of broadband spectrum behavior. In contrast to conditions in Fig. 15, this means that the reverse flow does not affect the blade inlet zone, which is sensitive to reverse flow excitation. How far upstream the reverse flow is moving from impeller outlet under these operating conditions was investigated again by an oil injection experiment with results shown in Fig. 18. The shroud wall after disassembly is shown, after compressor operation at $n_{red} = 14{,}500$ rpm and $\dot{m}_{red} = 3.84$ kg/s and oil injection near impeller outlet at $x/s = 0.8$. Two-cell rotating stall conditions, as represented by the data in Figs. 14 and 16, are obviously characterized by reverse flow in the impeller range near shroud ranging only up to $x/s \approx 0.35$, which is the location of the leading edge of the splitter blade.

Conclusions Concerning the Nature of Rotating Flow Patterns. The nature of rotating stall on centrifugal compressors with vaned diffusers has been interpreted by Haupt et al. (1988) and Chen et al. (1987) as a reverse flow phenomenon in the impeller as part of a Karman vortex system. According

to this model, rotating stall may occur when the reverse flow near shroud and close to the blade suction side extends upstream up to the blade leading edge and mixes with the downstream flow near impeller inlet. This behavior could experimentally be confirmed by results given above for the compressor with the straight channel diffuser and for the cambered vane diffuser as well.

Very important differences were obtained concerning the upstream extension of reverse flow for rotating stall of two lobes occurring at higher rotational speed and for the three-lobe rotating stall obtained for both diffuser configurations at lower impeller speed. According to the results described above, the three-cell rotating stall shows flow behavior in the impeller range near the shroud, characterized by reverse flow up to the *leading edge of the long blade*, mixing with the forward flow at impeller inlet ($x/s=0$). In contrast to this flow behavior near the shroud, the two-cell rotating stall could be analyzed as a rotating reverse flow, extending only up to the *leading edge of the splitter blade*, mixing with forward flow here at $x/s=0.35$. These characteristics were confirmed by pressure and blade vibration data and by results of oil injection experiments as well.

Results of an additional oil injection experiment in the intermediate zone at 13,150 rpm between the occurrence of a three and a two-cell rotating stall are shown in Fig. 19. Colored dye representing reverse flow conditions near the shroud can be observed on the shroud wall up to $x/s=0.35$ except for one location on the circumference—as shown in the figure—where the reverse flow intensity is strong enough to reach the leading edge of the long blade.

The important correlation between lobe number of occurring rotating stall and upstream extension of the reverse flow phenomenon is the coincidence between the results for both types of vaned diffuser. This correlation and the coincidence of rotational speed of different rotating patterns, as shown in Fig. 12, demonstrate the significant role of impeller flow characteristics for the unsteady flow behavior of centrifugal compressors with vaned diffusers.

Conclusions

1 Self-excited flow oscillations, which can be represented by the rotation of nonuniform flow patterns, have been clearly observed in a centrifugal compressor with a straight channel vaned diffuser, as the mass flow was reduced at constant rotational speed.

2 Several rotating patterns with two, three, and four lobes were observed at different compressor operating conditions. As was the case of the cambered vane diffuser investigated earlier, the direction of rotation of the patterns was always opposite to that of the impeller.

3 The intensity of the shroud wall pressure fluctuations during oscillation varied with compressor operating conditions. The highest intensity was obtained at an intermediate speed of 12,500 rpm. At lower and higher operating speeds the intensity was reduced sharply.

4 A comparison of unsteady flow characteristics for the compressor with the straight channel and the cambered vane diffuser shows great similarity in the speed of rotation of the observed nonuniform flow patterns for both diffusers, dependent on the number of lobes in the patterns. The smaller the number of lobes, the larger the speed of rotation. Generally the rotational speed of patterns decreases with increasing rotational impeller speed for a constant lobe number. Coincidence in the rotatonal speed of patterns and occurrence of lobe numbers could be demonstrated in addition for a cambered vane diffuser of $\approx$ 10 percent smaller width.

Differences in this comparison were obtained in the intensity of occurring unsteady pressure oscillations, showing maximum values at 12,500 rpm for the three-lobe rotating stall for the straight channel diffuser, while corresponding conditions on the cambered vane diffuser were obtained at 14,500 rpm for the occurrence of a two-cell rotating stall.

5 Results on the nature of rotating stall flow patterns were obtained by means of pressure and blade vibration data and, in addition, by oil injection experiments. A correlation valuable for both compressor configurations, the straight channel and the cambered vane diffuser, could be found between the lobe number of occurring rotating stall and the upstream extent of the reverse flow phenomenon. The three-cell rotating stall was associated with the occurrence of reverse flow up to the *leading edge of the long blade* before mixing with the forward flow in the impeller inlet zone. Conditions of the two-cell rotating stall for both diffuser configurations oc-

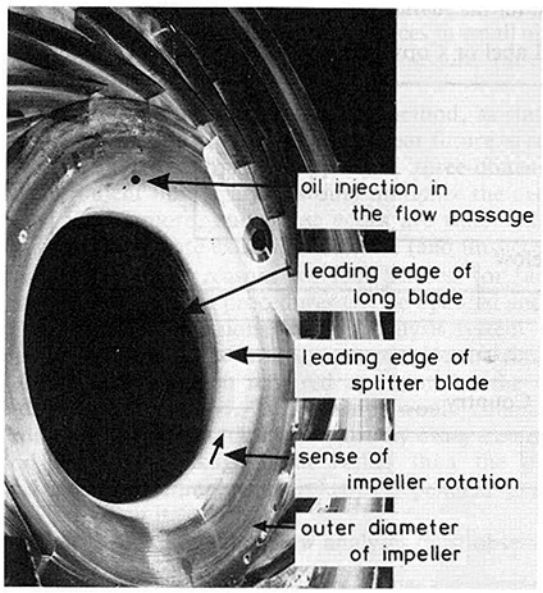

Fig. 18 Corresponding result of oil injection experiment at $n=14{,}500$ rpm; $\dot{m}_{red}=3.84$ kg/s; *RS two cells*; oil injection at $x/s=0.8$; for corresponding pressure and blade vibration analysis see Figs. 14 and 16

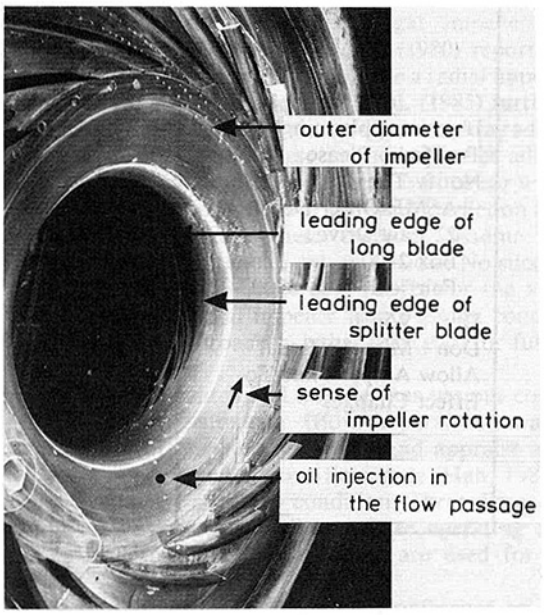

Fig. 19 Result of oil injection experiment when operating the compressor with the cambered vane diffuser in the intermediate range between the zones of two and three-cell rotating stall occurrence at $n=13{,}150$ rpm in the unsteady flow regime

curring at higher speed are characterized by reverse flow near shroud up to *the leading edge of the splitter blade*, and thus extending only up to a plane near $x/s = 0.35$. This coincidence and the correlation concerning the rotational speeds of rotating patterns show the significant role of impeller flow for the unsteady flow behavior of centrifugal compressors with vaned diffusers.

Acknowledgments

The research described in this paper was funded by the German Research Association (DFG). This institution also enabled Professor Abdel-Hamid to work in Hannover and to contribute to this paper. The authors gratefully acknowledge this support.

The authors would like to thank Mr. Tanneberg and Ms. Schleifer for their contribution to research work presented here.

References

Abdel-Hamid, A. N., Colwill, W. H., and Barrows, J. F., 1979, "Experimental Investigation of Unsteady Phenomena in Vaneless Radial Diffusers," ASME *Journal of Engineering for Power*, Vol. 101, pp. 52–60.

Abdel-Hamid, A. N., 1980, "Analysis of Rotating Stall in Vaneless Diffusers of Centrifugal Compressors," *Canadian Aeronautics and Space Journal*, Vol. 28, No. 2, pp. 118–128,; also ASME Paper No. 80-GT-184.

Abdel-Hamid, A. N., 1981, "Effects of Vaneless Diffusor Geometry on Flow Instability in Centrifugal Compression Systems," *Canadian Aeronautics and Space Journal*, Vol. 29, No. 3, pp. 259–288.

Abdel-Hamid, A. N., 1987, "A New Technique for Stabilizing the Flow and Improving the Performance of Vaneless Radial Diffusers," ASME JOURNAL OF TURBOMACHINERY, Vol. 109, pp. 36–40.

Bammert, K., et al., 1974, "Untersuchung der Laufradströmung in hochbelasteten Radialverdichterrädern," *Forschungsberichte Verbrennungskraftmaschinen*, Vol. 155.

Bammert, K., Jansen, M., and Rautenberg, M., 1983, "On the Influence of the Diffuser Inlet Shape on the Performance of a Centrifugal Compressor Stage," ASME Paper No. 83-GT-9.

Van den Braembussche, R. A., Frigne, P., and Roustan, M., 1980, "Rotating Non-uniform Flow in Radial Compressors," AGARD Conference Reprint 282, Paper No. 12.

Abdel-Hamid, A. N., Haupt, U., and Rautenberg, M., 1987, "Unsteady Flow Characteristics in a Centrifugal Compressor With Vaned Diffuser," ASME Paper No. 87-GT-142.

Chen, Y. N., Haupt, U., and Rautenberg, M., 1987, "On the Nature of Rotating Stall in Centrifugal Compressors With Vaned Diffusers, Part II: Karman Vortices as the Controlling Mechanism," Paper No. 87-TOKYO-IGTC-23.

Chen, Y. N., Haupt, U., and Rautenberg, M., 1988, "The Vortex-Filament Nature of the Reverse Flow at Rotating Stall Onset," ASME Paper No. 88-GT-120.

Frigne, P., and Van den Braembussche, R. A., 1985, "A Theoretical Model for Rotating Stall in the Vaneless Diffuser of a Centrifugal Compressor," ASME *Journal of Engineering for Gas Turbines and Power*, Vol. 107, pp. 507–513.

Haupt, U., and Rautenberg, M., 1982, "Investigation of Blade Vibration of Radial Impellers by Means of Telemetry and Holographic Interferometry," ASME *Journal of Engineering for Gas Turbines and Power*, Vol. 104, pp. 838–843.

Haupt, U., Abdel-Hamid, A. N., Kaemmer, U., and Rautenberg, M., 1986, "Excitation of Blade Vibration by Flow Instability in Centrifugal Compressors," ASME Paper No. 86-GT-283.

Haupt, U., Rautenberg, M., and Abdel-Hamid, A. N., 1988, "Blade Excitation by Broad-Band Fluctuations in a Centrifugal Compressor," ASME JOURNAL OF TURBOMACHINERY, Vol. 110, pp. 129–137.

Haupt, U., Chen, Y. N., and Rautenberg, M., 1987, "On the Nature of Rotating Stall in Centrifugal Compressors With Vaned Diffusers, Part I: Detection of Reverse Flow," Paper No. 87-TOKYO-IGTC-22.

Japikse, D., 1984, "Turbomachinery Diffuser Design Technology, The Design Technology Series (DTS-1)," Concepts ETI, Inc., Norwich, VT.

Kaemmer, U., and Rautenberg, M., 1986, "A Distinction Between Different Types of Stall in a Centrifugal Compressor Stage," ASME *Journal of Engineering for Gas Turbines and Power*, Vol. 108, pp. 83–93.

Kinoshita, Y., and Senoo, Y., 1985, "Rotating Stall Induced in Vaneless Diffusers of Very Low Specific Speed Centrifugal Blowers," ASME *Journal of Engineering for Gas Turbines and Power*, Vol. 107, pp. 514–521.

Stein, W., and Rautenberg, M., 1987, "Analysis of Measurements in Vaned Diffusers of Centrifugal Compressors," ASME Paper No. 87-GT-170.

Application of Viscous Flow Computations for the Aerodynamic Performance of a Backswept Impeller at Various Operating Conditions

C. Hah
Corporate Research and Development.

A. C. Bryans

Z. Moussa

M. E. Tomsho

Aircraft Engine Business Group.

General Electric Company,
Schenectady, NY 12301

Three-dimensional flowfields in a centrifugal impeller with backswept discharge at various operating points have been numerically investigated with a three-dimensional viscous flow code. Numerical results and experimental data were compared for the detailed flowfields and overall performance of the impeller at three operating conditions (optimum efficiency, choke, and near-surge conditions). The comparisons indicate that for engineering applications the numerical solution accurately predicts various complex real flow phenomena. The overall aerodynamic performance of the impeller is also well predicted at design and off-design conditions.

Introduction

The complexity of flow in a centrifugal impeller is well described and documented (Moore, 1973; Dean, 1978; Fowler, 1968). The design of three-dimensional passages has evolved and developed to the present status of the quasi-three-dimensional design method. These quasi-three dimensional design/analysis systems are backed by an extensive experimental data base. Presently, because of the highly advanced centrifugal impellers, experimental development programs are time consuming and costly. Further advances in small aircraft engine technology will require higher pressure ratio centrifugals to reduce size, weight, and cost.

Although the advanced flow analysis method, as stated by Hartmann (1980), will not be used in the near future to replace the experimental development approach, three-dimensional viscous/turbulent flow analyses would minimize the need for redesign. Furthermore, once these codes are validated, they can be used to evaluate existing successful (and unsuccessful) designs to explain the reasons for their success (or failure). Thus, design criteria and procedures can be updated and used in the quasi-three-dimensional design/analysis system. Also, three-dimensional viscous analysis can provide the final loss and blockage distribution required as input for the quasi-three-dimensional method. This strategy would enhance the capabilities of the present design method by using a consistent method for loss/blockage input rather than the present method of data matching, which is highly dependent on the individual executing it.

To be successful, advanced flow analyses must observe and suitably account for a wide variety of real flow phenomena shown to exist in a centrifugal impeller (Hartmann, 1980). Calculation methods, no matter how sophisticated they may be, are of no use unless they are properly verified against good, definitive test results.

In recent years, various attempts have been made to simulate the flowfield inside centrifugal impellers with numerical solutions. Moore and Moore (1980) reported the first successful solutions for the flow inside a radial impeller at design point with a PPNS code. Rhie et al. (1985) further extended the PPNS procedure for the solution inside a radial impeller at design condition. These methods predict adequate solutions at design condition. However, it is not clear whether these methods can be extended for the flow prediction at off-design condition, because these methods assume either parabolic or partially parabolic nature of flow. No successful numerical solutions have been reported yet for the viscous flow inside the centrifugal impeller at off-design conditions with any numerical approaches, either relaxation or full time marching.

The flow inside a centrifugal impeller has various complex three-dimensional phenomena (flow separation, wake-jet structure, etc.). In this study we apply and appraise a fully elliptic, three-dimensional viscous flow code (Hah, 1987) for the realistic geometry and flow condition. Three-dimensional flows inside a backswept impeller at three operating conditions (near-stall, optimum, and choke) are used for comparison and evaluation.

Inspired by the 1980–1981 Stanford Conference on Complex Turbulent Flow (Bradshaw et al., 1968), we have tried to follow a similar strategy and approach in assessing the prediction capability of the present code. The basic approach is to

Contributed by the International Gas Turbine Institute and presented at the 33rd International Gas Turbine and Aerospace Congress and Exhibition, Amsterdam, The Netherlands, June 5–9, 1988. Manuscript received at ASME Headquarters February 11, 1988. Paper No. 88-GT-39.

assess the test data and their uncertainties before attempting to assess the validity of the code capabilities. To establish the code's capability, it must be evaluated against a wide range of operating conditions.

For the appraisal of numerical results, we established the following purposes:

- offer a method of validating the code that is consistent with the proposals and recommendation found in Hartmann (1980) and Bradshaw et al., (1968), and
- delineate the importance of defining proper physical quantities when comparison is made.

In the following sections, the governing equations and numerical procedure are described. The evaluation of the experimental data for comparison with the numerical solution is discussed, and numerical results are then compared with the measured data. The conclusions drawn from this study are given in the final section.

Governing Equations

The equations used are the Reynolds-averaged Navier–Stokes equations, which can be written on a Cartesian frame as

$$\frac{\partial}{\partial x_i}(\rho U_i) = 0 \tag{1}$$

$$\frac{\partial}{\partial x_j}(\rho U_i U_j) + 2\rho\, \epsilon_{ijk}\Omega_j U_K = -\frac{\partial p}{\partial x_i} + \frac{\partial}{\partial x_j}\left[\mu\left(\frac{\partial U_i}{\partial x_j} + \frac{\partial U_j}{\partial x_i} - \frac{2}{3}\frac{\partial U_k}{\partial x_k}\delta_{ij}\right) - \rho\overline{u_i u_j}\right] + F_i \tag{2}$$

$$\frac{\partial}{\partial x_j}(\rho U_j e) = \frac{\partial}{\partial x_j}\left[\left(\frac{\mu}{\mathrm{Pr}}\right)_{\mathrm{eff}}\frac{\partial T}{\partial x_j}\right] - \frac{\partial}{\partial x_j}(pU_j) + U_i F_i + \frac{\partial}{\partial x_j}\left[U_i\mu\left(\frac{\partial U_i}{\partial x_j} + \frac{\partial U_j}{\partial x_i} - \frac{2}{3}\frac{\partial U_k}{\partial x_k}\delta_{ij}\right)\right] \tag{3}$$

$$p = \rho R T \tag{4}$$

where U_i = mean velocity, u_i = fluctuating velocity, e = total energy, Ω_i = angular velocity, F_i = additional body force,

$$-\overline{\rho u_i u_j} = \mu_{\mathrm{eff}}\left(\frac{\partial U_i}{\partial x_j} + \frac{\partial U_j}{\partial x_i}\right) - \frac{2}{3}\rho k\delta_{ij}$$

$$\left(\frac{\mu}{\mathrm{Pr}}\right)_{\mathrm{eff}} = \left(\frac{\mu}{\mathrm{Pr}}\right)_{\mathrm{laminar}} + \left(\frac{\mu}{\mathrm{Pr}}\right)_{\mathrm{turbulent}}$$

and

$$e = C_v T + \frac{1}{2}U_i U_i$$

Several previous studies have indicated that the turbulent flow inside the impeller is very complex and the turbulence structure is significantly affected by the streamline curvature and the rotation. Because the goal of this study is to integrate viscous flow calculation into the design system, rather simpler turbulence models have been considered. Although the zero-equation and one-equation models have the advantage of relative simplicity, specification of proper length scale of the models is not well known for the current flows. A modified k–ϵ, two-equation model is used to estimate Reynolds stresses for the current study. The turbulence model is extended to the solid wall following the studies of Chien (1982), and wall function treatment is not used. The following additional transport equations are solved to calculate turbulent stress terms:

$$\frac{\partial(\rho U_i k)}{\partial x_i} = \frac{\partial}{\partial x_i}\left(\frac{\mu_{\mathrm{eff}}}{\sigma_k}\frac{\partial k}{\partial x_i}\right) - \rho\,\overline{u_i u_j}U_{i,j} - \rho\epsilon - \frac{2\mu k}{\rho^2} \tag{5}$$

$$\frac{\partial(\rho U_i \epsilon)}{\partial x_i} = \frac{\partial}{\partial x_i}\left(\frac{\mu_{\mathrm{eff}}}{\sigma_\epsilon}\frac{\partial \epsilon}{\partial x_i}\right) + C_1\frac{\rho\epsilon}{k}(\overline{u_i u_j}U_{i,j}) - \frac{\rho\epsilon}{k}\left(c_2 f\epsilon + \frac{2\nu k e^{-c_4 u_* l/\nu}}{l^2}\right) \tag{6}$$

where

$$\mu_{\mathrm{eff}} = \mu + C_\mu(k^2/\epsilon)[1 - \exp(-c_3 u_* l/\nu)]$$

and

$$f = 1 - \frac{0.4}{1.8}e - (k^2/6\nu\epsilon)^2$$

The effects of turbulence modeling or modification of the currently employed model for the flow inside the centrifugal compressor are not the purpose of the present work. Therefore, standard values of various constants of the turbulence modeling are used; the values are

$$C_\mu = 0.09, \quad C_1 = 1.35, \quad C_2 = 1.8, \quad \sigma_k = 1.0, \quad \sigma_\epsilon = 1.3,$$
$$C_3 = 0.0115, \quad C_4 = 0.5$$

Nomenclature

$C_1, C_2, C_3, C_4, C_\mu, \sigma_k, \sigma_\epsilon$ = constants in turbulence closure models
CM = total relative velocity
C_V = specific heat
D_{ij} = diffusion coefficient in equation (7)
F_i = additional body force in equation (2)
G_1, G_2, G_3 = convection coefficients in equation (7)
k = turbulence kinetic energy
k_c = thermal conductivity
P = $-\overline{u_i u_j}U_{ij}$
p = static pressure
R = gas constant
U_2 = impeller speed at exit
y/t = normalized coordinate along the pitch
z/b = normalized meridional coordinates across the channel
β = coefficient of thermal expansion
δ_{ij} = Kronecker delta
ϵ_{ijk} = permutation tensor
ν = kinematic viscosity
ρ = density
Ω_i = angular velocity of impeller

Subscripts

t = total
w = value at the wall
0 = upstream condition

Superscripts

$(\bar{\ })$ = average value

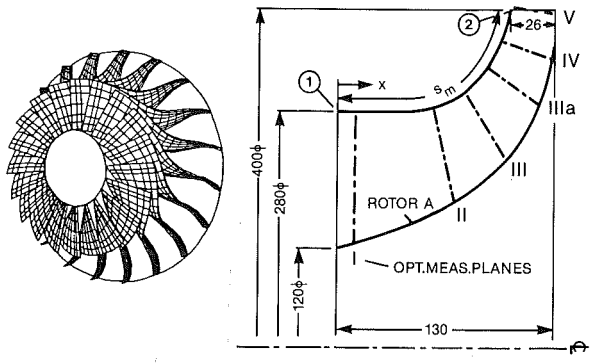

Fig. 1 Eckhardt impeller "A" and measurement planes

Numerical Scheme

The numerical solution scheme is based on a fully elliptic relaxation method with a fully conservative control volume approach. The finite difference equations (1)–(6) are formulated in terms of Cartesian momentum (ρU_i), static pressure (p), total internal energy (e), turbulence kinetic energy (k), and turbulence energy dissipation rate (ϵ). The steady-state solution is obtained through the elliptic relaxation of the finite difference equations and each relaxation step consists of one prediction and two correction steps.

With the static pressure field at the previous iteration, the momentum conservation equations are solved using the following equation on nonorthogonal body-fitted coordinates:

$$\frac{1}{J}\frac{\partial}{\partial\xi}(G_1\phi)+\frac{1}{J}\frac{\partial}{\partial\eta}(G_2\phi)+\frac{1}{J}\frac{\partial}{\partial\psi}(G_3\phi)$$
$$=\frac{1}{J}\frac{\partial}{\partial\xi}\left(\frac{\Gamma'_\phi}{J}D_{\xi\xi}\phi_\xi+\frac{\Gamma'_\phi}{J}D_{\xi\eta}\phi_\eta+\frac{\Gamma'_\phi}{J}D_{\xi\psi}\phi_\Psi\right)$$
$$+\frac{1}{J}\frac{\partial}{\partial\eta}\left(\frac{\Gamma'_\phi}{J}D_{\eta\xi}\phi_\xi+\frac{\Gamma'_\phi}{J}D_{\eta\eta}\phi_\eta+\frac{\Gamma'_\phi}{J}D_{\eta\psi}\phi_\Psi\right)$$
$$+\frac{1}{J}\frac{\partial}{\partial\psi}\left(\frac{\Gamma'_\phi}{J}D_{\psi\xi}\phi_\xi+\frac{\Gamma'_\phi}{J}D_{\psi\eta}\phi_\eta+\frac{\Gamma'_\phi}{J}D_{\psi\psi}\phi_\Psi\right)+\tilde{S}_\phi \tag{7}$$

where Γ'_ϕ is a diffusion coefficient, G_i is a velocity component along the transformed coordinates (ξ, η, ψ), and S'_ϕ consists of additional body force terms and pressure terms. A three-point central difference approximation is used for all the diffusion terms and a modified quadratic upwinding scheme is used for convection terms.

Because the coefficients of finite difference equation (7) are based on the values at the previous step, the resulting ρU_i does not satisfy mass conservation. Two correction steps are used to satisfy the mass conservation at each iteration. The concept of pressure-implicit splitting developed by Issa (1982) is used for the correction of p and ρU_i after the prediction step.

The two correction steps are as follows:

$$(\rho U_i)^{**}-(\rho U_i)^{*}=\Delta_p^{-1}\Delta_i(p^{*}-p^{n}) \tag{8}$$

$$(\rho U_i)^{n+1}-(\rho U_i)^{**}$$
$$=A_p^{-1}\Sigma A_{pm}[(\rho U)^{**}-(\rho U)^{*}]-\Delta_i(p^{n+1}-p^{*}) \tag{9}$$

For equations (8) and (9), the mass conservation condition is imposed as

$$\Delta_i(\rho U_i)^{**}=\Delta_i(\rho U_i)^{n+1}=0 \tag{10}$$

By combining equation (10) with equations (8) and (9), Poisson-type equations are obtained for ($p^{*}-p^{n}$) and ($p^{**}-p^{*}$) and the value of $(\rho U)_i^{n+1}$, p^{n+1} is calculated with the corrected pressure. With the correction step in equations (8)–(10), density is handled rather implicitly and (ρU_i) and p are updated. A single implicit step is used to calculate k, ϵ, and e with the corrected values of ρU_i and p. Further details of the method and applications to axial flow geometires are given by Hah (1987) and Hah and Leylek (1987).

Computational Grid and Boundary Conditions

Figure 1 shows the backswept impeller along with meridional measurement planes. The computations were carried out on H-type grids. The quality of the viscous flow solution, especially aerodynamic loss, depends on the density and topology of the computational grid (Hah and Leylek, 1987). Previous studies on the current impeller at design condition (Moore and Moore, 1980; Rhie et al., 1985) showed that relatively coarse grids (14 × 14 × 17 and 15 × 19 × 50) capture most of the flow structure for this geometry. Two sets of computational grids (16 × 21 × 56 and 26 × 31 × 56 in blade-to-blade, spanwise, and streamwise directions) were tested for the current flow. Because the solutions based on the finer grid do not change further, the solution based on the 16 × 21 × 56 grid was assumed to be close to grid-independent. In the spanwise direction, five nodes are located inside the tip clearance and exponential stretching is applied in all three grid directions. The flow inside tip leakage is computed as a part of the entire flow domain, with the shroud moving at constant circumferential speed. Details of the numerical handling of tip leakage flow are described in Hah (1986). No-slip and no-flux conditions are applied on the solid wall. The physical periodicity condition upstream and downstream of the blade row and inside tip clearance is imposed implicitly. At the inflow boundary, the distribution of total pressure, total temperature, and relative inlet flow angles are fixed. At the outflow boundary, which is located at $R/R_2 = 1.3$, the static pressure is fixed. For the turbulence, the experimental value of turbulent kinetic energy is used at the inflow boundary and the equilibrium condition is used to estimate the inflow condition of the turbulence dissipation rate. Residuals of each finite difference equation are integrated over the entire domain. When the integrated residuals of all the equations are reduced by four orders of magnitude from their initial value, the solution is considered to be converged. The code is vectorized on Cray-XMP and has an option to run an out-of-core solution (solid-state-disk storage on Cray-XMP) for large-scale problems.

Experimental Data Review and Comparison Criteria

When evaluating prediction results, particularly those of complicated phenomena, it is very important to assess the true quantitative certainty of the reference test data by which the validation process would be conducted (Bradshaw et al., 1968). Furthermore, when the validation process involves only one set of reference data, it is crucial to develop a hierarchic set of criteria by carefully reviewing such data. In this section we critically review the test data chosen for that particular objective, and we conclude this section by establishing the comparison criteria.

The data published by Eckardt (1980) were chosen as the test case for validating the present code results. The geometry data were obtained from Schuster and Schmidt-Eisenlohr (1980). Blade thickness distributions were obtained by scaling measurements from figures in Eckardt (1980). The Eckardt data are comprehensive and complete; the work offers detailed data of more than one operating point for the same impeller. Although Eckardt data are indispensible for the qualitative understanding of complex flow inside impellers, use of the data in validating numerical code necessitated the following review.

Eckardt carried out the flow measurements with three stages of instrumentation:

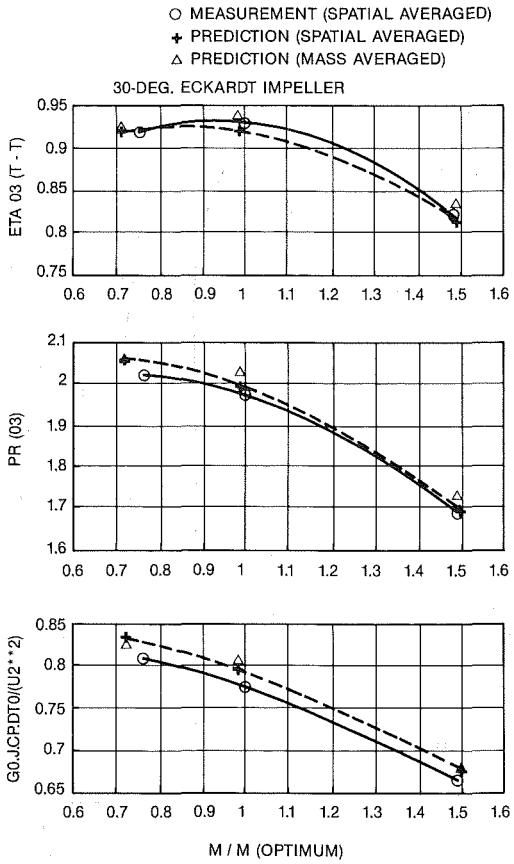

Fig. 2 Comparison of overall performance parameters

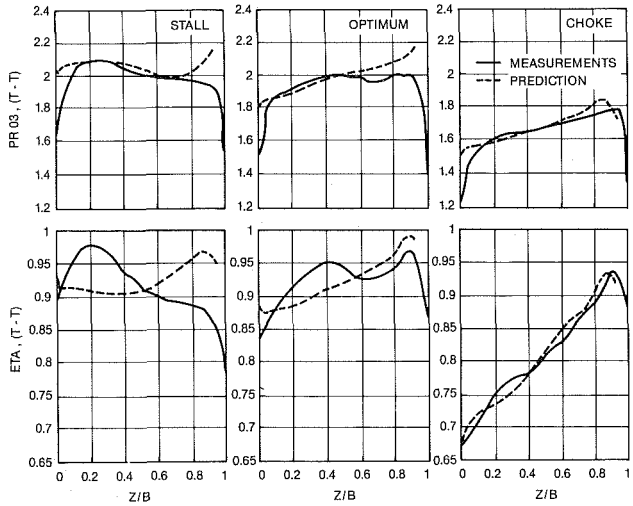

Fig.3 Comparison of total pressure and efficiency profiles

1 conventional, time-mean probe traverses of total pressure and temperature in the vicinity of the impeller and diffuser exits,

2 instantaneous static pressure recording over the shroud surface, and

3 local velocity measurements inside the impeller with Laser 2-Focus velocimeter (L2F). Measurements 1 and 2 are established techniques and direct by nature. The uncertainties involved with such techniques are known from vast experience to be within a narrow band, as stated by Eckardt (1976, 1980). Apart from instrument errors, the highest uncertainties usually are associated with correction and recovery factors for high Mach number operations.

The third type of measurement is statistical, as described by Schodl (1977). The basic outcomes of the L2F measurements are the component of the *absolute* velocity and its angle in a plane perpendicular to the beam axis. In addition to the basic instrument uncertainties, there are indirect uncertainties associated with the interpretation of statistical data. Such uncertainties depend on the assumptions and approximations made in interpreting the data and they are usually higher than those associated with the basic instruments. The following summarizes the basic features of the L2F method that pertain to data assessment:

1 The L2F acquires two-dimensional data in an absolute frame of reference, whereas the present data pertain to a rotating domain.

2 The combination of the rotor wheel speed and the finite time interval during which the laser beam is released results in a finite measuring volume; the tangential extent in the present case was 5 percent of blade spacing. The spanwise extent of the measuring volume is dictated by the active length of the beam. As a percent of blade span, surface V represents the worst conditions of 7.7 percent.

3 Interpretation of the data is based on the assumption of a stationary turbulent field (Schodl, 1977).

4 The data reduction, as reported in Eckardt (1976, 1980), implies that normal-type probability density distribution was assumed.

The above features can result in substantial ambiguities and uncertainties, as follows:

- Because of feature 1 above, the assumption made in feature 3 would be invalid. The degree of uncertainty is unclear.
- Because of feature 2, the limitations on the measurement interval, the resulting probability density distribution would suffer two effects: truncated and shifted. This uncertainty, along with the lack of longitudinal velocity component, can accentuate the interpretation error.
- In general, the probability density function in high layer (wakes, separation zones, etc.) is assymmetric, i.e., not of the normal distribution type. Thus, feature 4 implies that the reported data are the most probable values of velocity and angle rather than time-mean values.
- Unlike a single hot-wire measurement, a single L2F measurement is interpreted in terms of two events at relatively remote locations. Thus, the L2F measurements would include indiscernible time and space correlation effects.
- Rose (1962a, 1962b) delineates the difference between the mean flow angle and the angle of the mean flow. In the shear layer of a simple turbulent jet this difference can amount to up to 4 deg, mainly because of the cross correlation factor $\overline{u'v'}/U^2$. In the L2F measurements, there is ambiguity in the definition of the flow angle.

In view of the above considerations, the following criteria were established for comparison:

1 Overall performance parameters (mass average total temperature rise, total pressure, and adiabatic efficiency) must be met within the uncertainty band of the data acquired by conventional probes.

2 Spanwise variation of the circumferential average total pressure and adiabatic efficiency should compare favorably to that obtained by conventional probes.

3 Spatial as well as time-mean static pressure distribution on the shroud surface should be matched within the accepted instrument uncertainty band.

4 Spatial distribution of the measured velocity component perpendicular to the measurement surfaces C_m/U_2 should qualitatively compare well to the extent of depicting the complex developments of the flowfield.

Table 1 Comparison of overall performance

OVERALL PERFORMANCE COMPARISON:

$\dot{m}_{opt}$ = 4.540 Kg/sec
$P_{t,0}$ = 1.013×10^5 nt/m^2
$T_{t,0}$ = 288.1 °K
U_2^2/gJC_p = 85.6 °K

	Stall-Point		Optimum-Point		Choke-Point	
	Data	Code	Data	Code	Data	Code
Mass Flow Rate $\dot{m}/\dot{m}_{opt}$	0.752	0.714	1.000	0.987	1.487	1.493
Static Pressure $P_3/P_{t,0}$	—	1.549	1.490	1.483	1.195	1.212
Temp. Rise $gJC_p\ T_t/U_2^2$	0.810	0.833	0.770	0.792	0.661	0.674
Total Pressure Ratio $P_{t,3}/P_{t,0}$	2.015	2.054	1.965	1.986	1.681	1.690
Adiab. Efficiency η(t-t)	0.921	0.922	0.930	0.920	0.814	0.809

Table 2 Comparison of results obtained by different averaging methods

SPATIAL VS. MASS AVERAGES:

	Stall-Point		Optimum-Point		Choke-Point	
	Spat.	Mass.	Spat.	Mass.	Spat.	Mass
Temp. Rise $gJC_p\ \Delta T_t/U_2^2$	0.833	0.829	0.792	0.803	0.674	0.576
Total Pressure Ratio $P_{t,3}/P_{t,0}$	2.054	2.054	1.986	2.024	1.690	1.714
Adiab. Efficiency η(t-t)	0.922	0.927	0.920	0.936	0.809	0.828

Evaluation and Discussion of Code Results

Comparison of the numerical results with test data are presented below in the same sequence as established in the previous section.

Overall Performance Parameters. Figure 2 compares the overall performance parameters just downstream of the impeller exit (position 03 defined by Eckardt (1980) at radius ratio $R/R_2 = 1.075$). Test data in Fig. 2 are the *spatial* average of the traverse data in Fig. 6 of Eckardt (1980), which are also shown in Fig. 3 of the present paper. The numerical data shown represent two types of averages. The first average was obtained by mass average circumferentially (B-T-B) and then spatially averaged spanwise (H-T-S) for direct comparison with test data. The second type of average is a mass average over the whole surface. Note the remarkable agreement in both the shape of the performance characteristics and the quantitative values. Tables 1 and 2 provide the numerical information shown in Fig. 2. The predicted temperature rise curve is consistently higher than the test data by an almost fixed amount of 0.018. In absolute temperature units this amounts to 1.5 K. This difference may be due to test data uncertainties, uncertainties of tip clearance geometry, turbulence modeling, etc., and possibly the ambiguous definition of data average. The effect of ambiguity in defining averages is revealed by directly comparing the two types of averages of the numerical solution. It is quite clear that the difference displays inconsistent behavior, which is explained by the substantial differences of three-dimensional flow distribution at different operating points as discussed later (see Fig. 8). The total pressure distribution displays the same characteristics as the total temperature, and the same type of discussion applies. However, the agreement between numerical and test data probably is best when the overall adiabatic efficiency is considered. Comparing the data with the appropriate prediction curve (i.e., spatial average, one notes that the numerical results are lower than the data. This probably indicates that measured ΔT_0 are subject to negative error caused by heat

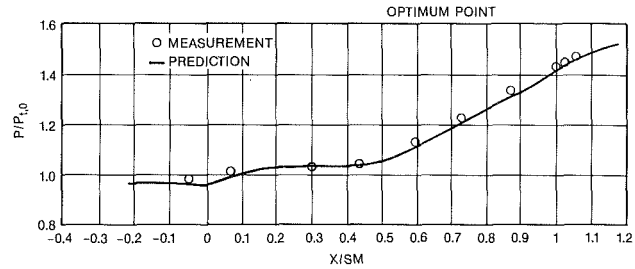

Fig. 4(a) Comparison of space-averaged shroud static pressure at optimum point

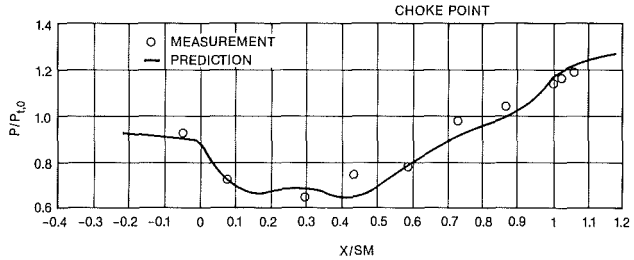

Fig. 4(b) Comparison of space-averaged shroud static pressure at choke point

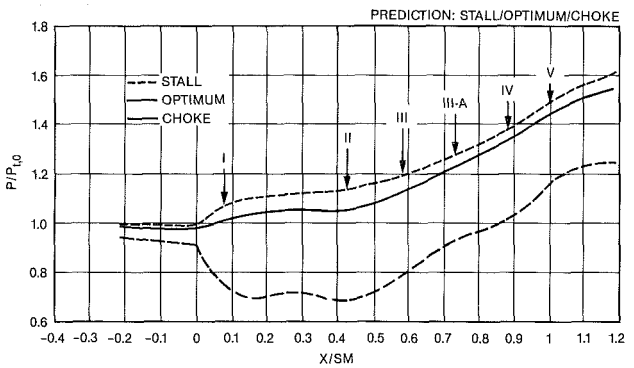

Fig. 4(c) Comparison of space-averaged shroud static pressure at three operating conditions

transfer, etc. On the other hand, the predicted total pressures are higher than data, probably indicating that the actual tip clearance is higher than that assumed in the model. There is also the question of the adequacy or inadequacy of the turbulent model. To sum up, considering the various uncertainties involved, the predicted overall results are remarkable.

Circumferential Average Results. Figure 3 compares the measured stagnation pressure and adiabatic efficiency profiles and those predicted by the code. The rotor efficiencies indicated by the data were based on stagnation pressure traverses at $R/R_2 = 1.075$ and temperature profiles measured at $R/R_2 = 1.687$ (consequently, they include jet-wake mixing in the vaneless diffuser). The numerical results are all circumferential mass averages at $R/R_2 = 1.076$.

The choke point displays an excellent agreement between data and numerical results, for both total pressure and efficiency. However, as the flow rate is progressively reduced from the choke point to the stall point, differences between the data and numerical results become progressively pronounced. This is particularly evident when the adiabatic efficiency is considered.

Note that the optimum efficiency occurs closer to stall point than choke point. In general, centrifugal compressors are very stable in the vicinity of stage choke. At the surge condition the structure of flow in the vaneless diffuser is highly unstable. The progressive variance between data and numerical results in the total pressure profile may be explained by the probe interference with a less stable pattern. On the other hand, the

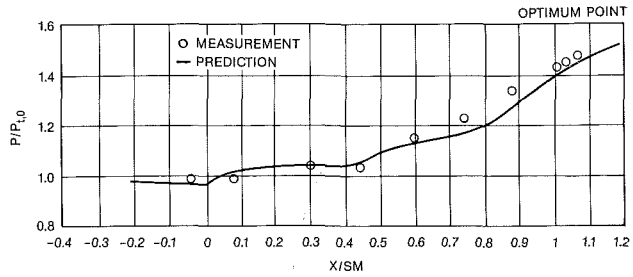

Fig. 5(*a*) Comparison of mass-averaged shroud static pressure at optimum point

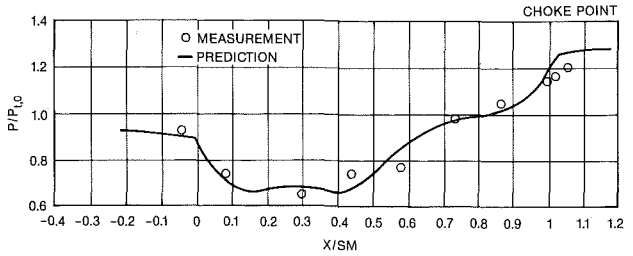

Fig. 5(*b*) Comparison of mass-averaged shroud static pressure at choke point

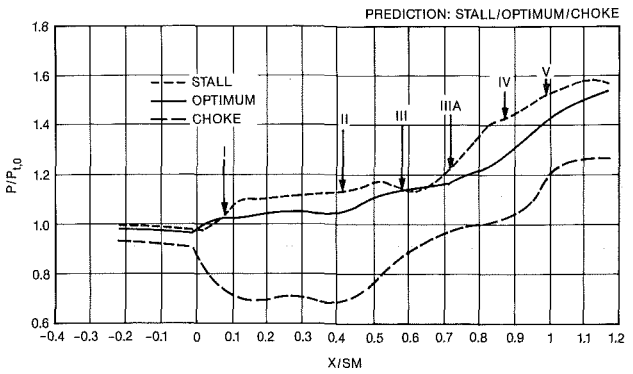

Fig. 5(c) Comparison of mass-averaged shroud static pressure at three operating conditions

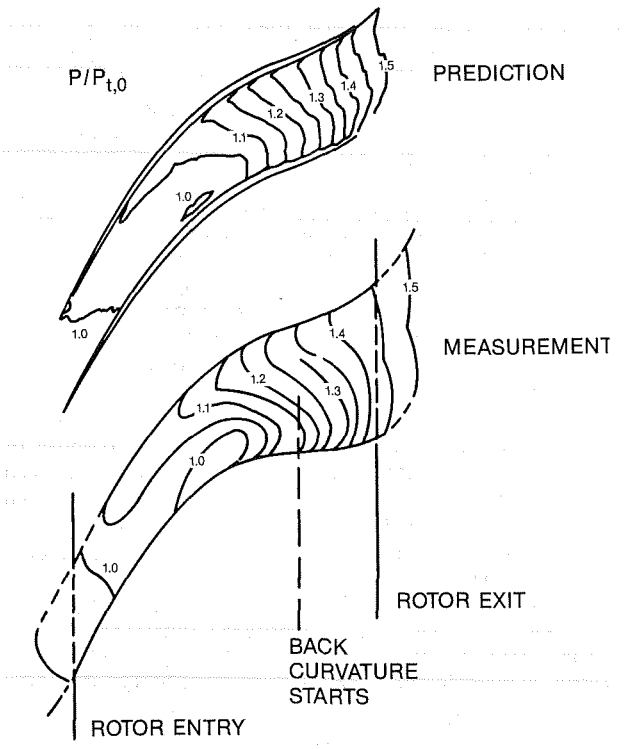

Fig. 6 Comparison of static pressure contours on the shroud

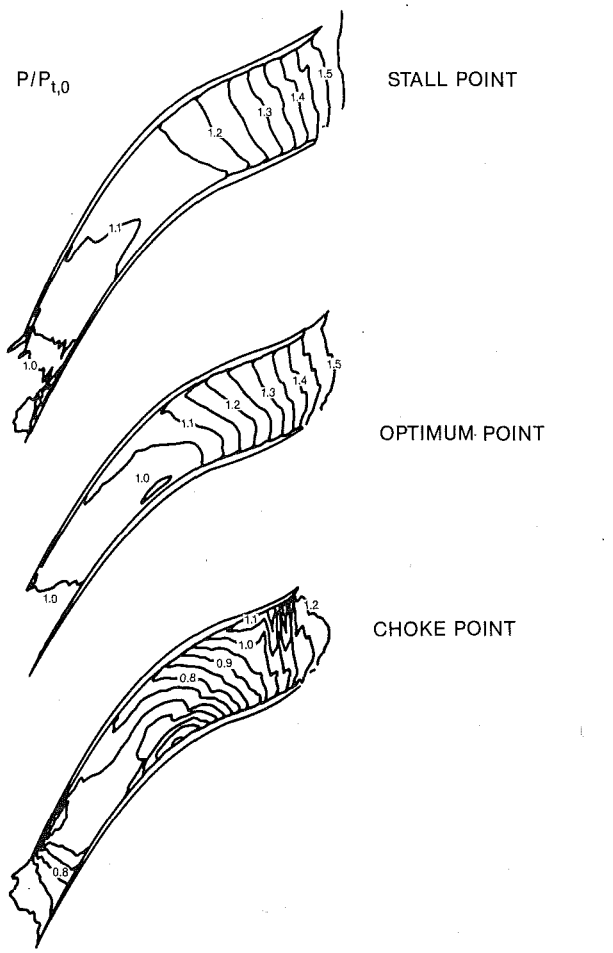

Fig. 7 Comparison of shroud static pressure distributions at three *operating conditions*

substantial variance of the adiabatic efficiency at the stall point is the result of flow development in the vaneless diffuser from $R/R_2 = 1.075$ to 1.687 where the total temperature traverses were made. Thus, based on the above discussion, the numerical results can be considered in good agreement with the test date.

Shroud Static Pressure. Figure 4 compares the circumferentially space-averaged shroud static-pressure distribution with the test time-mean counterpart. The later data are obtained from Schuster and Schmidt-Eisenlohr (1980).

Excellent agreement is noted in the case of optimum point; however, the choke point indicates some variance. The reasons behind this variance are unclear, especially when we consider that the best match in the previous comparison was for the choke point. Furthermore, the detailed C_m/U_2 of Fig. 8 also indicates an excellent match with the measured data.

Figure 4(*c*) compares stall, optimum, and choke shroud static pressure distribution obtained numerically. Note the different ways the distribution develops and the contrast between the three operating points. Also note the general similarity in the distribution developments in most of the passage region. At the leading edge, the static pressure gradient is indicative of the operating incidence. At choke point, negative incidence is clearly indicated in contrast to the stall point with a moderate positive incidence.

Figure 5 compares the same time-mean test data with the mass-averaged static pressure from the numerical solution. The mass-averaged static pressure on the shroud was obtained by extrapolating values from the adjacent nodes. This comparison is included for two purposes: The first is to show that

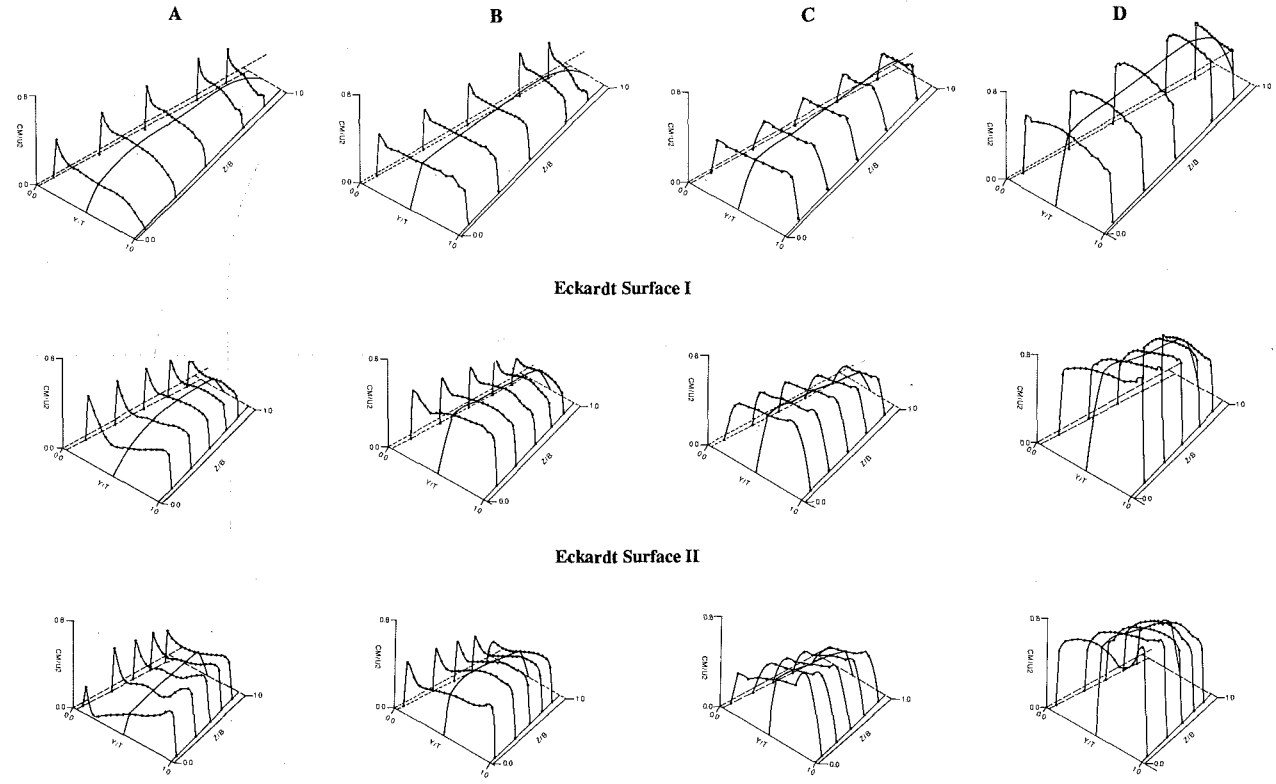

Fig. 8(a) Comparison of flow development at four different mass flow rates

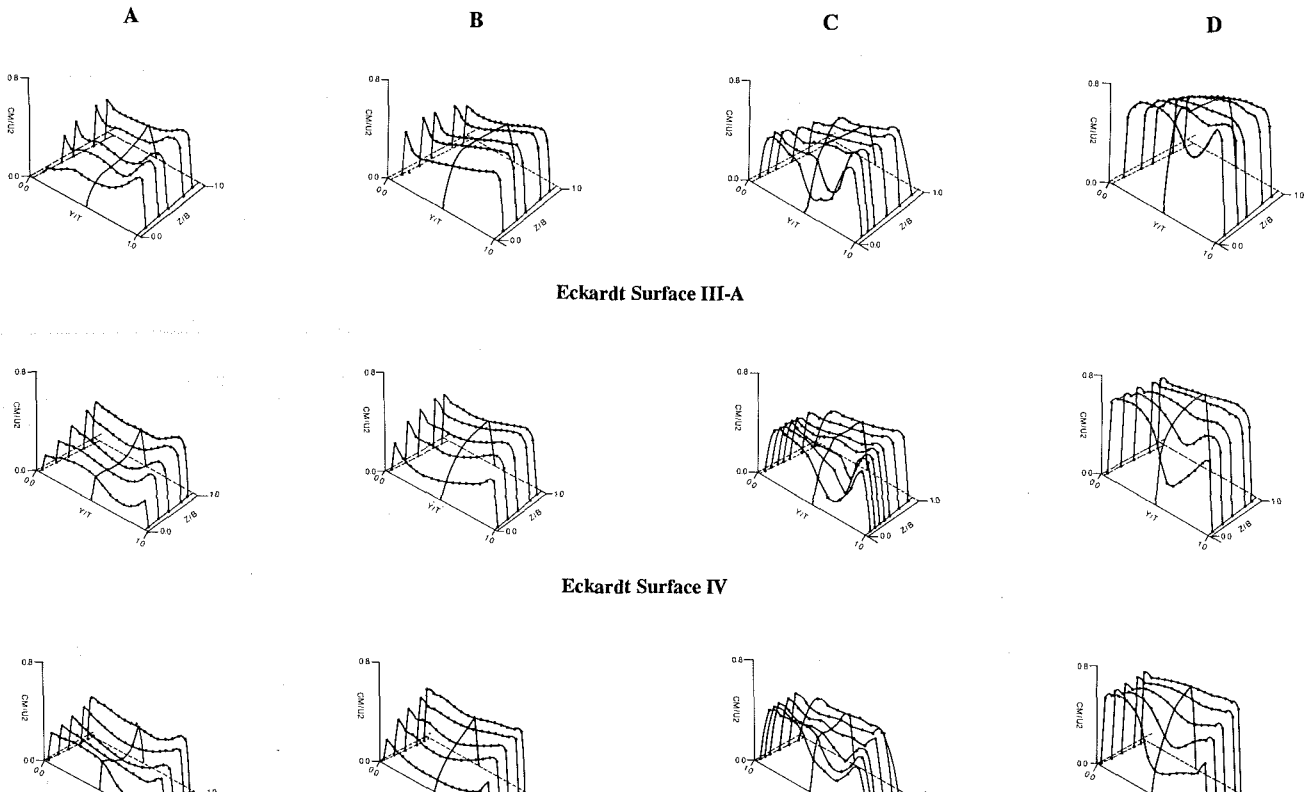

Fig. 8(b) Comparison of flow development at four different mass flow rates

the spatial averaging should be used for the comparison when the measured data are time averaged. The second purpose is that the mass-averaged static pressure, though in itself meaningless, can describe some aspects of the internal flow developments.

As shown in Fig. 5, the agreement is not as good as in Fig. 4, simply because in Fig. 5 comparison is made between distinctly different quantities by definition. On the other hand, Fig. 5(*c*) shows some unique developments near the stall, but Fig. 4(*c*) does not. In addition to the incidence effects discussed earlier, Fig. 5(*c*) shows some abnormal flow development between surfaces II and IV. Relative to the optimum point, the stall point indicates a sudden dip in static pressure in the vicinity of surface III, followed by a substantial pressure rise between surfaces IIIA and IV. As seen in Fig. 8, this development correlates very well with the occurrence of gross flow separation followed by the migration and convection of the separated flow zones to the other side of the blade passage. On the other hand, the choke point static pressure development shows a rapid pressure rise up to surface IIIA, followed flattening of the static pressure rise. Again, this development correlates with the flow structure shown in Fig. 8.

Figure 6 shows a remarkable agreement between the test data and the numerical results of the instantaneous static pressure contours on the shroud surface. Figure 7 compares the numerically obtained static pressure contours on the shroud surface for the three different operating points. Contour development similarity between the stall point and the optimum point is quite obvious. This is not surprising, considering the accepted interpretation of optimum diffuser performance, that optimum diffuser performance occurs at the point of incipient stall. If the same interpretation is applied here, it indicates that the optimum efficiency point should correspond to the point where separation is imminent. The choke point contour, on the other hand, displays quite a different development. Relative to either optimum or stall points, the choke points show much higher static pressure gradient across the passage (B-T-B) in general terms. Also, note the substantial pressure rise on the suction surface past middistance in the streamwise direction. This correlates very well with the C_m/U_2 development of Fig. 8, where flow separation is indicated near the suction surface at surfaces III and IIIA.

Detailed Velocity Field. Figure 8 is a composite of the flow development inside the impeller passage. It is composed of four columns: A, B, C, and D. Column A is the numerical results at surge condition, columns B and C are numerical and experimental results at optimum efficiency, column D represents numerical results at choke condition. The columns are arranged so that scanning from A to D corresponds to increased mass flow rates from stall rate to the limiting choke rate. Scanning from top to bottom corresponds to flow development from inlet to exit. Considering the stall point flow development (column A), the flow alignment for separation appears as early as surface II near the shroud on the pressure side of the blade. The separation reaches a full collapse at surface IIA and is washed away to the other corner of the passage (i.e., the shroud suction side of the blade) at surface IV. In contrast, at the choke point, column D, note the incipience of a separation zone near the shroud suction side of the blade at surface III. This zone continues to develop along the same corner of the passage to the exit. Despite the similarity of the flow distribution at surface V between the stall and choke points, the dynamics of the flow leading to the final stage are quite different.

Figure 9 compares the measurement and prediction of the rotor exit velocity profiles at choke condition. The numerical results predict the complex jet-wake structure very well and agreement with measured data is remarkable.

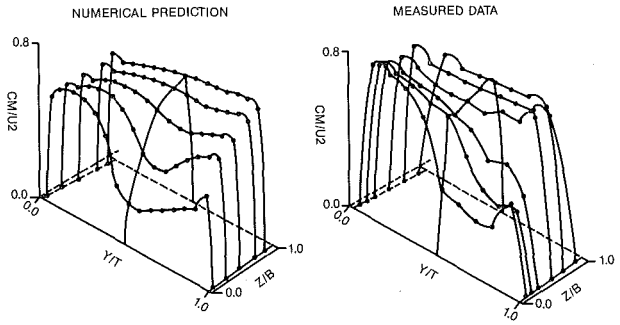

Fig. 9 Comparison of exit velocity profiles at choke condition

Considering the optimum performance point, the numerical results indicate a flow alignment at surface III near the shroud pressure side of the blade similar to the one occurring at the stall point, surface II. However, downstream of surface III, the results do not indicate a zone as distinct as in the stall or choke point that could be described as a separation zone. However, as column B indicates, the flow field deteriorates as it proceeds from surface III to the exit, surface V. It is of particular interest to note the similarities between stall and optimum efficiency points. In both cases, the separated region moves from the pressure side at surface III to the suction side at surface V. The flow structure does not change drastically.

Columns B and C of Fig. 8 compare the numerical optimum point and the optimum test point results. As explained in an earlier section, the flow rate inside the impeller is determined by the exit static pressure used for computation. Although measured exit static pressure is used, the flow rate of the numerical results is about 1.3 percent lower than that of the test data. As the performance map in Fig. 3 indicates, a small change of flow rate near this condition could change the flow development substantially. Also, column C in Fig. 8 shows that the shapes of experimental profiles are closer together toward the choke condition. Considering the discussion in the previous paragraph, and recognizing that the present code is for analyzing steady flows, and that the optimum performance point actually falls in the critically unstable zone of flow development, the code shows remarkable capabilities.

Conclusions

A three-dimensional viscous/turbulent flow analysis has been presented and appraised against test data. To validate the analysis with the highest degree of certainty, the test data were carefully reviewed and comparison criteria were established accordingly. The present analysis predicts the overall performance of centrifugal impellers as well as the intricate flow developments very well for engineering applications.

Also, the method describes the change of flow structure properly when the impeller is operated at various flow conditions.

Acknowledgments

The authors wish to thank D. Eckardt for providing the impeller geometry and measured data, and the General Electric Company for permission to publish this paper.

References

Bradshaw, P., Cantwell, B. J., Ferziger, J. H., and Kline, S. J., 1968, "Experimental Data Needs for Computational Fluid Dynamics—A Position Paper," *Complex Turbulent Flows, The 1980–1981 AFOSR-HTTM-Stanford Conference on Complex Turbulent Flows*, Vol. I, S. J. Kline et al., eds., pp. 28–35.

Chien, K. Y., 1982, "Predictions of Channel and Boundary-Layer Flows With a Low-Reynolds-Number Turbulence Model," *AIAA Journal*, Vol. 20, No. 1, pp. 33–38.

Dean, R. C., Jr., 1981, "On the Unresolved Fluid Dynamics of the Cen-

trifugal Compressor," *Advanced Centrifugal Compressors*, ASME Publication, pp 1–55.

Eckardt, D., 1976, "Detailed Flow Investigations Within a High Speed Centrifugal Compressor Impeller," ASME *Journal of Fluids Engineering*, Vol. 98, pp. 390–402.

Eckardt, D., 1980, "Flow Field Analysis of Radial and Backswept Centrifugal Compressor Impellers—Part I. Flow Measurements Using a Laser Velocimeter," *Performance Prediction of Centrifugal Pumps and Compressors*, Gopalakrishnan, ed, ASME Publication, pp. 77–86.

Fowler, H. S., 1968, "The Distribution and Stability of Flow in a Rotating Channel," ASME *Journal of Engineering for Power*, Vol. 90, pp. 229–236.

Hah, C., 1986, "A Numerical Modeling of Endwall and Tip-Clearance Flow of an Isolated Compressor Rotor," ASME *Journal of Engineering for Gas Turbines and Power*, Vol. 108, pp. 15–21.

Hah, C., 1987, "Navier–Stokes Calculation of Three-Dimensional Compressible Flow Across a Cascade of Airfoils With an Implicit Relaxation Method," *AIAA Journal of Propulsion and Power*, Vol. 3, No. 5, pp. 415–422.

Hah, C., and Leylek, J. H., 1987, "Numerical Solution of Three-Dimensional Turbulent Flows for Modern Gas Turbine Components," ASME Paper No. 87-GT-84.

Hartmann, M. J., 1980, "Technical Evaluation Report and Discussion," *Centrifugal Compressors, Flow Phenomena and Performance*, AGARD-CP-282, pp. vi–xi.

Issa, R. I., 1982, "Solution of Implicitly Discretized Fluid Flow Equations by Operator-Splitting," Internal Report, Dept. Min. Resources Engng., Imperial College, London.

Moore, J., 1973, "A Wake and an Eddy in a Rotating Radial Flow Passage," ASME *Journal of Engineering for Power*, Vol. 95, pp. 205–219.

Moore, J., and Moore, J. G., 1980, "Three-Dimensional Viscous Flow Calculation for Assessing the Thermodynamic Performance of Centrifugal Compressors, Study of the Eckardt Compressor," *Proceedings, AGARD Meeting on Centrifugal Compressors, Flow Phenomena and Performance*, Brussels.

Rhie, C. M., Delaney, R. A., and Mckain, T. F., 1985, "Three-Dimensional Viscous Flow Analysis for Centrifugal Impellers," *J. Propulsion*, Vol. 1, No. 4, pp. 257–258.

Rose, W. G., 1962a, "A Swirling Round Turbulent Jet: 1-Mean Flow Measurements," ASME *Journal of Applied Mechanics*, Vol. 84, pp. 615–625.

Rose, W. G., 1962b, "Corrections to Average Measurements in Unsteady Flow," ASME *Symposium on Measurement in Unsteady Flow*, pp. 85–89.

Schodl, R., 1977, "Laser Two-Focus Velocimetry (L2F) for Use in Aero Engines," *Laser Optical Measurement Methods for Aero Engine Research and Development*, AGARD Lecture Series No. 90, Lecture No. 4.

Schuster, P., and Schmidt-Eisenlohr, U., 1980, "Flow Field Analysis of Radial and Backswept Centrifugal Compressor Impellers—Part 2. Comparison of Potential Flow Calculations and Measurements," *Performance Prediction of Centrifugal Pumps and Compressors*, Gopalakrishnan, ed., ASME Publication, pp. 87–95.

Off-Design Performance of Supersonic Compressors With Fixed and Variable Geometry

K.-D. Broichhausen
Priv. Doz. Dr. Ing.,
Motoren- und Turbinen-Union,
Munich, Federal Republic of Germany

H. E. Gallus
Professor Dr.-Ing.
Mem. ASME

R. Mönig
Dipl.-Ing.

Institut für Strahlantriebe
und Turboarbeitsmaschinen,
Rheinisch-Westfälische Technische
Hochschule,
Aachen, Federal Republic of Germany

Regarding the extremely high pressure ratios of jet-engine compressors for the next decade, increasing interest belongs to the further development of supersonic compressors with supersonic relative flow at rotor inlet and supersonic absolute flow at stator inlet. In the past, different suitable design procedures for these components have been developed and tested successfully. However, there is a lack of information concerning the off-design performance of supersonic compressors. The present paper first systematically shows blading and flow path geometry of different experimentally investigated supersonic axial flow compressors. These investigations refer to combinations of characteristic rotors and stators with fixed and variable geometry. A comparison of these geometric data with the main characteristics of the flow pattern shows that, for the investigated stages, the three-dimensional passage geometry has an essential influence on the off-design performance. On the basis of this information semi-empirical models are established for a numerical description of the flow phenomena with predominant influence, as for example shock-, profile-, and endwall boundary layer losses and rotor–stator interactions. For the determination of the off-design performance, these models are incorporated into a streamline curvature calculation method. The computer model established is able to describe the off-design characteristics of the different investigated supersonic compressor stages in the most important operating range.

1 Introduction

The advantages of supersonic compressors were recognized very early; consequently a series of supersonic compressors have already been developed and tested. Previous investigations have already covered the main different compressor components ([1, 2, 3], Fig. 1). At the end of the NACA development period a remarkable standard was reached with regard to the rotors. The overall stage data, however, were still unsatisfying. Based on the NACA experience, further developments were performed at the AFARL [4], the VKI [5], and ONERA [6].

At the Technical University in Aachen the research activities were concentrated on three different stages [7, 8, 9], which are characterized in Fig. 2. All investigated compressors have an axial subsonic inlet and exit flow. They work either with tandem stators or with a turnable single-row stator developed at the DFVLR [10].

The deceleration of the supersonic flow in the tandem stators takes place in a single normal shock, stabilized by back pressure at the entrance of the cascade. The turnable stator is designed for a multiple shock deceleration [10].

In combination with these stators two different rotor types were tested:

(*a*) impulse-type rotors with supersonic passage flow, and
(*b*) shock rotors, where a strong shock is stabilized at the entrance of the rotor passage.

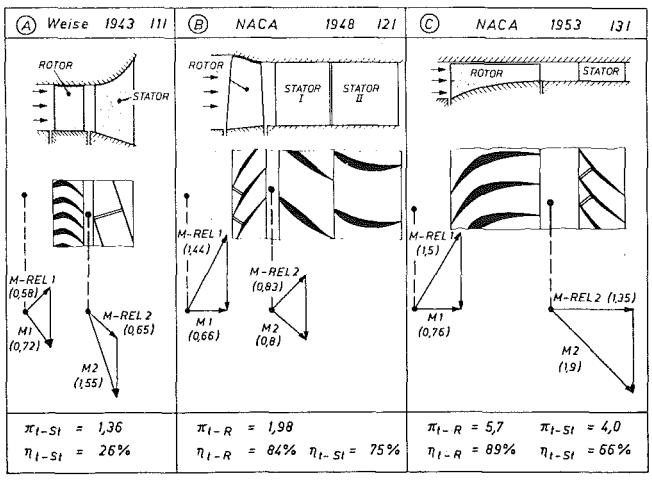

Fig. 1 Types of supersonic compressor

Contributed by the Gas Turbine Division of THE AMERICAN SOCIETY OF MECHANICAL ENGINEERS and presented at the 32nd International Gas Turbine Conference and Exhibit, Anaheim, California, May 31–June 4, 1987. Manuscript received at ASME Headquarters February 10, 1987. Paper No. 87-GT-116.

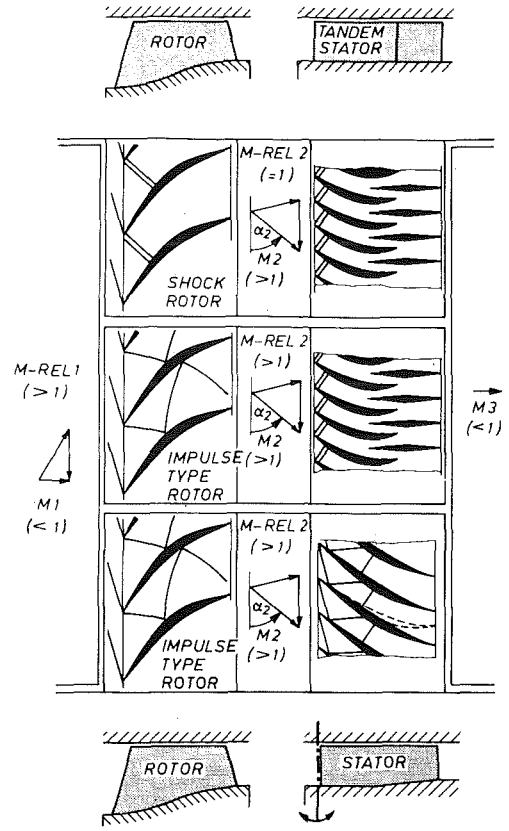

Fig. 2 Investigated supersonic compressor stages

With a combination of shock rotor and tandem stator the following data have been verified experimentally:

- mass flow: $\dot{m} = 11.0$ kg/s
- total pressure ratio: $\pi_t = 3.0$
- total efficiency: $\eta = 82$ percent

These data for a research compressor are promising for an application of supersonic compressors in small jet engines.

Recently, new activities in the field of supersonic compressors can be registered, due to the demands on the capacity of future jet engines. These developments can take advantage of established design methods for single components. They suffer, however, from a lack of information on off-design performance. For that purpose this item is discussed below.

2 Experimental and Theoretical Approach

2.1 Experiment. The off-design performance of the described compressor stages was tested in a single-stage closed-loop rig with extensive instrumentation [8, 9]. The data referred to in this paper were achieved by the following techniques:

- static wall pressure taps and semiconductor fast response pressure transducers in the compressor casing;
- pneumatic five-hole probes with incorporated temperature transducers upstream and downstream of the stage and in the gap between rotors and stators.

2.2 Basic Influence of the Passage Geometry on the Flow Pattern in Supersonic Compressors. The supersonic rotors under consideration can be characterized by:

- high turning angles,
- a strongly converging annulus,
- low aspect ratios, and
- high hub/tip ratios.

The geometric data of the rotors are outlined in Table 1(*a*).

The impulse-type rotor is designed for operation without strong shocks. It has a strongly cambered suction side, even near the leading edge. On the contrary, the suction side of the shock rotor is straight up to the design shock position. Thus the shock losses in the leading edge shock system are minimized. The increasing hub compensates for the enlargement of the blade-to-blade flowthrough area caused by the high turning of the profiles and the total pressure rise.

The basic principles of the aerodynamic design can be discussed by a comparison of the three-dimensional throughflow area. For that purpose, the resulting effective three-dimensional passage cross sections taken perpendicular to the meanline of the profiles are given in Fig. 3(*a*).

The passage of the impulse-type rotor diverges in the

Nomenclature

A = area
A^* = critical cross section
A_{3D} = total flow area
A_{2D} = passage width (blade to blade)
a = geometric streamline properties after damping (equation (2))
$\bar{a}$ = geometric streamline properties before damping (equation (2))
B_{min} = pitch diminished by maximum blade thickness
c = absolute velocity
c_p = specific heat at constant pressure
I_0 = relative stagnation enthalpy
k = damping parameter
L = chord length
M = Mach number
$\dot{m}$ = mass flow
n = rotational speed
n_0 = design speed
p = pressure
Q = entropy function (equation (1))
r = radius
r_m = radius of curvature in meridional plane
s = entropy
s = spacing (blade to blade)
T = temperature
$U(r)$, $V(r)$ = abbreviations (equation (1))
w = relative velocity
α = absolute flow angle $= \tan^{-1}(c_m/c)$
β = relative flow angle $= \tan^{-1}(w/c_m)$
η = efficiency
κ = ratio of specific heats
π = pressure ratio
ϕ = $\tan^{-1}(c_r/c_z)$

Subscripts

abs = absolute
ax = axial
h = hub
i = number of calculation plane in axial direction
j = number of streamline
m = meridional direction
p = pressure side
R = rotor
r = radial direction
rel = relative to rotating system
s = suction side
St = stage
st = stator
t = total
t = tip
z = axial direction
0 = stagnation condition
1 = in front of stage
2 = behind rotor
3 = behind stage

Table 1 Geometric data of the developed rotors and stators

Table 1a		impulse-type rotor	shock rotor
stagger	[°]	38.5	38.8
chord	[mm]	113.0	115.8
solidity	[-]	2.37	2.43
max. thickness	[mm]	5.2	7.8
pos. of max. thick.	[mm]	62.0	58.8
max. camber	[mm]	14.1	15.5
pos. of max. camber	[mm]	65.0	63.5
aspect ratio	[-]	0.312	0.309
turning angle	[°]	45.5	46.0

Table 1b		tandem-stator I / II cascade I	cascade II	turnable stator
stagger	[°]	18.5 / 13.1	1.0 / 1.4	16.0
chord	[mm]	64.5 / 54.8	61.7 / 46.9	50.9
solidity	[-]	3.26 / 2.77	3.13 / 2.38	3.86
max. thickness	[mm]	5.5 / 3.2	4.6 / 2.8	2.4
pos. of max. thick.	[mm]	33.8 / 31.3	28.5 / 27.3	7.8
max. camber	[mm]	9.8 / 6.9	0.5 / 0.3	4.1
pos. of max. camber	[mm]	30.4 / 27.0	22.5 / 24.8	31.9
aspect ratio	[-]	0.326 / 0.421	0.373 / 0.491	0.435
turning angle	[°]	46.0 / 36.0	0.0 / 0.0	35.0

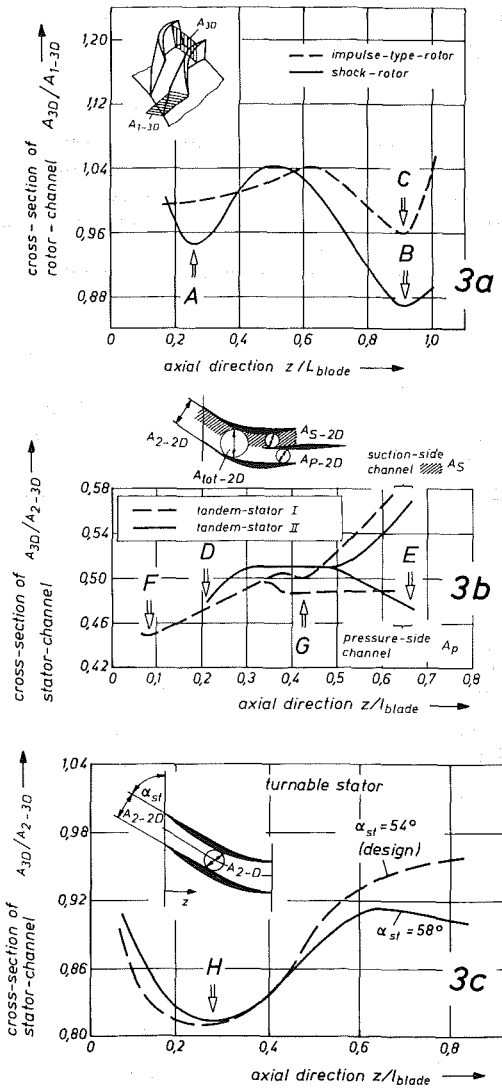

Fig. 3 Flow channel geometry of rotors and stators

upstream part of the passage and has a relative minimum (Position C) near the trailing edge. With regard to the shock rotor a leading edge blockage effect caused by the uncambered

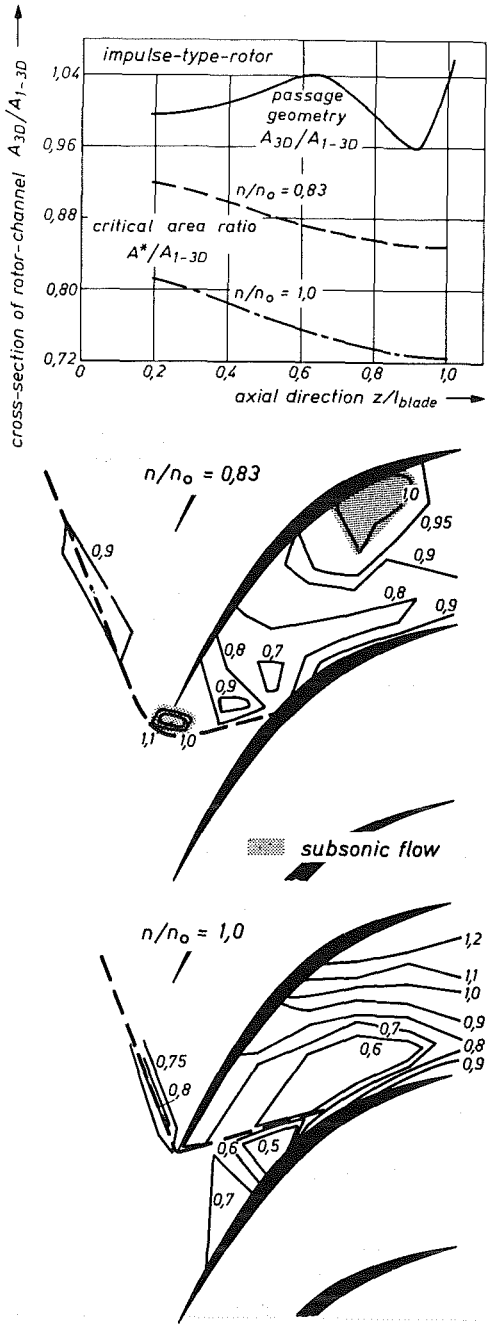

Fig. 4 Comparison of real and critical cross sections of an impulse-type rotor with measured pressure distribution

suction side is obvious (Position A). Near the rotor exit (Position B) an additional throat generates an absolute minimum of the area ratio in order to stabilize a strong shock wave at the entrance of the rotor.

The investigated tandem stators have a cylindrical annulus. They differ with regard to turning angle and blade geometry. A summary of the geometric data is given in Table 1(*b*). The passage geometry related to the inlet area is shown in Fig. 3(*b*).

Regarding the tandem stator passage, the geometry of the single passages (A_{S-2D}, A_{P-2D}) generated by the overlapping blades is important. The suction side channel (hatched) is mainly diverging for both stators. The pressure side channel of stator I has a constant cross section in the overlapping part of the cacade. The passage is, however, converging there in the case of stator II (Fig. 3*b*).

In Fig. 3(*c*) the area of the variable single-row stator is given as a function of the axial coordinates and the stagger angle.

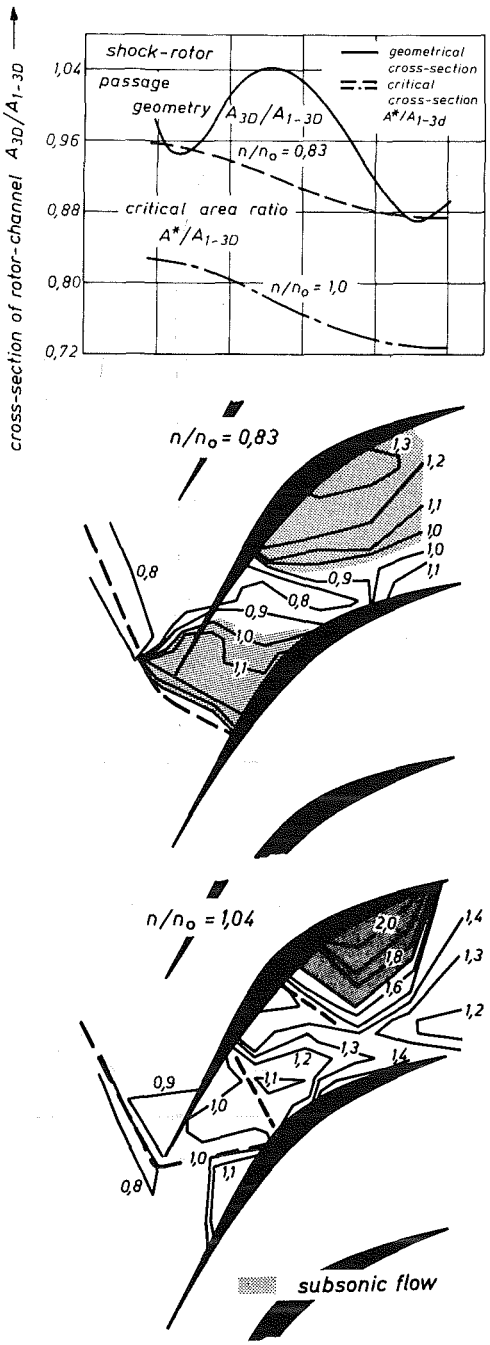

Fig. 5 Comparison of real and critical cross sections of a shock rotor with measured pressure distribution

The local area again is related to the inlet area, which is itself influenced by the stagger angle. In order to decelerate the supersonic flow in a multishock system, the inlet passage is slightly converging. The subsequent channel geometry is diverging, corresponding to a downstream subsonic diffusion.

Because of the low aspect ratio of the compressors under consideration, the flow is strongly dependent on the discussed three-dimensional passage geometry. This can be demonstrated, comparing the geometric passage cross section, the aerodynamic critical cross section (with $M_{rel} = M^* = 1$), and the wall pressure distribution (periodic pressure fluctuations superposed on the wall static pressure distribution) in the rotor passage (Figs. 4 and 5). Regions with subsonic isentropic Mach numbers are indicated by screening.

On the basis of the relative flow inlet conditions, the critical

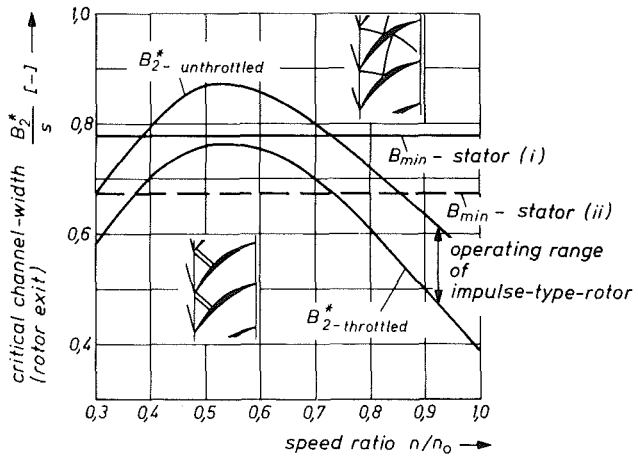

Fig. 6 Comparison of stator throat with rotor-required cross section

cross section $A^*/A_{1\text{-}3D}$ with $M_{rel} = 1$ is computed for isentropic flow and two different speeds. It decreases in the chordwise direction due to the energy transfer in the rotor. For supersonic/transonic inlet conditions, occurring at high-speed operation, a supersonic passage flow can only be established if the critical area ratio is smaller than the geometric one. This is the case for the impulse-type rotor (Fig. 4). Consequently, the wall pressure distribution indicates weak passage shocks and for the low-speed condition only local subsonic regions.

For the shock rotor (Fig. 5), similar conditions with supersonic relative flow can be detected only for design speed. In contrast to the impulse-type rotor, stronger passage shocks appear. For the low-speed condition, a comparison of passage geometry and critical cross section indicates choking at the leading edge and in the rear part of the rotor. This is confirmed by the pressure distribution, which shows a normal leading-edge shock and extensive subsonic regions.

This comparison of rotor passage geometry and aerodynamics shows that the flow in supersonic compressors is predominantly influenced by the integral choke margin of the components.

2.3 Theory

2.3.1 Throughflow Algorithm. According to Figs. 4 and 5 a theoretical approach has to cover

- supersonic relative and/or absolute inlet Mach numbers,
- weak or strong passage shocks, and
- supersonic/subsonic passage flow.

The experiments additionally indicate that the off-design performance of supersonic compressors with strongly cambered blades is influenced to a great extent by viscous effects. Furthermore, a computational off-design performance simulation, including the complex interaction between supersonic rotors and stators, requires a lot of computations along the operation line of the compressor. Therefore two different rather simple computation methods are applied:

(*a*) a meanline algorithm, and
(*b*) a streamline curvature algorithm on S2 surfaces.

The meanline algorithm solves the conservation equation of mass, energy, and momentum on a single representative streamline. The advantages of this method are:

- extremely short computation time,
- numerically stable,
- simple algorithm.

The streamline curvature algorithm, however, gives more detailed flow information. The present method is based on the

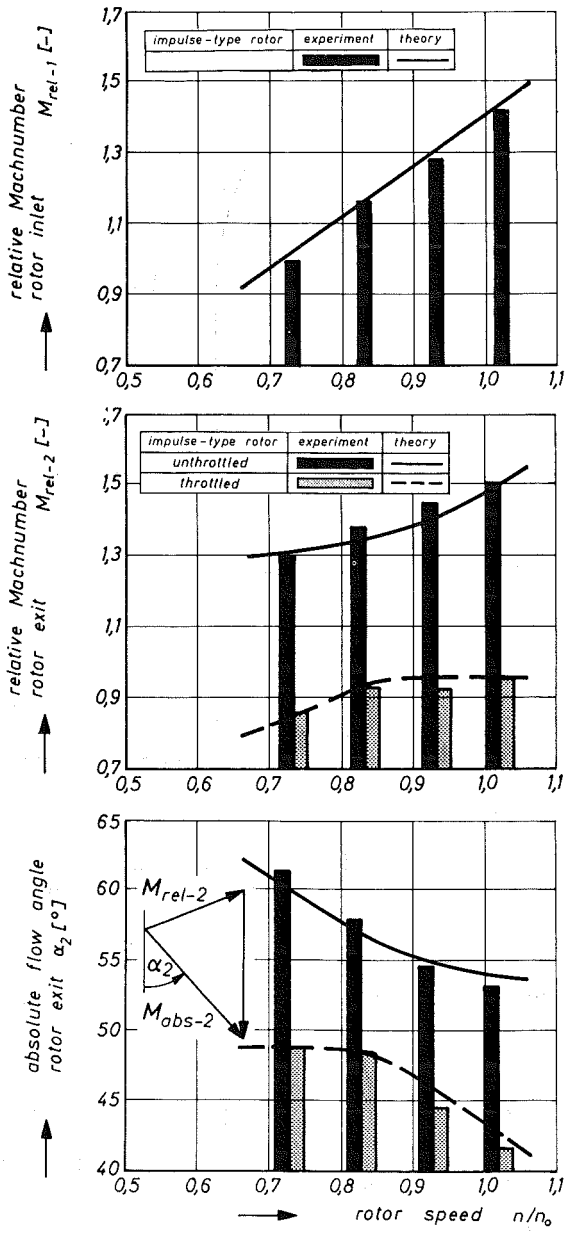

Fig. 7 Inlet and outlet flow conditions of impulse-type rotor

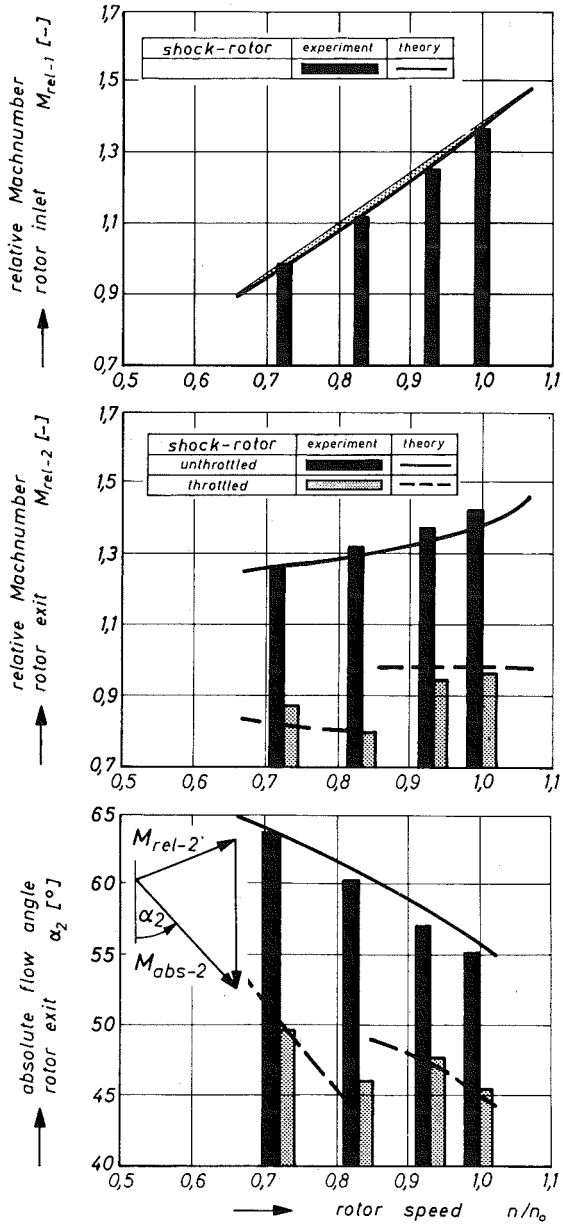

Fig. 8 Inlet and outlet flow conditions of shock rotor

scheme proposed by Novak [18] and was modified for application in transonic and supersonic flow fields. The radial velocity distribution for steady axisymmetric flow is given by the fundamental differential equation

$$\frac{\partial c_m}{\partial r} = \frac{1}{2c_m} V(r) - \frac{c_m}{2} U(r) \tag{1}$$

where

$$U(r) = 2\cos^2\beta \left(\frac{\sin\phi}{c_m} \frac{\partial c_m}{\partial_m} + \frac{\cos\phi}{r_m} + \frac{1}{2} \frac{\partial \tan^2\beta}{\partial r} \right.$$

$$\left. + \frac{1}{2\cos^2\beta} \frac{1}{Q} \frac{\partial Q}{\partial r} + \frac{\tan^2\beta}{r} - \frac{2\omega}{c_m} \tan\beta \right)$$

$$V(r) = 2\cos^2\beta \left(\frac{1}{Q} \frac{\partial I_0 Q}{\partial r} + \frac{\omega^2 r^2}{2} \frac{1}{Q} \frac{\partial Q}{\partial r} \right)$$

$$Q = \exp(-s/c_p)$$

The boundary condition for the subsonic and for the supersonic solution is determined by global conservation of mass. For the consideration of flow losses the value of Q must be calculated from additional loss correlations.

The iteratively improved streamline geometry is derived from conservation of mass between two adjacent streamlines in the whole flow field. As numerical instability may arise in certain cases [19], a geometric damping is applied for the radius of curvature and the local flow angle related to the axial direction

$$a_{i,j} = (\bar{a}_{i-1,j} + k\bar{a}_{i,j} + \bar{a}_{i+1,j})/(k+2) \tag{2}$$

The distances of the calculation planes in the axial direction are sufficiently small that the accuracy of the solution is only affected within the required accuracy limits. Nevertheless, k should be chosen as large as possible. The calculations in the present paper were performed with k equal to 4.

Viscous effects, choking, and deviation are considered by semi-empirical models.

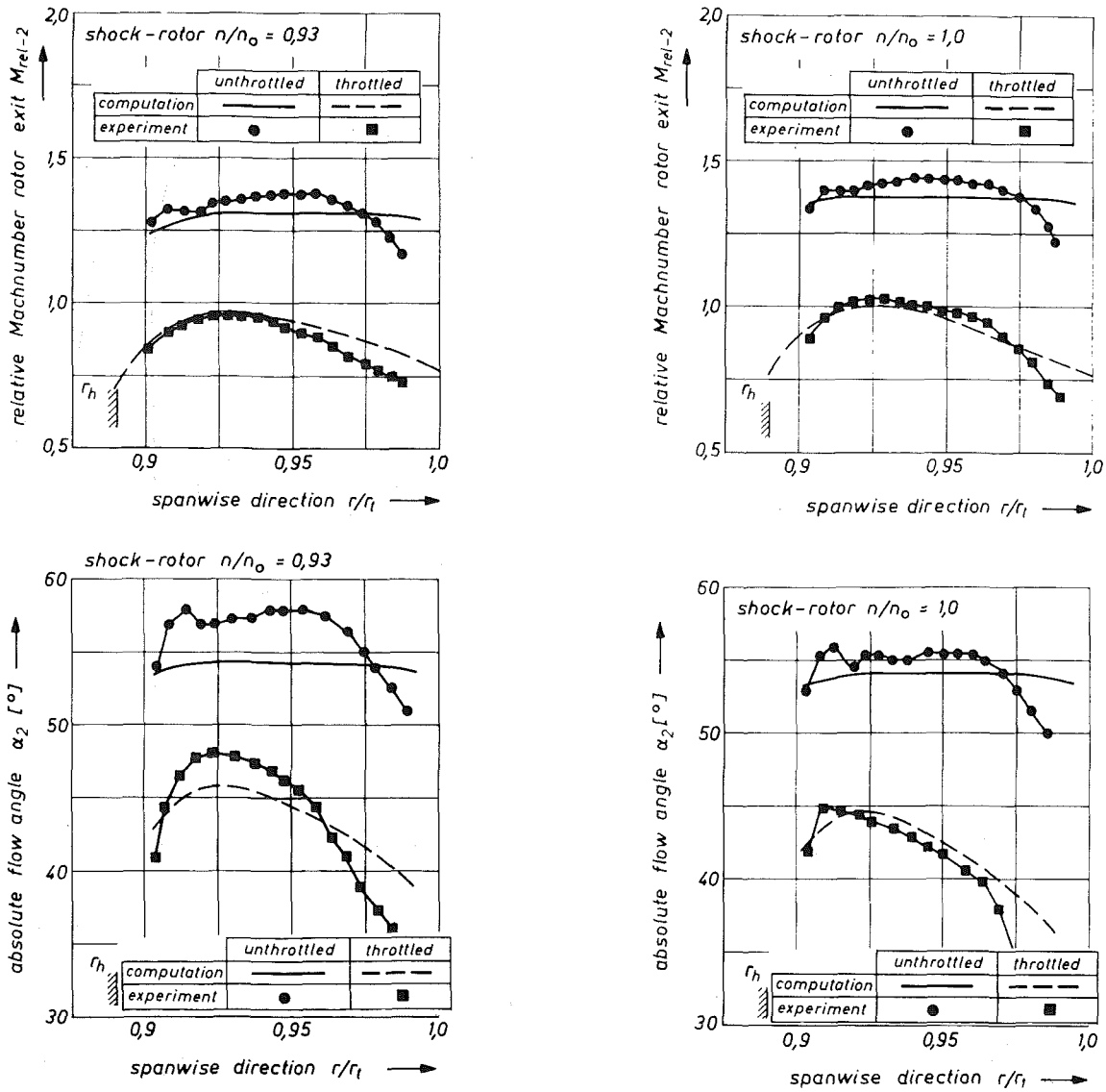

Fig. 9 Radial distribution of flow properties at the outlet of the shock rotor

2.3.2 Choking Effects. As mentioned before, for a detailed computational simulation of the off-design performance, the choking effects have to be taken into account accurately. Therefore the streamline curvature algorithm must be used as a throughflow approach. In the case of the meanline algorithm, additional computation planes have to be positioned in each of the aerodynamic throats of rotors and stators. The corresponding axial positions are marked in Fig. 3 (Positions A–H). Particularly at the leading edge of the rotors, the spanwise distribution of choking must be considered [11].

Additional choking may occur combining rotor and stator. Depending on the rotor speed, the rotor exit data can be computed by the aforementioned methods. From these data the critical cross section B_2^* for achieving sonic flow downstream of the rotor can be derived. The corresponding data for throttled and unthrottled rotor flow are plotted versus speed in Fig. 6. They indicate the operation limits (choke and surge) of the rotor.

A stator (*i*) with a certain throughflow area guarantees an unthrottled operation of the rotor for high-speed condition. For low-speed operation ($n/n_0 = 0.5$) the rotor is throttled.

A fictitious stator (*ii*) with an even smaller passage is still adapted well to the rotor exit flow for design speed. For low-speed operation, however, the rotor will exceed the surge margin.

2.3.3 Loss and Deviation Models. For a correct theoretical prediction of rotor and stage performance, the losses have to be described by semi-empirical models. In order to obtain general validity for the different components of supersonic compressors, the losses are divided with respect to their physical origin [11]:

- profile and endwall losses,
- losses caused by shock-induced boundary layer separation, and
- shock losses.

The profile losses are computed according to Monsarrat [12], who gives a spanwise correlation between diffusion factor and loss coefficient for transonic compressors. With regard to the low aspect ratios of the compressors being the subject of the presented investigations, only the correlations for endwall regions incorporating secondary flow effects are taken.

The pattern of the shock systems in the rotors and stators is strongly dependent on inlet conditions and back pressure.

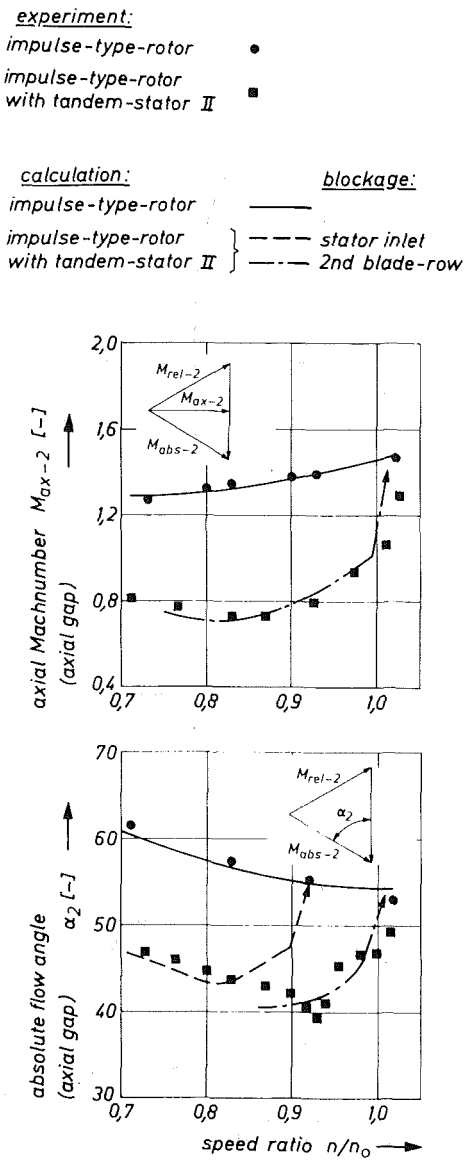

Fig. 10 Starting of impulse-type rotor in combination with tandem stator II

Regarding the operating point under consideration, the shock losses are split into three parts:

- bow shock, assumed to be of hyperbolic shape, according to Moeckel [13], who derives the bow-shock shape applying the conservation equations to the local sonic region near the stagnation point,
- normal leading edge shock, according to the model of Miller et al. [14], and
- additional normal passage shock, stabilized by passage geometry or back pressure.

Shock-induced separation is indicated by the Donaldson criterion [15], correlating the shock pressure rise for incipient separation with the upstream Mach number and Reynolds number. In the case of separation, losses are determined by an equivalent pseudoshock mixing process, which assumes a reacceleration to sonic conditions caused by the separation and a dump diffusion to the rotor exit [16, 17].

Referring to the tandem stators, the loss models are applied to each stator blade row separately [11].

For throughflow calculations a chordwise distribution of losses has been presumed. The losses caused by shock waves are placed at the rotor inlet, whereas the profile and separation losses are assumed to rise in a linear way from leading edge up to trailing edge. Concerning the radial distribution of the flow properties, the endwall losses were assumed to diminish according to a function of sixth order in the unthrottled case and of third order in the totally throttled case.

If the losses in the numerical simulation indicate choking in the rotor passage, the flow angle, corresponding to the experiment, is iterated to relative sonic conditions in the rotor exit. For unthrottled supersonic flow without choking, the flow angle is determined according to the blade angle at the suction-side trailing edge. In contrast, for higher back pressure without loss-induced choking, the rotor outlet angle is fixed to the pressure side surface.

3 Rotor Performance

The measured and calculated results concerning the off-design performance of the impulse-type rotor are plotted in Fig. 7. According to the "unique incidence" condition [20], the inlet Mach number depends on the rotor speed in a nearly linear way.

At the rotor exit the supersonic relative Mach number in the unthrottled case rises exponentially with rotor speed. This is due to a nearly isentropic flow in the rotor passage and the superposition of increasing energy transfer ($\sim u*u$) and mass flow ($\sim u$). A corresponding increase of the absolute flow turning is indicated by the development of the absolute flow angle.

For maximum back pressure and subsonic passage flow a rising relative Mach number can be observed in the lower speed range. Shock-induced separation keeps the Mach number constant at nearly sonic conditions in the upper speed range. The point of separation also is indicated by a diminution of the absolute flow angle.

In contrast, the shock rotor shows a deviation from the "unique incidence" inlet condition (Fig. 8), which can be explained by leading edge choking at part speed (Fig. 5). The deviation is marked by screening. This mass-flow reduction (maximum 4 percent) in combination with additional shock losses leads to a more moderate rise of the relative exit Mach number at increasing rotor speeds (low back pressure).

At maximum back pressure the outlet Mach number of the shock rotor is reduced continuously with rotor speed in the lower speed range. Again separation causes a characteristic jump of the outlet Mach number to nearly unity. It remains constant for a further increase of the rotor speed. A discontinuity due to separation can also be observed for the absolute flow angle.

The radial distribution of the outlet Mach number and flow angle for the shock rotor is shown as an example in Fig. 9. Regarding the unthrottled case, a uniform distribution in a wide range of span can be observed. Throttling the rotor causes an increase of shock and separation losses in the tip region, marked by a reduction of Mach number and flow angle.

4 Stage Performance

4.1 Supersonic Starting. As already mentioned (section 3.1), choking inside the stator of a supersonic compressor stage causes a throttled operation of the rotor (Fig. 6). If choking disappears beyond a certain rotor speed, the pressure in the axial gap diminishes. The rotor passage flow changes from subsonic to supersonic ("starting process").

This starting process can be demonstrated by the dependency of absolute flow angle and absolute Mach number in the gap betweeen rotor and stator. Corresponding experimental data are shown in Figs. 10–12 together with computational results for combinations of

- impulse-type rotor with tandem stator II (Fig. 10),
- impulse-type rotor with variable geometry (Fig. 11), and
- shock-rotor with tandem stator I (Fig. 12).

For the computation, the aforementioned loss, deviation, and choking models have been inserted into a pitchline throughflow calculation for a representative streamline.

Without a stator the impulse-type rotor generates a supersonic axial flow already at low part speeds (Fig. 10). The turning of the absolute flow is consequently rather small. In combination with the stator the impulse-type rotor is throttled for low-speed operation. The axial flow in the gap between rotor and stator is subsonic. Only beyond 90 percent of design speed does the starting process arise. At design speed the axial flow is still sonic. Even at overspeed the rotor flow in the stage still differs from the operation without a stator.

The discrepancy between the axial Mach number downstream of the rotor for rotor-alone operation and stage operation even at overspeed is caused by flow unsteadiness: Corresponding to time integrating (pneumatic measurements), the axial velocity component is supersonic. Measurements with techniques resolving unsteady effects (semiconductor probes, spark-schlieren technique), however, indicate a change to subsonic axial Mach numbers in the wake of the rotor blade [21]. Thus, also in the case of a time-mean supersonic axial Mach number, information about the stator flow (stator choking) can be transmitted upstream and influence the rotor.

The computation reproduces the starting rotor speed correctly. For this purpose it is necessary to examine the whole stator passage—including the losses—with regard to choking. If this is done only for the stator inlet region, the predicted starting speed is too low (dashed line in Fig. 10).

Combining the impulse-type rotor with the variable single-row stator leads to a considerably improved stage performance. As demonstrated in Fig 11, the rotor speed of supersonic starting is dependent on the stagger angle, which controls the cross section of the stator passage. If starting conditions are established once, a turning of the stator no longer has an influence on the rotor, and a stable operation of the whole compressor stage is guaranteed.

These starting problems are not valid for a combination of shock rotor and tandem stator I. The flow is prevented from starting by the stator geometry in the whole speed range. Thus, in stage conditions, the rotor always operates in the throttled range. The axial flow velocity between rotor and stator remains subsonic and only the absolute Mach number is greater than unity. The experiments did not indicate any problems arising from unsteady interactions between stator bow shocks and rotor flow.

4.2 Compressor Performance at Increasing Back Pressure. To operate at design condition, marked by peak pressure rise in the stage, a shock system is stabilized at the entrance of the stator. Figure 13 demonstrates the wall pressure

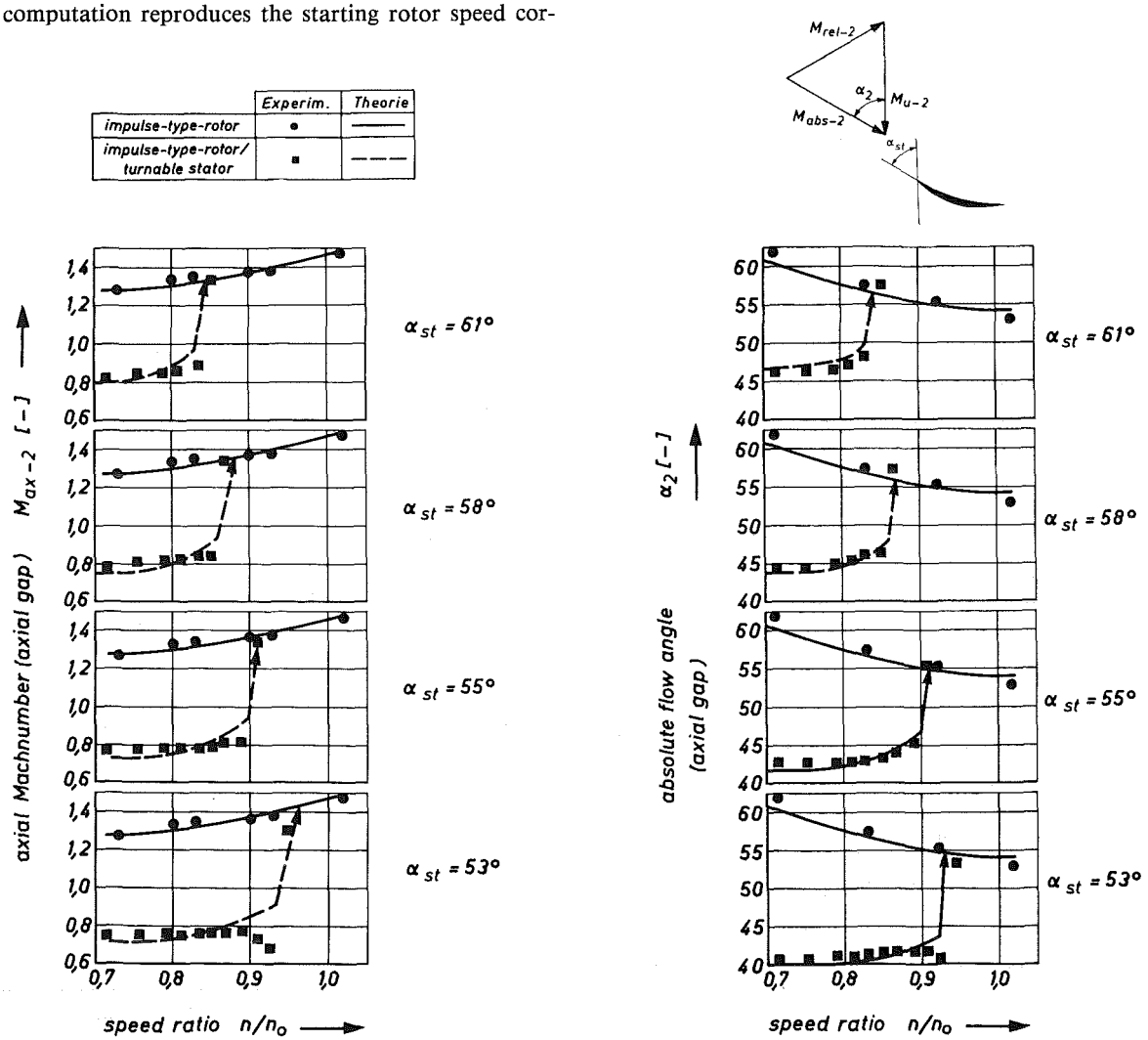

Fig. 11 Starting of impulse-type rotor in combination with turnable stator

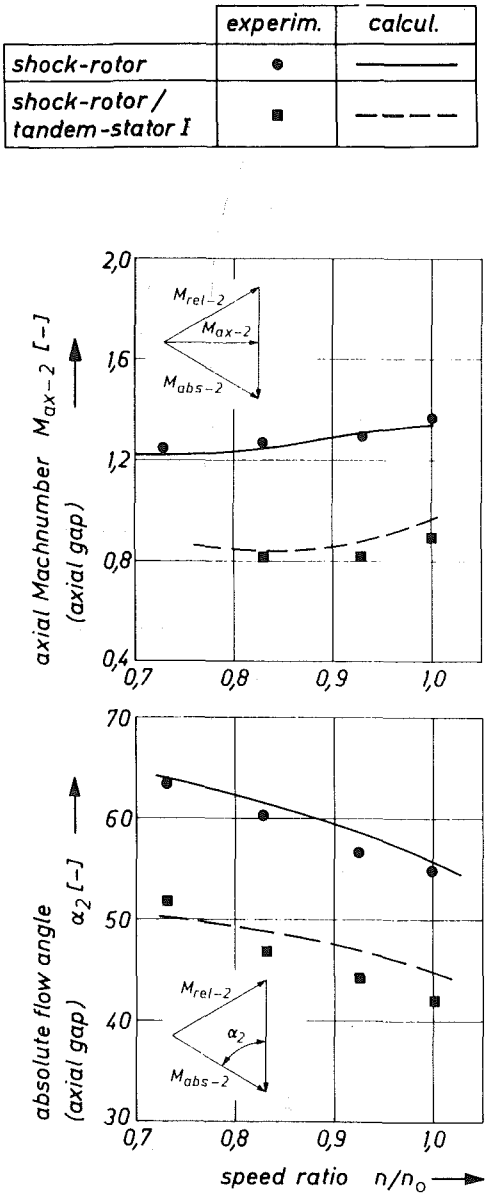

Fig. 12 Starting of shock rotor in combination with tandem stator I

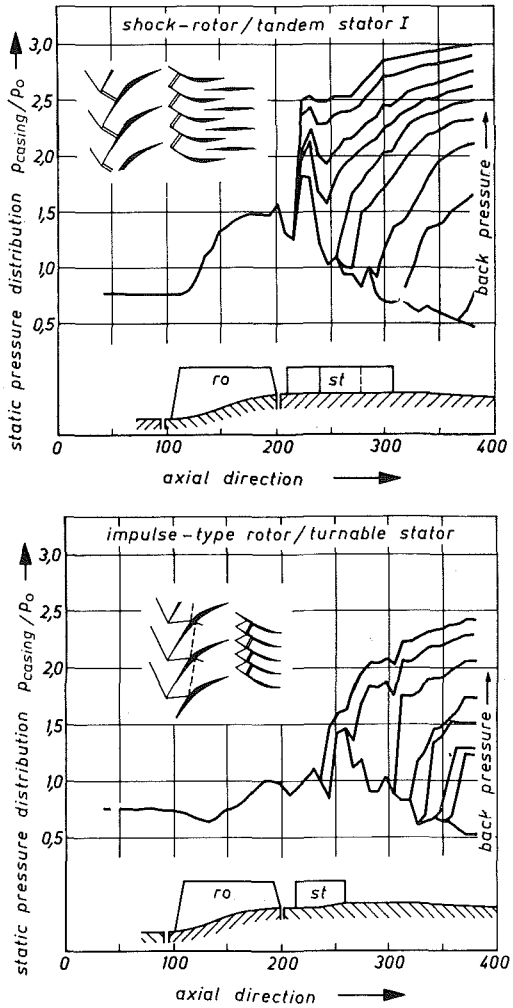

Fig. 13 Wall pressure distribution for different operating conditions at design speed

distribution, obtained by throttling the shock-rotor stage and the impulse-type rotor combined with the variable stator.

Regarding impulse-type rotor and tandem stator, the close vicinity of starting and design speed on the one hand and the converging pressure side channel in the stator on the other hand did not allow a throttling.

In both investigated cases, however, a shock system is forced to move upstream by increasing back pressure. The rotor flow obviously is not influenced by back-pressure variation.

For the impulse-type stage with one row stator the overall total pressure ratio increases slightly with increasing back pressure (Fig. 14). The exit Mach number, however, even at design conditions, is comparatively high ($M \simeq 1$).

The shock-rotor stage shows less uniform performance characteristics. For the unthrottled case and supersonic flow in the stator passage, the losses are low and consequently the total pressure is high. Positioning the throttling shock near the leading edge of the second blade row, the total pressure ratio is reduced remarkably due to a strong separation in the second stator passage. If the throttling shock enters the first blade row the separation effects are reduced by the special passage geometry. The overall total pressure rise increases again up to maximum back pressure. The exit Mach number of the stage is then close to design ($M \simeq 0.5$). The computational results correspond to the experimental data.

5 Conclusions

Highly loaded supersonic compressors generally are distinguished by low aspect ratios and high hub-tip ratios. Regarding these compressors, the passage geometry already gives considerable information on the off-design performance of the components. More detailed data can be achieved by the application of the described loss and deviation models in a throughflow algorithm. For a correct performance prediction it is necessary to consider the interaction between stators and rotors.

Summarizing the experimental and theoretical results, a stable operation of supersonic compressors can be obtained by:

- supersonic absolute flow but subsonic axial flow between rotor and stator, and
- a diverging stator passage.

Referring to supersonic compressors with axial supersonic Mach numbers between rotor and stator, unstable operation can be avoided if the starting speed and the design speed differ remarkably and if stable shock positions can be achieved

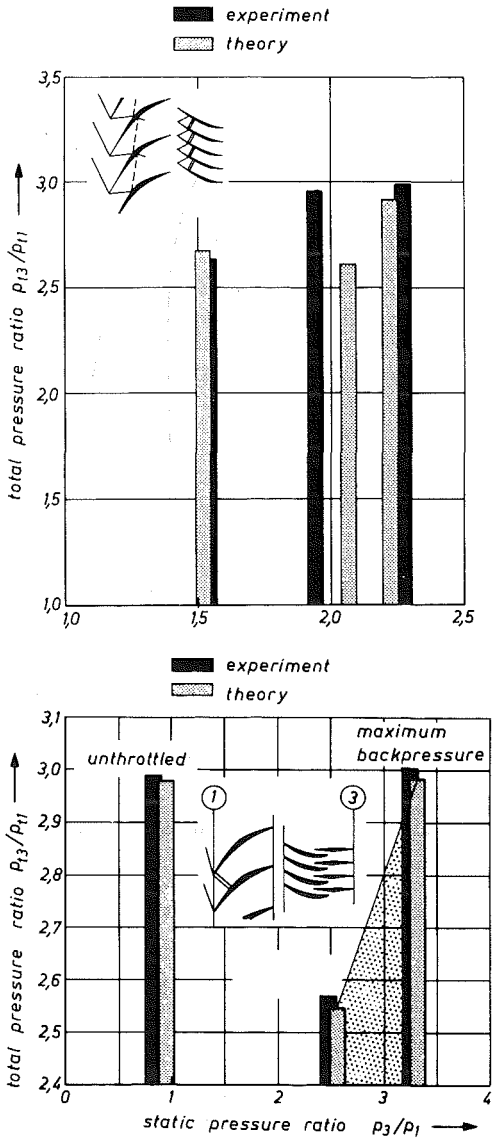

Fig. 14 Total pressure at the outlet of the impulse-type and shock-rotor stage

within the stator passage in the whole operation range. This can be realized by stators with variable geometry.

Acknowledgments

The presented investigations were supported by the "Deutsche Forschungsgemeinschaft," and the researching "Institut für Strahlantriebe und Turboarbeitsmaschinen, RWTH Aachen," and the authors would like to express their sincerest thanks for this promotion.

References

1 Weise, A., "Überschallaxialverdichter," Bericht 171 der Lilienthal-Gesellschaft, 1943.

2 Ritter, W. K., and Johnsen, I. A., "Performance of 24-Inch Supersonic Axial-Flow Compressor at Design Tip Speed of 1600 Feet per Second," NACA RM E7 L10, 1948.

3 Hartmann, M. J., and Tysl, E. R., "Investigation of a Supersonic-Compressor Rotor With Turning to Axial Direction. II—Rotor Component Off-Design and Stage Performance," NACA RM E53 L24, 1953.

4 Wennerstrom, A. J., Buzzel, W. A., and De Rose, R. D., "Test of a Supersonic Axial Compressor Stage Incorporating Splitter Vanes in the Rotor," ARL TR 75-0165, 1975.

5 Breugelmanns, F., "On the Use of a Pseudo-Shock System in Supersonic Compressors," *WGLR-Jahrbuch*, 1965.

6 Paulon, J., Reboux, J., and Sovrano, R., "Comparison of Test Results Obtained on Plane and Annular, Fixed or Rotating Supersonic Blade Cascades," ASME Paper No. 74-GT-49, 1974.

7 Simon, H., "Anwendung verschiedener Berechnungsverfahren zur Auslegung eines Überschallverdichter-Laufrades und dessen experimentelle Untersuchung," Diss. RWTH, Aachen, 1973.

8 Bohn, D., "Untersuchung zweier verschiedener axialer Überschallverdichter-Stufen unter besonderer Berücksichtigung der Wechsel wirkungen zwischen Lauf- und Leitrad," Diss. RWTH, Aachen, 1977.

9 Broichhausen, K.-D., and Gallus, H. E., "Theoretical and Experimental Analysis of the Flow Through Supersonic Compressor Rotors," *AIAA Journal*, Vol. 20, No. 8, 1982.

10 Fuchs, R., and Starken, H., "Experimental Investigations of Supersonic Cascades Designed for High Static Pressure Ratios," ASME Paper No. 77-GT-37, 1977.

11 Broichhausen, K.-D., and Gallus, H. E., "Influence of Shock and Boundary-Layer Losses on the Performance of Highly Loaded Supersonic Axial Flow Compressors," AGARD-CPP 400/401, 1986.

12 Monsarrat, N. T., Keenan, M. J., and Tramm, P. C., "Design Report: Single-Stage Evaluation of Highly Loaded High-Mach-Number Compressor Stages," NACA CR-72562, 1969.

13 Moeckel, W. E., "Approximate Method for Predicting Form and Location of Detached Shock Waves on Cones and Spheres," NACA TN 2000, 1950.

14 Miller, G. R., Lewis, G. W., and Hartmann, M. J., "Shock Losses in Transonic Compressor Blade Rows," ASME *Journal of Engineering for Power*, Vol. 83, 1961.

15 Donaldson, C., and Lange, R. H., "Study of the Pressure Rise Across Shock Waves Required to Separate Laminar and Turbulent Boundary Layers," NACA TN 2770, 1952.

16 Boxer, E., "A Method for Predicting the Performance of High Reaction Supersonic Compressor Blade Sections," AIAA Paper No. 69-522, 1969.

17 Volkmann, H., Fottner, L., and Scholz, N., "Aerodynamische Entwicklung eines dreistufigen Transsonik Frontgebläses," *ZFW*, Vol. 22, 1974.

18 Novak, R. A., "Streamline Curvature Computing Procedures for Fluid-Flow Problems," ASME *Journal of Engineering for Power*, Vol. 89, 1967.

19 Spindler, G., and Pätzold, H., "The Classical Streamline Curvature Method in the Supersonic Range: A Numerically Ill-Posed Boundary Value Problem," *ZFW*, Vol. 2, 1986.

20 Lichtfuss, H.-J., and Starken, H., "Supersonic Cascade Flow," *Progress in Aerospace Science*, Vol. 15, 1974.

21 Kauke, G., "Untersuchungen zur Nachlaufwechselwirkung im Tandem-Leitrad einer axialen Überschallverdichterstufe," Diss. RWTH, Aachen, 1986.

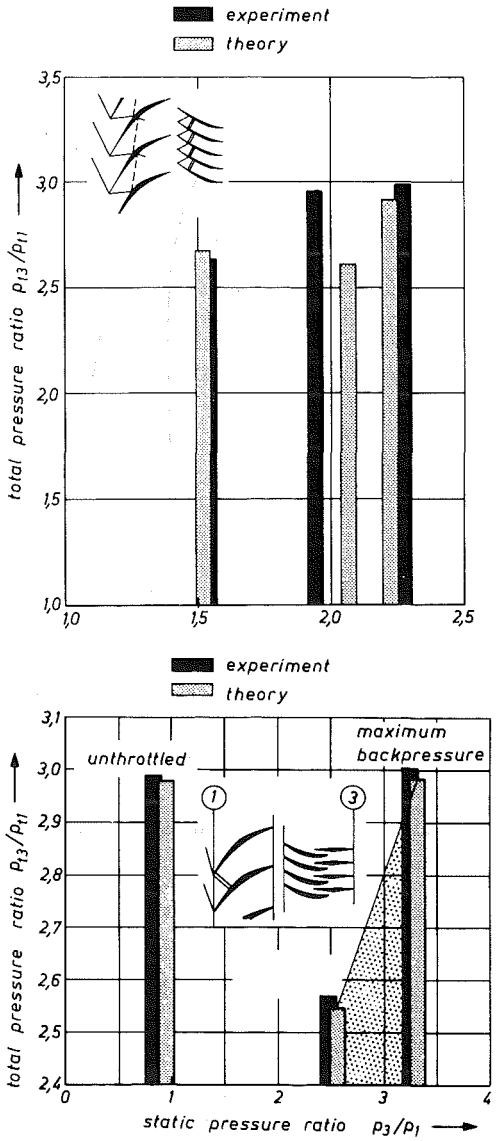

Fig. 14 Total pressure at the outlet of the impulse-type and shock-rotor stage

within the stator passage in the whole operation range. This can be realized by stators with variable geometry.

Acknowledgments

The presented investigations were supported by the "Deutsche Forschungsgemeinschaft," and the researching "Institut für Strahlantriebe und Turboarbeitsmaschinen, RWTH Aachen," and the authors would like to express their sincerest thanks for this promotion.

References

1 Weise, A., "Überschallaxialverdichter," Bericht 171 der Lilienthal-Gesellschaft, 1943.

2 Ritter, W. K., and Johnsen, I. A., "Performance of 24-Inch Supersonic Axial-Flow Compressor at Design Tip Speed of 1600 Feet per Second," NACA RM E7 L10, 1948.

3 Hartmann, M. J., and Tysl, E. R., "Investigation of a Supersonic-Compressor Rotor With Turning to Axial Direction. II—Rotor Component Off-Design and Stage Performance," NACA RM E53 L24, 1953.

4 Wennerstrom, A. J., Buzzel, W. A., and De Rose, R. D., "Test of a Supersonic Axial Compressor Stage Incorporating Splitter Vanes in the Rotor," ARL TR 75-0165, 1975.

5 Breugelmanns, F., "On the Use of a Pseudo-Shock System in Supersonic Compressors," *WGLR-Jahrbuch*, 1965.

6 Paulon, J., Reboux, J., and Sovrano, R., "Comparison of Test Results Obtained on Plane and Annular, Fixed or Rotating Supersonic Blade Cascades," ASME Paper No. 74-GT-49, 1974.

7 Simon, H., "Anwendung verschiedener Berechnungsverfahren zur Auslegung eines Überschallverdichter-Laufrades und dessen experimentelle Untersuchung," Diss. RWTH, Aachen, 1973.

8 Bohn, D., "Untersuchung zweier verschiedener axialer Überschallverdichter-Stufen unter besonderer Berücksichtigung der Wechsel wirkungen zwischen Lauf- und Leitrad," Diss. RWTH, Aachen, 1977.

9 Broichhausen, K.-D., and Gallus, H. E., "Theoretical and Experimental Analysis of the Flow Through Supersonic Compressor Rotors," *AIAA Journal*, Vol. 20, No. 8, 1982.

10 Fuchs, R., and Starken, H., "Experimental Investigations of Supersonic Cascades Designed for High Static Pressure Ratios," ASME Paper No. 77-GT-37, 1977.

11 Broichhausen, K.-D., and Gallus, H. E., "Influence of Shock and Boundary-Layer Losses on the Performance of Highly Loaded Supersonic Axial Flow Compressors," AGARD-CPP 400/401, 1986.

12 Monsarrat, N. T., Keenan, M. J., and Tramm, P. C., "Design Report: Single-Stage Evaluation of Highly Loaded High-Mach-Number Compressor Stages," NACA CR-72562, 1969.

13 Moeckel, W. E., "Approximate Method for Predicting Form and Location of Detached Shock Waves on Cones and Spheres," NACA TN 2000, 1950.

14 Miller, G. R., Lewis, G. W., and Hartmann, M. J., "Shock Losses in Transonic Compressor Blade Rows," ASME *Journal of Engineering for Power*, Vol. 83, 1961.

15 Donaldson, C., and Lange, R. H., "Study of the Pressure Rise Across Shock Waves Required to Separate Laminar and Turbulent Boundary Layers," NACA TN 2770, 1952.

16 Boxer, E., "A Method for Predicting the Performance of High Reaction Supersonic Compressor Blade Sections," AIAA Paper No. 69-522, 1969.

17 Volkmann, H., Fottner, L., and Scholz, N., "Aerodynamische Entwicklung eines dreistufigen Transsonik Frontgebläses," *ZFW*, Vol. 22, 1974.

18 Novak, R. A., "Streamline Curvature Computing Procedures for Fluid-Flow Problems," ASME *Journal of Engineering for Power*, Vol. 89, 1967.

19 Spindler, G., and Pätzold, H., "The Classical Streamline Curvature Method in the Supersonic Range: A Numerically Ill-Posed Boundary Value Problem," *ZFW*, Vol. 2, 1986.

20 Lichtfuss, H.-J., and Starken, H., "Supersonic Cascade Flow," *Progress in Aerospace Science*, Vol. 15, 1974.

21 Kauke, G., "Untersuchungen zur Nachlaufwechselwirkung im Tandem-Leitrad einer axialen Überschallverdichterstufe," Diss. RWTH, Aachen, 1986.

DISCUSSION

R. Fuchs[1] and H. Starken[1]

The authors present a very interesting paper on an important field of compressor research activity. Three different supersonic stages have been examined (Fig. 2) using fixed and variable geometry stators. It would be very interesting to compare these different types of stage, especially to see the payoff by the variable stator stage configuration.

The authors give some hints in Section 4.1 on a considerable improvement of stage performance by combining the impulse-type rotor with the variable single-row stator. In order to verify this, a presentation and comparison of the different performance maps would be very valuable. Of course, the performance map of the variable geometry stage is more complex due to the additional stagger angle parameter. But it is not easy to evaluate the different stage results from the diagrams in the paper. Using performance maps not only off-design comparisons would be possible, but also design performance comparisons, which are of great interest too.

If no performance map can be presented, it would be very useful to get additional information on the following matters:

In the introduction the authors present only the experimental results at design point for one rotor/stator combination (shock-rotor/tandem stator) under consideration. What about the design performance of the other configurations, especially the variable geometry one?

[1]DFVLR, Institut für Antriebstechnik, Köln, Federal Republic of Germany.

We would like to point out that in the bottom diagram of Fig. 3 the stagger angle α_{st} of the turnable stator is measured toward the blade pressure side, whereas in Fig. 11 α_{st} is measured toward the suction side. That results in a difference of 7 deg [22]. In the definition of Fig. 11 the design value of α_{st} is 47 deg.

The results presented in Fig. 11 extend from $\alpha_{st} = 61$ to 53 deg. Therefore the lowest value of α_{st} is still 6 deg above design. Are there any results close to the design value of $\alpha_{st} =$ 47 deg? Also results for the rotor/stator combination of Fig. 11 taken at higher than the starting rotor speed would be of great interest.

From Fig. 13, where the fixed and the turnable stator stages are compared at design speed, the question arises as to whether the results of the turnable stator are taken at the design stagger angle. From the shock system on the stator cascade sketch given in this diagram, this seems not to be the case. The flow case shown in Fig. 13 with no suction surface leading edge oblique shock wave [22] belongs to a stator blade stagger position of 7 deg or more above design.

Similar questions arise for Fig. 14 (upper part): Have the compared results been obtained at design speed, design stator blade stagger angle position of $\alpha_{st} = 47$ deg and, as in the lower part of this diagram for the fixed tandem stator blade stage, at maximum back pressure? The maximum back pressure presented for the turnable stator blade stage seems to be quite low.

References

22 Fuchs, R., *Design and Investigation of Static Pressure Compressor Cascades Behind Impulse Rotors*, ESA-TT-629, Nov. 1980.

Authors' Closure

The authors thank Dr. Fuchs and Dr. Starken for their detailed discussion.

The following closure is arranged systematically with respect to the main topics of the discussion.

1 Influence of the Stator Setting on the Starting Process (Impulse-Type Rotor/Variable Geometry Stator). The definition of the stagger angle in Fig. 3 representing blade geometry data is correct. In Fig. 11, explaining mainly the velocity triangle at stator inlet, the stagger angle should also be measured with respect to the pressure side. This inaccuracy in the preprint is already corrected in the printed version. Thus $\alpha_{St} = 53$ deg corresponds to the closest stator setting (Design 54 deg).

2 Lack of Results Regarding the Impulse-Type Rotor/Variable Geometry Stator at Speeds Higher Than the Starting Speed (Fig. 11). As can be seen from the axial Mach number distribution versus speed ratio in Fig. 11, the axial flow is clearly supersonic if the starting speed is exceeded. For this case the rotor exit average data coincide with the data for rotor-alone operation and are omitted for clearness reasons.

3 Design Performance Comparison of the Different Supersonic Compressor Stages. The main features of the flow at design speed and increased back pressure are described in Section 4.2.

"Regarding the *impulse-type rotor and tandem stator*, the close vicinity of starting and design speed . . . did not allow a throttling" (Section 4.2). Consequently no data for design back pressure can be presented.

The design-speed line of the *shock-rotor/tandem stator* combination is given in Figs. 13 and 14. Stable operation and the design data (see introduction) have been achieved with satisfying efficiency.

Regarding the *impulse-type rotor and variable geometry stator* the corresponding data are also shown in Figs. 13 and 14. The results at maximum back pressure refer to the closest throttle position with stable operation corresponding to the surge margin of the compressor stage. Contrary to design condition the interaction of shocks with wall boundary layers at hub and casing prevents a deceleration of the flow to subsonic exit conditions. In the real compressor a pseudoshock system is achieved, generating nearly sonic speed at the stator exit (see section 4.2).

For these reasons further investigation of supersonic compressors at the Technical University Aachen is mainly focused on the development of shock rotors in combination with tandem stators [23].

References

23 Mönig, R., Broichhausen, K.-D., and Gallus, H. E., "Applications of Highly Loaded Single-Stage Mixed-Flow Compressors in Small Jet-Engines," AGARD Conference Proceedings No. 421, 1987.

Experimental Investigations of Flows Through a Plane Cascade at Large Angles of Attack With Separations

Chuan-Gang Gu
Postdoctoral Research Fellow.

Lai-Qin Luo
Director of Laboratory.

Yong-Miao Miao
Professor.

Department of Power Mechanical Engineering,
Xi'an Jiaotong University,
People's Republic of China

Measurements of various parameters in the flows through a cascade at different angles of attack have been performed. The parameters, such as Reynolds stresses (uu/U^2, vv/U^2, *and* uv/U^2), *pressure distribution on the blade surface, velocity distribution in the blade passage, position of the separation point, and so on, are measured at a large angle of attack with separations. In addition, the development of wake is also investigated. A new formula with second-order accuracy has been developed to analyze hot-wire signals in flows with high turbulence intensity. The hot-wire data are compared with those by conventional measurement techniques and by flow visualizations. The results are satisfactory.*

Introduction

Separations in flows through a cascade at large angle of attack are important phenomena. They are directly related to output work, efficiency, and the operating range of turbomachinery. In order to design a cascade with good aerodynamic properties, the phenomena of separation should be thoroughly investigated. Most previous experimental studies about cascades are confined to the blade surface pressure distributions and the flow parameters ahead of and behind the cascade. However, in order to understand the separation phenomenon better, the parameters such as Reynolds stresses ($\overline{uu}/U^2$, $\overline{vv}/U^2$, $\overline{uv}/U^2$), detailed velocity development in blade passage, and turbulence intensities must be measured.

In the case of small angle of attack (i.e., at design operation), separation, if it occurs at all, is only limited to a tiny region in the cascade passage. When the angle of attack increases this region will gradually grow and eventually produce a violent effect on the aerodynamic properties of the cascade flow. As the flow in turbomachines is mainly turbulent, various turbulence model theories have been proposed in recent years to predicate the flow field (Gu and Miao, 1985; Gu, 1985; Launder and Spading, 1974; Nakayama et al., 1983). They in turn need detailed turbulence measured quantities to verify and adjust the numerical results.

The purpose of the present work is to measure the average parameters and turbulence quantities of the flow through a plane cascade with and without separation. In addition, a visualization technique has been developed to indicate the separation point on the blade surface. Its location will provide valuable information to the numerical investigators.

Tests of the setup of plane cascade are usually two dimensional. To ensure two dimensionality, it is necessary to suck the boundary layers off the endwalls of the blades. We did the same during the tests. However, separation is a three-dimensional and unsteady phenomenon. In our experiments, we found that at a certain angle of attack, this unsteady effect made the separation point fluctuate back and forth. In spite of this we do believe that when separation takes place in the cascade passage, the flow can be treated as quasi-steady and two-dimensional at least in a limited central region of the cascade.

High turbulence intensity usually occurs in the neighborhood of the separation region. A new formula with second-order accuracy has been developed to analyze the signals sampled by hot wire, because in this case the conventional methods are not suitable (Rodi, 1975; Hinze, 1975).

Experimental Apparatus

Wind Tunnel Parameters. The experiments have been conducted in an open-circuit wind tunnel, in the Gas Dynamics Laboratory of Xi'an Jiaotong University. The plane cascade experimental apparatus is schematically shown in Fig. 1. It consists of a blower, stabilizing tank, grid, and test cascade of blades. The blower is driven by 100 kW d-c motor, which permits continuous variation of speed, up to a maximum of 3000 rpm. The diameter and length of the stabilizing tank are 2 m and 4 m, respectively.

The maximum average velocity in the cascade is about 120 m/s, which corresponds to a Mach number of 0.34 and the Reynolds number, based on the chord length, is 4.8×10^5.

The grid placed in front of the test section can be changed to get a different turbulence intensity of the incoming flow. The

Contributed by the Gas Turbine Division of THE AMERICAN SOCIETY OF MECHANICAL ENGINEERS and presented at the 32nd International Gas Turbine Conference and Exhibit, Anaheim, California, May 31–June 4, 1987. Manuscript received at ASME Headquarters February 6, 1987. Paper No. 87-GT-96.

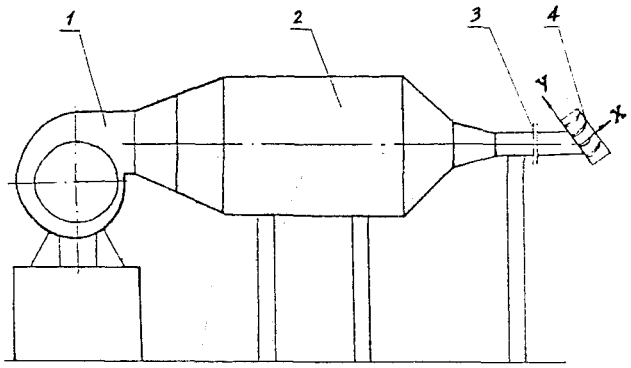

Fig. 1 Schematic diagram of the experimental apparatus: (1) blower; (2) stabilizing tank; (3) grid; (4) blades

area of test section of cascade is 120 mm × 300 mm. The plane cascade, which consists of the eight blades with a C_4 profile, is fixed to a circular plate. It is easy to get various inlet flow angles by means of rotating this circular plate. The detail of the cascade is listed as follows:

chord length	C = 60 mm
height	L = 120 mm
pitch	t = 45 mm
solidity	$\sigma = c/t$ = 1.33 mm
stagger angle	λ = 25.8 deg
incidence	$i = \beta - \lambda$
camber	30 deg
max. thickness of blade	7.2 mm
L.E.R.	R2.1 mm

In order to measure pressure distribution on the blade surfaces, 32 static pressure-tap holes are arranged on two adjacent blades, which are located in the middle of the cascade. The number of holes on the convex side is 17 and on the concave side, 15. The geometry of the cascade is shown in Fig. 2.

Equipment of Boundary Layer Suction. To make the flow through the cascade two dimensional, the equipment of artificial suction of the boundary layer is arranged on the endwall of the cascade duct. Adjustable plates A and B (Fig. 3) can be used to make incoming flow parallel. The amount of suction should be maintained at 4 ~ 5 percent of the total flow rate by a separate centrifugal fan.

Because the test of plane cascade wind tunnel is to simulate an infinite cascade flow field, the flow in the test section must be two dimensional. This means that boundary layer suction of the endwalls is needed.

As a matter of fact, it is difficult to get real two-dimensional flow. The effectiveness of boundary layer suction is only limited. There are various standards for checking the two dimensionality of flow. Two main standards adopted in the present work are as follows:

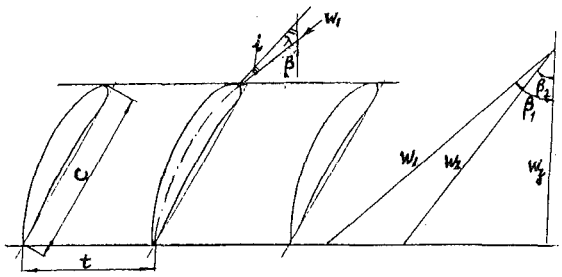

Fig. 2 Geometric and aerodynamic parameters of cascade

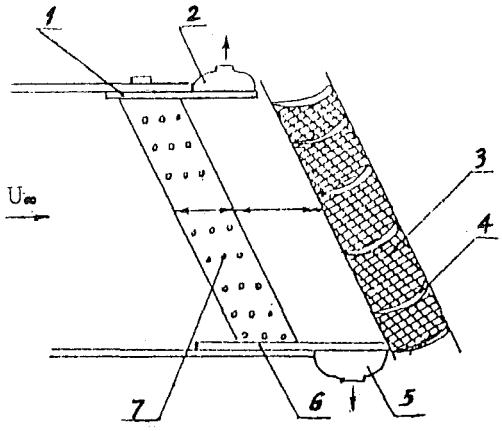

Fig. 3 Schematic diagram of boundary layer suction equipment: (1, 6) adjustable plates A and B, respectively; (2, 5) suction collectors; (3) copper filter gauze; (4) cascade; (7) small holes for suction

(*a*) The contraction coefficient of the flow should not be less than 0.9

$$\xi = \frac{\int \rho_1 w_1 \cos \beta_1 dx}{\int \rho_2 w_2 \cos \beta_2 dx} \tag{1}$$

(*b*) For a certain distance along the blade height, the distribution of pressure and velocity behind the blade is approximately uniform along the blade height and should be periodic along the pitch line. According to the previous suggestions and experiences [4, 5], it may be considered as uniform flow when the variation of total pressure in the vicinity of middle flow plane of cascade (about 40 ~ 50 mm along the blade height) is less than 1.5 percent and that of the velocity direction is less than 1 deg.

Our experiments show that when the angle of incidence is nearly zero, the method of boundary layer suction can greatly improve the two dimensionality of flow. The contraction coefficient ξ could be greater than 0.91, which conforms to standard (*a*). However, at the large angle of incidence with separation, the contraction coefficient ξ can only be increased up to 0.78 by boundary layer suction. If still more suction is applied,

Nomenclature

Cx = drag coefficient of a cascade $= Fx/(\frac{1}{2} \cdot \rho U_m^2 \cdot c)$
Cy = lift coefficient of a cascade $= Fy/(\frac{1}{2} \cdot \rho U_m^2 \cdot c)$
c = chord length
c_p = static pressure coefficient $= (P - P_{in})/\frac{1}{2} U^2$
P_{10} = total pressure of incoming flow
P_{20} = total pressure of the outlet at $x/c = 2.5$
p = pressure
Re_c = chord Reynolds number
t = pitch
Um = geometric mean velocity of a cascade
U_∞ = incoming velocity
U, V = components of mean velocity
u, v = fluctuating velocities
x, y = coordinate
β = angle of incoming flow
$\bar{\epsilon}$ = turbulent intensity in two-dimensional flow
ρ = density
σ = solidity
ω = total pressure loss coefficient $= (P_{10} - P_{20})/\frac{1}{2} \rho U_\infty^2$
$\bar{\omega}$ = total pressure loss coefficient

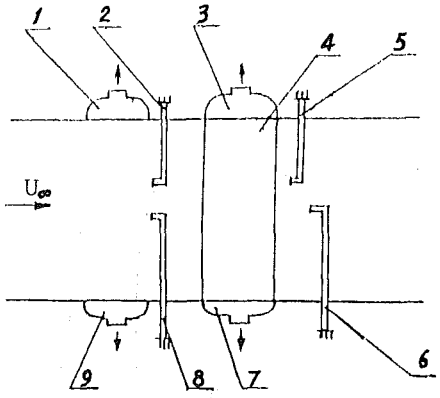

Fig. 4 Sectional elevation of Fig. 3: (1, 3, 7, 9) suction collectors; (2, 5) hot wires; (4) blades; (6, 8) probes

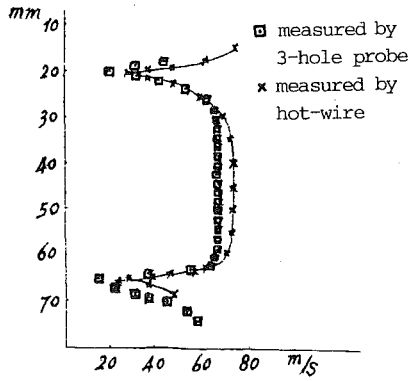

Fig. 5 Comparison of mean velocity distribution at x/c = 1.2

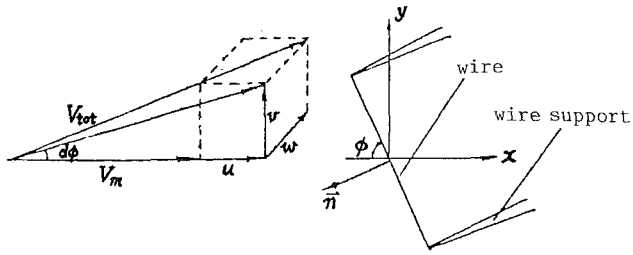

Fig. 6 Orientation of the hot wire in the flow field

the flow within the passage would be seriously distorted. In this case standard (*b*) should be adopted. The measurements show that by boundary layer suction the distributions of total pressure and velocity in a region 40 mm × 150 mm of the test section, which corresponds to three pitches, can be maintained as uniform and periodic.

System of Measurement

Ordinary Measuring Instruments. The three-hole wedge probes are fixed on the left of the test section ahead of and behind the cascade, as shown in Fig. 4. On the right of the test section, a three-dimensional traversing mechanism is arranged for measuring the development of wake.

The three-hole wedge probes have been calibrated in the calibrated tunnel. The deviation is less than 1 percent in velocity and less than 0.25 deg in direction.

Hot-Wire Anemometer. The mean velocity and turbulent quantities $\overline{uu}$, $\overline{vv}$, and $\overline{uv}$ are measured by a single constant temperature hot-wire sensor (TSI 1210-T1.5), which has a diameter $d = 4\ \mu$m, with an aspect ratio I/d of about 350 and an overheat ratio of 1.75. The frequency response of the hot-wire anemometer is over 160 kHz.

The calibration of the hot wire has been carried out on a calibrator (TSI Model 1125). To ensure high accuracy of measurement, the constants A, B, and n in King's equation have been determined individually. The sensitivity to velocity direction of the hot wire is carefully calibrated.

When mean velocity = 80 m/s, we find that the maximum measuremental variation of the hot wire is 8.4 percent if the variation of temperature in the incoming flow is 7.5°C. For convenience, we control the inlet temperature of the fluid to be within 2~3°C in the experimental processes in order to keep the deviation of measurements to be less than 2.5 percent.

The comparison of mean velocities measured by the hot wire with that by three-hole probe is shown in Fig. 5; its relative error is less than 5 percent.

Measurements and Treatment of Turbulent Quantities. For analyzing and treating the signals measured by a hot wire in flow with high turbulence intensity, a new formula has been developed [3] as follows:

$$\frac{\overline{e^4}}{4E^2}+\overline{e^2} = \frac{1}{K^2}\left(\frac{\overline{u^2}}{V_m^2}\sin^2\phi+2\frac{\overline{uv}}{V_m^2}\sin\phi\cos\phi+\frac{\overline{v^2}}{V_m^2}\cos^2\phi\right) \quad (2)$$

where V_m is average velocity of the incoming flow; ϕ is angle of the axis of a hot wire with the direction of the incoming flow; E_m is the d-c voltage; e is the fluctuating voltage; B and n are the constants of King's formula ($E^2 = A+B\cdot V_N^n$); $K = 2E_m/[B\cdot V_m^n\cdot n\cdot \sin^{(n-1)}\phi]$.

Figure 6 shows the orientation of the hot wire in the flow field, where V_{TOT} is instantaneous flow velocity and the hot wire is in the x–y plane.

Three values of $\overline{e^2}$ at different angles of ϕ = 90, 45, and −45 deg can be measured; three corresponding equations of equation (2) can be formed to solve the values of $\overline{uu}/V_m^2$, $\overline{uv}/V_m^2$, $\overline{vv}/V_m^2$:

$$\begin{cases} \dfrac{\overline{u^2}}{V_m^2} = \left[K^2\left(\dfrac{\overline{e^4}}{4E_m^2}+\overline{e^2}\right)\right]_{90\ \deg} \\ \dfrac{\overline{uv}}{V_m^2} = \dfrac{1}{2}\left\{\left[K^2\left(\dfrac{\overline{e^4}}{4E_m^2}+\overline{e^2}\right)\right]_{45\ \deg} - \left[K^2\left(\dfrac{\overline{e^4}}{4E_m^2}+\overline{e^2}\right]_{-45\ \deg}\right\} \\ \dfrac{\overline{v^2}}{V_m^2} = \left[K^2\left(\dfrac{\overline{e^4}}{4E_m^2}+\overline{e^2}\right)\right]_{45\ \deg} + \left[K^2\left(\dfrac{\overline{e^4}}{4E_m^2}+\overline{e^2}\right)\right]_{-45\ \deg} - \dfrac{\overline{u^2}}{V_m^2} \end{cases} \quad (3)$$

Test Procedure

Experiments are performed at angles of incoming flow β = 43 deg (close to zero incidence angle) and β = 58 deg (in-

cidence angle = 15 deg), with incoming velocity about 80 m/s. Measurements include mean velocity, turbulence intensity of the incoming flow, pressure distribution on the surfaces of blade, position of the separation point, and velocity distribution behind the cascade. In case of β = 58 deg with separation, the distributions of fluctuating velocities in the cascade passage and behind the cascade are also measured.

Mean Velocity and Turbulence. In regions ahead of and behind the cascade, mean velocities are measured by three-hole probe and hot wire. Their relative deviation is less than 5 percent.

In the cascade passage, both mean and fluctuating velocities are measured by a single hot wire with 90 deg angle-adapter. To avoid the wall effect, the minimum distance of the hot wire from the wall is 0.5 mm. The space of cascade passage is so narrow that only mean velocity and turbulence intensity can be measured. However, in the region behind the cascade, the Reynolds stresses are measured by turning the hot wire.

Separation Point. The phenomenon of separation is always unsteady actually, and both the separation point on the blade surface and the region of separation are unstable. So it is difficult to measure the position of the separation point accurately. However, the experiments show that the position of the separation point shifts itself about a point. Thus, the flow with separation can be considered as a quasi-steady flow.

A visualization method has been devised by coating the blade with a special glycerin mixture liquid, to indicate the position of separation point.

Results

Velocity and Pressure Distribution, Separation. The turbulence intensities of the incoming flow in the main flow ahead of test section are uniform and their measured value is about 2 percent.

Under the condition of β = 43 deg (about zero incidence angle), the incoming velocity U = 73 m/s, Mach number M = 0.21, Reynolds number $Re_c = 2.8 \times 10^5$, the experiments have been performed without separation. Figure 7 shows the experimental pressure distribution. Figure 8 shows the average velocity component profiles at x/c = 1.2.

At β = 58 deg (incidence angle = 15 deg), the incoming velocity U = 80 m/s, M = 0.23, and $Re_c = 3.2 \times 10^5$, several experiments are also performed. By a visualization method the

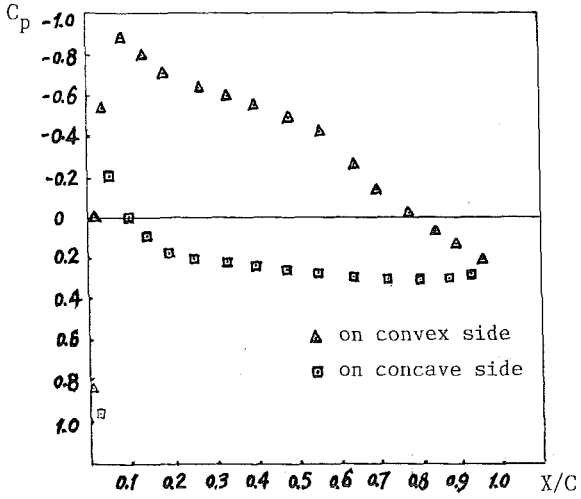

Fig. 7 Pressure distribution on blade surface (β = 43 deg)

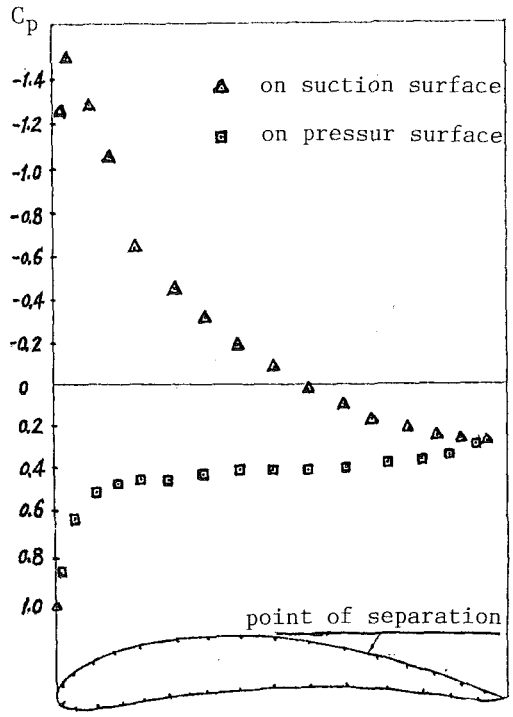

Fig. 9 Pressure distribution on the surface of the blade at β = 58 deg

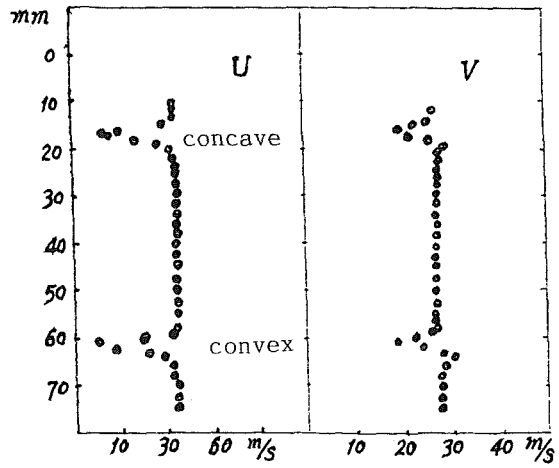

Fig. 8 Distribution of velocity (β = 43 deg) at x/c = 1.2

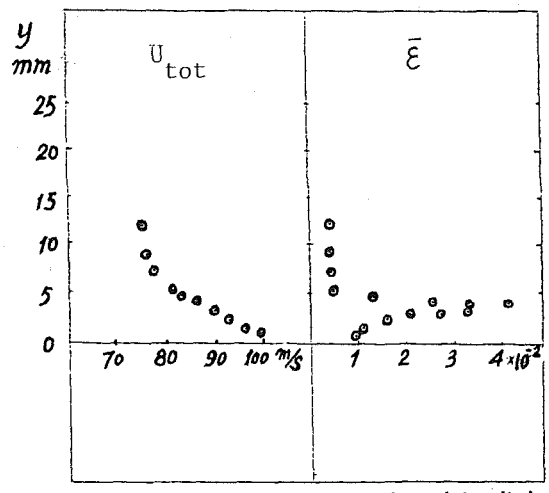

Fig. 10 Distribution of mean velocity and turbulence intensity in plane cascade passage (β = 58 deg) at x/c = 0.085

separation point is located at $x/c = 0.7 \sim 0.75$. Figure 9 shows the distribution of pressure, which is quite different from Fig. 7 at $\beta = 43$ deg. The lift coefficients of the cascade, Cy, are determined as 0.713 at $\beta = 43$ deg and 1.117 at $\beta = 58$ deg. The drag coefficients of the cascade, Cx, are determined as 0.039 at $\beta = 43$ deg and 0.226 at $\beta = 58$ deg.

Figures 10 and 11 show the distributions of mean velocity and turbulence intensity in the cascade passage at $x/c = 0.085$ and $x/c = 0.34$, respectively. It can be seen that the velocities near the convex side take big values in the leading region of the blade (Fig. 10) and decelerate along the surface (Fig. 11). The change of $\bar{\epsilon}$ at these points is not so distinct.

Figure 12 indicates the distribution of mean velocity and turbulence intensity at $\beta = 58$ deg and $x/c = 0.75$. Notice their sharp variations near the wall. Figure 13 shows the distribution of mean velocity components in the wake at $\beta = 58$ deg and $x/c = 1.2$. Comparing Fig. 13 with Fig. 8, we can see that at large angle of attack the wake becomes wider and the variation of velocity increases about twice (as shown in Fig. 13, the maximum difference of velocity is about 30 m/s, in Fig. 8 only 15 m/s), which means in this case the loss of momentum in the wake is bigger. The total pressure loss coefficients are determined as 0.152 at $\beta = 58$ deg and 0.048 at $\beta = 43$ deg.

Turbulence Intensity in the Cascade Passage. At large angle of attack ($\beta = 58$ deg), the separation occurred on the convex side of the blade, as shown in Fig. 14 (because of the limited photograph angle, the view is only a part of the blade). Scouring of airflow on the coating film of glycerin mixture on the convex side of blade piles up a "heaping belt," which indicates an approximate position of separation. A lot of parallel streaks are seen in the regions up and downstream of the "heaping belt." By the visualization method, the belt is located at about $x/c = 0.75$. Its occurrence is demonstrated by variation of the turbulence intensity (defined here as the ratio of rms value of the fluctuating velocity and incoming velocity) observed on the oscilloscope screen. Figure 14 is a picture with four oscilloscope waveforms at $x/c = 0.75$ in the passage, which indicate the variation of turbulence intensity. In waveform 4 the signal of the hot wire is sampled at a point located at a distance of 1.5 mm from the convex side, where the fluctuation velocity is a maximum. While the hot wire moves close to the convex side of blade to a distance of 0.5 mm, $\bar{\epsilon}$ is decreasing. Waveforms 3 and 2 show the oscillogram of the hot-wire output at a distance of 2.5 mm and 3.5 mm from the convex side of the blade, respectively. After reaching a distance of 4.5 mm ~ 5.5 mm from the convex side of the blade (point A in Fig. 15), $\bar{\epsilon}$ decreases sharply and remains stationary, as shown in waveform 1 up to point B at a distance of 8 mm from concave surface of blade. When the hot wire moves from point B close to the concave side, $\bar{\epsilon}$ increases again until the hot-wire sensor reaches to its limitation of accessibility of 4 mm from the concave surface. These numerical values are expressed in Fig. 12.

By the method of the visualization and oscillograms of the hot-wire output, the separation point can be located at about $x/c = 0.7 \sim 0.75$. The measurements along the pitch line at $x/c = 0.085$ and $x/c = 0.34$ are similar to those at $x/c = 0.75$. Generally speaking, the trend of variation of $\bar{\epsilon}$ in the cascade passage in the direction of pitch line (parallel to line $\overline{AB}$ in Fig. 15) is comparable, i.e., it increases from the wall to a max-

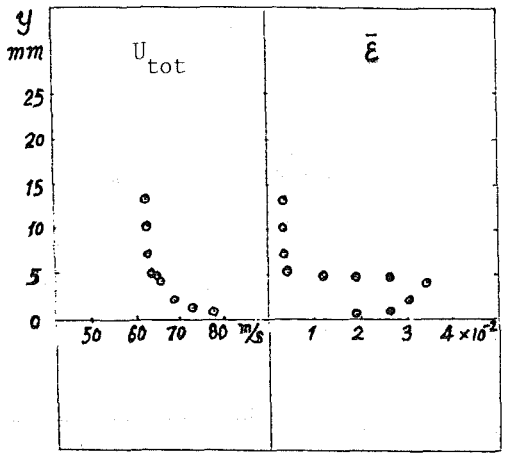

Fig. 11 Distribution of mean velocity and turbulence intensity in plane cascade passage ($\beta = 58$ deg) at $x/c = 0.34$

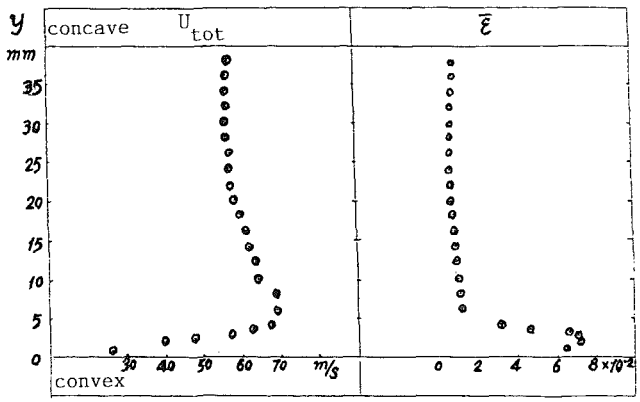

Fig. 12 Distribution of mean velocity and turbulence intensity in plane cascade passage ($\beta = 58$ deg) at $x/c = 0.75$

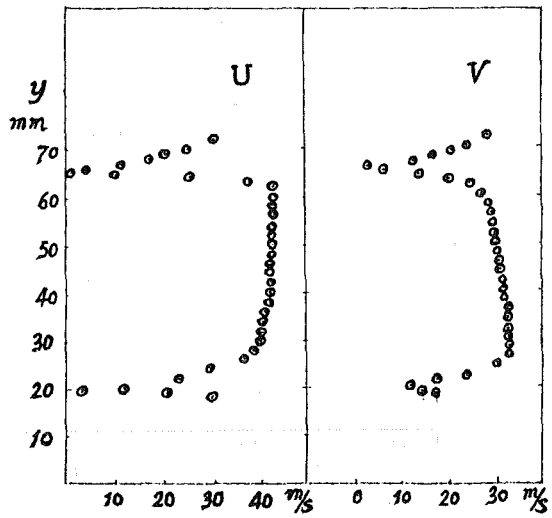

Fig. 13 Distribution of mean velocity ($\beta = 58$ deg) at $x/c = 1.2$

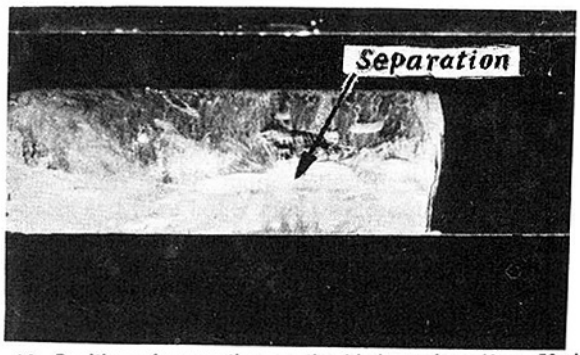

Fig. 14 Position of separation on the blade surface ($\beta = 58$ deg) viewed by visualization at $x/c = 0.75$

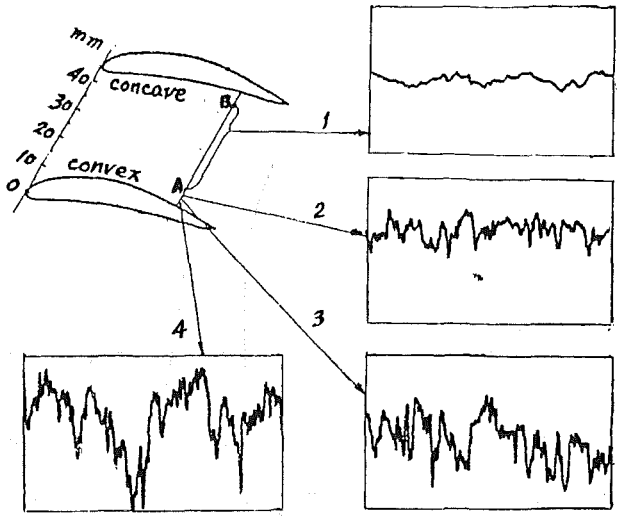

Fig. 15 Variation of fluctuating velocities in cascade passage (β = 58 deg) at x/c = 0.75

imum then sharply falls to much smaller stationary value in the region of main flow.

Reynolds Stresses Behind the Cascade. In the flow field behind the cascade, by rotating a single hot wire to directions $\phi = 90$, 45, and -45 deg, the Reynolds stresses $\overline{uu}/U^2$, $\overline{vv}/U^2$, and $\overline{uv}/U^2$ can be determined by equation (3). The results are shown in Fig. 16.

Downstream of the cascade the Reynolds stresses in the wake are very large. Their tendency is correct and comparable to [10]. As shown in Fig. 16 at a distance y/c less than -0.1 and greater than 0.3 their values are practically zero. Notice the variation of the Reynolds shear stress $\overline{uv}/U^2$ is as expected. The position, where its value changes from positive to negative at y/c = 0.05, is close to the trailing edge of the blade. The maximum value of Reynolds stress $\overline{u}^2/U^2$ is about 1.4 times that of $\overline{v}^2/U^2$.

Conclusions

1 Investigation shows that the distributions of the turbulence intensity in various regions of the cascade flow field are different: In the cascade passage, $\bar{\epsilon}$ increases from the surface to a maximum and then sharply falls to a much smaller stationary value in the region of main flow; ahead of the separation point the variation trends along the pitch line direction are the same, but smaller in numerical value and narrower in width (see Figs. 10, 11, and 12); in the separation region and its neighborhood, the $\bar{\epsilon}$ increases obviously; in the region behind the cascade and near the trailing edge, $\bar{\epsilon}$ is also large; in

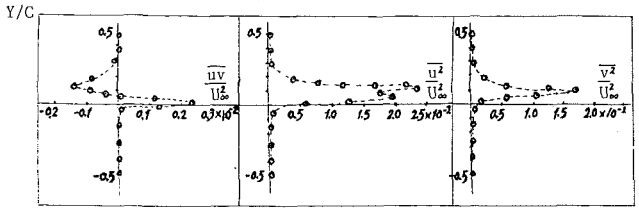

Fig. 16 Distribution of Reynolds stresses $\overline{uv}/U^2$, $\overline{u}^2/U^2$, $\overline{v}^2/U^2$ (β = 58 deg) at x/c = 1.2

the wake downstream of the cascade at x/c = 1.2 the values are estimated roughly 20 to 40 times larger than those in cascade passage. With the development of wake, at a distance of 1.5 times chord length from the trailing edge, the values of $\bar{\epsilon}$ are gradually leveled off; however, they are still several times as high as those of the incoming flow. The steady parameters are approximately uniform at the outlet of the cascade about 1.5 times chord length from the trailing edge.

2 The experimental methods on turbulent flow through a plane cascade with or without separation have been investigated. A new formula (equation (3)) with second-order accuracy has been developed. It is suitable to analyze and treat the data of turbulent flows with high turbulence intensity.

3 In order to make the flow in a cascade wind tunnel two dimensional, the method of boundary layer suction must be used.

References

1 Gu, Chuan Gang, and Miao, Yong Miao, 1985, "Study of Turbulent Flow Through a Plane Cascade at Various Angles of Attack With Separation," *Proc. of International Symposium on Refined Flow Modelling and Turbulence Measurement*, Vol. 1, p. A25.

2 Gu, Chuan Gang, 1985, "Numerical and Experimental Study on the Incompressible Viscous Flow Through a Plane Cascade at Various Angles of Attack," Ph.D. Thesis, Xi'an Jiaotong University, China.

3 Luo, Lai Qin, and Gu, Chuan Gang, 1985, "An Application of Hot Wire Anemometer on the Flow With High Fluctuating Velocity in Turbomachines," *Report of Xi'an Jiaotong University*, No. 85-069.

4 Tsui Chin-ya, Zhou Sheng, Lu Ren-fu, and Zhang Lian-chi, 1980, "An Experiment to Improve the Surge Margin by Use of Cascade With Splitter Blade," *J. of Engineering Thermophysics*, Vol. 1, No. 2, p. 128.

5 Stuart, P. J. K., 1955, "Analysis of Reynolds Number Effects in Fluid Flow Through Two-Dimensional Cascade," *R&M*, No. 2920.

6 Launder, B. E., and Spalding, D. B., 1974, "The Numerical Calculation of Turbulent Flows," *Comput. Method in Applied Mech. and Eng.*, Vol. 3, No. 1, p. 269.

7 Nakayama, A., Chow, W. L., and Sharma, D., 1983, "Calculation of Fully Developed Turbulent Flows in Ducts of Arbitrary Cross-Section," *J. Fluid Mechanics*, Vol. 128, p. 199.

8 Rodi, W., 1979, "A New Method of Analysing Hot-Wire Signal in Highly Turbulent Flow and Its Evaluation in a Round Jet," *DISA Information*, No. 17.

9 Hinze, J., 1975, *Turbulence*, 2nd ed., New York.

10 McCroskey, W. J., 1982, "Incompressible Separated Flow External Flow Two-Dimensional Stalled Airflow – Flow Case 0441 Technical Report," *Proc. of the 1980-1981 Conf. on Complex Turbulent Flow*, Vol. II, pp. 873-884.

Interaction Mechanisms Between Tip Leakage Flow and the Passage Vortex in a Linear Turbine Rotor Cascade

A. Yamamoto
National Aerospace Laboratory,
Chofu, Tokyo, Japan

In order to study the loss generation mechanisms due to the tip-leakage flow in turbine rotor passages, extensive traverse measurements were made of the three-dimensional flows in a low-speed linear cascade for various tip-clearance sizes and for various cascade inlet flow angles (or incidences). Effects of the leakage flow on the cascade downstream flow fields and interactions between the leakage flow and the passage vortices are discussed in detail based on the traverse measurements and flow-visualization tests in terms of secondary flows and the associated losses. Other traverses were also performed of the tip-casing endwall flows both inside and outside the tip-clearance gap using a micro five-hole pitot tube to reveal the axial development of the interaction throughout the cascade passage. Overall loss characteristics of the present high-turning cascade with blunt leading and trailing edges are obtained and compared with those predicted by the Ainley–Mathieson method.

Introduction

Recent secondary flow research has revealed a number of complex flow phenomena in turbine cascade passages: Many three-dimensional vortical flows exist as illustrated in Fig. 1. The figure was drawn schematically based on much of the previous secondary flow research as reviewed by Sieverding (1985) and on the author's experience. The detailed explanation of Fig. 1 may be found in Yamamoto (1986). Most of these flow pictures have been obtained near the design inlet flow conditions. One can, therefore, expect that the flow pictures will easily change under various off-design conditions, for example, with different cascade inlet flow angles (or incidences). Among these three-dimensional flows, the passage vortices forming in the cascade passage and the leakage flow passing through the blade tip clearance will be the most important factors contributing to the loss production in rotor blade rows with tip clearance, although the extent of their contribution, of course, will depend on the cascade incidence (or turning) and the clearance size. Overall cascade loss characteristics with the incidence variation have been known well, as shown in for example Ainley's incidence-loss curve (e.g., Ainley, 1948), but details of the mechanism have not been fully understood yet, in particular for such modern turbine blade rows with high turning and with thick blade profiles as widely adopted for high-temperature turbines. More experimental information is needed to understand the loss mechanisms as well as the overall loss characteristics of modern blade rows.

Contributed by the Gas Turbine Division for publication in the JOURNAL OF TURBOMACHINERY. Manuscript received by the Gas Turbine Division July 30, 1987.

Recently, a lot of advanced computer programs have been developed for solving three-dimensional viscous flows in turbomachinery flow passages (e.g., Hah, 1983; Moore and Moore, 1985; Shikano et al., 1985; Weinberg et al., 1986; Rhie, 1986; Dawes, 1986; Nakahashi et al., 1987). They will provide accurate overall losses themselves for arbitrary blade rows in the near future. In the theoretical work, however, detailed and reliable experimental data on the loss mechanisms are urgently needed, since such data are absolutely essential for making the theoretical work successful, i.e., for understanding real flow physics to determine the boundary conditions or assumptions, for constructing the turbulence models used in the theories, and for verifying the predicted results.

In such theoretical work, Hah (1986), Pouagare and Delaney (1986), and Dawes (1987) have recently predicted the endwall flows both inside and outside the tip clearance using Navier–Stokes equations, and shown strong interactions between the leakage flows and the cascade endwall flow (or the tip-side passage vortex). Their calculated results, however, are limited to compressor cascades. In turbine cascades, the flows are generally much more deflected than in compressor cascades and have larger pitchwise pressure gradients in the passages. Therefore, the interaction would be stronger in turbines than in compressors. In the experimental work, on the other hand, a number of studies on the leakage flow have been made, but most of them present the flows only "around" the blade tip, such as static pressures on the blade tip, blade surfaces near the tip, or on the casing wall. No direct traverse measurements of the leakage flow vectors inside the tip

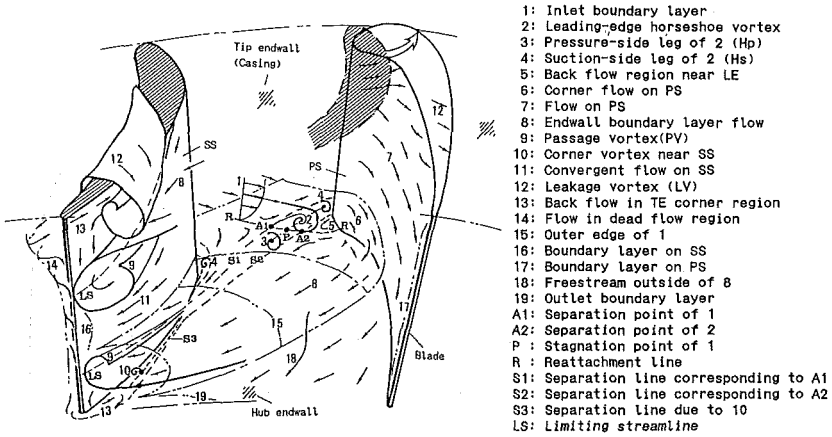

Fig. 1 Review of flows in turbine passage (drawn with the right blade a little opened in order to see the flows near *PS*)

clearance have been reported yet, for both turbine and compressor cascades. Such measurements are necessary to see the leakage flows and their characteristics in detail.

The major purposes of the present paper are (1) to give some detailed experimental data on the mechanisms of secondary losses, especially of the leakage loss, at design and off-design conditions with incidence change; (2) to analyze the interaction mechanism between the leakage flow and the passage vortices in the cascade downstream secondary flow fields; (3) to show the axial development of the interaction through the cascade passage and show some characteristics of the leakage flow inside the tip-clearance; and (4) to provide the test overall loss for the present high-turning cascade and compare it with that predicted by the Ainley–Mathieson method. However, an important effect on the loss mechanism due to the casing wall rotation, which exists in real turbines, is not presently taken into account.

Test Facilities and Test Methods

Low-Speed Linear Cascade Facility

The major specifications of the present rotor cascade are as follows:

Blade chord $C = 73.5$ mm
Axial blade chord $Cax = 72.6$ mm
Blade pitch $S = 61.42$ mm
Aspect ratio $H/C = 1.37$
Solidity $C/S = 1.20$
Blade maximum thickness/$C = 0.257$
Blade LE radius = 8.17 mm; TE radius = 4.08 mm
Number of blades $N = 6$
Cascade camber angles: inlet = 49.8 deg, outlet = −63.5 deg
Design flow angles: inlet = 43.6 deg, outlet = −63.5 deg
Design turning angle = 107.1 deg

The cascade is a suction-type, six-bladed, linear cascade with a large turning angle, thick leading and trailing edges,

Nomenclature

Cax = cascade axial chord
CPs = static pressure coefficient based on mass-averaged outlet velocity at Plane 12 (Fig. 2) $= (Ps - Patm)/(0.5 \times \rho \times \bar{\bar{V}}^2_{m,12})$
CPt = total pressure loss coefficient based on mass-averaged outlet velocity at Plane 12 (Fig. 2) $= (Patm - Pt) / (0.5 \times \rho \times \bar{\bar{V}}^2_{m,12})$
H = span of cascade passage
i = incidence
LE = blade leading edge
$Patm$ = atmospheric pressure
Ps = static pressure
PS = blade pressure surface
Pt = total pressure
$Re_{,c}$ = Reynolds number based on mass-averaged outlet velocity at Plane 12 and blade chord
SS = blade suction surface
TCL = blade tip clearance, or ratio of tip-clearance gap against H
TE = blade trailing edge
Vm = resultant flow velocity
Vs = magnitude of secondary flow vector defined based on the local midspan flow directions
Vs' = magnitude of secondary flow vector defined based on the mass-averaged flow direction
W = velocity projected onto casing wall
Y = spanwise distance from hub endwall
Z = axial distance from blade leading edge
δ_{99} = boundary layer thickness
δ^* = displacement thickness $= \int_0^{H/2} (1 - \bar{V}_m/\bar{V}_{m,mid}) dY$
δ^{**} = momentum thickness $= \int_0^{H/2} (1 - \bar{V}_m/\bar{V}_{m,mid}) \cdot (\bar{V}_m/\bar{V}_{m,mid}) dY$
Δ = interval of contour plot
θ_y = yaw angle measured from the cascade axial direction
ρ = density

Subscripts

0–12 = number of traverse measuring planes (Fig. 2)
g = inlet guide plate (IGP)
mid = midspan
net = net loss subtracted by inlet endwall (BL) loss

Superscripts

$\bar{}$ = pitchwise mass-averaged value
$\bar{\bar{}}$ = overall mass-averaged value
$\tilde{}$ = locally mass-averaged value

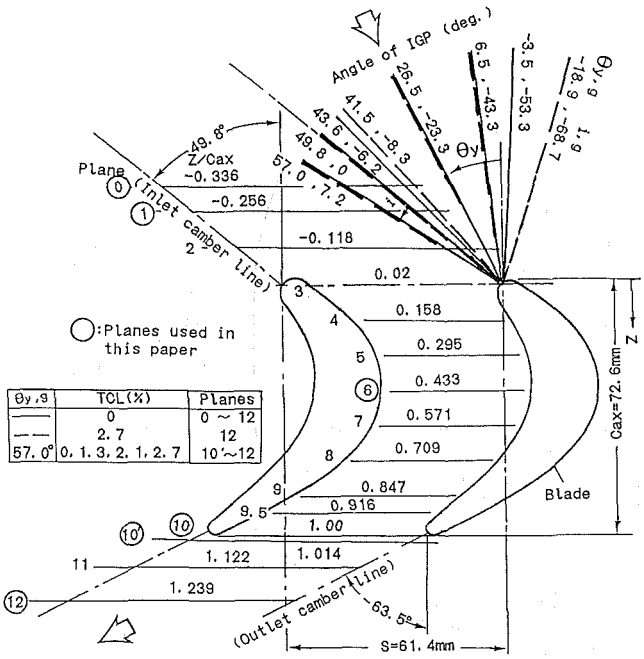

Fig. 2 Traverse planes and test incidences in terms of IGP angles

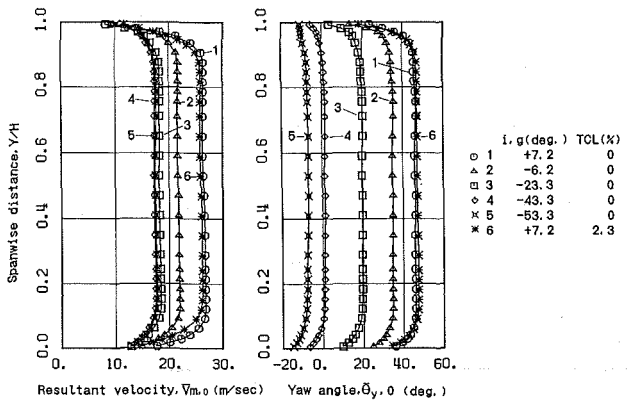

Fig. 3 Inlet velocity and flow angle (at Plane 0, $Z/Cax = -0.336$)

low aspect ratio, and low solidity. Two inlet guide plates are set upstream of the blades to change the cascade inlet flow angle. One of the endwalls, which contains a rotatable disk, can be moved in the pitchwise direction of the cascade. On the rotatable disk, two traverse gears are installed for driving a probe in the spanwise direction of the cascade and for rotating the probe about the probe axis. These mechanisms having four motors can locate the probe at any position in the cascade. The clearance gap between the movable wall and the blade tip was sealed by felt material for zero clearance tests. For the tests with clearance, the gap was changed by adjusting the width between the two cascade endwalls or by replacing the test blades with those of a different span height. Some additional information on the blade coordinates may be found in Yamamoto (1987).

Traverse Measurements. Figure 2 shows the traverse measuring planes and the test inlet angles $\theta_{y,g}$ or $i_{,g}$, which correspond to the setting angles of the inlet guide plates (IGP). $\theta_{y,g}$ is the yaw angle measured from the cascade axial direction and $i_{,g}$ is the incidence measured from the direction of the cascade inlet camber line. In the first test series without tip clearance, the traverses were made at all planes shown in Fig. 2 for six various $\theta_{y,g}$ as shown by solid lines. The Reynolds number $Re_{,c}$ of this test series was about 1.8×10^5. In the second test series with tip clearance (TCL) of 2.7 percent span, the transverses were made only at a downstream Plane 12 for six $\theta_{y,g}$ as shown by dashed lines. The $Re_{,c}$ was about 1.6×10^5. In the third test series with four TCL from 0 to 2.7 percent, the traverses were also made downstream of the cascade but more in detail, i.e., at ten planes located between planes 10′ and 12 (these planes are not shown here). The $Re_{,c}$ was about 2.0×10^5. These Reynolds numbers (1.6–2.0×10^5) are close to the typical Reynolds number of Ainley's cascade data correlation (2×10^5) but lower by about an order of magnitude than engine conditions. This does not mean the present cascade cannot simulate the flows in real machines. In the author's opinion, unless the Reynolds number is extremely low, the difference to this extent would not be so effective as to change the flow mechanisms completely. In other words, if the effect exists, it could be studied as the difference in boundary layer development on cascade solid walls, although the so-called Reynolds number effect has still been a vague problem.

All of the above traverses were made by using miniature five-hole pitot tubes with a head size of 1.5 mm with the yaw angle of the probe fixed. However, endwall-flow surveys inside and outside the tip clearance were made by using a micro five-hole pitot tube with a head size of only 0.6 mm, which is probably the smallest five-hole pitot tube that has been reported so far. The size may not be small enough to measure the gap flows (the ratio against the gap is about 22 percent). The author believes, however, from a fairly good agreement between the static pressures obtained in the gap flows (by the probe) and on the endwall (by the pressure taps), that the present probe could detect real flow vectors without serious errors. Further study on the errors is being made using some pitot tubes with various head sizes.

All the pitot tubes used were made **L**-shaped in order to reduce the probe effect on the flows to be sensed, as well as to be able to measure the flows very close to both endwalls. The ratio of the projected part **L** to the head size is 6 and 15 for the miniature probe and the microprobe, respectively. The (absolute) error on the total pressures is about 0.5 percent of dynamic pressures of the cascade outlet flows, and the error on both yaw and pitch angles is about 0.5 deg. The error overranging on the integral loss, however, may be more (say, 1 percent at downstream planes and a few percent within cascade) due to the extrapolation of pressure data between the solid walls (endwalls and/or blade surfaces) and the first traverse lines closest to the corresponding solid walls, and also due to possible interference of the probe with flows. Note that the pressure resolution (i.e., the relative error among the data in the same plane) was much smaller than the absolute errror and could be smaller than 0.1 percent of the dynamic pressure.

Because of the vast amount of data, the present paper focuses on the data obtained downstream of the cascade. Some limited traverse data obtained within the blade row will be referred to, when necessary, for explaining the present purposes. More detailed flow analyses within the cascade and in the clearance gap will be summarized in separate papers.

Inlet Flow Conditions. Figure 3 shows spanwise distributions of inlet velocity and the yaw angle for five incidences obtained without tip clearance at Plane 0 ($Z/Cax = -0.336$), and the distributions obtained with 2.3 percent tip clearance at Z/Cax of -0.35. The tip clearance did not affect the inlet flows significantly. The inlet velocity varies with incidence in the present tests where the outlet velocity far downstream from the cascade is maintained at a constant value. The yaw angle ($\theta_{y,0}$) becomes small near both endwalls and so does the incidence. The overall mass-averaged yaw angle at Plane 0, $\theta_{y,0}$, was always smaller than the corresponding physical IGP setting angle $\theta_{y,g}$, and the difference between the two is from 4 to 12 deg, corresponding to $\theta_{y,g}$ from -3.5 to 57 deg, respec-

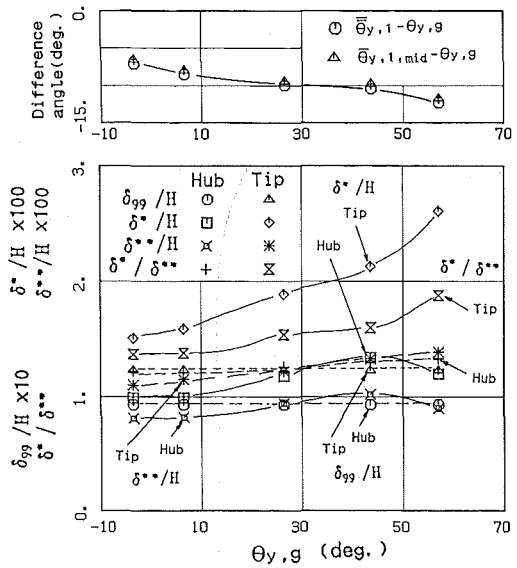

Fig. 4 Difference between IGP angle and inlet flow angle, and inlet boundary layer parameters (at Plane 1, *Z/Cax* = −0.256, TCL = 0 percent)

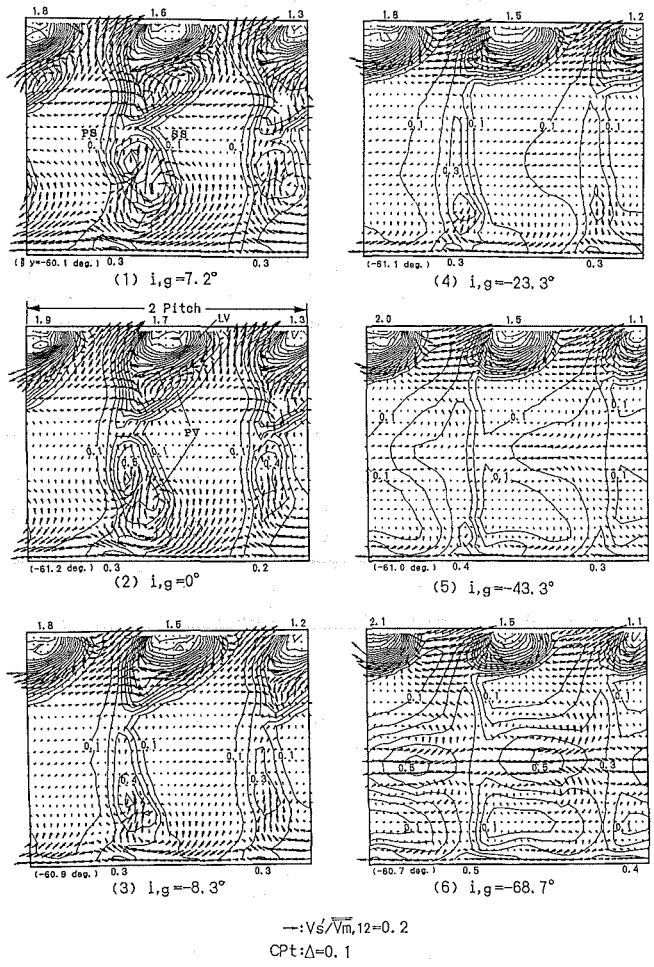

Fig. 5 Effect of inlet flow angle on secondary flow/loss field at plane 12 for TCL = 2.7 percent

tively. The difference at the midspan is a little smaller and is 3 to 11 deg, respectively.

As was used in the previous study (Yamamoto, 1987), plane 1 with the same *Z/Cax* of −0.256 was chosen for the inlet boundary layer analysis in the present study. Figure 4 (bottom) shows the inlet boundary layer parameters versus the IGP setting angle $\theta_{y,g}$. The tip-side endwall boundary layer was a little thicker than the hub-side one in the present tests. The shape factor of the tip-side boundary layer varies from 1.37 to 1.60 for $\theta_{y,g} = -3.5$ to 43.6 deg and 1.88 for $\theta_{y,g} = 57.0$ deg. The hub-side shape factor varies less, i.e., from 1.21 to 1.33 depending on the incidence. This indicates the tip-side inlet boundary layer to be in a transitional state (typically the value is 1.7) from turbulent (1.37) to laminar (1.88), and the hub-side layer to be always fully turbulent (nearly 1.3).

Figure 4 (top) shows the difference between the actual flow angle at Plane 1 and the IGP setting angle: The inlet mass-averaged flow angle (of both overall mass-averaged flow angle $\bar{\bar{\theta}}_{y,1}$ and pitchwise mass-averaged midspan flow angle $\bar{\theta}_{y,1,\mathrm{mid}}$) is smaller than the setting angle by about 7 to 12 deg. The difference values at this plane are larger than those at Plane 0. Farther upstream of the cascade, the flow is thought to flow in parallel to the inlet guide plates more closely. Since the inlet flow angle varies depending on the location measured, the nominal IGP setting angle will be referred to in the subsequent figures.

Flow Visualization Method. In the present flow visualization tests, a newly designed light-sheet device was used in which a great number of fine flexible optic fibers (0.05 mm diameter) were arrayed to lead a circular light of 8 mm diameter from a halogen bulb to a small head with a semicylindrical lens so as to make a line light of 0.83 mm × 60 mm. The device can supply a very bright light-sheet (up to about 50,000 lux) with the thickness of 3 mm at 0 to 150 mm distance from the lens. With this flexible device, the cascade flows (oil-smoke flows) at any location were easily illuminated and visualized from arbitrary directions. To photograph the smoke flows clearly, a fine-resolution color video camera/recorder system with a mechanism for clear still pictures was used and also the test velocity was reduced by about an order of magnitude of the traverse velocity. Even when the velocity was increased up to about a third of the traverse velocity, the flow patterns as shown in the paper were still recognized but with reduced clarity. Therefore, the present flow visualization results could hold true for Reynolds number from about 2×10^4 to 6×10^4 at least.

Experimental Results and Discussion

Incidence Effects on Cascade Downstream Flow Field. Figure 5 shows downstream secondary flow vectors and the associated total pressure losses obtained at Plane 12 for six incidences. The TCL is 2.7 percent. Flow directions at midspan ($\bar{\theta}_{y,12,mid}$) varied significantly with incidence (as will be seen in Fig. 13*a*) but the mass-averaged values ($\bar{\bar{\theta}}_{y,12}$) were found nearly constant (the averaged values $\bar{\bar{\theta}}_y$ are shown in each figure). Therefore, for easy comparison of the serial figures, the secondary flow vectors (Vs') were drawn by projecting the local flow velocities onto the plane normal to the nearly constant mass-averaged flow directions, and by being looked at from the downstream side of the cascade. Some of the vectors inside the leakage vortices (LV) were omitted because they were out of the probe calibration ranges of yaw or pitch angles or velocity. The overrange occurs due mainly to the strong shear flows inside the vortices and due to the use of the miniature probe with relatively large head size of 1.5 mm compared to the velocity gradients in the shear flows. In fact, such overranged data could be reduced when a micropitot tube with a much smaller head size of 0.6 mm was used.

From the serial figures in Fig. 5, one can visualize how the secondary flow and the associated loss distribution change under various off-design incidences: As shown in Fig. 5(1) or (2), where i_g is 7.2 or 0 deg and where the flows are highly

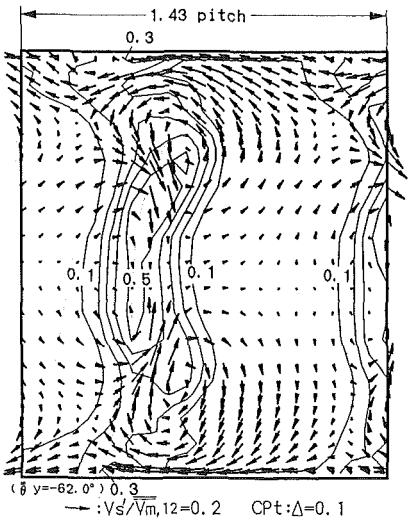

Fig. 6 Secondary flow/loss at plane 12 for zero tip clearance, $i_{,g} = 0$ deg

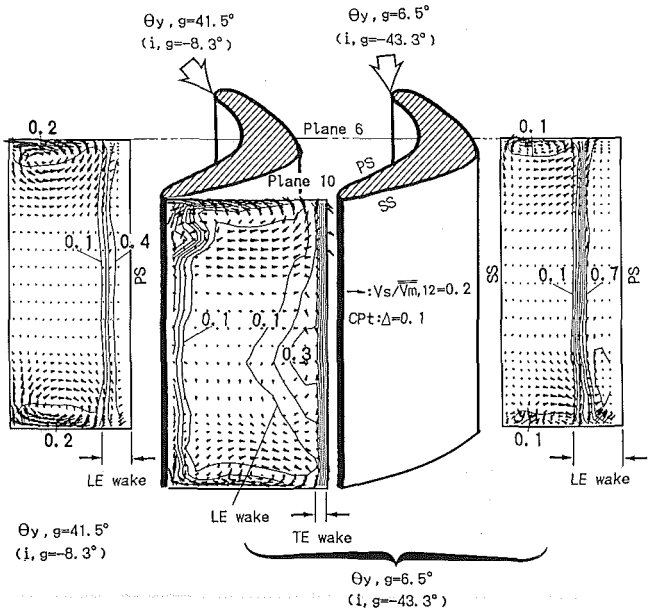

Fig. 7 Leading-edge wake for TCL = 0 percent

turned, a strong interaction occurs between the tip-side passage vortex (*PV*) and the leakage vortex (*LV*), which rotate in opposite directions. Compared to the zero tip-clearance case with $i_{,g}$ of 0 deg shown in Fig. 6, Fig. 5(2) reveals significant effects of the leakage flow upon the secondary flow and loss fields; the leakage vortex pushes the tip-side passage vortex toward the midspan and makes the wake width of the tip-side half much wider. On the other hand, the "hub-side" passage vortex is very strong at these two $i_{,g}$ and has swept out the boundary layer fluid from the hub endwall completely and accumulated the fluid with low energy in the wakes. The fluid on the hub endwall is thus replaced with high-energy fluid coming from the free stream. (These movements of the free stream and of the boundary layer are illustrated in Fig. 1 by 18 and 19.)

As $i_{,g}$ is reduced to -8.3 deg, both the tip-side and the hub-side passage vortices become significantly weak, and therefore, the migration of the low-energy fluid from both endwalls into the wakes is reduced. The interaction between the leakage vortex and the tip-side passage vortex appears to get weaker.

At $i_{,g}$ of -23.3 deg, the tip-side passage vortex almost disappears but the hub-side passage vortex is still recognizable. The tip-leakage vortex, on the other hand, appears to be less sensitive to the incidence variation than the passage vortex and apparently exists near the casing. As the incidence decreases, the wake near the midspan starts to expand from the pressure side of the wake: At $i_{,g}$ of -43.3 deg, the expanding part of the wake reaches the adjacent wake, due to the new secondary flows generated near the midspan. The expanding part of the loss contours corresponds to "leading-edge (LE) wake" i.e., the low-energy fluids separated from the pressure side of the leading edge, as will be seen in Fig. 7.

At the smallest $i_{,g}$ of -68.7 deg tested, the wake finally dominates the whole midspan region, being driven by the midspan secondary flows; the so-called free stream with low loss (e.g., $CPt < 0.1$) is then divided into the hub and tip-side parts. Even in this small turning flow, the tip leakage flow and the associated loss are still significant. This insensitivity of the leakage flow to the incidence change is due mainly to the following two facts: (1) that the leakage flow depends strongly on the inlet endwall flow, which is not as sensitive to the incidence variation as the free stream is, and (2) that the major part of leakage flow that contributes to the vortex formation occurs in the rear half of the passage where the flows are less affected by the incidence. Figure 5 also reveals that the corner loss peaks seen at the hub-side wake roots are kept almost constant ($CPt = 0.2$–0.3) at incidences between 7.2 and -23.3 deg and increase a little (0.3–0.5) with the incidence decreased to -43.3 and -68.7 deg. This tendency will be recognized more clearly in the pitchwise mass-averaged loss as shown later in Fig. 13(*b*).

Figure 7 shows the generation of the "leading-edge (*LE*) wake" for two incidences. The secondary flow vectors (*Vs*) here are defined as the deviated flows from the local midspan flows at each plane. In linear cascades, the original shape of the *LE* wake is straight along the span but is deformed downstream as shown. At the negative $i_{,g}$ of -43.3 deg (which corresponds to an actual flow turning angle from Plane 1 to Plane 12 of about 60 deg), the loss due to the *LE* wake appears to fill almost half the channel at the midspan. Note that the *LE* wake (separation) does exist even at $i_{,g}$ of -8.3 deg, which is near the design incidence.

Effects of Tip-Clearance Sizes on Interaction. The previous results were obtained with a somewhat large tip clearance (2.7 percent TCL). Most of the clearances in real turbines lie between 1 and 2 percent of span. When the present rotor blades are installed in a real machine, for example, they are to have the design clearance of 1.5 percent. Figure 8 shows the effects of the clearance sizes on the interaction patterns at Plane 12. The results show only the tip-side halves of the full planes traversed. When the clearance diminishes (TCL = 0 percent), the secondary flow fields are occupied by only the passage vortex (*PV*) and the trailing shedding vortex (*TV*) accompanied by the *PV*, and become symmetric to the midspan. When TCL is 1.3 percent, a small tip leakage vortex (*LV*) appears at the wake root where a corner loss existed for zero TCL. The small leakage vortex, however, affects the loss distribution significantly. The leakage and the passage vortices are rotating smoothly without any significant interaction in this case. This is because the distance between the vortex centers is far enough apart, compared to the size of the leakage vortex. The radius of the leakage vortex is about 10 percent of the distance between the two vortex centers. As TCL increases to 2.1 or 2.7 percent, the radius increases to about 35 or 50 percent, respectively, and the leakage vortex is involved more deeply inside the wakes. The interaction becomes stronger, making the wake region wider, and pushing the passage vortex center toward the pressure side of the cascade passage. In other words, the amount of endwall fluid

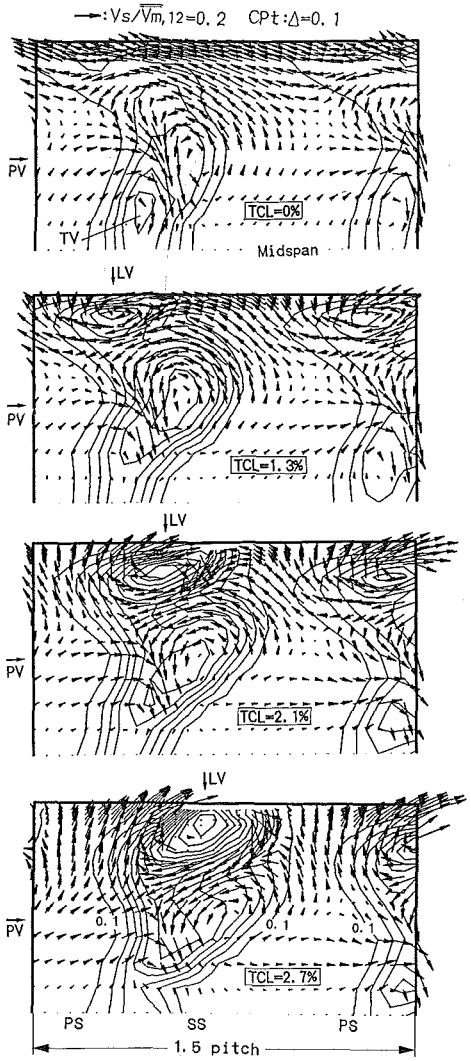

Fig. 8 Effects of TCL sizes on *LV/PV* interaction downstream of the cascade (plane 12), $i_{,g} = 7.2$ deg

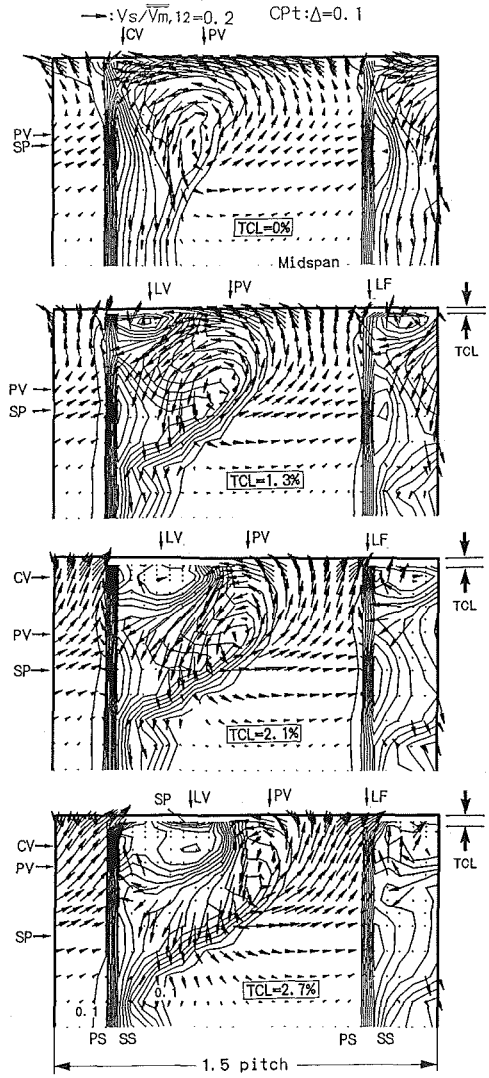

Fig. 9 Effects of TCL sizes on *LV/PV* interaction at the cascade exit plane (plane 10′), $i_{,g} = 7.2$ deg

being sucked into the tip clearance increases with increase of the gap size and so the leakage vortex gets stronger, while the passage vortex becomes weak.

Figure 9 will give further detail about the interaction mechanism. The figure was obtained at Plane 10′, which is located just downstream of the cascade trailing edge ($Z/Cax = 1.014$). Therefore, the vortices (*PV* and *LV*) have mixed little with the low-energy fluids in the dead flow regions along the trailing edges, and the loss due to each vortex can be more clearly identified. When TCL is 1.3 percent, a small leakage vortex appears at the suction surface (*SS*)/casing corner, but the loss increases significantly, compared to the loss for zero TCL. When TCL becomes 2.1 or 2.7 percent, the leakage loss core gets larger. An additional small loss core, indicated by *CV*, can be recognized on the *SS* close to the blade tip. This might indicate a small flow separation of the leakage flow from the suction-side tip edge. Near the pressure surface (*PS*), some part of the fluids, which formed the passage vortex at zero clearance, are sucked into the clearance to become the leakage flow (*LF*). As the clearance increases, the location of the high-loss core on the *SS* (indicated by *SP*) moves away from the endwall. According to Langston and others (1977), this high-loss core is considered to be generated due to three-dimensional flow separation of the passage vortex (*PV*). The leakage vortex pushes the *PV* to the pressure side in the cascade passage and makes the *PV* roll down more abruptly from the casing. As a result, the center of *PV* looks to move toward the casing. Farther downstream at Plane 12, however, the center moves to almost the same spanwise location for all test incidences due to the interaction of two vortices, as was shown in Fig. 8.

Flow Visualization of Interaction Mechanism. Figure 10 shows two different types of leakage flows visualized at the cascade exit plane for two different TCL sizes. Both flows were visualized on a light-sheet plane nearly normal to the suction surface near the trailing edge, and the pictures were taken from the upstream side. Figure 11 shows two schematic drawings corresponding to the above two visualization results in order to explain the details and to reveal much finer mechanisms on the *LF/PV* interaction. The following discussions will concern mainly Fig. 11.

In the case of 1.7 percent TCL (Fig. 11*a*), the fluid at the pressure side moves toward the blade tip along the pressure surface, passes the tip clearance, and departs from the tip along the *SS*, and finally is involved in the "counterclockwise-rotating" vortex indicated by *Hp*. Except for the leakage flow (*LF*) in this figure, the vortical *Hp/Hs* system shown here is very similar to those found by Sieverding and Van den Bosch (1983) (at about 1.5×10^5 of $Re_{,c}$) and confirmed by Sonoda (1985) (at $Re_{,c} = 4.8 \times 10^4$), both for zero TCL. Also in the zero TCL case of the present visualization study, the system

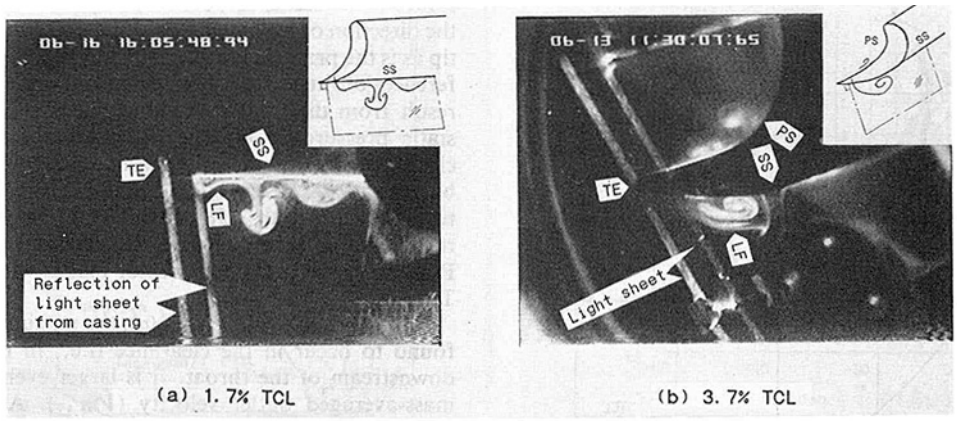

Fig. 10 Flow visualization of leakage flows at the cascade exit plane for $i_{,g} = 7.2$ deg (seen from the upstream side)

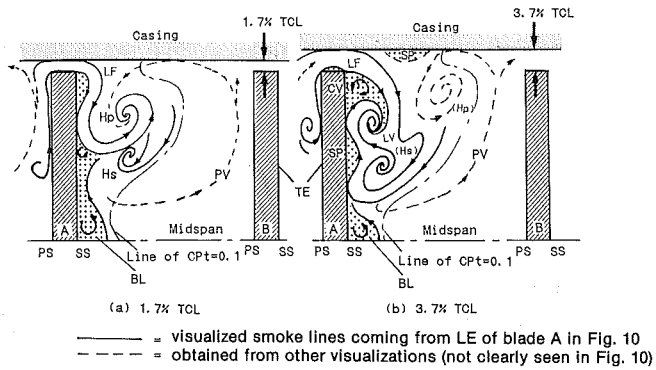

Fig. 11 Detailed interaction mechanism of *LF* with other vortices at the cascade exit plane for $i_{,g} = 7.2$ deg (seen from the downstream side)

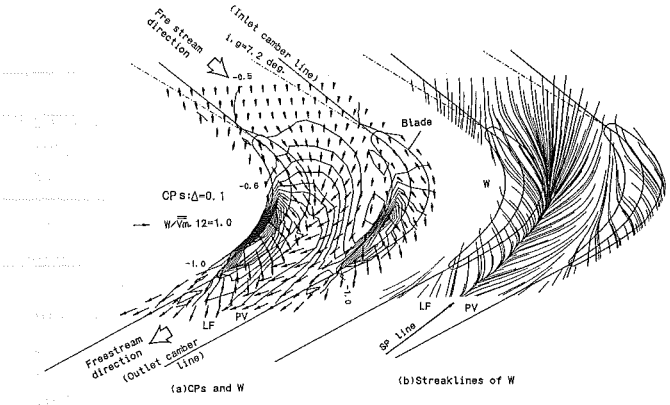

Fig. 12 Near-endwall flows on the midheight plane between the blade tip and the casing for TCL = 2.7 percent and $i_{,g} = 7.2$ deg: (*a*) static pressures and flow vectors; (*b*) streaklines

was not so different from that shown here. From this and from other visualization tests in which these vortices were followed back to their origins, it was tentatively concluded that the *Hp* shown here consists of both the passage vortex (*PV*) and the pressure-side leg of the leading-edge (*LE*) horseshoe vortex, and that the clockwise-rotating vortex *Hs* accompanied by the *Hp* is the suction-side leg of the *LE* vortex. Sjolander and Amrud (1987), however, have recently reported that the pressure-side leg of the *LE* horseshoe vortex did not contribute to the *PV* when TCL increased to 1.2 percent span (0.96 percent of their blade chord) in their flow visualization (at $\mathrm{Re}_{,c} = 1.27 \times 10^5$).

In the case of larger TCL of 3.7 percent (Fig. 11*b*), the visualized leakage flow (*LF*) is more complicated including two clockwise-rotating vortices. The leakage flow mixes firstly with one of the vortices indicated by (*Hs*). A part of the mixing fluids then rolls upward strongly along the *SS* with a separation bubble (*SP*) on the SS and is finally involved into the other vortex noted by *LV* (leakage vortex). One of the legs of the *LV* originates from the suction side tip edge. The shape of the visualized leakage flow with a "shoulder," and other visualizations focusing on the *PV*, suggests that a vortex exists outside the *LF*. The vortex is indicated by a dotted line (*Hp*). This corresponds also to the core of the passage vortex. The paths of the (*Hs*) and the (*Hp*) back to their origins have not been successfully followed yet. The brackets with *Hp* and *Hs*, therefore, indicate only that these (*Hp*) and (*Hs*) "may" include the pressure-side and the suction-side legs of the *LE* horseshoe vortex, respectively.

A small corner vortex indicated by *CV* can also be recognized at the tip *SS* corner. Rotational direction of this vortex is not always the same: sometimes clockwise and sometimes counterclockwise as shown in Fig. 11(*b*). Some of the fluids in this separated region were seen to flow back in the upstream direction, as was seen in an annular cascade (Yamamoto and Yanagi, 1986) and as also illustrated in Fig. 1 by 13. Backflows in this region, however, could hardly be recognized in the case of the smaller TCL of 1.7 percent. In both cases of the clearances tested, a pair of contrarotating vortices were clearly visible in the boundary layer separation bubble on the *SS* near the midspan (only the tip-side vortex is illustrated by *BL* here but both are seen in Fig. 10*a*). The rotational motion of the vortex is very slow compared to fast motion of the leakage flow. A part of this boundary layer fluid is absorbed into the *Hs*/*Hp* vortex system in the 1.7 percent case and into (*Hs*)/*LV* system in the 3.7 percent case. The *PV* separates from the casing as shown in Figs. 11(*a*) and 11(*b*). This separation root could be clearly visualized by oil-smoke. In Fig. 11(*b*), a possible separation bubble (*SP*) due to this separation is also sketched on the casing. This might correspond to the measured high-loss core indicated by *SP* in the lowest figure (TCL = 2.7 percent) in Fig. 9. Connecting the separation points on the casing through the cascade passage would make a three-dimensional separation or interaction line, toward which two endwall flows (*LF* and *PV*) migrate as will be seen in Fig. 12(*b*).

Development of Interaction Throughout the Cascade Passage. Figure 12 is a typical result obtained on a blade-to-blade plane located at the midheight inside the clearance of 2.7 percent. The vectors *W* shown in the figure correspond to the

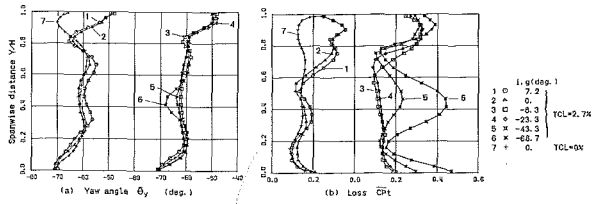

Fig. 13 Pitchwise mass-averaged yaw angle and loss

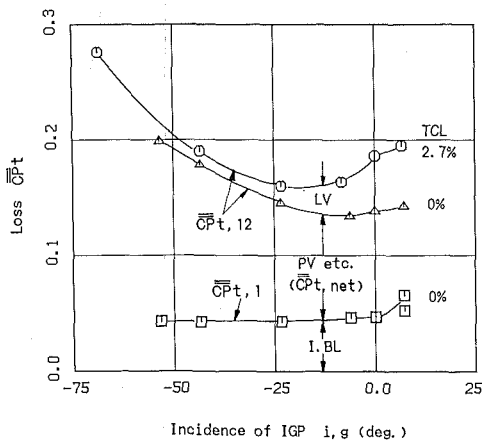

Fig. 14 Overall loss characteristics

velocities projected onto the endwall (or the blade-to-blade plane). The present test incidence of IGP ($i_{,g}$) is 7.2 deg. As seen before, incidence of the midspan free stream is smaller than this $i_{,g}$ by about 11 deg at Z/Cax of -0.35 and therefore, the inlet free-stream direction is almost parallel to the inlet camber line as shown by a large arrow. The inlet endwall flow, however, is already deflected from the free stream significantly. This deflection of inlet endwall fluids is caused mainly by the low momentum (or inertia) of the fluids and by the pressure gradient near the wall in the front part of the passage. The former cause was checked by changing the inlet boundary layer with various trips; as the trip height increased, velocities of the endwall fluids measured at the same distance from the wall increased and the directions became parallel to the inlet guide plates, probably because the trips put more momentum (inertia force) into the endwall fluids. Variation of incidence does not affect the inlet endwall flows as significantly as it does the inlet free stream. Therefore, the tip leakage flow, which depends on the endwall flow more strongly than on the free stream, is insensitive to the incidence. For the same reason, the change of incidence does not affect the leading edge separation as significantly near the endwall as it does in the free stream.

As clearly shown in Fig. 12(*b*), some of the inlet endwall fluids pass the blade tip to become leakage flows and start to interact with the passage endwall flows near the *SS* at about half axial chord from the leading edge. In the present case with 2.7 percent clearance (or 9.1 percent of the blade maximum thickness), the leakage flow passes through the clearance parallel to the blade camber line near the leading edge and pass almost normal to the camber line near the cascade throat. With a smaller clearance (1.3 percent), however, the leakage flow passed almost normal to the camber line also near the leading edge, as was seen in flow visualizations made by Sjolander and Amrud (1987) and Booth and others (1982), and predictions made by Pouagare and Delaney (1986) in other cascades where most of their leakage flows pass the tip clearance nearly normal to the camber lines. In the present larger gap case, however, the inertia force of the entrance flows seems to be a very important factor determining the direction of leakage flows in the upstream half of the blade tip as is the pressure gradient. In addition to this force, the differences of the leakage flow directions among the studies may result from different cascade geometries (i.e., blade surface static pressure or loading distributions) and different tip-clearance sizes used: The present cascade used thick turbine blades with 2.7 percent TCL, Sjolander and Amrud used thin turbine blades with 3.58 percent TCL, Booth et al. used also relatively thin turbine blades with about 1 percent TCL, and Pouagare et al. used compressor blades with about 1 percent TCL.

From the vectors in Fig. 12(*a*), the maximum velocity can be found to occur in the clearance (i.e., in the leakage flows) downstream of the throat. It is larger even than the cascade mass-averaged outlet velocity ($\bar{\bar{V}}m_{,12}$). Another interesting feature seen in the static pressure distribution (*CPs*) is a very low pressure peak with very large pressure gradients located along the *PS*. This is very similar to a result recently found by Bindon (1986) in his endwall static pressure measurements of a linear cascade with tip clearance. According to his explanation, the large pressure occurs when the flows at the pressure side turn around the 90-deg edge corner to enter the clearance with much accelerated velocity, as was seen in Fig. 9 (*LF*). In the present study, it was found that the location with large pressure gradients moved as the incidence was varied. When the $i_{,g}$ was less than about -20 deg, for example, another low pressure peak appeared at the suction-side leading edge. Complete analyses of the leakage flow surveys with various clearances and various incidences are going to be published in a separate paper by the author.

Downstream from the cascade trailing-edge plane, the endwall flows indicated here by *PV* roll down below the leakage flow (*LF*). This can be more clearly seen from Figs. 8 and 9.

Overall Loss Characteristics With Incidence Change. Figure 13(*a*) shows effects of the incidence on the spanwise distribution of pitchwise mass-averaged outlet flow angle at Plane 12 ($Z/Cax = 1.239$). Near the tip casing, the outlet flow is strongly underturned due to the leakage flow in all cases with tip clearance compared to the result without clearance. Decreasing the incidence tends to cause the midspan flow to overturn. Figure 13(*b*) of loss distribution shows that the leakage flow causes very high loss near the tip casing. As the incidence decreases, a large loss occurs near the midspan and it tends generally to increase, due to the leading-edge wake (separation) as discussed previously.

Figure 14 shows the mass-averaged overall loss obtained at Planes 1 and 12 versus the setting angle $i_{,g}$. $\overline{\overline{CPt}}_{,1}$ corresponds to the loss due to the inlet endwall boundary layers (*I.BL*) at Plane 1 and is almost constant for all test setting angles except for the maximum incidence where $\overline{\overline{CPt}}_{,1}$ tends to increase. Noting that the loss at Plane 12 ($Z/Cax = 1.239$) has not yet been mixed out completely, the following discussion will be made: The two $\overline{\overline{CPt}}_{,12}$ obtained with and without tip clearance show that both $\overline{\overline{CPt}}_{,12}$ have different optimum (minimum) values of $i_{,g}$: at about -6 deg for zero TCL and about -20 deg for 2.7 percent TCL. The leakage loss can be recognized as the difference between the two $\overline{\overline{CPt}}_{,12}$, as shown by *LV*. The loss *LV* tends to increase with increase of $i_{,g}$ (or with increase of the cascade turning angle) for $i_{,g}$ larger than about -30 deg. For the rest of $i_{,g}$ less than about -30 deg, the leakage loss seems to be fairly constant.

It is important to separate the overall loss into several losses that have been used in design methods such as the Ainley-Mathison (A-M) method (Ainley and Mathieson, 1951), but the accurate separation of each loss in three-dimensional flow fields is extremely difficult. Figure 15 shows an attempt in which separation of various losses was attempt-

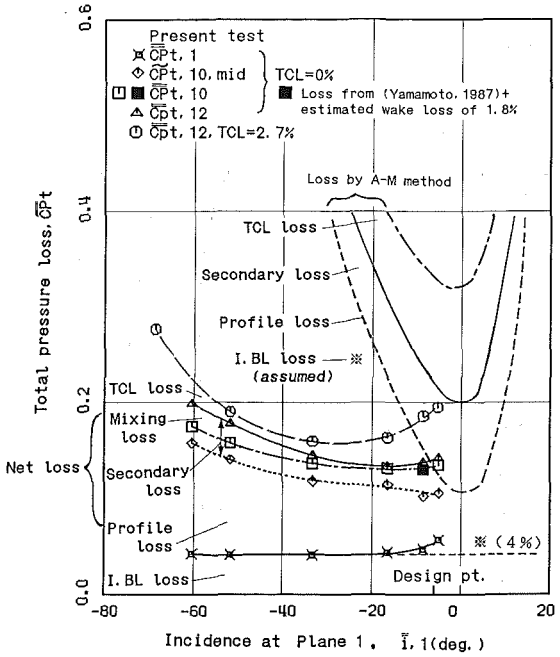

Fig. 15 Comparison of test losses with prediction by Ainley-Mathieson method

ed, and the results were compared to a prediction by the A–M method. The differences in losses obtained at several traverse planes would correspond to the losses named in the figure very roughly. Because of the leading-edge separation, the mass-averaged loss calculated at midspan only was very large (as seen at Plane 10 in Fig. 7) and even beyond the overall loss. It was thought that the midspan loss did not represent the profile loss reasonably in the highly three-dimensional flows due to the accumulation of the pressure-side *LE* wake loss around the midspan by the new secondary flow. The test profile loss $\widetilde{CPt}_{,10,\mathrm{mid}}$, therefore, was obtained not as the midspan mass-averaged loss but as the mass-averaged loss "around" the midspan between two spans where the pitchwise mass-averaged loss becomes minimum. The test loss $\overline{\overline{CPt}}_{,10}$ includes some part of the *TE* wake loss generated behind the trailing edge, as seen in Fig. 7. The loss difference between $\overline{\overline{CPt}}_{,10}$ and $\overline{\overline{CPt}}_{,12}$ corresponds to the mixing loss occurring only between Planes 10 and 12, and not the whole mixing loss downstream of the cascade. The so-called secondary loss of the present test to be compared to that of the A–M prediction would correspond to the difference between the profile loss ($\widetilde{CPt}_{,10,\mathrm{mid}}$) and the overall loss ($\overline{\overline{CPt}}_{,12}$) without TCL. The test secondary loss, therefore, includes only some part of the mixing loss.

A comparison shows that that test overall loss $\overline{\overline{CPt}}_{,12}$ is, in general, much lower, and also less sensitive to the incidence variation than the prediction. An A–M method tends to overestimate the profile loss for the present cascade with high turning and thick blades. Further discussion cannot be made at present on the basis of the present data only. More studies are needed on the loss characteristics for high-turning blade rows with blunt leading and trailing edges that have been widely adopted these days. More comparisons with some other methods, such as that of Dunham and Came (1970), are also needed.

The A–M method, however, can accurately predict the ratio of the leakage loss against the net loss, as shown in Fig. 16. Here, the net loss is defined to be the overall loss minus the inlet endwall loss without tip clearance, and therefore, the test net loss was obtained by subtracting the inlet endwall loss $\overline{\overline{CPt}}_{,1}$ from $\overline{\overline{CPt}}_{,12}$ for zero clearance as shown in Figs. 14 or

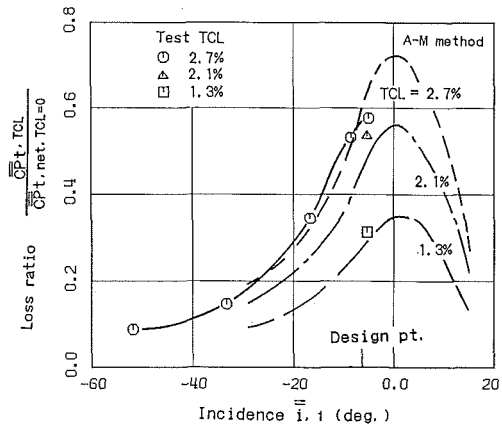

Fig. 16 Ratio of leakage loss to net loss

15. In the present A–M prediction, the net loss was assumed to be equal to the predicted overall loss (profile loss plus secondary loss) minus 4 percent corresponding to the test $\overline{\overline{CPt}}_{,1}$ as shown in Fig. 15. This is because the A–M cascade loss correlation does not specifically exclude the inlet endwall boundary layer loss. Figure 16 shows that as the incidence increases, the ratio tends to increase in the negative incidence and decrease in the positive incidence. In other words, the role of the leakage loss in the net loss production mechanism becomes significantly more important particularly near the design point operation (usually near zero incidence) than at the off-design point operations. In the present cascade with design TCL of 1.5 percent, for example, the ratio will be about 40 percent at the design incidence.

Conclusions

The present paper gave a detailed description on the loss generation mechanisms in a linear turbine rotor cascade with tip clearance. The results were presented mainly in terms of secondary flow vectors and the associated total pressure losses with parameters of the cascade inlet flow angle (or incidence) and the clearance size. The major conclusions are as follows:

1 The incidence variation significantly affects the secondary flow and the associated loss fields downstream of the cascade, where the leakage flow and the passage vortex exist as the major contributors on the fields. The leakage vortex is less sensitive to the incidence variation than the passage vortex and it still exists alone when the incidence is much reduced. As the incidence decreases, the "leading-edge wake" due to the separation from the pressure-side leading edge comes to play an important role in the fields.

2 The interaction between the leakage vortex and the tip-side passage vortex gets stronger with increases of the flow turning and of the clearance size.

3 Flow visualizations provided further detailed interaction mechanisms at the cascade exit plane. The mixing flow patterns of the leakage flow with the other vortices depend strongly on the clearance sizes.

4 Blade-to-blade traverse measurements of the tip-side endwall flow were made inside and outside the tip clearance using a micro five-hole pitot tube. This study gives new and clear experimental information on the interaction mechanism in the axial direction and on the three-dimensional characteristics of the leakage flow.

5 The test overall losses were compared with predicted losses by the Ainley–Mathieson method. The A–M method tends to overestimate the profile loss for the present high-turning cascade with blunt leading edges. The method, however, could predict fairly accurately the ratio of the leakage loss against the net loss produced within the cascade.

The leakage flow contributes to the loss production more significantly near the design point operation than at the off-design operation.

Acknowledgments

The author wishes to sincerely thank Mr. H. Nouse, Director of the Aeroengine Division, for his continuous support of the present study, Mr. K. Kaba, a student of Nihon University, and Mr. F. Mimura, a staff member of the Turbine Laboratory, for their assistance in the flow visualization test, and Mr. H. Usui, a staff member of the Turbine Laboratory, for his improvement in the data transfer system.

References

Ainley, D. G., 1948, "The Performance of Axial Flow Turbines," *Proc. IMechE.*, Vol. 159, p. 235, Fig. 67.

Ainley, D. G., and Mathieson, G. C. R., 1951, "A Method of Performance Estimation for Axial-Flow Turbines," British ARC, RM2974.

Bindon, J. P., 1986, "Pressure and Flow Field Measurements of Axial Turbine Tip Clearance Flow in a Linear Cascade," Cambridge University Engineering Department, Report No. CUED/A-Turbo TR 123.

Booth, T. C., Dodge, P. R., and Hepworth, H. K., 1982, "Rotor-Tip Leakage: Part 1—Basic Methodology," ASME *Journal of Engineering for Power*, Vol. 104, pp. 154–161.

Dawes, W. N., 1986, "A Numerical Method for the Analysis of 3D Viscous Compressible Flow in Turbine Cascades; Application to Secondary Flow Development in Cascade With and Without Dihedral," ASME Paper No. 86-GT-145.

Dawes, W. N., 1987, "A Numerical Analysis for the Three-Dimensional Viscous Flow in a Transonic Compressor Rotor and Comparison With Experiment," ASME JOURNAL OF TURBOMACHINERY, Vol. 109, pp. 83–90.

Dunham, J., and Came, P. M., 1970, "Improvements to Ainley-Mathieson Method of Turbine Performance Prediction," ASME *Journal of Engineering for Power*, Vol. 92, pp. 252–256.

Hah, C., 1983, "A Navier-Stokes Analysis of Three-Dimensional Turbulent Flows Inside Turbine Blade Rows at Design and Off-Design Conditions," ASME *Journal of Engineering for Gas Turbines and Power*, Vol. 106, pp. 421–429.

Hah, C., 1986, "A Numerical Modeling of Endwall and Tip-Clearance Flow of an Isolated Compressor Rotor," ASME *Journal of Engineering for Gas Turbines and Power*, Vol. 108, pp. 15–21.

Langston, L. S., Nice, M. L., and Hooper, R. M., 1977, "Three Dimensional Flow Within a Turbine Cascade Passage," ASME *Journal of Engineering for Power*, Vol. 99, No. 1, pp. 21–28.

Moore, J., and Moore, J. G., 1985, "Performance Evaluation of Linear Turbine Cascades Using Three-Dimensional Viscous Flow Calculations," ASME *Journal of Engineering for Gas Turbines and Power*, Vol. 107, pp. 969–975.

Nakahashi, K., Nozaki, O., Kikuchi, K., and Tamura, A., 1987, "Navier-Stokes Computations of Two- and Three-Dimensional Cascade Flow Fields," AIAA Paper No. 87-1315.

Pouagare, M., and Delaney, R. A., 1986, "Study of Three-Dimensional Viscous Flows in an Axial Compressor Cascade Including Tip Leakage Effects Using a SIMPLE-Based Algorithm," ASME JOURNAL OF TURBOMACHINERY, Vol. 108, pp. 51–58.

Rhie, C. M., 1986, "A Pressure Based Navier-Stokes Solver Using the Multigrid Method," AIAA Paper No. 86-0207.

Shikano, Y., Ikegawa, M., and Nakano, S., 1985, "A Numerical Analysis of Three-Dimensional Compressible Turbulent Flows Inside Blade Rows of Turbomachineries," *Transactions of the Japan Society of Mechanical Engineers*, Series B, pp. 461–469.

Sieverding, C. H., 1985, "Recent Progress in the Understanding of Basic Aspects of Secondary Flows in Turbine Blade Passages," ASME *Journal of Engineering for Gas Turbines and Power*, Vol. 107, pp. 248–257.

Sieverding, C. H., and van den Bosch, P., 1983, "The Use of Coloured Smoke to Visualize Secondary Flows in a Turbine-Blade Cascade," *Journal of Fluid Mechanics*, Vol. 134, pp. 85–89.

Sjolander, S. A., and Amrud, K. K., 1987, "Effects of Tip Clearance on Blade Loading in a Planar Cascade of Turbine Blades," ASME JOURNAL OF TURBOMACHINERY, Vol. 109, pp. 237–245.

Sonoda, T., 1985, "Experimental Investigation on Spatial Development of Streamwise Vortices in a Turbine Inlet Guide Vane Cascade," ASME Paper No. 85-GT-20.

Weinberg, B. C., Yang, R.-J., McDonald, H., and Shamroth, S. J., 1986, "Calculations of Two- and Three-Dimensional Transonic Cascade Flow Fields Using the Navier-Stokes Equations," ASME *Journal of Engineering for Gas Turbines and Power*, Vol. 108, pp. 93–102.

Yamamoto, A., and Yanagi, R., 1986, "Production and Development of Secondary Flows and Losses Within a Three-Dimensional Turbine Stator Cascade," *International Journal of Turbo and Jet-Engines*, Vol. 3, No. 1, pp. 79–90.

Yamamoto, A., 1986, "Review: Mechanism of Secondary Flows and Losses Within Turbine Blade Rows," *Turbomachinery*, Vol. 14, No. 4, pp. 234–241.

Yamamoto, A., 1987, "Production and Development of Secondary Flows and Losses in Two Types of Straight Turbine Cascades: Part 2—A Rotor Case," ASME JOURNAL OF TURBOMACHINERY, Vol. 109, pp. 194–200.

Navier-Stokes Solution for Steady Two-Dimensional Transonic Cascade Flows

O. K. Kwon
Senior Project Engineer,
Allison Gas Turbine Division,
General Motors Corporation,
Indianapolis, IN
Assoc. Mem. ASME

A robust, time-marching Navier-Stokes solution procedure based on the explicit hopscotch method is presented for solution of steady, two-dimensional, transonic turbine cascade flows. The method is applied to the strong conservation form of the unsteady Navier-Stokes equations written in arbitrary curvilinear coordinates. Cascade flow solutions are obtained on an orthogonal, body-conforming "O" grid with the standard k-ϵ turbulence model. Computed results are presented and compared with experimental data.

Introduction

Recently, significant effort has been devoted to the development of numerical procedures for predicting compressible, transonic, and viscous flows in turbine and compressor passages. These flows in blade rows are predominantly three dimensional. Accurate predictions of such flows, which are essential for developing high-performance gas turbine engines, require a reliable three-dimensional viscous flow solution procedure. Several studies have been made to develop three-dimensional Navier-Stokes procedures (see Briley and McDonald, 1977; Hah, 1984; Rhie, 1986; Weinberg et al., 1986). However, these procedures are still far from being used as a practical design tool due to severe computer storage and computational time requirements. A common practice for predicting viscous flow in blade passages to date is a two-dimensional analysis.

Currently available two-dimensional full viscous analyses involve solution of the Reynolds-averaged Navier-Stokes equations, and can be categorized into "steady approaches" and "time-dependent approaches." The first approach solves the steady-state Navier-Stokes equations by means of relaxation methods. The methods developed by Hah (1984) and Rhie (1986) can be classified in this category. In this steady approach, the pressure, which is treated as a primary variable, is evaluated from the Poisson equation derived from the continuity equation and the finite-difference representation of the momentum equations. This approach is known to be advantageous for analyzing steady incompressible flows where no density variation occurs but pressure variation exists. For compressible transonic and supersonic flows, the efficiency of this scheme is uncertain, although Rhie demonstrated attractive features of the approach when coupled with a multigrid technique for high-speed flows. A drawback of this approach is that it is restricted to steady mean flow analyses.

The time-dependent approach commonly used for compressible flow analyses is based upon the use of the unsteady formulation of the Navier-Stokes equations (Briley and McDonald, 1977; Pullium and Steger, 1980; Chima and Johnson, 1985; Kwon and Delaney, 1985; Weinberg et al., 1986). In this approach, the governing partial differential equations are integrated using a robust time-marching procedure. Steady solutions are established as the temporal asymptote of the unsteady equations of motion subjected to time-independent boundary conditions. An advantage of this procedure is that it can be extended to time-accurate transient analyses with minimal effort. The time-marching algorithms used at present can be categorized as either explicit or implicit. Explicit methods are in general easily programmable and vectorizable, allowing an easy application of boundary conditions. A major shortcoming of this method is its numerical stability, which constrains the time step size rather severely. The implicit schemes, on the other hand, are generally known to be unconditionally stable, in a linear sense, so that relatively large time steps can be taken. In practice, excessively large time steps may excite nonlinear instability. Further, a stability limit may be introduced through the process of implementing boundary conditions. In addition to these explicit and implicit algorithms, there exists a family of hybrid algorithms, known as the hopscotch schemes, first proposed by Gordon (1965). These algorithms combine the positive features of the explicit and implicit algorithms such as ease of programming, relatively rapid convergence, and less restricted stability constraints than most explicit schemes (Holst, 1976; Rudy et al., 1975; Ballhaus and Briley, 1980). The essence of this algorithm is the use of explicit and implicit finite-difference formulae at alternative computational mesh points. Recently, Kwon and Delaney (1985) utilized a generalized hopscotch algorithm for developing a two-dimensional unsteady compressible Navier-Stokes solver for transonic nozzle flows and demonstrated its efficiency and accuracy. This paper presents a reliable two-dimensional Navier-Stokes solution technique for predicting steady transonic flows in turbomachinery cascades, based on an extension of the nozzle flow analysis.

Contributed by the Gas Turbine Division of THE AMERICAN SOCIETY OF MECHANICAL ENGINEERS and presented at the 32nd International Gas Turbine Conference and Exhibit, Anaheim, California, May 31-June 4, 1987. Manuscript received at ASME Headquarters February 4, 1987. Paper No. 87-GT-54.

The hopscotch algorithm used is second-order accurate in space and first-order accurate in time. In the present work, the algorithm is applied to the unsteady compressible Navier–Stokes equations written in conservation law form in arbitrary curvilinear coordinates. The body-centered "O" grid generation procedure developed by Adamczyk (1980) has been used in collaboration with an algebraic grid-stretching technique in the direction normal to the airfoil surface. The "O" grid generation procedure provides minimum grid skewness and is found to be suitable for cascades with thick and rounded trailing edges. A two-equation turbulence model (k–ϵ model) has been used. Present predictions for highly loaded turbine cascades show good agreement with experimental data and other numerical solutions.

Governing Equations

The differential equations used are the two-dimensional, time-dependent, Reynolds-averaged Navier–Stokes equations which can be written in Cartesian tensor form as:

Continuity:

$$\frac{\partial \rho}{\partial t}+\frac{\partial}{\partial x_i}(\rho u_i)=0 \tag{1}$$

Momentum:

$$\frac{\partial(\rho u_j)}{\partial t}+\frac{\partial}{\partial x_i}(\rho u_i u_j)=-\frac{\partial P}{\partial x_j}+\frac{\partial}{\partial x_i}\left[(\mu+\mu_t)\left(\frac{\partial u_i}{\partial x_j}+\frac{\partial u_j}{\partial x_i}-\frac{2}{3}\delta_{ij}\frac{\partial u_k}{\partial x_k}\right)\right] \tag{2}$$

Energy:

$$\frac{\partial(\rho H)}{\partial t}+\frac{\partial}{\partial x_j}(\rho u_j H)=\frac{\partial}{\partial x_j}\left[(K+K_t)\frac{\partial T}{\partial x_j}\right]+\frac{\partial P}{\partial t}+\frac{\partial}{\partial x_j}\left[u_i(\mu+\mu_t)\left(\frac{\partial u_i}{\partial x_j}+\frac{\partial u_j}{\partial x_i}-\frac{2}{3}\delta_{ij}\frac{\partial u_k}{\partial x_k}\right)\right] \tag{3}$$

where ρ is the density; u, the mean velocity; p, the pressure; μ, the molecular viscosity; μ_t, the turbulent viscosity; H, the total enthalpy; K, the molecular conductivity; and K_t, the turbulent conductivity.

The turbulent viscosity and the turbulent conductivity are evaluated using the two-equation k–ϵ turbulence model (Launder and Spalding, 1974) as follows:

$$\mu_t=C_\mu \rho k^2/\epsilon \tag{4}$$

$$K_t=C_p\mu_t/\sigma_t \tag{5}$$

where k is the turbulent kinetic energy; ϵ, the turbulence energy dissipation rate; σ_t, the turbulent Prandtl number; and C_p, the specific heat. The values of k and ϵ are determined by the modeled form of their transport equations, respectively

$$\frac{\partial(\rho k)}{\partial t}+\frac{\partial}{\partial x_j}(\rho u_j k)=\frac{\partial}{\partial x_j}\left(\frac{\mu_t}{\sigma_k}\frac{\partial k}{\partial x_j}\right)+P-\rho\epsilon \tag{6}$$

$$\frac{\partial(\rho\epsilon)}{\partial t}+\frac{\partial}{\partial x_j}(\rho u_j \epsilon)=\frac{\partial}{\partial x_j}\left(\frac{\mu_t}{\sigma_\epsilon}\frac{\partial \epsilon}{\partial x_j}\right)+\frac{\epsilon}{k}(C_1P-C_2\rho\epsilon) \tag{7}$$

where $P(=-\overline{\rho u_i' u_j'}\partial u_j/\partial x_i)$ is the rate of production of turbulence kinetic energy. The empirical constants contained in the model are assigned the following values:

$$C_\mu=0.09,\quad C_1=1.44,\quad C_2=1.92 \tag{8}$$

$$\sigma_k=1.0,\quad \sigma_\epsilon=1.3$$

With this turbulence model, wall functions are used in order to eliminate a large number of grid points required to resolve the viscous sublayer (Launder and Spaulding, 1974).

In the present work, the total enthalpy H was assumed constant and the energy equation has been replaced by $H=$ const. This leads to a significant reduction in computer run time when such an assumption is warranted. The fluid under consideration was assumed to be a perfect gas. In addition to the

Nomenclature

C_μ, C_1, C_2 = constants in turbulence closure model
C_p = specific heat
C_x = airfoil axial chord
G_1, G_2 = contravariant velocity component in ϵ and η directions
H = total enthalpy
J = Jacobian of coordinate transformation
K = thermal conductivity
k = turbulence kinetic energy
M = Mach number
P = rate of production of turbulence kinetic energy
p = pressure
Re_c = Reynolds number based on airfoil chord
T = temperature
t = time
Tu = freestream turbulence intensity
u, v = velocity component in x and y directions, respectively
x, y = Cartesian coordinates
$y+$ = nondimensionalized boundary layer coordinate
α, β = coordinate transformation parameters
Γ = diffusion coefficient
δ_{ij} = Kronecker delta
ϵ = turbulence energy dissipation
μ = viscosity
ξ, η = nondimensional nature coordinates
$\Delta\xi$, $\Delta\eta$ = cell boundary sizes in ξ and η directions
ρ = density
σ = Prandtl number
σ_k, σ_ϵ = effective Prandtl numbers for turbulence kinetic energy and turbulence energy dissipation
τ = nondimensional time
$\Delta\tau$ = nondimensional time increment
ϕ = general scalar quantity

Subscripts and Superscripts

i, j, k, = tensor, grid indices
n = time index
T = total condition
t = turbulent flow
x, y = derivatives in x and y coordinates, respectively
ξ, η = derivatives in ξ and η coordinates, respectively
1 = inlet
2 = exit
∞ = freestream condition
$[\ ]^T$ = transpose of vector
$(\ )'$ = fluctuating quantity
$\overline{(\ )}$ = time-averaged quantity

governing differential equations, the equation of state for a perfect gas has been used to relate pressure, density, and temperature. The fluid properties have been evaluated from a standard gas table such as in Eckert (1972).

Coordinate Transformation

For the numerical solution of the governing differential equations, it is desirable first to transform the equations to an arbitrary curvilinear coordinate system (ξ, η). Invoking the general transformation equations $\xi=\xi(x, y)$, $\eta=\eta(x, y)$, the continuity, momentum, and turbulence transport equations can be written in strong conservation form as follows:

$$\frac{\partial}{\partial\tau}(\rho\phi)+\frac{\partial}{\partial\xi}(\rho G_1\phi)+\frac{\partial}{\partial\eta}(\rho G_2\phi)$$
$$=\frac{\partial}{\partial\xi}\left(\frac{\Gamma}{\mathrm{J}}\alpha\phi_\xi\right)+\frac{\partial}{\partial\eta}\left(\frac{\Gamma}{\mathrm{J}}\beta\phi_\eta\right)+S \tag{9}$$

where

$$\begin{aligned}\phi &= [1,u,v,k,\epsilon]^T\\ \alpha &= \xi_x^2+\xi_y^2\\ \beta &= \eta_x^2+\eta_y^2\\ G_1 &= (\xi_x u+\xi_y v)/\mathrm{J}\\ G_2 &= (\eta_x u+\eta_y v)/\mathrm{J}\\ \mathrm{J} &= \xi_x\eta_y-\xi_y\eta_x=1.0/(x_\xi y_\eta-x_\eta y_\xi)\\ \tau &= \mathrm{J}t\end{aligned}$$

Here, G_1 and G_2 are the contravariant velocity components in the ξ and η directions, respectively; Γ, the diffusion coefficient; J, the Jacobian of the transformation; and S represents all remaining terms. The metric coefficients are determined from the following identities:

$$\xi_x=\mathrm{J}y_\eta,\quad \xi_y=-\mathrm{J}x_\eta,\quad \eta_x=-\mathrm{J}y_\xi,\quad \eta_y=\mathrm{J}x_\xi \tag{10}$$

Numerical Procedure

The numerical procedure used to solve the governing equations is an extension of the Navier–Stokes solution procedure developed by Kwon and Delaney (1985) based on an explicit hopscotch algorithm for two-dimensional transonic nozzle flows. The essence of the hopscotch algorithm is a two-sweep procedure using explicit and implicit finite-difference formulae at alternate mesh points. Thus, the algorithm combines the positive features of the explicit and implicit algorithms.

In the previous work by Kwon and Delaney (1985), the viscous terms of the governing transport equations were treated explicitly as source terms for both the explicit and implicit sweeps of solution procedure. However, the present study indicates that, at the implicit sweep, an implicit treatment of the viscous terms enhances the numerical stability of the procedure. Application of the hopscotch algorithm, employing central differences for the spatial derivatives and forward and backward differences for the time derivatives, to equation (9) provides the following set of finite difference expressions for the two consecutive sweeps:

First sweep $(i+j+n$ *even*$)$

$$(\rho\phi)_{i,j}^{n+1}=(\rho\phi)_{i,j}^{n}-\frac{\Delta\tau}{2\Delta\xi}[(\rho G_1\phi)_{i+1,j}^{n}$$
$$-(\rho G_1\phi)_{i-1,j}^{n}]-\frac{\Delta\tau}{2\Delta\eta}[(\rho G_2\phi)_{i,j+1}^{n}$$
$$-(\rho G_2\phi)_{i,j-1}^{n}]+\frac{\Delta\tau}{2\Delta\xi^2}\left[\left\{\left(\frac{\Gamma}{\mathrm{J}}\alpha\right)_{i+1,j}\right.\right.$$
$$\left.+\left(\frac{\Gamma}{\mathrm{J}}\alpha\right)_{i,j}\right\}(\phi_{i+1,j}^{n}-\phi_{i,j}^{n})-\left\{\left(\frac{\Gamma}{\mathrm{J}}\alpha\right)_{i,j}$$
$$\left.+\left(\frac{\Gamma}{\mathrm{J}}\alpha\right)_{i-1,j}\right\}(\phi_{i,j}^{n}-\phi_{i-1,j}^{n})$$
$$-\frac{\Delta\tau}{2\Delta\eta^2}\left[\left\{\left(\frac{\Gamma}{\mathrm{J}}\beta\right)_{i,j+1}+\left(\frac{\Gamma}{\mathrm{J}}\beta\right)_{i,j}\right\}(\phi_{i,j+1}^{n}\right.$$
$$-\phi_{i,j}^{n})-\left\{\left(\frac{\Gamma}{\mathrm{J}}\beta\right)_{i,j}+\left(\frac{\Gamma}{\mathrm{J}}\beta\right)_{i,j-1}\right\}(\phi_{i,j}^{n}$$
$$\left.-\phi_{i,j-1}^{n})\right]+S_{i,j}^{n} \tag{11}$$

Second sweep $(i+j+n$ *odd*$)$

$$(\rho\phi)_{i,j}^{n+1}=(\rho\phi)_{i,j}^{n}-\frac{\Delta\tau}{2\Delta\xi}[(\rho G_1\phi)_{i+1,j}^{n+1}$$
$$-(\rho G_1\phi)_{i-1,j}^{n+1}]-\frac{\Delta\tau}{2\Delta\eta}[(\rho G_2\phi)_{i,j+1}^{n+1}$$
$$-(\rho G_2\phi)_{i,j-1}^{n+1}]+\frac{\Delta\tau}{2\Delta\xi^2}\left[\left\{\left(\frac{\Gamma}{\mathrm{J}}\alpha\right)_{i+1,j}\right.\right.$$
$$\left.+\left(\frac{\Gamma}{\mathrm{J}}\alpha\right)_{i,j}\right\}(\phi_{i+1,j}^{n+1}-\phi_{i,j}^{n+1})-\left\{\left(\frac{\Gamma}{\mathrm{J}}\alpha\right)_{i,j}$$
$$\left.+\left(\frac{\Gamma}{\mathrm{J}}\alpha\right)_{i-1,j}\right\}(\phi_{i,j}^{n+1}-\phi_{i-1,j}^{n+1})\right]$$
$$-\frac{\Delta\tau}{2\Delta\eta^2}\left[\left\{\left(\frac{\Gamma}{\mathrm{J}}\beta\right)_{i,j+1}+\left(\frac{\Gamma}{\mathrm{J}}\beta\right)_{i,j}\right\}(\phi_{i,j+1}^{n+1}\right.$$
$$-\phi_{i,j}^{n+1})-\left\{\left(\frac{\Gamma}{\mathrm{J}}\beta\right)_{i,j}+\left(\frac{\Gamma}{\mathrm{J}}\beta\right)_{i,j-1}\right\}(\phi_{i,j}^{n+1}$$
$$\left.-\phi_{i,j-1}^{n+1})\right]+S_{i,j}^{n+1} \tag{12}$$

Equations (11) and (12) are applied to the computational grid points alternately. The implicit differencing of the viscous terms during the second (implicit) sweep (equation (12)) results in a strong coupling between the governing momentum equations. Due to this coupling, a simultaneous solution of the momentum equations for the unknown velocities of u and v is required. When steady-state solutions are of interest, the explicit sweep (equation (11)) can be replaced as suggested by Kwon and Delaney (1985) with a simple linear extrapolation of the dependent variables, i.e.

$$(\rho\phi)_{i,j}^{n-1}=2(\rho\phi)_{i,j}^{n}-(\rho\phi)_{i,j}^{n-1} \tag{13}$$

Equation (13) can be obtained by the repetitive application of the explicit and implicit finite-difference formulae in equations (11) and (12) at the same grid point with the additional assumption that, as the (time) iteration proceeds, steady-state solutions are achieved and the difference in the source terms (a part of S in equations (11) and (12)) of the explicit and implicit finite-difference formulae diminishes. This simplification reduces computation time significantly. However, when time-accurate transient solutions are required, equation (11) must be solved instead of equation (13).

Solution of the finite-difference equations (12) and (13) requires initial conditions for two time levels be supplied. The present procedure assumed stagnated flow conditions initially (at $n=1$). At the second time step ($n=2$), the explicit finite-difference equation (11) was solved in the entire computation domain using the assumed stagnated condition. From the third time step equations (12) and (13) were solved at alternate grid points. Each time step is composed of two sweeps as discussed above. With this procedure, the density was computed from the continuity equation; the velocities from the

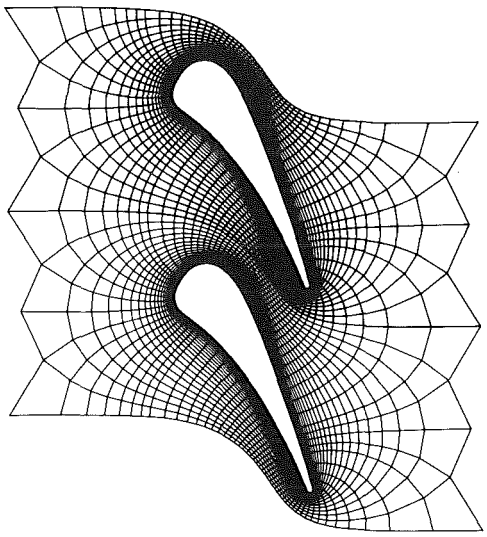

Fig. 1 Airfoil geometry and coordinate system for C3X cascade

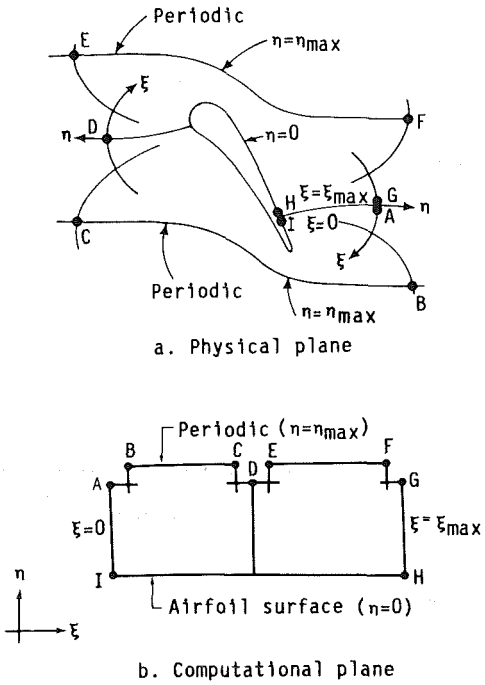

Fig. 2 Schematic of mapping from physical plane to computational plane for "O" grid

simultaneous solution of the momentum equations; and the kinetic energy and dissipation rate from their transport equations. Pressures and temperature-dependent properties were evaluated by the constant total enthalpy assumption and the linear interpolation of the tabulated values in a standard gas table, respectively. This process is repeated until convergence is achieved. Further details of the solution procedure can be found elsewhere (Kwon and Delaney, 1985).

Grid Generation

The grid generation is generally affected by the geometric configuration of the flow passages. For modern turbine airfoils, which are often characterized by blunt leading edges, thick trailing edges, and high stagger angles, an "O" grid is considered to be most appropriate. The present computation for turbine cascade flows utilizes an orthogonal, body conforming "O" grid, shown in Fig. 1. This grid system was constructed using the Adamczyk (1980) grid-generation procedure with an algebraic grid redistribution technique.

The Adamczyk grid generation scheme combines an elliptic Laplace equation solver for establishing the interior point coordinates and a singularity technique for determining the grid point distribution on the airfoil surface. The singularity technique is based on an electrostatic analog that describes the potential field around an infinite cascade. With this grid generation procedure, the physical flow region is mapped onto a rectangular computation domain as shown in Fig. 2. Attractive features of this procedure include the automatic mesh clustering in the region of high surface curvature in the streamwise direction, the achievement of high grid orthogonality especially in the near wall region, and the establishment of periodic grids for ease of enforcing the cascade periodic flow condition.

The Adamczyk grid-generation procedure, however does not provide a sufficient concentration of grid points near the airfoil surface in the cross-passage direction. In this work, the grid points were redistributed in the cross-passage direction in order to cluster grids in the near wall region after the "O" grid was constructed using the Adamczyk procedure. A hyperbolic tangent function similar to that used by Weinberg et al. (1986) was used as the redistribution function. It is noted that, for convenience, the trailing edges of the turbine cascades considered in this work have been rounded as shown in Fig. 1.

Boundary Conditions

Boundary conditions were imposed at the inlet boundary points, the exit boundary points, and the airfoil surface. For the "O" grid shown in Fig. 2, these boundary points are represented by C, D, and E for the inlet points; A, B, F, and G for the exit points, and H–I for the airfoil surface points. The points along the periodic boundaries B–C, E–F, A–I, and G–H in Fig. 2 were treated as regular interior points by periodically extrapolating the data outside the computation domain. At the inlet total pressure P_{T1}, total temperature T_{T1}, and flow angle were specified. The static conditions were obtained using a reference plane characteristic method combined with the isotropic relations. The boundary condition fixed at the exit was a constant static pressure. Velocity components at the exit were evaluated by extrapolation. Along the airfoil surface, the no-slip condition was imposed. The wall pressure was evaluated from the zero normal gradient conditions in accordance with boundary layer theory.

Results and Discussion

The present Navier–Stokes solution procedure was tested for a two-dimensional circular arc bump, the low solidity Allison C3X turbine cascade (Hylton et al., 1983), and a low solidity Rolls-Royce turbine rotor blade (Nicholson et al., 1984). The circular arc bump problem was chosen especially to demonstrate and assess the present method since it has been tested by various workers (Rhie, 1986; Chima and Johnson, 1985; Davis et al., 1986).

Figure 3 shows the coordinate system for a 5 percent thick circular arc bump. A 65 × 33 "H" grid was used since the previous computations by Chima and Johnson, Rhie, and Davis et al. were made using similar "H" grids. It is noted that the present grid is the same as Rhie's. The flow was assumed subsonic, laminar, with the free-stream condition of $M_\infty = 0.5$ and $Re_c \sim 8100$. A symmetry boundary condition was imposed on the upper boundary and the lower boundary upstream of the bump. The no-slip condition was imposed on the bump surface and the lower boundary downstream of the bump. These boundary conditions simulate the bicircular arc

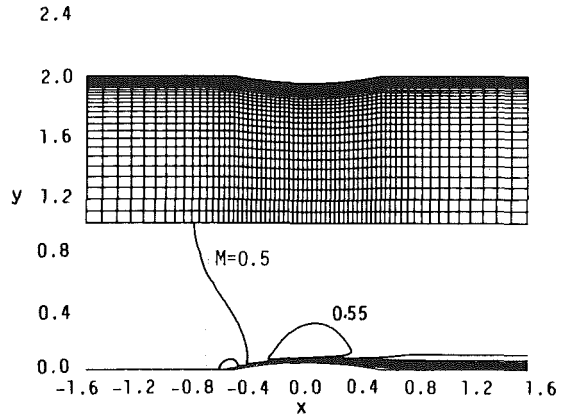

Fig. 3 Computational grids and Mach number contours for a subsonic laminar flow over a 5 percent thick circular arc bump

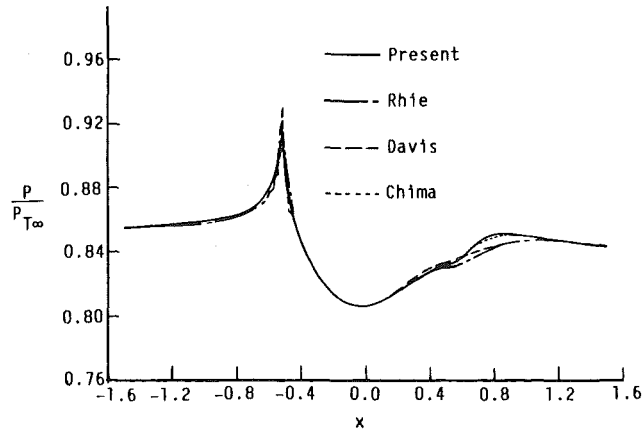

Fig. 4 Surface static pressure distribution for a subsonic laminar flow over a 5 percent thick circular arc bump

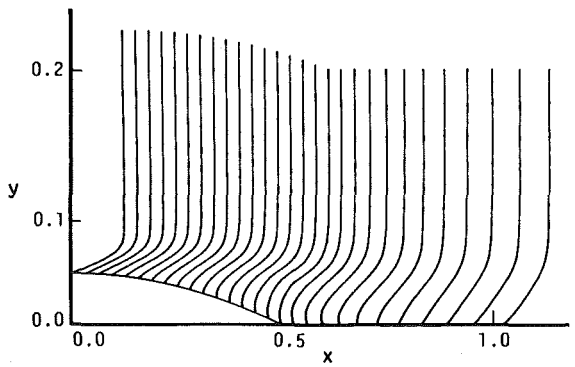

Fig. 5 Velocity profiles for a subsonic laminar flow over a 5 percent thick circular arc bump

cascade with a zero thickness sting emanating from the airfoil trailing edge as noted by the previous workers.

The present computed results for Mach number contours, surface static pressure distribution, and velocity profiles are presented in Figs. 3–5. The Mach number contours shown in Fig. 3 indicate a continuous flow acceleration along the airfoil surface in the front half of the airfoil, with maximum free-stream velocity occurring near the midchord. As the airfoil trailing edge is approached, the surface pressure increases gradually (Fig. 4) with a resultant rapid growth of the wall boundary layer, followed by separation near the airfoil trailing edge, as shown in Fig. 5. Further downstream, the flow reattaches and redevelops under a slight favorable surface pressure gradient. The present results, overall, compare well with other Navier–Stokes solutions (Rhie, Chima and Johnson, and Davis et al.) except for the airfoil trailing edge where the separation bubble occurs. In the separated flow region, the previous computations by Chima, Rhie, and Davis et al. differ from each other (Fig. 4). The present solution in this region is found to compare more closely with the predictions by Chima than with those by Rhie and Davis et al. as shown in Fig. 4. The present solution was obtained after approximately 3500 iterations.

The first cascade flow considered corresponds to case 144 for the highly loaded two-dimensional low-solidity C3X turbine cascade (Hylton et al.). The coordinate system for the cascade is shown in Fig. 1. This "O" grid consists of 101 points in the pseudoazimuthal direction and 25 points in pseudoradial direction. The upstream and downstream boundaries located at 1.25 axial chords upstream of the airfoil leading edge and downstream of the trailing edge, respectively. The locations of these boundaries are automatically determined in the Adamczyk method based on the number of grid points specified. The first grid point away from the airfoil surface is located at a value of $y+$ which varies from 30-200. This is the well-known equilibrium region where the logarithmic law holds for fully developed, turbulent boundary layers. The geometric inlet and exit angles of the airfoil are approximately 0 deg and 72 deg , respectively.

The flow conditions of case 144 are upstream total pressure $P_{T1} = 7.899$ kPa, total temperature $T_{T1} = 815$ K, inlet Mach number $M_1 = 0.16$, exit Mach number $M_2 = 0.9$, inlet Reynolds number based on true chord $Re_c = 0.63 \times 10^6$, and the free-stream turbulence intensity $Tu = 6.5$ percent. In the present computation, the flow was assumed fully turbulent in the entire computation domain. Total pressure, total temperature, flow angle at the inlet, and static pressure at the exit were prescribed. The measured ratio of exit static to inlet total pressure was approximately 0.59.

Figure 6 shows the comparison of the present predictions for surface static pressure distribution with experimental data measured by Hylton et al., Euler predictions by Delaney (Hylton et al.), and Navier–Stokes predictions by Weinberg et al. (1986). The present results compare well with experimental data for both the suction and pressure surfaces of the airfoil. The comparison of the present solutions with those of Weinberg et al. is good. The comparison of the Navier–Stokes solution with the Euler solution tends to imply that the surface static pressure on the front portion of the suction surface where a strong acceleration takes place can be more accurately represented by full-viscous solutions than inviscid solutions. The predicted Mach number contours plotted in Fig. 7 indicate the flow is entirely subsonic. The maximum Mach number computed is about 0.925.

Figure 8 shows the results of a grid refinement study for case 144. The number of grid points in the pseudoradial direction was increased to 33 while that in the pseudoazimuthal direction was kept the same. On the refined grid system, grid points near the wall region were redistributed such that the value of $y+$ at the first coordinate line is approximately 15.0. The surface static pressures obtained with the refined grid are shown to be almost indistinguishable from those with the original 101×25 grids except in the region near the trailing edge.

The second example corresponds to case 143 for the C3X cascade (Hylton et al.). The inlet flow conditions for this case are almost identical to those discussed above. The major difference between the two cases is in the cascade pressure ratio. The measured exit static pressure for case 143 is about 0.498 of the upstream total pressure. The present prediction with a

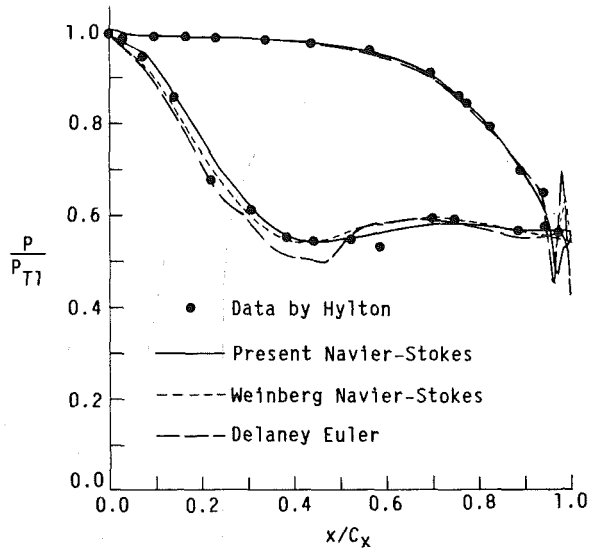

Fig. 6 Airfoil surface static pressure distribution for C3X cascade; Run No. 144, $p_2/p_{T1} = 0.59$

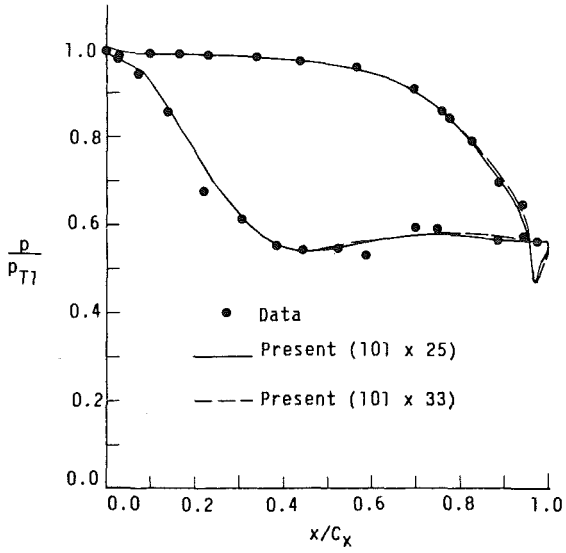

Fig. 8 Effect of grid refinement on surface static pressure distribution

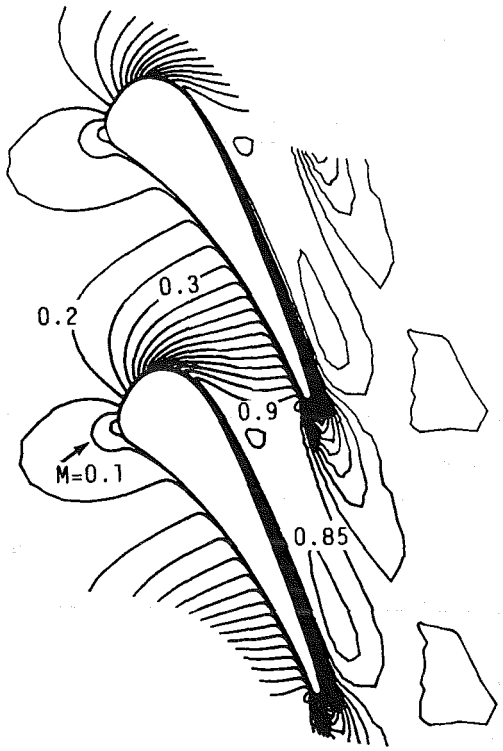

Fig. 7 Calculated Mach number contours for C3X cascade; Run No. 144, $p_2/p_{T1} = 0.59$

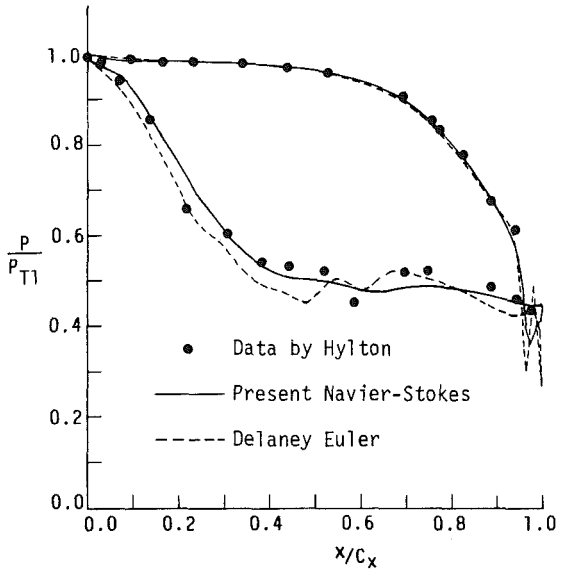

Fig. 9 Airfoil surface static pressure distribution for C3X cascade; Run No. 143, $p_2/p_{T1} = 0.498$

101×25 grid shows that the flow for case 143 is transonic with a computed maximum Mach number of approximately 1.10. The predicted wall static pressure distribution compares well with measurements as shown in Fig. 9. The Euler solutions obtained by Delaney present a slight underprediction on the front portion of the suction surface as was noticed for case 144. The predicted pressure contours for both cases show a rapid acceleration of flow until the geometric throat of the flow passage is reached (see Fig. 10). Downstream of the throat, a sudden decrease in the pressure gradient was observed. The computation for each case took approximately 3000 time steps to reach steady state.

The final example is a two-dimensional low-solidity Rolls-Royce turbine blade shown at the top of Fig. 11. Nicholson et al. (1984) tested the blade to measure surface static pressures and surface heat transfer for three expansion ratios corresponding to ideal exit Mach numbers of $M_2 = 0.78$, 0.96, and 1.10. In the present computations, the heat transfer prediction was excluded. The flow inside the blade row was predicted for two exit flow conditions of $M_2 = 0.78$ and 1.10 that corresponds to values of p_2/p_{T1} of 0.669 and 0.468, respectively. The upstream flow conditions are: total pressure $p_{T1} = 501.5$ kPa, total temperature $T_{T1} = 432$ K, and a flow angle of 27.32 deg. The exit Reynolds number based on the axial chord is $Re_c = 1.113 \times 10^6$. The computational grid used consists of 103 points in a pseudoazimuthal direction and 25 points in the pseudoradial direction (Fig. 11).

The predicted airfoil surface static pressure distributions for both expansion ratios are presented in Fig. 11. The present solutions compare well with the measured data. These surface pressure distributions, as well as the predicted static pressure

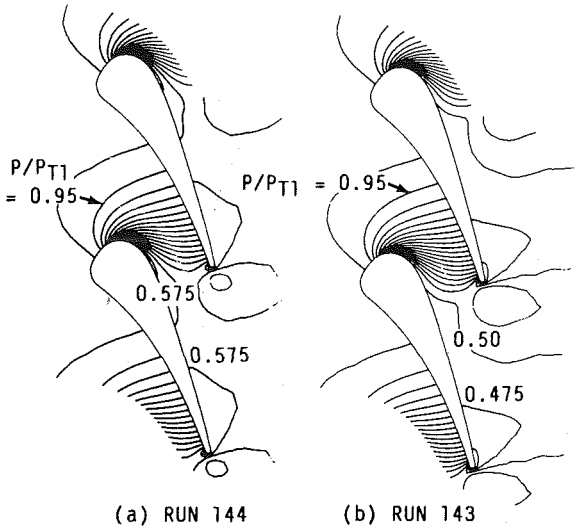

Fig. 10 Calculated static pressure contours for C3X cascade

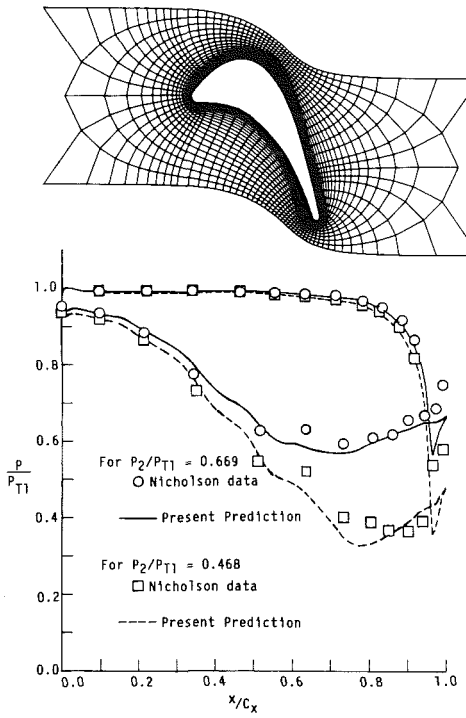

Fig. 11 Airfoil surface static pressure distribution for Rolls-Royce low-solidity turbine cascade

contours presented in Fig. 12, show that for both exit flow conditions the flow acceleration on the pressure surface was delayed until about 80 percent axial chord.

Along the suction surface, the flow is shown to undergo a relatively strong acceleration up to approximately 75 percent axial chord. Further downstream, the suction surface flow was diffused and a rapid buildup in the wall boundary layer took place. For the exit condition of $p_2/p_{T1} = 0.468$, a flow separation was predicted on the suction surface at about 0.89 axial chord as was experimentally observed. For $p_2/p_{T1} = 0.665$, the flow was predicted entirely subsonic and no separation occurred until the rounded section of the trailing edge was reached. The predicted maximum Mach numbers are 0.865 and 1.278 for $P_2/P_{T1} = 0.665$ and 0.468, respectively. The experimental data reveal a shock located on the suction surface at about 90 percent axial chord for the exit static to inlet total pressure ratio of 0.468. The present computation, however, was unable to resolve this shock clearly due to the coarse grid arrangement in the region. The present solutions were obtained after approximately 3500 iterations.

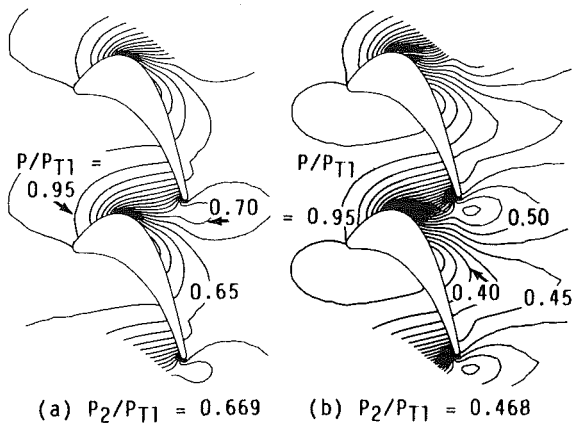

Fig. 12 Calculated static pressure contours for Rolls-Royce low-solidity turbine cascade

Conclusion

A reliable hopscotch Navier–Stokes solution procedure has been presented for the prediction of two-dimensional, compressible, transonic flows in turbomachinery cascades. The solution procedure developed by Kwon and Delaney for transonic nozzle flow was generalized to arbitrary curvilinear coordinates for application to an "O" grid system. The method is computationally explicit and has a substantial computational speed advantage for steady flow analyses over other explicit schemes not utilizing multigrid acceleration. An orthogonal, body-conforming "O" grid has been used for solution of turbine cascade flows. The present grid system modeled appropriately the blunt leading edge and thick trailing edge of the turbine cascades examined.

A two-dimensional circular arc bump flow and four turbine cascade flows were computed with the present procedure using the standard k–ϵ turbulence model. The computed results agreed well with experimental data and other numerical solutions. Although the present computations were carried out on a scalar computer, the explicit hopscotch scheme is readily modified for efficient operation on vector machines. Finally, the present hopscotch algorithm is directly extendable to three spatial dimensions for full three-dimensional blade passage flow solutions.

Acknowledgments

The author expresses his thanks to Allison Gas Turbine Division, General Motors Corporation, for permission to publish this paper. The author also would like to thank Mr. Stacy Thompson and Dr. Dave Nealy for their continuous support and cooperation, and to his colleague, Mr. William Dalton, for patiently reading the manuscripts and providing valuable suggestions.

References

Adamczyk, J. J., 1980, "An Electrostatic Analog for Generating Cascade Grids," *NASA Conference Publication 2166: Numerical Grid Generation Techniques*, pp. 129–142.

Ballhaus, W. F., and Bailey, F. R., 1980, "Computer Aerodynamics on Large Computers," *Computers and Fluids*, Vol. 8, No. 1, pp. 133–144.

Briley, W. R., and McDonald, H., 1977, "Solution of the Multidimensional Compressible Navier-Stokes Equations by a Generalized Implicit Method," *Journal of Computational Physics*, Vol. 24, pp. 263–293; 372–397.

Chima, R. V., and Johnson, G. M., 1985, "Efficient Solution of the Euler and Navier-Stokes Equations With a Vectorized Multiple-Grid Algorithm," *AIAA Journal*, Vol. 23, No. 1, pp. 23–32.

Davis, R. L., Ni, R. H., and Carter, J. E., 1986, "Cascade Viscous Flow Analysis Using the Navier-Stokes Equations," AIAA Paper No. 86–33.

Eckert, E. R. G., and Drake, R. M., 1972, *Analysis of Heat and Mass Transfer*, McGraw-Hill, New York.

Gordon, P., 1965, "Nonsymmetric Difference Equations," *Journal of the Society of Industrial and Applied Mathematics*, Vol. 1, No. 3, pp. 667–673.

Hah, C., 1984, "A Navier-Stokes Analysis of Three-Dimensional Turbulent Flows Inside Turbine Blade Rows at Design and Off-Design Conditions," ASME *Journal of Engineering for Gas Turbines and Power*, Vol. 106, pp. 421–429.

Holst, T. L., 1976, "Nonsymmetric Difference Equations," *Journal of the Society of Industrial and Applied Mathematics*, Vol. 1, No. 3, pp. 667–673.

Hylton, L. D., Mihelc, M. S., Turner, E. R., Nealy, D. A., and York, R. E., 1983, "Analytical and Experimental Evaluation of the Heat Transfer Distribution Over the Surfaces of Turbine Vanes," NASA-CR-168015.

Kwon, O. K., and Delaney, R. A., 1985, "A Navier-Stokes Solution Procedure for Analysis of Steady Two-Dimensional Transonic Nozzle Flows," AIAA Paper No. 85-1597.

Launder, B. E., and Spalding, D. B., 1974, "The Numerical Calculation of Turbulent Flows," *Computational Methods in Applied Mechanics and Engineering*, Vol. 3, pp. 269–289.

Nicholson, J. H., Forest, A. E., Oldfield, M. L. G., and Schultz, D. L., 1984, "Heat Transfer Optimized Turbine Rotor Blades—An Experimental Study Using Transient Technique," ASME *Journal of Engineering for Gas Turbines and Power*, Vol. 106, pp. 173–182.

Pulliam, T. L., and Steger, J. L., 1980, "Implicit Finite-Difference Simulations of Three-Dimensional Compressible Flow," *AIAA Journal*, Vol. 18, No. 2, pp. 159–167.

Rhie, C. M., 1986, "A Pressure Based Navier-Stokes Solver Using the Multigrid Method," AIAA Paper No. 86-0207.

Rudy, H. D., Morris, D. J., Blanchard, D. K., Cooke, C. H., and Rubin, S. G., 1975, "An Investigation of Several Numerical Procedures for the Time Asymptotic Compressible Navier-Stokes Solutions," *NASA SP-347, Aerodynamic Analyses Requiring Advanced Computers*, Part 1, pp. 437–468.

Weinberg, B. C., Yang, R. J., McDonald, H., and Shamroth, S. J., 1986, "Calculations of Two- and Three-Dimensional Transonic Cascade Flow Fields Using the Navier-Stokes Equations," ASME *Journal of Engineering for Gas Turbines and Power*, Vol. 108, pp. 93–102.

Shock Embedding Discontinuous Solution of Elliptic Equation for Inverse Problem of Transonic S_2 Flow

Chen Hongji

Wu Chung-Hua

Institute of Engineering Thermophysics,
Chinese Academy of Sciences,
Beijing, People's Republic of China

In the case of the inverse problem of S_2 surface flow in a transonic turbomachine, if the meridional component of the relative velocity is subsonic, the equation governing the flow is elliptic. Through the use of a proper conservative form of the streamfunction principal equation and embedding the shock relations into the principal equation, the transonic flow over the whole S_2 surface containing the discontinuity of the passage shock can be calculated. A computer code employing this method has been programmed. The algorithm, which is only a little different from the subsonic code, is simple, accurate, and reliable. This program is particularly useful in the solution of the three-dimensional transonic flow in a fan or compressor through iterative computation of transonic S_1 and S_2 flows, when the former is carried out by the recently developed method of "separate-region calculation with shock fitting." The new computer code is used to calculate the S_2 flow in a typical transonic rotor and the difference between the result obtained by this method and that by the commonly used one, in which the shock discontinuity is not taken into account, can be clearly seen.

Introduction

In the work presented by Wu (1950), the calculation of the inverse (design) problem starts with a mean S_2 streamsurface, $S_{2,m}$, on which certain desirable variations of the angular momentum of the fluid $V_\theta r$ and of the thickness of the stream filament are prescribed by the designer. In the iterative solution of three-dimensional flow based on the successive calculations of the flows on S_1 and S_2 surfaces, the prescribed variations are continuously corrected by the results obtained in the S_1 solutions. In these cases the streamfunction principal equation governing the S_2 flow remains elliptic as long as the meridional component of the relative velocity of the flow is smaller than the local speed of sound. Hence the calculation of the inverse problem of the flow on the S_2 surface is applicable to transonic turbomachines, and many transonic turbomachines have been designed (Seyler, 1967; Monsarrat, 1969; Janetzke, 1972; Chinese Academy of Sciences and Shenyang Aeroengine Co., 1980) or analyzed (McDonald et al., 1980; Zhao et al., 1986; Wang et al., 1986) on the basis of the solution of the elliptic equation (or its variants).

If in the inverse problem of transonic S_2 flow a distribution of $V_\theta r$ that is smoothed out slightly at a shock (for example, the one obtained by the shock-capturing calculations of S_1 surface flows) is taken as the input, the calculation at the shock, as in the shock-capturing method, need not be specially dealt with and the resulting shock will be correspondingly smoothed out over several mesh points. Such an algorithm has no marked difference from that of the subsonic one and in the past all the calculations did not exceed this level. If a distribution of $V_\theta r$ with a discontinuity across the shock (for example, the one obtained by the "separate-region calculation with shock fitting" of S_1 surface flows (Wu, C. H., et al., 1984; Wu, W., et al., 1984)), is taken as the input, no continuous solution can be obtained. But, as in the method of separate-region calculation with shock fitting for S_1 flow, when the special shock relations are applied to the discontinuity in the S_2 calculation a more accurate flow field containing a clear shock will be obtained. In virtue of the fact that the equation is uniformly elliptic here in the case of S_2 flow, the difficulty of dealing with the mixed type equation is avoided. However, the parameters in front of the shock and behind the shock must be solved simultaneously with the whole flow field, whereas in the separate-region calculation with shock fitting in the direct problem, these parameters are obtained by starting the calculation from the inlet to the shock and across the shock.

In this paper a method to solve this kind of problem of transonic flow over an S_2 streamsurface containing a shock discontinuity will be presented with its theoretical basis and an illustrative example.

Contributed by the Gas Turbine Division of THE AMERICAN SOCIETY OF MECHANICAL ENGINEERS and presented at the 32nd International Gas Turbine Conference and Exhibit, Anaheim, California, May 31–June 4, 1987. Manuscript received at ASME Headquarters Feburary 10, 1987. Paper No. 87-GT-115.

Theoretical Basis

To describe the three-dimensional, adiabatic, inviscid, compressible and steady relative flow in turbomachines, the following basic equations are used (Wu, 1950):

$$\nabla \cdot (\rho \mathbf{W}) = 0 \tag{1}$$

$$\mathbf{W} \times (\nabla \times \mathbf{V}) = \nabla I - T \nabla s \tag{2}$$

$$DI/Dt = 0 \tag{3}$$

$$Ds/Dt = 0 \tag{4}$$

Employing the partial derivative following motion on the S_2 streamsurface, the continuity equation (1) can be written as (Wu, 1950)

$$\frac{\bar{\delta}(\tau \rho W_r)}{\partial r} + \frac{\bar{\delta}(\tau \rho W_z)}{\partial z} = 0 \tag{5}$$

By the use of thermodynamic relations it can be further transformed into the following form:

$$\left(1 - \frac{W_r^2}{a^2}\right)\frac{\bar{\delta} W_r}{\partial r} - \frac{W_r W_z}{a^2}\frac{\bar{\delta} W_z}{\partial r} - \frac{W_z W_r}{a^2}\frac{\bar{\delta} W_r}{\partial z} + \left(1 - \frac{W_z^2}{a^2}\right)\frac{\bar{\delta} W_z}{\partial z} - \frac{1}{2a^2}\frac{D(W_\varphi^2)}{Dt} + \frac{\omega^2 r W_r}{a^2} + W_r \frac{\bar{\delta} \ln \tau}{\partial r} + W_z \frac{\bar{\delta} \ln \tau}{\partial z} = 0 \tag{6}$$

The radial and tangential components of the equation of motion (2) are, respectively (Wu, 1950)

$$-\frac{W_\varphi}{r}\frac{\bar{\delta}(V_\theta r)}{\partial r} + W_z\left(\frac{\bar{\delta} W_r}{\partial z} - \frac{\bar{\delta} W_z}{\partial r}\right) + \frac{\bar{\delta} I}{\partial r} - T\frac{\bar{\delta} s}{\partial r} - F_r = 0 \tag{7}$$

and

$$\frac{W_r}{r}\frac{\bar{\delta}(V_\theta r)}{\partial r} + \frac{W_z}{r}\frac{\bar{\delta}(V_\theta r)}{\partial z} - F_\varphi = 0 \tag{8}$$

By eliminating $\mathbf{F}$, there is obtained

$$-\frac{\bar{\delta} W_z}{\partial r} + \frac{\nu}{r}\frac{\bar{\delta}(V_\theta r)}{\partial r} - \frac{\mu}{r}\frac{\bar{\delta}(V_\theta r)}{\partial z} + \frac{\bar{\delta} W_r}{\partial z} + \frac{1}{W_z}\frac{\bar{\delta} I}{\partial r} - \frac{T}{W_z}\frac{\bar{\delta} s}{\partial r} = 0 \tag{9}$$

where $\mu = n_r/n_\varphi = F_r/F_\varphi$ and $\nu = n_z/n_\varphi = F_z/F_\varphi$. From the orthogonality relation between $\mathbf{n}$ and $\mathbf{W}$

$$\mu W_r + W_\varphi + \nu W_z = 0 \tag{10}$$

and from the integrability condition of the streamsurface (Wu, 1950)

$$\frac{\bar{\delta}}{\partial r}\left(\frac{\nu}{r}\right) = \frac{\bar{\delta}}{\partial z}\left(\frac{\mu}{r}\right) \tag{11}$$

there is obtained

$$\mu\frac{\bar{\delta} W_r}{\partial r} + \nu\frac{\bar{\delta} W_z}{\partial r} + W_r\frac{\bar{\delta}\mu}{\partial r} + W_z\frac{\bar{\delta}\mu}{\partial z} + \frac{\bar{\delta} W_\varphi}{\partial r} + \frac{\nu W_z}{r} = 0 \tag{12}$$

In the inverse problem, $V_\theta r$ (or V_θ or W_φ) and τ are the prescribed functions of r and z, I and s are to be determined along the streamlines according to equations (3) and (4) with an appropriate change in s across the shock. Thus, equations (6), (9), and (12) define a system of first-order partial differential equations whose unknowns are W_r, W_z, and μ (ν and a are respectively related to the unknowns through the orthogonality relation and the thermodynamic relation). The characteristic equation of the system of equations (Courant and Hilbert, 1962) yields the following:

$$W_r - W_z\lambda = 0 \tag{13}$$

$$\left(1 - \frac{W_z^2}{a^2}\right)\lambda^2 + \frac{2W_r W_z}{a^2}\lambda + \left(1 - \frac{W_r^2}{a^2}\right) = 0 \tag{14}$$

It is known from the second equation that only when the meridional velocity $W_l = \sqrt{W_r^2 + W_z^2}$ is greater than the speed of sound can the two distinct real wave characteristic lines exist.

By the use of the stream function based on the continuity equation (Wu, 1950), equation (9) can be transformed into a

Nomenclature

a = speed of sound
c_p = specific heat at constant pressure
D/Dt = differentiation with respect to time following relative motion of fluid particle
$\frac{\bar{\delta}}{\partial x^i}, \frac{\bar{\delta}}{\partial r} \ldots$ = partial differentiation following motion on streamsurface
$\mathbf{e}^i, \mathbf{e}_i$ = contravariant and covariant coordinate bases, respectively
$\mathbf{F}$ = force acting on S_2 surface per unit mass of gas $= -(1/n_\varphi \rho r)(\partial p/\partial \varphi)\mathbf{n}$
H = absolute stagnation enthalpy $= h + V^2/2$
h = enthalpy per unit mass of gas
I = relative stagnation rothalpy $= (h - \omega^2 r^2/2) + W^2/2$
M = Mach number
M_n = component of Mach number normal to shock surface
$\mathbf{n}$ = unit vector normal to streamsurface
p = gas pressure
R = gas constant
r, θ, z = absolute cylindrical coordinates
r, φ, z = relative cylindrical coordinates
s = entropy per unit mass of gas
T = absolute temperature, K
$\mathbf{V}$ = absolute velocity of gas
$\mathbf{W}$ = relative velocity of gas
W_l = meridional component of $\mathbf{W}$
W_{ts} = projection of $\mathbf{W}$ to the intersection line of shock surface and streamsurface
W^i = physical component of $\mathbf{W}$ along coordinate x^i
x^1, x^2 = nonorthogonal curvilinear coordinates in meridional plane
κ = ratio of specific heats
λ = slope of characteristic line
ρ = density of gas
τ = circumferential thickness of S_2 stream filament
ψ = stream function defined on streamsurface
ω = angular velocity of rotor

Superscripts

$(-)(+)$ = in front of and behind shock, respectively

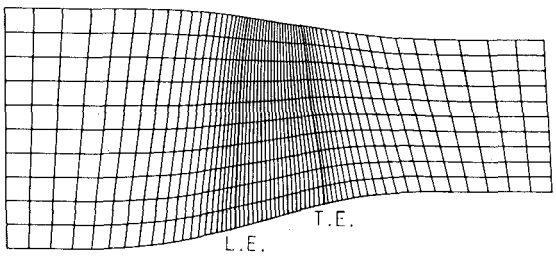

Fig. 1(*a*) Grid used in calculations I and II, 61 × 11

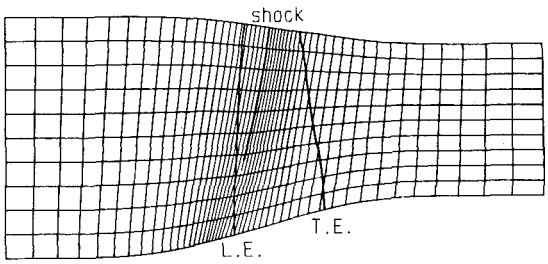

Fig. 1(*b*) Grid used in calculation III, 49 × 11

Fig. 1 Grids in S_2 calculations and projections of blade and shock on meridional plane

second-order stream-function principal equation, which is of the form

$$\left(1-\frac{W_r^2}{a^2}\right)\frac{\partial^2\psi}{\partial r^2}-2\frac{W_rW_z}{a^2}\frac{\partial^2\psi}{\partial r\partial z}+\left(1-\frac{W_z^2}{a^2}\right)\frac{\partial^2\psi}{\partial z^2}+N\frac{\partial\psi}{\partial r}+\mathrm{M}\frac{\partial\psi}{\partial z}=0 \tag{15}$$

Whether this equation is hyperbolic or elliptical depends as well on whether W_l is greater or less than the speed of sound (for details of the analysis see Chen and Wu, 1985).

That the type of equation depends on the meridional velocity may appear to be bewildering (in the direct problem, the type of the equation depends on the entire relative velocity). However, through the use of the propagation rule of disturbance in supersonic flow, this can be shown to be consistent with physics, as has been done by Chen and Wu (1985).

The solution of the partial differential equation describing the supersonic or transonic flow containing shocks is a generalized and discontinuous solution. As is well known, the hyperbolic and mixed-type equations may have such solutions. For the elliptic equation, the solution is smooth if the coefficients (including the nonhomogeneous term) are smooth, but it may also be discontinuous if the coefficients have discontinuities. When $W_l < a$, the quality $V_\theta r$ (or W_φ), which is the known variable and is in the definition of the coefficients of the elliptic equation in the S_2 inverse problem, can be proved to be discontinuous at the shocks as follows:

If it is assumed that any one of the shock wave surfaces is parallel to the φ coordinate, it is contradictory to the condition $W_l < a$, because the normal (to shock surface) velocity component of the flow in front of the shock must be greater than the speed of sound. Thus the shock surfaces are not parallel to $V_\theta r$, and the value of $V_\theta r$ (or W_φ) must have an abrupt jump across each shock surface accompanying the jump of the normal velocity component.

In such a case, the flow parameters W_r, W_z, I, s, p, a, and T cannot satisfy the system of equations governing the flow if they are all continuous. For instance, it is easy to see the continuity equation (6) can not be satisfied. From the point of view of mathematics, different generalized solutions can be obtained when different connecting conditions are exerted on the discontinuities. However, here the connecting condition should definitely be the set of shock relations, and this condition determines which parameters are discontinuous and in what manner. As to the known variable τ, it may be discontinuous but not necessarily.

Shock Relations

The parameters of the flow on S_2 surface satisfy the following thermo-aerodynamic relations across a shock wave:

The continuity equation is simply expressed in terms of the stream function as

$$\psi^{(+)}=\psi^{(-)} \tag{16}$$

One of the equations of motion is

$$W_{ts}^{(+)}=W_{ts}^{(-)} \tag{17}$$

This equation is in the direction tangent to the S_2 surface and also tangent to the shock surface. When the thermodynamic relations of a perfect gas are used, the other two equations of motion, the one normal to the shock surface and the one in the direction tangent to the shock surface, but not tangent to the S_2 surface can be, respectively, represented by the following equations:

$$k\left(\frac{2}{k-1}+\mathrm{M}^{(+)2}\right)\mathrm{M}_n^{(-)4}+\left[\frac{2k}{k-1}(\mathrm{M}^{(+)2}-\mathrm{M}^{(-)2})-\frac{k-1}{2}(\mathrm{M}^{(+)2}+\mathrm{M}^{(-)2})-2\right]\mathrm{M}_n^{(-)2}-\left(\mathrm{M}^{(+)2}+\frac{2}{k-1}\right)=0 \tag{18}$$

and

$$\frac{s^{(+)}-s^{(-)}}{R}=\frac{k}{k-1}\ln\left[\frac{2}{(k+1)\mathrm{M}_n^{(-)2}}+\frac{k-1}{k+1}\right]+\frac{1}{k-1}\ln\left[\frac{2k}{k+1}\mathrm{M}_n^{(-)2}-\frac{k-1}{k+1}\right] \tag{19}$$

The energy equation is expressed in terms of the relative stagnation rothalpy as

$$I^{(+)}=I^{(-)} \tag{20}$$

The condition of continuity of the streamsurface (the integrability condition is also one of its expressions) is

$$\varphi^{(+)}=\varphi^{(-)} \tag{21}$$

where φ is the value of the coordinate of the S_2 surface.

In the calculations of the direct problems of the streamsurfaces, usually the plane-flow shock relations are used. This is equivalent to assuming the shock surfaces perpendicular to the streamsurfaces. The error involved appears to be somewhat different for S_1 and S_2 flows and its magnitude depends on particular configurations. In the present paper, this assumption is not made and the preceding formulation is truly three dimensional.

Embedding Shock Relations

We employ nonorthogonal curvilinear coordinates x^1, x^2 lying in the meridional plane such that the intersection of the shock with the S_2 surface just projects on one of the x^2 coordinate lines (see Fig. 1*b*); we take $x^3=\varphi$ along the circumferential direction. The components of the equation of motion in the directions of $\mathbf{e}^2$ and $\mathbf{e}^3$ are, respectively (Wu, 1976),

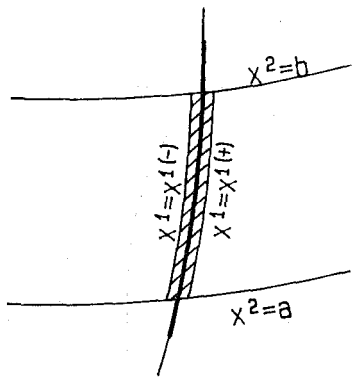

Fig. 2 The infinitely small domain of integration containing the shock line

$$\frac{W_\varphi}{r}\left[\frac{\partial(V_\theta r)}{\partial x^2}-\frac{\partial w_2}{\partial\varphi}\right]-\frac{W^1}{\sqrt{a_{11}}}\left[\frac{\partial w_2}{\partial x^1}-\frac{\partial w_1}{\partial x^2}\right]=\frac{\partial I}{\partial x^2}-T\frac{\partial s}{\partial x^2} \tag{22}$$

and

$$\frac{W_1}{\sqrt{a_{11}}}\left[\frac{\partial w_1}{\partial\varphi}-\frac{\partial(V_\theta r)}{\partial x^1}\right]-\frac{W^2}{\sqrt{a_{22}}}\left[\frac{\partial(V_\theta r)}{\partial x^2}-\frac{\partial w_2}{\partial\varphi}\right]=\frac{\partial I}{\partial\varphi}-T\frac{\partial s}{\partial\varphi} \tag{23}$$

Subtracting equation (23) multiplied by n_z/n_φ from equation (22) and using the partial derivatives following motion on the S_2 surface give (Chen, 1984)

$$\frac{\bar\delta}{\partial x^1}\left(w_2-\frac{n_2}{n_\varphi}V_\theta r\right)-\frac{\bar\delta}{\partial x^2}\left(w_1-\frac{n_1}{n_\varphi}V_\theta r\right)=-\frac{1}{w_1}\left(\frac{\bar\delta I}{\partial x^2}-T\frac{\bar\delta s}{\partial x^2}\right) \tag{24}$$

This is the equation of motion in the direction tangent to the curve $x^1=$ const on the S_2 surface and in which the streamsurface force $\mathbf{F}$ does not appear. Taking the double integral of equation (24) over an arbitrary domain D and applying Green's formula, we obtain

$$\oint_L\left(w_2-\frac{n_2}{n_\varphi}V_\theta r\right)dx^2+\left(w_1-\frac{n_1}{n_\varphi}V_\theta r\right)dx^1=\int\int_D-\frac{1}{w^1}\left(\frac{\bar\delta I}{\partial x^2}-T\frac{\bar\delta s}{\partial x^2}\right)dx^1dx^2 \tag{25}$$

In the smooth area equations (24) and (25) are equivalent. It can be proved that equation (25) still holds even in a region that contains a shock wave.

If we let the domain D be taken as the rectangular strip shown in Fig. 2, which crosses the projection of the shock line and two of its sides are parallel to the projection of the shock line, equation (25) becomes

$$\int_a^b\left[\left(w_2-\frac{n_2}{n_\varphi}V_\theta r\right)_{x^{1(+)}}-\left(w_2-\frac{n_2}{n_\varphi}V_\theta r\right)_{x^{1(-)}}\right]dx^2+\int_{x^{1(-)}}^{x^{1(+)}}\left[\left(w_1-\frac{n_1}{n_\varphi}V_\theta r\right)_a-\left(w_1-\frac{n_1}{n_\varphi}V_\theta r\right)_b\right]dx^1=-\int_a^b\int_{x^{1(-)}}^{x^{1(+)}}\frac{1}{w_1}\left(\frac{\bar\delta I}{\partial x^2}-T\frac{\bar\delta s}{\partial x^2}\right)dx^1dx^2 \tag{26}$$

Although the integrand in the second integral is discontinuous, it is of finite value, so that the integral will vanish when the difference between $x^{1(+)}$ and $x^{1(-)}$ becomes infinitely small. In the third integrand, since the direction of the partial derivatives does not cross the shock, $\bar\delta s/\partial x^2$ is of finite value although it may be discontinuous, and the other terms are also of finite value, the third integral will vanish. Thus, because a and b are arbitrary, in order that equation (26) may hold, the sufficient and necessary condition is that the integrand of the first integral is identically equal to zero, that is

$$\left(w_2-\frac{n_2}{n_\varphi}V_\theta r\right)_{x^{1(+)}}=\left(w_2-\frac{n_2}{n_\varphi}V_\theta r\right)_{x^{1(-)}} \tag{27a}$$

or

$$\left(w_2-\frac{n_2}{n_\varphi}w_\varphi-\frac{n_2}{n_\varphi}\omega r^2\right)_{x^{1(+)}}=\left(w_2-\frac{n_2}{n_\varphi}w_\varphi-\frac{n_2}{n_\varphi}\omega r^2\right)_{x^{1(-)}} \tag{27b}$$

Because the values of $(n_2/n_\varphi)\omega r^2$ on either side of the shock are identical, that equation (27) holds is equivalent to that

$$\left(w_2-\frac{n_2}{n_\varphi}w_\varphi\right)_{x^{1(+)}}=\left(w_2-\frac{n_2}{n_\varphi}w_\varphi\right)_{x^{1(-)}} \tag{28}$$

holds. However,

$$\begin{aligned}w_2-\frac{n_2}{n_\varphi}w_\varphi&=w_2+\frac{\bar\delta\varphi}{\partial x^2}w_\varphi\\&=\frac{1}{dx^2}\left(w_2dx^2+\frac{\bar\delta\varphi}{\partial x^2}dx^2w_\varphi\right)\\&=\frac{1}{dx^2}\mathbf{W}\cdot\left(0\mathbf{e}_1+dx^2\mathbf{e}_2+\frac{\bar\delta\varphi}{\partial x^2}dx^2\mathbf{e}_\varphi\right)\\&=\mathbf{W}\cdot\frac{\mathbf{dx}_s^2}{dx^2}=(\mathbf{W}\cdot\mathbf{u}_{2s})\frac{|\mathbf{dx}_s^2|}{dx^2}=W_{ts}\frac{|\mathbf{dx}_s^2|}{dx^2}\end{aligned} \tag{29}$$

where $\mathbf{dx}_s^2$ denotes the increment of the position vector of the S_2 surface with respect to the increment in x^2 coordinate, dx^2, and $\mathbf{u}_{2s}$ denotes its unit vector. In equation (29), $\mathbf{W}\cdot\mathbf{u}_{2s}=W_{ts}$ because $\mathbf{u}_{2s}$ is tangent to the intersection of the shock surface and the S_2 surface. Hence, since the values of $|\mathbf{dx}_s^2|/dx^2$ on either side of the shock are identical, that equation (28) holds is equivalent to

$$(W_{ts})_{x^{1(+)}}=(W_{ts})_{x^{1(-)}} \tag{30}$$

which is just equation (17) of the shock relations mentioned previously. Thus the equivalence between equations (26) and (17) is proved. Further owing to the additive property of double integrals, equation (25) is available to use when D is an arbitrary domain containing a shock and the shock relation (17) has been embedded into it.

Not all conservative forms of the equation of motion are applicable to the shock. Two points are indicated here:

1 When I and s are used to describe the thermodynamic state in the equation of motion, none of its projections other than those in the directions tangent to the shock surface are rigorously valid at the shock place (this is different from the case where p and ρ are used to describe the thermodynamic state). For instance, in the projection of equation of motion that is in the direction tangent to the curve $x^2=$ const on the S_2 surface (Chen, 1984)

$$w^2\left[\frac{\bar\delta}{\partial x^1}\left(w_2-\frac{n_2}{n_\varphi}V_\theta r\right)-\frac{\bar\delta}{\partial x^2}\left(w_1\frac{n_1}{n_\varphi}V_\theta r\right)\right]=\frac{\bar\delta I}{\partial x^1}-T\frac{\bar\delta s}{\partial x^1} \tag{31}$$

the left-hand side is of finite value while the term $T(\bar\delta s/\partial x^1)$

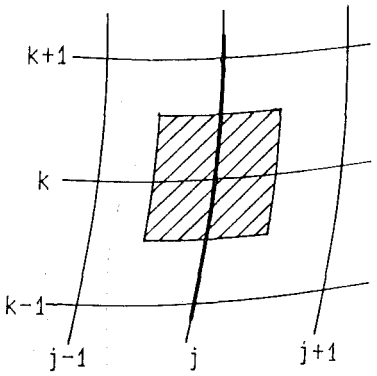

Fig. 3 The domain of integration applied to deduce the difference equation at the point (*j*, *k*) on the shock line

on the right-hand side is infinitely large. If we divide the preceding equation by T and integrate over the domain shown in Fig. 2, it can be still seen that the left-hand side approaches zero but the right-hand side approaches a finite value. In general, the equation of motion in a direction that is not tangent to the shock surface can be expressed as a combination of the equation of motion (31) and one of the equations of motion in a direction tangent to the shock surface, and consequently, is not rigorously valid.

2 $V_\theta r$ undergoes a jump across the shock and therefore

$$F_\varphi = \frac{D(V_\theta r)}{rDt} \tag{32}$$

becomes an infinite quantity. Therefore, it is desirable, in the calculation over a region where shock exists, that a form of equation of motion which does not contain the **F** term should be used.

Difference Equation

For the mesh point (j, k) where the shock line just passes through, the domain of integration $[x^1_{j-1/2}, x^1_{j+1/2}]$, $[x^2_{k-1/2}, x^2_{k+1/2}]$ (the shaded area in Fig. 3) is taken. Equation (26) becomes

$$\begin{aligned}
&\int_{x^2_{k-1/2}}^{x^2_{k+1/2}} \left[\left(w_2 - \frac{n_2}{n_\varphi} V_\theta r\right)_{x^1_{j+1/2}} - \left(w_2 - \frac{n_2}{n_\varphi} V_\theta r\right)_{x^1_{j-1/2}}\right] dx^2 \\
&- \int_{x^1_{j-1/2}}^{x^1_{j+1/2}} \left[\left(w_1 - \frac{n_1}{n_\varphi} V_\theta r\right)_{x^2_{k+1/2}} - \left(w_1 - \frac{n_1}{n_\varphi} V_\theta r\right)_{x^2_{k-1/2}}\right] dx^1 \\
&= -\int_{x^2_{k-1/2}}^{x^2_{k+1/2}} \int_{x^1_{j-1/2}}^{x^1_{j+1/2}} \frac{1}{w^1}\left(\frac{\delta I}{\partial x^2} - T\frac{\delta s}{\partial x^2}\right) dx^1 dx^2
\end{aligned} \tag{33}$$

To obtain the difference equation, the numerical integration is applied to the integrals in equation (33). If the integrand has a discontinuity in the interval of integration, the interval is divided into two parts and the integration is carried out separately. For instance

$$\begin{aligned}
&\int_{x^1_{j-1/2}}^{x^1_{j+1/2}} \left(w_1 - \frac{n_1}{n_\varphi} V_\theta r\right)_{x^2_{k+1/2}} dx^1 \\
&\approx \left(w_1 - \frac{n_1}{n_\varphi} V_\theta r\right)_{j-1/4,\, k+1/2} (x^1_j - x^1_{j-1/2}) \\
&+ \left(w_1 - \frac{n_1}{n_\varphi} V_\theta r\right)_{j+1/4,\, k+1/2} (x^1_{j+1/2} - x^1_j)
\end{aligned} \tag{34}$$

The velocity components are expressed by the stream function through the use of the following relations:

$$w_1 = \sqrt{a_{11}}\,(W^1 + W^2 \cos\theta_{12}) \tag{35}$$

$$w_2 = \sqrt{a_{22}}\,(W^2 + W^1 \cos\theta_{12}) \tag{36}$$

$$W^1 = \frac{\partial\psi}{\partial x^2} \Big/ \tau\rho\sqrt{a_{22}}\,\sin\theta_{12} \tag{37}$$

$$W^2 = -\frac{\partial\psi}{\partial x^1} \Big/ \tau\rho\sqrt{a_{11}}\,\sin\theta_{12} \tag{38}$$

When the partial derivatives appearing in the equation are expressed by the corresponding differences, notice of the avoidance of taking values across the discontinuities is taken. The difference equation finally obtained contains the ψ values at the nine mesh points around the point (j, k). Although most of the parameters have two values at the j-mesh line, which coincides with the shock line, ψ has only a single value (see equation (16)). The resulting difference equation has the form

$$\begin{aligned}
&A_{11}\psi_{j-1,k-1} + A_{12}\psi_{j-1,k} + A_{13}\psi_{j-1,k+1} + A_{21}\psi_{j,k-1} \\
&+ A_{22}\psi_{j,k} + A_{23}\psi_{j,k+1} + A_{31}\psi_{j+1,k-1} \\
&+ A_{32}\psi_{j+1,k} + A_{33}\psi_{j+1,k+1} = B
\end{aligned} \tag{39}$$

At the other points in the flow field, the difference equations of stream function resulting from the principal equation contain ψ values at nine points as well. The form is the same as equation (39), but the constitutions of the coefficients are different. The system of algebraic equations formed by the difference equations at all the mesh points can be solved by the existing methods that are employed in the numerical solution of elliptic equation. However, if the shock relation (17) is not embedded into the principal equation as we have done here, the shock has to be treated as a boundary of calculation and the conditions, which should be prescribed on it, need to be determined through a process of successive corrections in the calculation.

Computer Program and Illustrative Example

The computer program reported by Zhu (1980) has been proved by practice to be quite effective for the smooth solution of the inverse problem of the S_2 streamsurface. It adopts a line-relaxation technique to solve the elliptic principal equation in the stream function, and is applicable provided the meridional velocity is subsonic. In practical application the increases of entropy along the streamlines are taken into consideration to account for the accumulated effect of the viscosity. The program for the discontinuous solution of the transonic flow containing a shock is a modification of this program. At the mesh line that coincides with the shock line (Fig. 1*b*), an additional computation j station together with the regular one store the parameters at both sides of the shock. The same value of ψ at the double station is obtained by relaxing the difference equation (39). The value of $M_n^{(-)2}$ is obtained by solving the second-degree algebraic equation (18) and the $s^{(+)}$ is found by using equation (19). Finally, the original chordwise distribution of entropy is accordingly corrected (Fig. 4). The other formulas used to evaluate the parameters include

$$H^{(+)} = H^{(-)} + \omega[(V_\theta r)^{(+)} - (V_\theta r)^{(-)}] \tag{40}$$

$$T = (H - V^2/2)/c_p \tag{41}$$

$$\rho^{(+)} = \rho^{(-)}\,(T^{(+)}/T^{(-)})^{\frac{1}{k-1}} \cdot e^{\frac{s^{(-)} - s^{(+)}}{R}} \tag{42}$$

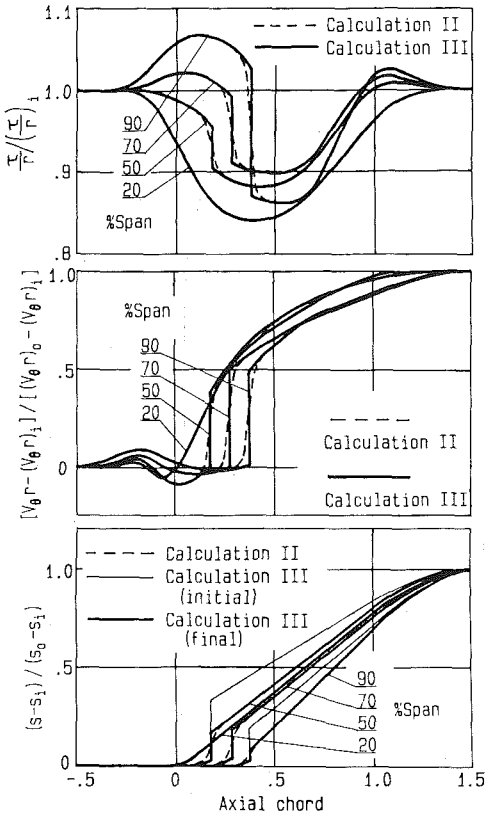

Fig. 4 Input variations of τ, $V_\theta r$, and s on the $S_{2,m}$ surface

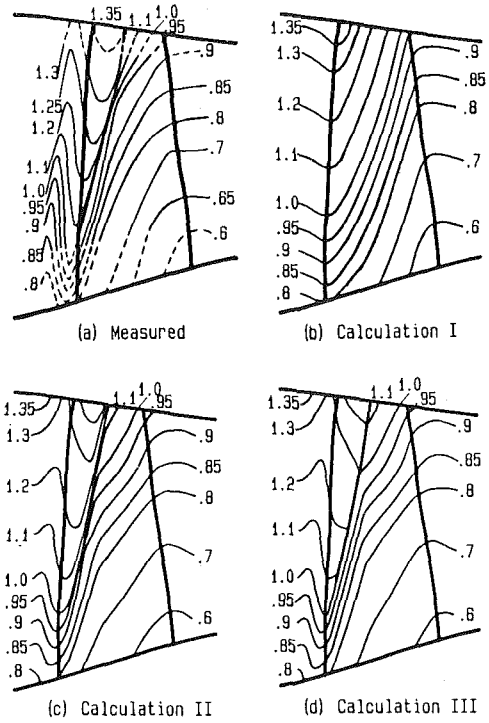

Fig. 5 Mach number contours on the $S_{2,m}$ surface

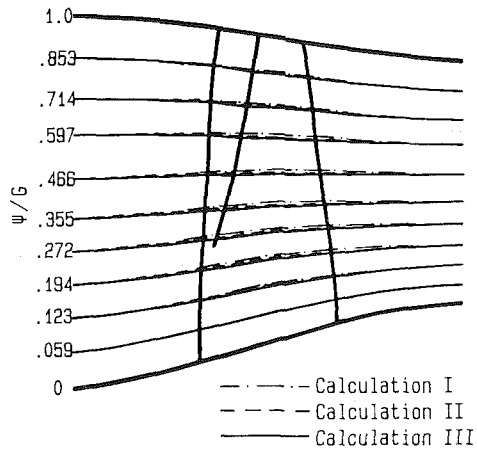

Fig. 6 Distribution of streamlines on the $S_{2,m}$ surface

and equations (20), (21), (37), and (38). The parameters $V_\theta r$, $\mathbf{W}$, s, H, T, ρ, etc. possess double values at the double j station near the case and approach a single value near the hub where the shock does not exist.

To demonstrate the present method, the $S_{2,m}$ flow in the transonic compressor rotor, which was designed by DFVLR (Strinning and Dunker, 1975) for a total pressure ratio of 1.51, has been calculated. Its relative tip Mach number reaches 1.4, but the meridional velocity component is still subsonic. From the available Mach number contour plots on the sections located at several spanwise positions for peak efficiency operating conditions at 100 percent design speed (McDonald et al., 1980), the projection of the Mach number contours on the $S_{2,m}$ surface on the meridional plane is constructed and presented in Fig. 5(*a*). The increases of $V_\theta r$ and s from inlet to exit used in the calculation are determined from the measured data given in that paper.

In order to see the effects of the different values of $V_\theta r$, s, and τ prescribed in the solution of the inverse problem of the transonic flow on the $S_{2,m}$ surface, the following three calculations have been carried out for the DFVLR rotor:

Calculation I. In this calculation, variations of $V_\theta r$, s, and τ usually prescribed for subsonic flow are used.

Calculation II. In this calculation, the prescribed values of $V_\theta r$, s, and τ are smooth but have steep gradients at the passage shock. The grid system used in calculation I and II is the same (Fig. 1*a*).

Calculation III. The prescribed values of $V_\theta r$, s, and τ having proper discontinuities across the passage shock furnished by S_1 calculations at several blade heights (Fig. 4) are used. The shock relations are embedded into the equation and are thus automatically satisfied in the solution. The grid system used (Fig. 1*b*) is different from that used in calculations I and II.

From results obtained in the three calculations, it is seen from the streamline distributions shown in Fig. 6 and the Mach number contours shown in Fig. 5, the solution obtained in calculation I is quite different from those obtained in II and III; in particular, it does not give the shock discontinuity. It is also seen that the difference between the results obtained in calculations II and III is not large. The differences in the S_1 surface shape and in the corresponding τ, which should be used in the S_1 calculations, are indicated, respectively, in Figs. 6 and 7.

Relative flow angle β corresponding to the prescribed values of $V_\theta r$ and τ are compared with the measured values (Dunker and Strinning, 1976) in Fig. 8. The variations of the pressure obtained in the calculations are shown in Fig. 9.

Concluding Remarks

1 The fact that in the case of the inverse problem of S_2 surface flow in a transonic turbomachine, if the meridional velocity is subsonic, the equation governing flow is elliptic and its solution can be obtained by an elliptic algorithm is clearly demonstrated by the calculations presented in this paper.

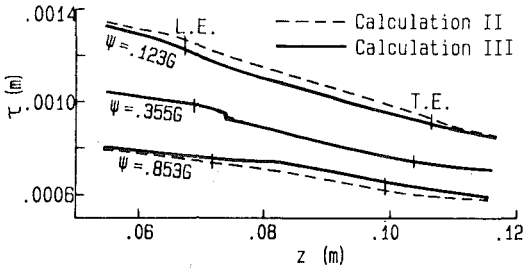

Fig. 7 Variation of the normal distance between two adjacent streamlines (1 percent total mass flow passes through them)

2 When the prescribed values of $V_\theta r$, s, and τ possess steep gradients or discontinuities the flow field obtained contains a clear passage shock.

3 It is recommended that the smooth type variation of $V_\theta r$ commonly prescribed in subsonic turbomachine design be used only in the preliminary design stage. The variations with steep gradient or with discontinuity, which are to be furnished by the transonic S_1 calculations, should be used in the final design.

References

Chen, H., 1984, "On the Equations of Motion on S_1 and S_2 Stream Surfaces, Their Independence and Selection," *Symposium on Aerothermodynamics in Heat Engines*, Chinese Society of Engineering Thermophysics, Paper No. 842069.

Chen, H., and Wu, C. H., 1985, "Accurate Solution of Inverse Problem of Transonic Flow on S_2 Surface by Means of Elliptic Algorithm," *Proceedings of 7th ISABE*, pp. 465–473; *AIAA Journal*, Vol. 25, No. 3, 1987, pp. 448–456.

Chinese Academy of Sciences and Shenyang Aeroengine Co., 1976, "Theory, Method and Application of Three-Dimensional Flow Design of Transonic Axial-Flow Compressor," Res. Rep. Chinese Academy of Sciences; *Journal of Engineering Thermophysics* [in Chinese], Vol. 1, No. 1, Feb. 1980.

Courant, R., and Hilbert, D., 1962, *Methods of Mathematical Physics*, Vol. II, Interscience Publishers, New York, Chap. III, Section 2.

Dunker, R. J., and Strinning, P. E., 1976, "Flow Velocity Measurements Inside of a Transonic Axial Compressor Rotor by Means of an Optical Technique and Compared With Blade-to-Blade Calculations," *Proceedings of the 3rd International Symposium on Air Breathing Engines*, Munich, DGLR-Fachbuch No. 6, Mar. 7–12, pp. 217–232.

Janetzke, D. C., Ball, C. L., and Hager, R. D., 1972, "Performance of 1380-Foot-Per-Second-Tip-Speed Axial-Flow Compressor Rotor With Blade Tip Solidity of 1.1," NASA TM x-2449.

McDonald, P. W., Bolt, C. R., Dunker, R. J., and Weyer, H. B., 1980, "A Comparison Between Measured and Computed Flow Fields in a Transonic Compressor Rotor," ASME *Journal of Engineering for Power*, Vol. 102, pp. 883–889.

Monsarrat, N. T., Keenan, K. J., and Tramm, P. C., 1969, "Design Report, Single-Stage Evaluation of Highly-Loaded High-Mach-Number Compressor Stages," NASA CR-22562, Appendix I.

Seyler, D. R., and Smith, L. H., Jr., 1967, "Single Stage Experimental Evaluation of High Mach Number Compressor Rotor Blading, Part I—Design of Rotor Blading," NASA CR-54581, Appendix B.

Strinning, P. E., and Dunker, R. J., 1975, "Aerodynamische und Schanfelauslegung einer Transsonischen Axial-verdichterstufe," *Forschungsberichte Verbrennungs-Kraftmaschinen*, Vol. 178.

Wang, Z., Chen, H., Hua, Y., and Wu, C. H., 1986, "Solution of Transonic Flow in DFLVR Axial Compressor Rotor by Quasi-3D Iteration Between S_1 and S_2 Stream Surface," Chinese Society of Engineering Thermophysics, Paper No. 86-2-81.

Wu, C. H., 1950, "A General Theory of Three-Dimensional Flow in Subsonic and Supersonic Turbomachines of Axial, Radial, and Mixed-Flow Types," Paper No. 50-A-79; *Trans. ASME*, Vol. 74, 1952; NACA TN 2604.

Wu, C. H., 1976, "Three-Dimensional Turbomachinery Flow Equations Expressed With Respect to Non-orthogonal Curvilinear Coordinates and Methods of Solution," *Proceedings of 3rd ISABE*, pp. 233–252.

Wu, C. H., Wu, W., Hua, Y., and Wang, B., 1984, "Transonic Cascade Flow With Given Shock Shape Solved by Separate Subsonic and Supersonic Computations," *Computational Methods in Turbomachinery*, IMechE, Paper No. C79/84, pp. 133–140.

Wu, W., Wu, C. H., and Yu, D., 1984, "Transonic Cascade-Flow Solved by Separate Supersonic and Subsonic Computations With Shock Fitting," ASME *Journal of Engineering for Gas Turbines and Power*, Vol. 107, 1985, pp. 329–335.

Zhao, X., Qin, L., and Wu, C. H., 1986, "Quasi-Three-Dimensional Solution of Transonic Flow in CAS Axial Compressor Rotor," Chinese Society of Engineering Thermophysics, Paper No. 86-2-80.

Zhu, R., 1980, "Flow-Field Line-Relaxation Solution for Inverse Problem of Flow Along S_2 Relative Stream Surface Employing Non-orthogonal Curvilinear Coordinates and Corresponding Non-orthogonal Velocity Components," *Journal of Engineering Thermophysics* [in Chinese], Vol. 1, No. 1.

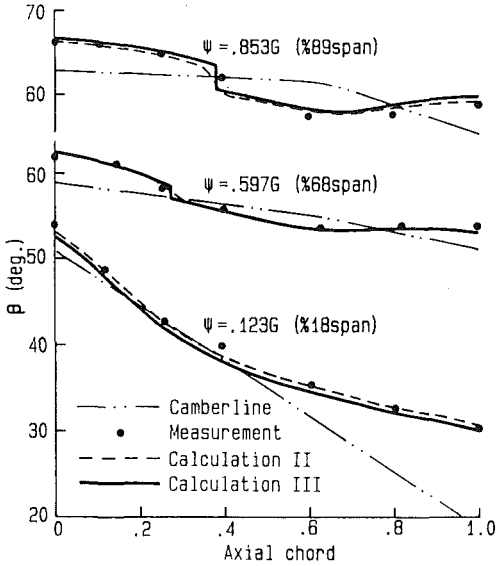

Fig. 8 Variation of the relative flow angle on the $S_{2,m}$ surface (the indications of "% span" are for camberline and measurement)

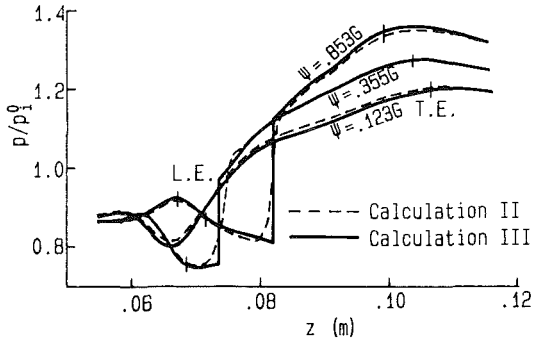

Fig. 9 Variation of pressure on the $S_{2,m}$ surface obtained in calculations

The Design of Shock-Free Compressor Cascades Including Viscous Boundary-Layer Effects

A. A. Hassan
Mechanical and Aerospace Engineering Department,
Arizona State University,
Tempe, AZ 85287

A numerical procedure has been developed for the design of shock-free transonic compressor cascades with an allowance for viscous effects, providing that the boundary layer is fully attached over the blade. The method described combines, in an iterative process, a modified inviscid hodograph-based inverse-design algorithm (CIDA), originally developed by the author for the design of shock-free airfoils, and the inverse boundary-layer algorithm (LTBLCEQL) of Miner et al. [22]. In the numerical procedure, the inviscid subsonic and supersonic regions of the flow are decoupled allowing the solution of either an elliptic or hyperbolic-type partial differential equation for the full stream function. For the subcritical portion of the flow, the inviscid calculation is performed in a computational plane which is obtained through a sequence of conformal and numerical transformations of the two-sheeted hodograph plane. For the supercritical portion, a characteristic calculation is carried out in the hodograph plane. The results are then mapped back to the physical plane to determine the inviscid blade configuration. Viscous effects are then incorporated via the boundary-layer displacement surface concept. The boundary-layer algorithm incorporates a two-layer eddy viscosity turbulence model and allows for gradual, rather than instantaneous, transition to turbulence. Two examples of shock-free compressor blades are given to demonstrate the capabilities of the numerical coupling procedure.

Introduction

In practice it is easy to obtain a smooth and continuous transition from subsonic to supersonic speeds. The reverse process, that is, a smooth and continuous transition from supersonic to subsonic speeds, has proved extremely difficult to realize [1, 2]. The deceleration of the flow through the speed of sound is, with a few exceptions, usually accompanied by shock waves. In the simplest model the embedded supersonic region over a supercritical compressor blade may be thought of as containing two families of characteristic waves. The first is comprised of those running downstream from a point on the surface that carry its expansive disturbances; since these cannot continue into the subsonic flow beyond the sonic line, they are reflected at the constant-pressure sonic line as waves of equal strength but opposite sign. These reflected waves form the second family and carry compressive disturbances. These incoming compression waves will themselves be reflected when they meet the surface and, unless the surface is convex enough, the reflections will again be compressive [3]. Therefore, careful blade "profiling" or shaping is required in this velocity range, especially for the decelerated compressor cascade flow. In any event, waves reflected from the sonic line may coalesce to form a discontinuous shock wave. Unfortunately, once local regions of supersonic flow occur, shock waves are likely with the attendant wave drag and boundary-layer separation losses. A shock-free flow would, of course, be desirable as it avoids these losses.

In the mid-1950s Morawetz [4–6] showed that shock-free, two-dimensional, irrotational, near-sonic flows are mathematically isolated (i.e., any arbitrary changes in the upstream or downstream flow conditions or in the blade shape that provide a shock-free flow will lead to the formation of a shock wave). For example, changes in thickness on the same order of magnitude as the boundary layer displacement thickness can change a transonic shockless cascade flow into a transonic shocked flow [7] and vice versa. Moreover, such small changes in shape can unchoke an already choked cascade [8].

Due to the importance of viscous effects in the range of Mach numbers and Reynolds numbers at which a typical cascade blade is designed to operate [9, 10], a number of numerical viscous-inviscid interaction methods [11, 12] have been developed in recent years for the analysis (direct problem) of airfoils and compressor cascade blades at design and off-design conditions. The ability to control specific aerodynamic characteristics (e.g., eliminating an existing shock wave or delaying the separation of the turbulent boundary layer) using these methods is absent, and is usually

Contributed by the Gas Turbine Division of THE AMERICAN SOCIETY OF MECHANICAL ENGINEERS and presented at the 32nd International Gas Turbine Conference and Exhibit, Anaheim, California, May 31–June 4, 1987. Manuscript received at ASME Headquarters February 5, 1987. Paper No. 87-GT-71.

approached by "trial and error." Parallel with these efforts, shock-free supercritical cascade flows have been generated in the hodograph plane by Korn [13]. In his method of design, a finite-difference scheme based on analytic continuation into the complex domain was used to solve the hodograph equations. The method relies upon the fact that solutions of elliptic partial differential equations can be represented by solutions of initial value problems, if the domain of real dependent and independent variables is extended to complex values. In his formulation, the complex characteristic initial value problem is numerically solved by a standard characteristic method. Although the method is mathematically elegant, even in its user-oriented version, practical use of the method requires much experience and mathematical insight. Nevertheless, some useful viscous shock-free supercritical compressor blade designs were found. These have served us well as examples for various analysis codes as well as for extensive cascade design studies. An intermediate position between analysis and design (i.e., semi-inverse) is taken by the fictitious gas approach developed by Sobieczky [14] and later used by Dulikravich and Sobieczky [15] in the design of shock-free compressor blades. In their approach, the subsonic boundary of the blade is fixed and the supersonic boundary is redesigned (reshaped) to eliminate any existing shock waves. An integral boundary layer calculation is then incorporated to account for the viscous effects.

This paper represents an extension of earlier research on the inviscid design of transonic shock-free cascades for compressor blade applications [16]. Here, in the absence of shocks, only weak interactions between the inviscid and viscous flows need be considered over the entire surface of the blade. The numerical coupling procedure, which is two orders of magnitude faster than that developed by Korn [13], is a purely inverse one requiring less than 4 min of CPU time on an IBM 3081 for the design of a shock-free compressor blade.

Inviscid Blade Design

The inviscid compressor blade configuration (displacement surface or effective blade normal ordinate plus displacement thickness) is computed using the inverse-design algorithm (CIDA) developed by Hassan and Dulikravich [16]. We consider steady, two-dimensional, compressible, irrotational flow of a perfect gas. The governing equations of motion are

Continuity

$$\nabla \cdot \rho \mathbf{q} = 0 \tag{1}$$

Irrotationality

$$\nabla \times \mathbf{q} = 0 \tag{2}$$

and

$$P\rho^{-\gamma} = \text{const} \tag{3}$$

Equations (1) and (2) are satisfied by introducing the usual compressible stream function ψ and the velocity potential ϕ defined through the following relations:

$$\rho u = \psi_y = \phi_x, \qquad \rho v = -\psi_x = \phi_y \tag{4}$$

Introducing the complex velocity

$$u - iv = qe^{-i\theta} \tag{5}$$

with u, v, q and θ being functions of a complex variable

$$z = x + iy \tag{6}$$

equations (4)–(6) can be combined to yield the following total differential relation:

$$d\phi + i\frac{1}{\rho}\,d\psi = qe^{-i\theta}dz \tag{7}$$

Through cross differentiation equations (4) can be reduced to a single equation in either ϕ or ψ, i.e.,

$$\psi_{xx} + \psi_{yy} = \left(\frac{\rho_x}{\rho}\right)\psi_x + \left(\frac{\rho_y}{\rho}\right)\psi_y \tag{8}$$

$$\phi_{xx} + \phi_{yy} = -\left(\frac{\rho_x}{\rho}\right)\phi_x - \left(\frac{\rho_y}{\rho}\right)\phi_y \tag{9}$$

where

$$\rho = \rho(q), \qquad q = |\nabla\phi|$$

Equations (8) and (9) are elliptic for $M<1$ (subsonic flow), hyperbolic for $M>1$ (supersonic flow), and parabolic where $M=1$ (sonic flow). To solve either of equations (8) or (9) two boundary conditions must be provided. The first represents the behavior of the flow far ahead and behind the blade, and the second represents the flow tangency condition (vanishing normal velocity) on the blade surface. In the inverse procedure presented here, the pressure distribution is used as an input rather than the blade physical coordinates, and our goal is to find the shape that the blade must have to achieve this input

Nomenclature

a, b, c, d = coefficients in stream-function equation
A_1, A_2, A_3 = upstream and downstream singularity strengths or coefficients in boundary-layer equations
I = upstream or downstream singularity
J = numerical transformation Jacobian
M = Mach number
P = static pressure
q = nondimensional velocity $= V/V^*$
r = radial distance in circle plane
s, t = computational plane coordinates
u, v = velocity components in physical plane
W = nondimensional dependent variable in boundary layer equation
x, y = physical plane coordinates
β, ζ = Levy–Lees boundary layer variables
γ = ratio of specific heats
δ = boundary-layer thickness
δ^* = displacement thickness
θ = flow deflection angle
ν = Prandtl–Meyer function
ξ, η = characteristic coordinates in hodograph plane
ρ = fluid density
σ = solidity of cascade (gap/chord)
ϕ = velocity potential
ψ = compressible stream function
Ψ = incompressible stream function

Subscripts

1 = upstream infinity
2 = downstream infinity
e = effective coordinate

Superscripts

* = critical conditions

pressure distribution. Accordingly, for the inverse problem, neither a Neumann boundary condition for ϕ nor a Dirichlet boundary condition for ψ can be given on the blade surface since its location is unknown a priori. The problem of a prescribed pressure on a given blade configuration is ill posed [17]. Here we prescribe a general pressure distribution and find the blade geometry that has a pressure distribution very close to this target pressure distribution.

Hodograph Transformation

For two-dimensional irrotational flow the nonlinear equations (8), (9) for steady flow can be rendered linear by changing the role of the dependent and independent variables. Introducing the hodograph variables ν, θ defined by

$$\nu = \int_{q^*}^{q} \sqrt{|1-M^2|}\,\frac{dq}{q}$$

$$\theta = \tan^{-1}\left(\frac{v}{u}\right) \tag{10}$$

and reformulating the partial derivatives in equations (4) in terms of the new variables, we obtain

$$\begin{aligned} \phi_\theta &= K(\nu)\psi_\nu \\ \phi_\nu &= \pm K(\nu)\psi_\theta \end{aligned} \tag{11}$$

Here the $\pm$ signs refer to supersonic and subsonic conditions, respectively, and

$$K(\nu) = K[\nu(M)] = [\,|1-M^2|\,]^{1/2}/\rho[q(M)] \tag{12}$$

A typical physical and hodograph plane representation (with ν and θ as hodograph variables) of the flow field is sketched in Figs. 1 and 2. The blade maps into an open curve containing the stagnation point S at infinity and the sonic line at points a, b. The upstream and downstream singularities of the flow map into points I_1 and I_2, respectively. The analytical structure of ψ near $\nu=0$ and a smooth curvature of the blade at the sonic line require the local structure of the blade contour near the θ axis to be $(\theta-\theta^*)\alpha\pm\nu^{2/3}$. This weakly singular behavior, which is obtained from a limiting study of equations. (11) as $\nu\to 0$, is of importance in the solution of the boundary-value problem, with ψ given along the elliptic boundary. The region of the flow in Fig. 1, bounded by the dotted contour and the blade, represents a region in which every point has a velocity and flow angle equal to that of some other point outside this region, e.g., $q_e=q_f$ and $\theta_e=\theta_f$. Therefore, points e and f will correspond to the same point in the hodograph plane, which must be considered as a Riemann surface consisting of two sheets with a branch cut (lines dn, cn) connecting them. The local nature of this flow was studied by Lighthill [18] in his hodograph study of compressible flows past lifting airfoils.

Since equations (8) are linear in the ν–θ hodograph plane, there is usually no particular difficulty in finding solutions to them, by numerical methods if necessary. However, the presence of the second sheet of the two-sheeted Riemann surface and the a priori unknown location of the blade surface represent major obstacles in solving the governing equations in this plane. From equations (11) it can also be shown that the second-order derivatives for both ϕ and ψ form the Laplacian or the wave operator depending on whether the flow is subsonic or supersonic. Thus the inviscid equations for the subsonic portion of the flow are invariant in their general form under a conformal transformation.

Subsonic Flow Domain

We proceed by assuming a conformal map of the subsonic portion of the two-sheeted Riemann surface of Fig. 2 into the unit circle of Fig. 3. (The double-connected infinite domain is mapped into a finite simply connected domain through an exponential mapping which is then followed by a square root mapping to unfold the Riemann sheets.) Here part of the circumference of the unit circle corresponds to the blade surface which is wetted by subsonic flow; the remaining part corresponds to the sonic line. The segment comprising the sonic line, $\omega_a \le \omega \le \omega_b$ is chosen and the Mach number M (or equivalently the pressure) on the subsonic part of the blade is prescribed. On the sonic line segment the Mach number is equal to one.

With the Mach number given on the boundary of the unit circle, and with the subsonic portion of the flow inside the circle, we take advantage of the fact that the mapping to the ξ_0 plane is conformal. Thus, the Prandtl–Meyer function ν and the flow deflection angle θ are conjugate harmonics, i.e.,

$$F(\xi_0) = \nu + i\theta$$

or

$$\nabla^2\nu(\xi_0) = 0 \tag{13}$$

$$\nabla^2\theta(\xi_0) = 0 \tag{14}$$

Here $F(\xi_0)$ is the mapping function and $\xi_0 = re^{i\omega}$ with r and ω being the radial and angular coordinates measured in the ξ_0 plane. Boundary conditions for equation (13) are provided through the use of equation (10) relating ν and M; that is, knowing the Mach number distribution on the unit circle, we calculate ν employing equation (10). We then solve Laplace's equation for ν inside the unit circle using Fourier series, which accordingly determines the flow deflection angle θ to within an arbitrary constant. However, the Prandtl–Meyer function ν is logarithmically singular in q ($\nu \propto \log(q)$) at the stagnation

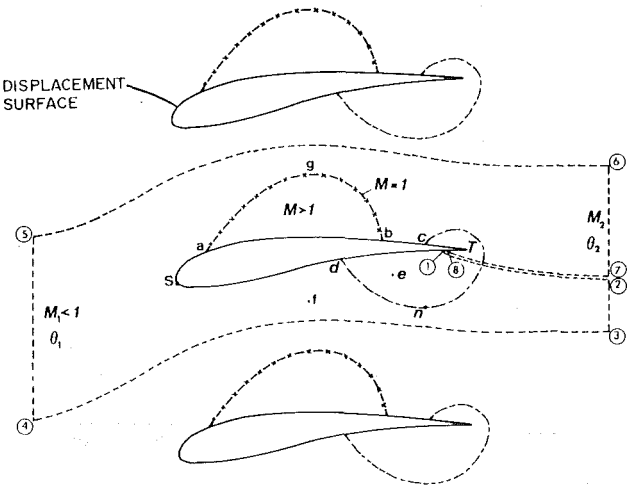

Fig. 1 Sketch of shock-free flow past a rectilinear cascade

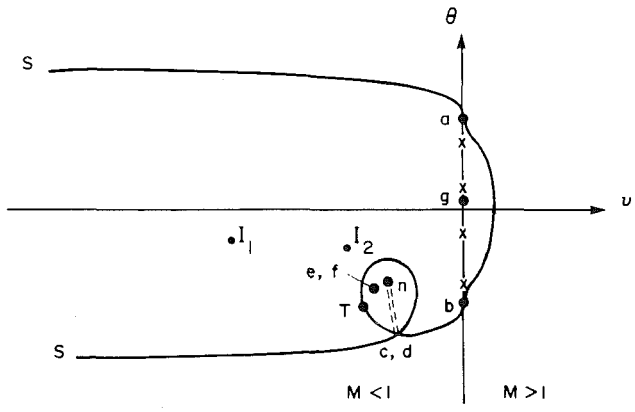

Fig. 2 Hodograph plane representation of a single blade in a rectilinear cascade

point S, which for convenience is positioned at $\xi_0 = -1$ in the plane. Therefore, in order to solve the boundary-value problem for ν using Fourier series we need first to subtract the logarithmic behavior at point S. This is done as follows:

let $\bar{F}(\xi_0) = F(\xi_0) - \log(\xi_0 + 1)$

$G(\xi_0) = \nu(\xi_0) - \mathrm{Re}\{\log(\xi_0 + 1)\}$

$H(\xi_0) = \theta(\xi_0) - \mathrm{Im}\{\log(\xi_0 + 1)\}$

then equations (13)–(14) become

$$\nabla^2 G(\xi_0) = 0 \tag{15}$$

$$\nabla^2 H(\xi_0) = 0 \tag{16}$$

Here Re $\{\ldots\}$ and Im $\{\ldots\}$ are the real and imaginary parts of $\log(\xi_0 + 1)$, respectively. Equation (15) for the regular (nonsingular) Prandtl–Meyer function G is then solved inside the unit circle using a discrete Fourier series subject to the following boundary condition:

$$G(r = 1, \omega) = \nu(1, \omega) - \mathrm{Re}\{\log(e^{i\omega} + 1)\}$$

Having obtained the solution for $G(r, \omega)$ in the unit circle, we then add back the logarithmic singularity to preserve the singular behavior of ν at the stagnation point S.

Elimination of ϕ from equations (11) through cross differentiation and expressing the resulting partial derivatives for ψ in terms of the ξ_0 plane coordinates r, ω we obtain the governing equation for the full stream function ψ

$$r^2\psi_{rr} + r\psi_r + \psi_{\omega\omega} = f(\mathrm{M})\{r^2\nu_r\psi_r + \nu_\omega\psi_\omega\} \tag{17}$$

Here $f(\mathrm{M})$ is a function of the local Mach number M [16] which is determined following the numerical solution of equation (13) for ν. The transformation to hodograph variables ν, θ, followed by a conformal transformation to the ξ_0 plane results in a linear second-order partial differential equation (Poisson equation) for ψ. In addition to this linearity, the major advantages of these two transformations are the unfolding of the two-sheeted hodograph surface to a single sheet, and the representation of the subsonic–sonic boundary of the unknown blade by a unit circle. However, these advances are not without an attendant complexity, albeit a minor one. This difficulty is due to the presence of points I_1, I_2 which represent the upstream and downstream singularities of the flow inside the unit circle depicted in Fig. 3. To circumvent this difficulty, a numerial coordinate transformation of the ξ_0 plane into the rectangular computational s, t plane, shown in Fig. 4, is carried out. To exclude the two singularities at points I_1, I_2 from the ξ_0 plane, referring to Fig. 3, we introduce two branch cuts; the first 3–4–5–6 connecting the two circles with radii ϵ and centers at points I_1, I_2, and the second connecting the circle with center at I_2 and any point on the subsonic blade surface (i.e., on the unit circle). To maintain consistency with the physical boundary conditions, periodic numerical boundary conditions are imposed along the branch cuts 1–2, 7–8. It is noteworthy to mention here that in a direct procedure where the blade shape is prescribed the second branch cut would be equivalent to an initial guess made for the wake position. Conversely, in the present formulation since the blade shape is unknown a priori a branch cut connecting any point on the subsonic surface of the blade (not necessarily the trailing edge) to the outflow boundary is utilized (Fig. 1). The resulting simply connected domain S–1–2–3–4–5–6–7–8–b–a–S is then numerically mapped to the rectangular computational s–t plane ($0 \le s \le 2\pi$, $0 \le t \le 1$) depicted in Fig. 4. Here, the nonorthogonal boundary-fitted grid is generated using the Thompson, Thames, Mastin (TTM) method [19], which employs two coupled Poisson equations as the generating system.

With s and t as new independent variables, we obtain the following governing equation for $\psi(s, t)$:

$$\psi_{ss} + a(s, t)\psi_{tt} = b(s, t)\psi_s + c(s, t)\psi_t + d(s, t)\psi_{st} \tag{18}$$

In equation (18) $a(s, t)$, $d(s, t)$ are purely functions of the local Jacobian J, $\mathrm{J} = \partial(s, t)/\partial(\bar{x}, \bar{y})$, and metrics of the transformation. The functions $b(s, t)$ and $c(s, t)$ are also functions of the local Jacobian, metrics of the transformation as well as the local Mach number M.

Numerical Boundary Conditions

On the blade surface wetted by subsonic flow we have

$$\psi(s, 0) = 0 \qquad s_a \ge s \ge s_b$$

On the sonic line, an arbitrary distribution for the stream function ψ is prescribed

$$\psi(s, 0) = \psi_{\mathrm{sonic}} = g(s) \qquad s_a \le s \le s_b$$

It should be mentioned here that the sonic line presumed stream function distribution $g(s)$ is by no means indicative of the shape of the sonic line in the physical plane. However, the exact shape is only determined after the elliptic problem for the full stream function is solved and the mapping of the inviscid subsonic-sonic boundary, equation (7), computed. The compressible upstream and downstream stream function distributions ψ_{I_1}, ψ_{I_2} are related to their incompressible counterparts Ψ_{I_1}, Ψ_{I_2} by the following relations [16]:

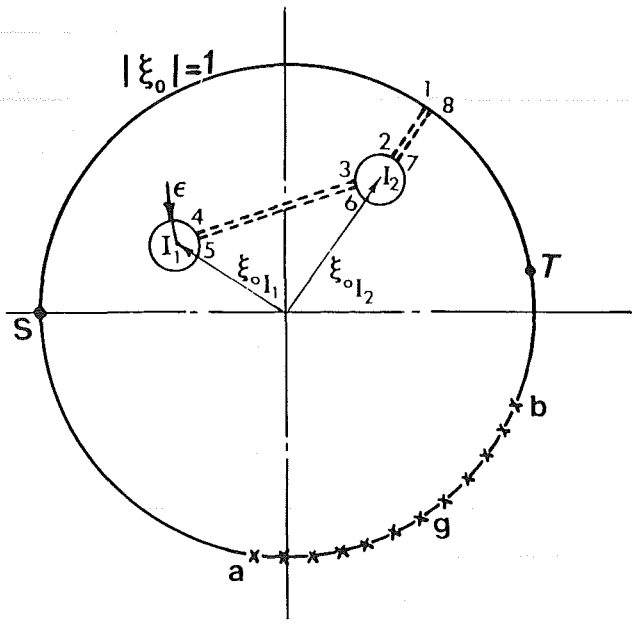

Fig. 3 Cascade subsonic-sonic boundary in the circle plane

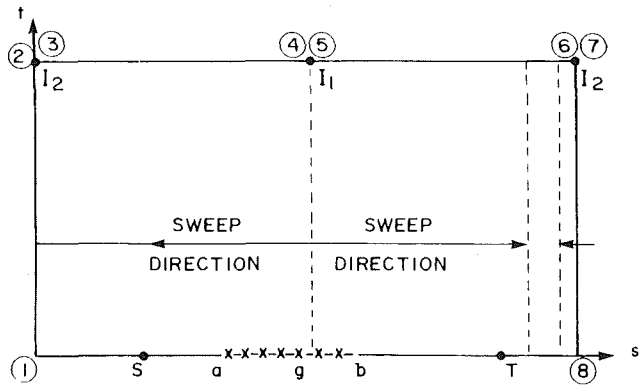

Fig. 4 Computational plane image of the ξ_0 plane as $\epsilon \to 0$

$$\psi_{I_1} = \frac{1}{k(\nu(M_1))}\,\Psi_{I_1} = \frac{1}{k(\nu(M_1))}\,\mathrm{Im} \times \{(1+iA_1)\ln(\xi_0 - \xi_{0_{I1}})\} \tag{19}$$

$$\psi_{I_2} = \frac{1}{k(\nu(M_2))}\,\Psi_{I_2} = \frac{1}{k(\nu(M_2))}\,\mathrm{Im} \times \{(A_2+iA_3)\ln(\xi_0 - \xi_{0_{I_2}})\}$$

Here

$$A_1 = -\tan(\theta_1)/\sqrt{1-M_1^2}$$

$$A_2 = -\sigma\,\frac{M_2\cos(\theta_2)}{M_1\cos(\theta_1)}\sqrt{\frac{(1-M_2^2)}{(1-M_1^2)}}\sqrt{\frac{1+\dfrac{\gamma-1}{\gamma+1}(M_1^2-1)}{1+\dfrac{\gamma-1}{\gamma+1}(M_2^2-1)}} \tag{20}$$

and

$$A_3 = -\tan(\theta_2)/\sqrt{1-M_2^2}$$

In equations (20) M_1, M_2 are the upstream and downstream Mach numbers, respectively; θ_1, θ_2 are the upstream and downstream flow deflection angles; and σ is the solidity of the cascade. Equations (19) in conjunction with the metrics of the numerical transformation are then employed to express the upstream and downstream stream function distributions in the s–t plane (Fig. 4). The condition of periodicity is imposed on the computational plane image of the branch cuts 1–2, 7–8 shown in Fig. 3. Continuity of the stream function ψ across the branch cuts 3–4, 5–6 requires that $\psi(s, 1) = \psi(2\pi - s, 1)$. This condition is satisfied by updating each ψ value on the $t = 1$ line as soon as its corresponding value is altered by the line relaxation calculation. At points I_1, I_2 the stream function is singular. To remove this singular behavior we let

$$\psi = \psi_1 + \psi_2 \tag{21}$$

where ψ_1 is the singular portion due to sources and vortices at point I_1, I_2, and ψ_2 is a regular (nonsingular) stream function. In the present formulation, ψ_1 is obtained through the utilization of equations (19), i.e.,

$$\psi_1 = \mathrm{Im}\{\psi_{I_1} + \psi_{I_2}\}$$

where $\mathrm{Im}\{\ldots\}$ is the imaginary part of ψ_{I_1}, ψ_{I_2}. The Jacobian of the numerical mapping J is also singular at points I_1, I_2 in the s–t plane. To remove this singular behavior of J we define a new Jacobian $\bar{J}$ such that

$$\bar{J} = J\sqrt{\cosh(1-t) - \cos(2s)} \tag{22}$$

Upon substitution of equations (21)–(22) into equation (18) we obtain a regularized two-dimensional stream function equation in terms of ψ_2, $\bar{J}$ and the derivatives of $\psi_{1_{I_1}}$ which are easily found from equations (19). Since the stream function is undefined to within a constant we set $\psi_{2_{I_1}}(\pi, 1) = 0$. To avoid special handling of the regularized stream function at I_2, we construct a grid system which excludes this point as a node [20].

The boundary value problem for ψ_2 is now complete, and equation (18), now expressed in terms of ψ_2, is solved iteratively using a line relaxation procedure. The sweep direction is indicated by the arrows in Fig. 4. The stagnation streamline leaves the contour of the blade at a cusped or wedged trailing edge. This defines, in direct analysis, the amount of circulation around the blade and the location of the stagnation point near the leading edge. For an indirect method such as the present one, the situation is exactly the reverse: Since the (mapped) stagnation point location is given, we have to vary either M_2 or θ_2 for a fixed M_1, θ_1 and solidity σ. In the present formulation M_2 is fixed and θ_2 is initially guessed and then left free. Hence its correct value is determined as part of the numerical solution. The mapped location T of the trailing edge results from this adjustment and the trailing edge shape is then cusped. In the computational plane the stagnation streamline leaves the blade contour at point T at a 90 deg angle.

The results for the gradients $\psi_s(s, 0)$ and $\psi_t(s, 0)$ along the elliptic boundary consisting of the subsonic portion of the blade and its sonic line are then utilized in finding the inverse-map to the physical plane, equation (7). The resulting subsonic–sonic line configuration is then checked to see if it has a reasonable thickness distribution. If not, then the input design parameters must be altered and the design procedure repeated. In this context, a suitable subsonic–sonic line configuration (or equivalently an elliptic boundary configuration) implies one with no trailing edge crossings and reasonable trailing edge gaps in the horizontal and vertical directions. In this study, the size of the horizontal gap is automatically adjusted through the addition of a constant, $\Delta\theta$, to the solution of equation (14) (note that the solution to equation (14) is determined to within an arbitrary constant). This process results in a shift in the locations of the upstream and downstream singularities I_1, I_2 in the ξ_0 plane. Consequently, the upper surface of the elliptic boundary is stretched such that the x location of the upper surface trailing edge matches that of the lower surface. Fortunately, the horizontal gap size is a linear function of the additional constant $\Delta\theta$, hence allowing for a simple iteration procedure to determine the appropriate $\Delta\theta$ necessary to reduce the x gap to a preset value of 0.0001 chord. To minimize the vertical gap size two approaches are utilized. In the first approach, we increase the slopes of the input Mach number at the stagnation point S (Fig. 8). This in turn implies a very rapid acceleration from the front stagnation point therefore requiring a smaller leading edge radius and eventually a blade configuration with a smaller maximum thickness. Naturally, the trailing edge vertical gap size is reduced on the account of obtaining a blade with smaller maximum thickness. In the second approach, the Mach number is altered at or near the trailing edge location of the resulting blade. For example, if increasing the trailing edge Mach number increases the vertical gap, we proceed in the opposite direction whereby reducing the trailing edge Mach number results in a smaller vertical gap. Unfortunately, unlike the horizontal trailing edge gap, the vertical gap size seems to be a nonlinear function of the Mach number at the trailing edge. This, of course, prohibits the use of a simple automated iteration procedure to minimize the vertical gap which, as indicated in Fig. 7, requires a manual check. In this approach, the overall thickness distribution of the blade remains unchanged except in the trailing edge region to reflect the changes that took place in the input Mach number at or near the trailing edge point. When a suitable subsonic–sonic line configuration is found, the first of equations (11) is numerically integrated to find the potential distribution along the elliptic boundary.

Results obtained from the solution of the subsonic flow region on the sonic line (i.e., ϕ^*, x^*, y^*, θ^*) are then used in addition to the prescribed sonic line stream function ψ_{sonic} as initial values for solving the supersonic flow equations in the hodograph plane using the method of characteristics described below.

Supersonic Flow Domain

It follows from equations (11) for the flow in the embedded supersonic region that both ψ and ϕ satisfy the linear wave equations

$$\psi_{\nu\nu} - \psi_{\theta\theta} = -\frac{1}{K(\nu)}\left[\frac{\partial}{\partial \nu} K(\nu)\right]\psi_\nu$$

and

$$\phi_{\nu\nu} - \phi_{\theta\theta} = -K(\nu)\left[\frac{\partial}{\partial \nu}\frac{1}{K(\nu)}\right]\phi_\nu$$

The above equations have two real characteristics whose slopes are given by $d\nu/d\theta = \pm 1$. Introducing the characteristic coordinates ξ, η defined by

$$\xi = \nu + \theta, \qquad \eta = \nu - \theta \tag{23}$$

and reformulating the partial derivatives in equations (11) in terms of the new coordinates, we obtain

$$\phi_\xi = K(\nu)\psi_\xi \text{ and } \phi_\eta = -K(\nu)\psi_\eta \tag{24}$$

Equations (24) may also be expressed in total differential form as

$$\begin{aligned} &\text{for } \xi = \text{const} \quad d\phi + K(\nu)d\psi = 0 \\ \text{and} \quad &\text{for } \eta = \text{const} \quad d\phi - K(\nu)d\psi = 0 \end{aligned} \tag{25}$$

With the stream function $\psi_{\text{sonic}}(\theta)$ and the potential $\phi_s(\theta)$ data known on the sonic line with coordinates $x_s(\theta)$ and $y_s(\theta)$, we proceed to solve equations (25), which hold along the two families of characteristic, using a step-by-step numerical scheme. The basic concept of this marching scheme is discussed in length by Hassan [21]. Consequently, equations (25) applied along two characteristics of opposite families, e.g., b_1 and a_2 of Fig. 5, give two equations relating ϕ_G to ψ_G. These can be solved to obtain ϕ and ψ at point G as functions of ϕ and ψ at the points A and B

$$\psi_G = 1/2(\psi_A + \psi_B) + \frac{1}{2K(\nu)}(\phi_A - \phi_B)$$

$$\phi_G = 1/2(\phi_A + \phi_B) + \frac{K(\nu)}{2}(\psi_A - \psi_B) \tag{26}$$

In equations (26), if we think of ν as a specified function of ξ and η on a rectangular grid, the coefficient $K(\nu)$ may be approximated by average values such that the numerical step-by-step scheme becomes second-order accurate in the mesh size h. The flow deflection angle θ and the Prandtl-Meyer function ν are evaluated at the grid nodes using equations (23).

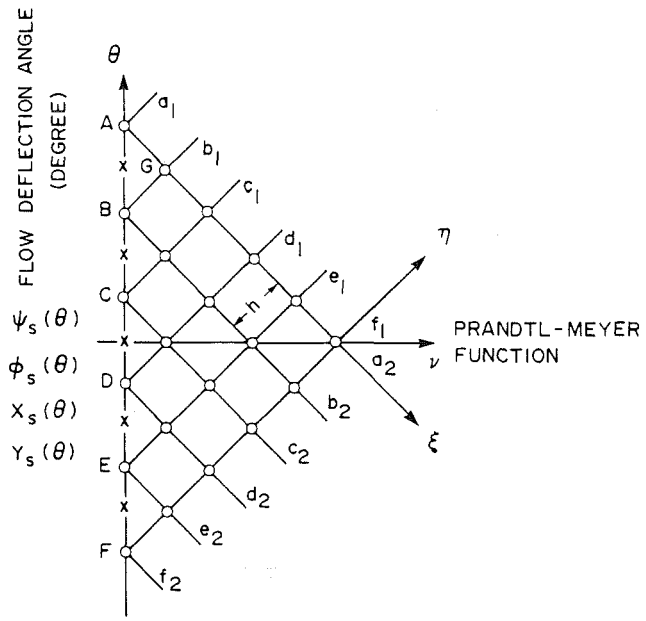

Fig. 5 Computation of the supersonic portion of the flow using the method of characteristics

Having solved for the flow properties at all grid nodes, we then proceed to search for points of zero stream line values as they represent points on the blade's upper surface. Moreover, the supercritical pressure distribution is then found through the knowledge of the Prandtl-Meyer function at these points. Finally, the inverse transformation from the hodograph ν–θ plane to the physical x–y plane, equation (7), yields the supercritical coordinates of the blade.

At this junction it is noteworthy to mention that the results obtained from the numerical integration of equation (7) (first along the subsonic-sonic boundary of the blade and secondly along the supersonic portion of the blade) define in the physical plane a blade configuration (or displacement surface) having a preset trailing edge gap. The input pressure distribution and its corresponding inviscid blade configuration are then utilized as input in the numerical procedure described below for calculating the development of the boundary layer.

Boundary Layer Effects

To include viscous effects the basic approach is to calculate for the weak interaction regions a boundary layer displacement thickness δ^* and to use it to correct the location of the displacement surface (Fig. 6). That is,

$$\{\text{blade effective ordinate} + \delta^*\} - \{\delta^*\} = n_e \tag{27}$$

In equation (27) the boundary layer calculation is carried out using the LTBLCEQL (Laminar and/or Turbulent Boundary Layers in Chemical Equilibrium) algorithm developed by Miner et al. [22]. In their method the laminar and turbulent boundary layer equations are expressed in Levy-Lees variables [23], β: streamwise direction; ζ: normal direction. The streamwise momentum equation and the energy equation are then cast into the general parabolic form

$$W_{\zeta\zeta} + A_1 W_\zeta + A_2 W + A_3 + A_4 W_\beta = 0 \tag{28}$$

Here W is the nondimensional dependent variable (e.g., $W = u$ for the streamwise momentum equation or $W = H$, the total enthalpy for the energy equation) and the coefficients A_1, A_2, A_3, and A_4 are functions of W and the Levy-Lees boundary layer variables β, ζ [23]. The finite-difference forms of equations (28) are then solved using a Crank-Nicolson type implicit finite-difference scheme originally employed by Blottner and Lenard [24].

In the present work, a laminar boundary layer is assumed to commence from the front stagnation point of the blade and to continue until the onset of transition which is triggered once the local vorticity Reynolds number (defined as $\text{Re}_\omega = (\delta^2/\nu)(\partial u/\partial y)$) reaches a critical preset value. In this study, a vorticity Reynolds number of 3000 was selected based on the experimental observations of Owen [25] and the exceptionally good agreement between the available experimental data and the numerical results obtained by Anderson and Lewis [23]. The transition model utilized allows for a gradual

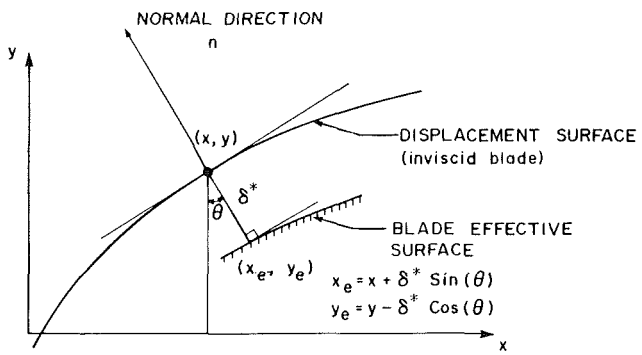

Fig. 6 Sketch illustrating the relative positions of the displacement surface and the resulting effective blade surface

laminar–turbulent transition which takes place over a finite length of the blade's assumed adiabatic surface. The length of the transition region is based on the criteria given by Owen [25]. For the subsequent turbulent flow the Reynolds stresses are related to the velocity and temperature gradients via the use of an eddy viscosity and an eddy thermal conductivity. The eddy viscosity is evaluated using the Cebeci et al. [26] two-layer eddy viscosity model, and the eddy thermal conductivity is determined from the equation defining the turbulent Prandtl number Pr_t ($\mathrm{Pr}_t = 0.9$ for a perfect gas).

Inviscid-Viscous Coupling

To start the solution of the boundary-layer equations, initial guesses of the profiles for the dependent variables (i.e., u and H) are generated. Here, the inviscid pressure distribution (or Mach number) is utilized to compute the conditions at the edge of the boundary layer. It is noteworthy to mention here that this starting approach is equivalent to those methods [15, 27] requiring an initial guess for the displacement thickness δ^* which, for example, could be calculated from the initial streamwise velocity profile. Equations (28) in conjunction with the transformed continuity equation are then solved iteratively, until convergence, at each streamwise station on the displacement surface. The convergence criteria used are based on the percentage change in the value of the streamwise velocity u, and the total enthalpy H at every nodal point across the boundary layer in two successive iterations. The additional requirement that the number of iterations at the new streamwise station be two or more was found to be satisfactory for both laminar and turbulent flows.

Having achieved convergence, we utilize the computed streamwise velocity profiles to calculate the compressible displacement thickness δ^*. This in turn is subtracted from the normal ordinate of the displacement surface to yield the effective blade normal ordinate n_e, equation (27). The effective blade coordinates x_e, y_e are then obtained using the following geometric relations:

$$x_e = x + \delta^* \sin(\theta)$$
$$y_e = y - \delta^* \cos(\theta) \tag{29}$$

Here, θ is the slope of the displacement surface (known from the inviscid design procedure) at the point x, y in question (Fig. 6). Therefore, application of equations (29) at all stations along the displacement surface results in an effective blade geometry similar to those depicted in Figs. 8 and 9. It is noteworthy to mention here that following the solution of equations (29) a check is carried out to search for blade contour crossings (i.e., whether the resulting effective blade has a fishtail). Should these occur, usually in the trailing edge region, the entire inviscid-viscous design procedure is repeated with a slightly modified pressure distribution near the trailing edge. For the inviscid portion of the inviscid-viscous procedure this usually results in a displacement surface with a larger trailing edge gap, hence correcting the crossings problem when viscous effects are subsequently incorporated. A flow chart depicting the numerical inviscid-viscous coupling procedure is given in Fig. 7.

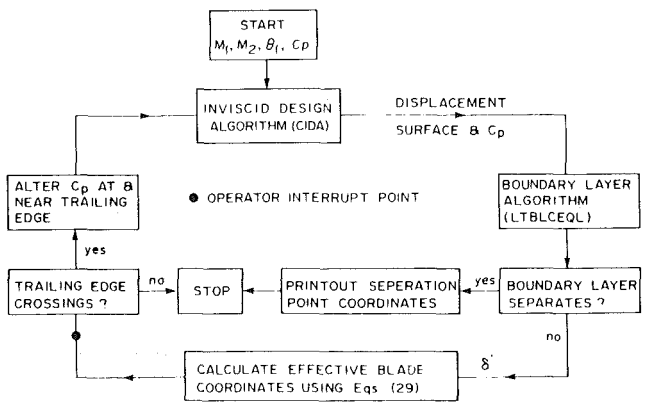

Fig. 7 Flow chart illustrating the present numerical inviscid-viscous coupling procedure

Numerical Results and Discussion

To demonstrate the capabilities of the present numerical viscous-inviscid coupling procedure, two examples representing the design of shock-free compressor-type blades are presented. To perform the inviscid portion of the calculation, a mesh with 150 grid points in the s direction and 60 grid points in the t direction was used. For the viscous portion, the boundary layer calculations were performed on a mesh having 250 grid points in the streamwise direction with grid clustering in the leading edge region of the blade. In the lateral direction, 100 unevenly spaced grids were utilized. This choice permits close spacing of grid points in the region near the wall where variation of fluid and dynamic properties is greatest. The procedure utilized to distribute the grid is identical to that given by Cebeci et al. [26]. In their procedure, the ratio of adjacent intervals is a constant k ($k = 1.04$ for laminar flows, $k = 1.09$ for turbulent flows). These particular values of k proved to yield the best agreement with experimental data for similar flows. It should be emphasized here that the inviscid blade configuration is intentionally required to have a trailing edge vertical gap. This configuration with a gap lends itself to viscous corrections when displacement effects are later incorporated. That is, for an initially closed trailing edge, subtracting the displacement thickness at this location will undoubtedly result in a meaningless effective blade configuration having a fishtail (see Fig. 7). On the other hand, with a vertical gap at the trailing edge, including viscous effects to correct the location of the displacement surface may or may not give an effective blade having a fishtail. If trailing edge crossings oc-

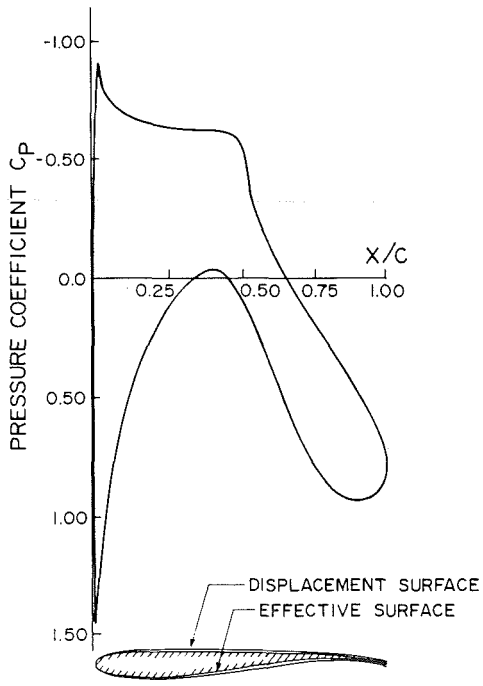

Fig. 8 Pressure distribution and the corresponding inviscid and viscous compressor blade configurations (solidity = 1.0, $Re_c = 3.2 \times 10^6$)

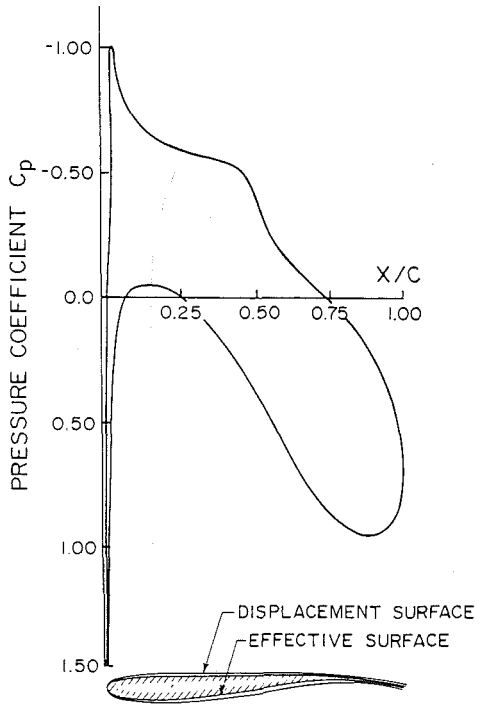

Fig. 9 Pressure distribution and the corresponding inviscid and viscous compressor blade configurations (solidity = 0.85, $Re_c = 3.0 \times 10^6$)

cur, local modification of the input pressure distribution near the trailing edge usually resolves this problem. If blade contour crossings do not occur, an effective blade (see Figs. 8 and 9) with an open trailing edge is obtained. This trailing edge gap can be further reduced to any preset value therefore requiring more interaction iterations. For the two designed compressor blades four interaction iterations were performed requiring 3.6 and 3.82 CPU minutes on an IBM 3081 main frame computer. Numerical results indicate that as the solidity of the cascade increases the CPU time required to perform the inviscid computation also increases.

In the first example, the prescribed Mach numbers at the cascade inlet and outlet are 0.75 and 0.652, respectively. The specified inlet flow deflection angle θ_1 is -35.0 deg and the computed flow deflection angle at the outflow boundary θ_2 is -3.17 deg. Figure 8 illustrates the input pressure distribution required for the design procedure and the resulting shock-free inviscid (displacement surface) and viscous (effective surface) blade configurations. For this example, at a chord Reynolds number of 3.2×10^6, transition to turbulence in the boundary layer occurred at approximately 15 percent chord on the suction surface and at about 10 percent chord on the pressure surface.

The second example is that of a shock-free compressor blade (solidity = 0.85) with a cusped trailing edge. The inflow Mach number M_1, outflow Mach number M_2, and flow deflection angle θ_1 are 0.75, 0.60, and -30.0 deg, respectively. The converged inverse solution results in an outflow turning angle $\theta_2 = -7.82$ deg. The input pressure distribution required for the design procedure and the resulting shock-free inviscid and viscous blade configurations for this example are depicted in Fig. 9. At a chord Reynolds number of 3.0×10^6 transition to turbulence occurred at 19 percent chord and 14 percent chord on the suction and pressure surfaces, respectively, of the resulting effective blade.

Similar to the transonic shock-free airfoil design problem, our numerical results indicate that only one blade configuration exists for a given pressure distribution [28]. In this numerical procedure, Lighthill's [29] first constraint on the existence of a solution to the inviscid inverse problem is implicitly satisfied since we do allow for slight variations in the prescribed input pressure distribution. These variations, of course, result in slightly different shock-free blade designs.

Conclusion

A viscous-inviscid coupling procedure has been developed for the design of two shock-free compressor-type blades. The procedure in its present form has some limitations, most notably in its applicability to shocked flows with boundary layer separation. For severe flow situations, such as massive boundary layer separation, a Navier–Stokes approach to model viscous effects within the numerical calculations would undoubtedly be required. Further study is also needed to incorporate wake and wake curvature effects in the overall viscous-inviscid interaction iteration. Comparisons should now be made with experimental data to assess the quantitative accuracy of this iteration procedure. In spite of the present emphasis on computational design techniques, shock-free blade design for turbomachinery applications remains somewhat of an art. Therefore, it falls upon the designer of such blades to make the necessary changes in the input design parameters to obtain a practical blade configuration.

References

1 Shapiro, A. H., *The Dynamics and Thermodynamics of Compressible Fluid Flow*, Vol. II, The Ronald Press Company, New York, 1954.

2 Liepmann, H. W., and Roshko, A., *Elements of Gas Dynamics*, Wiley, New York, 1957.

3 Oswatitsch, K., and Zierep, J., "Das Problem des Senkrechten Stosses an einer Gerkummten Wand," *Zeitschrift für angewandte Mathematik und Mechanik*, Vol. 40, 1960, pp. 143–152.

4 Morawetz, C. S., "On the Non-existence of Continuous Transonic Flows Past Profiles, I," *Communications on Pure Applied Mathematics*, Vol. 9, 1956, pp. 45–68.

5 Morawetz, C. S., "On the Non-existence of Continuous Transonic Flows Past Profiles, II," *Communications on Pure Applied Mathematics*, Vol. 10, 1957, pp. 107–131.

6 Morawetz, C. S., "On the Non-existence of Continuous Transonic Flows Past Profiles, III," *Communications on Pure Applied Mathematics*, Vol. 11, 1958, pp. 129–144.

7 Dulikravich, G. S., and Sobieczky, H., "CAS22—Fortran Program for Fast Design and Analysis of Shock-Free Airfoil Cascades," NASA CR3507, 1982.

8 Sobieczky, H., and Dulikravich, G. S., "A Computational Design Method for Transonic Turbomachinery Cascades," ASME Paper No. 82-GT-117, April 1982.

9 Green, J. E., "Some Aspects of Viscous-Inviscid Interaction at Transonic Speeds and Their Dependence on Reynolds Number," AGARD-CP-83, 1971.

10 Bavitz, P. C., "An Analysis Method for Two-Dimensional Transonic Viscous Flow," NASA TND-7718, 1975.

11 Melnik, R. E., Mead, H. R., and Jameson, A., "A Multi-grid Method for the Computation of Viscid/Inviscid Interactions on Airfoils," AIAA 21st Aerospace Sciences Meeting, Jan. 1983, AIAA Paper No. 83-0234.

12 Calvert, W. J., "An Inviscid-Viscous Interaction Treatment to Predict the Blade-to-Blade Performance of Axial Compressors With Leading Edge Normal Shock Waves," ASME Paper No. 82-GT-135, Apr. 1982.

13 Korn, D., "Numerical Design of Transonic Cascades," Courant Institute of Mathematical Sciences, ERDA Research and Development Report C00-3077-72, Jan. 1975.

14 Sobieczky, H., "Transonic Fluid Dynamics—Lecture Notes," The University of Arizona, Tucson, AZ, Report No. TFD 77-01, Oct. 1977.

15 Dulikravich, G. S., and Sobieczky, H., "Design of Shock-Free Compressor Cascades Including Viscous Boundary Layer Effects," ASME Paper No. 83-GT-134, March 1983.

16 Hassan, A. A., and Dulikravich, G. S., "A Hodograph-Based Method for the Design of Shock-Free Cascades," AIAA Paper No. 87-0606, Jan. 1987.

17 Volpe, G., and Melnik, R. E., "The Role of Constraints in the Inverse Design Problem for Transonic Airfoils," AIAA Paper No. 81-1233, June 1981.

18 Lighthill, M. J., "On the Hodograph Transformation for High Speed Flow," *Quarterly Journal of Mechanics and Applied Mathematics*, Vol. 1, 1948, pp. 442–450.

19 Thompson, J. F., Thames, F. C., and Mastin, C. W., "Automatic Numerical Generation of Body Fitted Curvilinear Coordinate Systems for Fields Containing Any Number of Arbitrary Two-Dimensional Bodies," *J. of Comp. Physics*, Vol. 15, 1974, pp. 299–319.

20 Ives, D. C., and Liutermoza, J. F., "Analysis of Transonic Cascade Flow Using Conformal Mapping and Relaxation Techniques," AIAA Paper No. 76-370, July 1976.

21 Hassan, A. A., "Subcritical and Supercritical Airfoils for Given Pressure Distributions," Ph.D. Dissertation, The University of Arizona, Tucson, AZ, Aug. 1981.

22 Miner, E. W., Anderson, E. C., and Lewis, C. H., "A Computer Program for Two-Dimensional and Axisymmetric Nonreacting Perfect Gas and Equilibrium Chemically Reacting Laminar, Transitional and/or Turbulent Boundary Layer Flows," Virginia Polytechnic Institute and State University, College of Engineering Report No. VPI-E-71-8, May 1971.

23 Anderson, E. C., and Lewis, C. H., "Laminar or Turbulent Boundary-Layer Flows of Perfect Gases or Reacting Gas Mixtures in Chemical Equilibrium," NASA CR-1893, Oct. 1971.

24 Blottner, F. G., and Lenard, M., "Finite Rate Plasma Generation in the Laminar Air Boundary Layer of Slender Reentry Bodies," *Transactions of the 8th Symposium on Ballistic Missile and Space Technology*, San Diego, CA, Oct. 1963, pp. 3–33.

25 Owen, F. K., "Transition Experiments on a Flat Plate at Subsonic and Supersonic Speeds," *AIAA Journal*, Vol. 8, No. 3, 1970.

26 Cebeci, T., Smith, A. M. O., and Mosinskis, G., "Calculation of Compressible Adiabatic Turbulent Boundary Layers," AIAA Paper No. 69-687, June 1969.

27 Collyer, M. R., and Lock, R. C., "Prediction of Viscous Effects in Steady Transonic Flow Past an Aerofoil," *Aeronautical Quarterly*, Vol. 30, 1979, p. 485.

28 Hassan, A. A., Sobieczky, H., and Seebass, A. R., "Transonic Airfoils With a Given Pressure Distribution," AIAA Paper No. 81-1235, June 1981.

29 Lighthill, M. J., "A New Method of Two-Dimensional Aerodynamic Design," Aeronautical Research Council, London, R&M 2112, Apr. 1945.

Numerical Computation of Nonisentropic Potential Equations for Transonic Cascade Flows

J. Z. Xu

J. Y. Du

W. Y. Ni

Institute of Engineering Thermophysics,
Academy Sinica,
Beijing, People's Republic of China

Based on the analysis of the momentum equations and the nonisentropic flow, an "isentropic density," which is computed according to the isentropic relation and is dependent on the temperature only, is separated from the density. The entropy increase across the shock may be directly calculated from the momentum equations in the divergence form. Iterating with the classical potential equation may solve the nonisentropic transonic flowfield conveniently. It is seen from the calculations of transonic cascade flow on the surface of revolution that the shock in the nonisentropic calculation is weaker and is located farther upstream compared to the classical potential solution, and is in agreement with the experimental results. In the calculations, the effect of entropy increase on both the Kutta condition and the outlet boundary conditions has been taken into consideration.

Introduction

In recent years, there has been remarkable progress in solving both external and internal transonic flow fields. Among a lot of methods, the potential formulation is one of the most advanced approaches.

The potential calculation has its advantages and has been used in analysis and design problems. There are, however, severe limitations in its applicable range and calculation accuracy because the flow is assumed to be irrotational and isentropic.

To remove the isentropic assumption, a nonisentropic potential formulation was suggested and it was demonstrated that its results are closer to the solution of Euler equations (Klopfer and Nixon, 1983). For the sake of calculating the entropy increase across a shock, a Poisson equation for the pressure was obtained from the momentum equations and was solved numerically (Hafez et al., 1984). At the same time it was pointed out by Osher et al. (1985) that the nonisentropic potential formulation produces a unique solution and the nonuniqueness problem of solution arising in the isentropic potential equation (Steinhoff and Jameson, 1982) may be prevented.

It is the purpose of this paper to develop a nonisentropic potential model within the scope of irrotational assumption. The so-called "isentropic density," which is dependent only on temperature, is separated from the density, and the entropy increase through the shock may be directly calculated from the momentum equations. It is obvious that the entropy increase in the stream function calculations may also be calculated based on the method presented in this paper.

Contributed by the Gas Turbine Division of THE AMERICAN SOCIETY OF MECHANICAL ENGINEERS and presented at the 32nd International Gas Turbine Conference and Exhibit, Anaheim, California, May 31-June 4, 1987. Manuscript received at ASME Headquarters February 17, 1987. Paper No. 87-GT-159.

Nonisentropic Potential Model

For the irrotational motion of a nonviscous gas, a potential Φ may be defined

$$\nabla\Phi=\mathbf{v} \tag{1}$$

Substituting equation (1) into the continuity equation, a second-order partial differential equation of Φ may be obtained. Introducing artificial density and using a proper difference scheme, the equation may be solved numerically under certain boundary conditions. In the calculation procedure, density is computed from the energy equation and isentropic relation. This is the isentropic or classical potential method to solve transonic flow.

For the nonisentropic potential formulation, the variation of density is related to the change of entropy. To calculate entropy increase after the shock, it is necessary to solve the momentum equations. Considering the characteristic features of these equations and the nonisentropic flow, an "isentropic density" ρ_i computed in the isentropic condition is extracted from the nonisentropic density

$$\begin{aligned}\rho&=\rho_0\,(T/T_0)^{\frac{1}{k-1}}\exp\,[-(s-s_0)/R]\\&=\rho_i\exp\,(-\tilde{s}/R)\end{aligned} \tag{2}$$

where $\tilde{s}$ denotes the entropy variation and ρ_i is dependent on the temperature only.

From the equation of state and equation (2), the following relation may be derived:

$$\begin{aligned}\frac{1}{\rho}\nabla p&=R\nabla T+RT\nabla(\ln\rho_i)-T\nabla\tilde{s}\\&=\frac{kR}{k-1}\nabla T-T\nabla\tilde{s}\end{aligned} \tag{3}$$

It is seen that when equation (3) is substituted into the

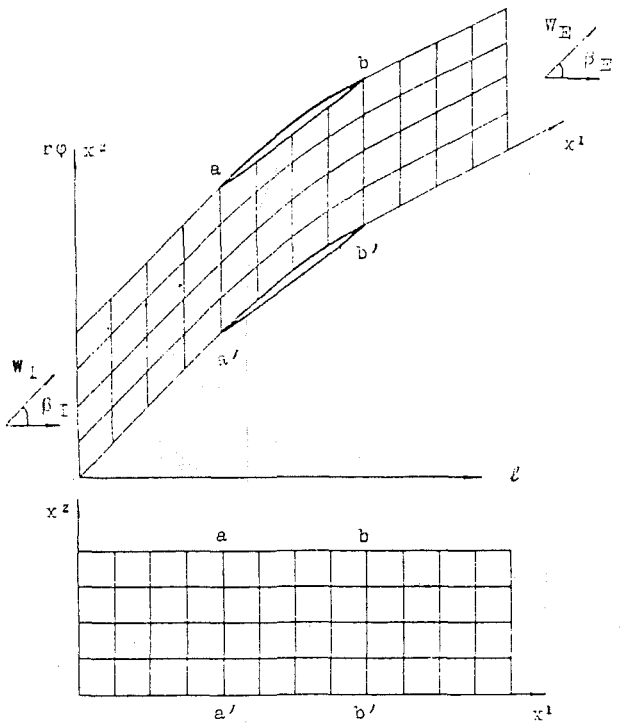

Fig. 1 Coordinates on physical plane and computational plane

momentum equations, the temperature T and the entropy increase $\tilde{s}$ appear in the equations, instead of pressure p and density ρ, which are directly influenced by entropy. So it is possible to obtain the entropy increase from the momentum equations directly and then to compute other nonisentropic variables. Here the distinguishing feature of the momentum equations has been shown clearly.

The equation used to calculate the change of entropy may be one of the momentum equations or a combination of the momentum equations. In order to ensure the accuracy and reliability of the computational results, it is better to differentiate each momentum equation and add them to form a second-order partial differential equation of $\tilde{s}$.

It is noted that the nonisentropic potential model suggested in this paper is more strict theoretically and very simple numerically. Compared with the classical potential calculation, this model only adds the computation of $\tilde{s}$ and the iteration between $\tilde{s}$ and Φ, which are easy to perform. The entropy increase after the shock is captured automatically during the process of solving the whole flow field. It is expected that the calculation results of this nonisentropic potential should be close to the Euler solution. All these will extend the range of validity of the potential formulation.

Taking the transonic cascade flow on a surface of revolution in a turbomachinery as an example, the computation of the present nonisentropic potential model will be discussed further. For the numerical solution of external and other internal transonic flows, the method suggested in this paper is also applicable.

Transonic Nonisentropic Potential Equations on the Surface of Revolution and Their Boundary Conditions

When the flow is assumed to be irrotational in the absolute motion, the governing equations for the steady relative flow of an inviscid gas in a cascade on the surface of revolution are

$$\tilde{\nabla} \cdot (\tau \rho \mathbf{w}) = 0 \tag{4}$$

$$\nabla \times \mathbf{v} = 0 \tag{5}$$

$$\tilde{d}I/\tilde{d}t = 0 \tag{6}$$

$$Tds = dh - dp/\rho \tag{7}$$

From equation (5) a potential function Φ may be defined as equation (1). With the aid of nonorthogonal curvilinear coordinates (Fig. 1), in which x^1 is chosen as pseudostreamlines and is fixed and x^3 is perpendicular to the surface, equation (4) becomes the potential equation in a form of divergence (Zhang and Wu, 1984; Xu and Ni, 1985):

$$[D_1\rho(A_1\Phi_{x^1} + A_2\Phi_{x^2} + A_3)]_{x^1} + [D_2\rho(B_1\Phi_{x^1} + B_2\Phi_{x^2} + B_3)]_{x^2} = 0 \tag{8}$$

where

$$\begin{aligned} D_1 &= \tau\sqrt{a_{22}}\sin\theta_{12} \\ D_2 &= \tau\sqrt{a_{11}}\sin\theta_{12} \\ A_1 &= 1/(\sqrt{a_{11}}\sin^2\theta_{12}) \\ A_2 &= -\cos\theta_{12}/(\sqrt{a_{22}}\sin^2\theta_{12}) \\ A_3 &= -U^1 \\ B_1 &= -A_1\cos\theta_{12} \\ B_2 &= -A_2/\cos\theta_{12} \\ B_3 &= -U^2 \end{aligned}$$

The density ρ in equation (8) may be calculated from equations (6) and (7)

$$\rho = \rho_I \left[1 - \frac{(w)^2 - (U)^2}{2I}\right]^{\frac{1}{k-1}} \exp(-\tilde{s}/R) \tag{9}$$

The corresponding boundary conditions for equation (8) are:

Nomenclature

a_{ij} = metric tensor elements of two-dimensional x^i coordinate system
h = enthalpy of gas per unit mass
I = relative stagnation rothalpy of gas per unit mass
L = blade chord in axial direction
l = generator of stream surface of revolution
M = relative Mach number
p = pressure of gas
R = gas constant
r = radius
s = entropy of gas per unit mass
$\tilde{s}$ = change of entropy of gas per unit mass
T = absolute temperature of gas
$\mathbf{v}$ = absolute velocity of gas
$\mathbf{w}$ = relative velocity of gas
x^i = nonorthogonal curvilinear coordinates
β = relative flow angle
θ_{12} = angle between x^1 and x^2 lines
κ = ratio of specific heats of gas
μ = artificial viscosity coefficient
ρ = density of gas
$\tilde{\rho}$ = artificial density
σ = relaxation factor
τ = normal thickness of S_1 stream filament
Φ = potential function
ω = angular velocity of rotor

Superscripts

i = contravariant component of vector
n = number of iterations

Subscripts

0 = stagnation state
I = reference state where $h = I$
i = covariant component of vector

1 At the inlet boundary, relative stagnation temperature, stagnation pressure, flow angle, and mass flow are specified.

2 For the inlet region of cascade, the periodicity condition is fulfilled.

3 Along the cascade surfaces, the condition of flow tangency is satisfied.

4 For the outlet region of cascade, the influence of the entropy increase on the Kutta condition should be considered. On both sides of the wake pressures may still be assumed equal, though the velocities may be different. So the periodicity condition in this case can be expressed by the following equation (Xu and Ni, 1985):

$$\Delta\Phi_i = \Delta\Phi_{i+1} - \sqrt{a_{11}}\ \Delta w_i / g$$

where $\Delta w_i = w_i^+ - w_i^-$, $\Delta\Phi_i = \Phi_i^+ - \Phi_i^-$, and g is a coefficient.

5 At the outlet boundary, the pressure ratio is given. The other quantities may be calculated as in the case of an isentropic flow. But it is stressed that the stagnation pressure and density in the present condition have changed. The exit flow angles are obtained from the periodic average of entropy increase on all streamlines and the outlet velocities at all grids are determined one by one according to the different entropy values along each streamline.

For the calculation of entropy variation, the following momentum equations are employed:

$$\frac{1}{\sqrt{a_{11}}}\left[(\tau\rho w^1 w^1)_{x^1} + \cos\theta_{12}\ (\tau\rho w^1 w^2)_{x^1}\right]$$

$$+\frac{1}{\sqrt{a_{22}}}\left[(\tau\rho w^1 w^2)_{x^2} + \cos\theta_{12}\ (\tau\rho w^2 w^2)_{x^2}\right]$$

$$+\frac{\tau}{\sqrt{a_{11}}}p_{x^1} = \tau\rho\left\{\frac{(w^2)^2-(w^1)^2}{\sqrt{a_{11}}}(\ln\sqrt{a_{22}})_{x^1}\right.$$

$$-\frac{2w^2(w^1+w^2\cos\theta_{12})}{\sqrt{a_{22}}}(\ln\sqrt{a_{11}})_{x^2} - \frac{(w^2)^2}{\sqrt{a_{22}}}(\cos\theta_{12})_{x^2}$$

$$-(w^1+w^2\cos\theta_{12})\left[\frac{w^1}{\sqrt{a_{11}}}(\ln\sin\theta_{12})_{x^1}\right.$$

$$\left.\left.+\frac{w^2}{\sqrt{a_{22}}}(\ln\sin\theta_{12})_{x^2}\right] + 2w^2\,\omega\sin\theta_{12} + |\omega|^2\frac{r_1}{\sqrt{a_{11}}}\right\}$$

$$\frac{1}{\sqrt{a_{11}}}\left[\cos\theta_{12}\ (\tau\rho w^1 w^1)_{x^1} + (\tau\rho w^1 w^2)_{x^1}\right]$$

$$+\frac{1}{\sqrt{a_{22}}}\left[\cos\theta_{12}\ (\tau\rho w^1 w^2)_{x^2} + (\tau\rho w^2 w^2)_{x^2}\right] + \frac{\tau}{\sqrt{a_{22}}}p_{x^2}$$

$$= \tau\rho\left\{-\frac{2w^1(w^1\cos\theta_{12}+w^2)}{\sqrt{a_{11}}}(\ln\sqrt{a_{22}})_{x^2}\right.$$

$$+\frac{(w^1)^2-(w^2)^2}{\sqrt{a_{22}}}(\ln\sqrt{a_{11}})_{x^2} - \frac{(w^1)^2}{\sqrt{a_{22}}}(\cos\theta_{12})_{x^1}$$

$$-(w^1\cos\theta_{12}+w^2)\left[\frac{w^1}{\sqrt{a_{11}}}(\ln\sin\theta_{12})_{x^1}\right.$$

$$\left.\left.+\frac{w^2}{\sqrt{a_{22}}}(\ln\sin\theta_{12})_{x^2}\right] - 2w^1\omega\sin\theta_{12} - |\omega|^2\frac{r_2}{\sqrt{a_{22}}}\right\}$$

From these equations a Poisson equation for $\tilde{s}$ may be derived

$$\tau\rho\ (\tilde{s}_{x^1x^1} + \tilde{s}_{x^2x^2}) + (\tau\rho)_{x^1}\tilde{s}_{x^1} + (\tau\rho)_{x^2}\tilde{s}_{x^2}$$

$$= \frac{kR}{k-1}\left[(\tau\rho T_{x^1})_{x^1} + (\tau\rho T_{x^2})_{x^2}\right]$$

$$+\left\{(\tau\rho w^1 w^1)_{x^1} + \cos\theta_{12}\ (\tau\rho w^1 w^2)_{x^1} + \sqrt{\frac{a_{22}}{a_{11}}}\right.$$

$$\left.\left[(\tau\rho w^1 w^2)_{x^2} + \cos\theta_{12}\ (\tau\rho w^2 w^2)_{x^2}\right]\right\}_{x^1}$$

$$+\left\{\sqrt{\frac{a_{22}}{a_{11}}}\left[\cos\theta_{12}\ (\tau\rho w^1 w^1)_{x^1} + (\tau\rho w^1 w^2)_{x^1}\right]\right.$$

$$\left.+\cos\theta_{12}\ (\tau\rho w^1 w^2)_{x^2} + (\tau\rho w^2 w^2)_{x^2}\right\}_{x^2}$$

$$-(\tau\rho C_1)_{x^1} - (\tau\rho C_2)_{x^2} \qquad (10)$$

where

$$C_1 = [(w^2)^2 - (w^1)^2]\ (\ln\sqrt{a_{22}})_{x^1} - 2w^2\ (w^1 + w^2\cos\theta_{12})$$

$$\sqrt{\frac{a_{11}}{a_{22}}}\ (\ln\sqrt{a_{11}})_{x^2} - \sqrt{\frac{a_{11}}{a_{22}}}\ (w^2)^2\ (\cos\theta_{12})_{x^2}$$

$$-(w^1 + w^2\cos\theta_{12})\sqrt{a_{11}}\left[\frac{w^1}{\sqrt{a_{11}}}(\ln\sin\theta_{12})_{x^1}\right.$$

$$\left.+\frac{w^2}{\sqrt{a_{22}}}(\ln\sin\theta_{12})_{x^2}\right] + 2w^2\omega\sqrt{a_{11}}\sin\theta_{12} + |\omega|^2 r_1$$

$$C_2 = -2w^1(w^1\cos\theta_{12} + w^2)\sqrt{\frac{a_{22}}{a_{11}}}\ (\ln\sqrt{a_{22}})_{x^1}$$

$$-[(w^1)^2 - (w^2)^2]\ (\ln\sqrt{a_{11}})_{x^2} - \sqrt{\frac{a_{22}}{a_{11}}}\ (w^1)^2\ (\cos\theta_{12})_{x^1}$$

$$-(w^1\cos\theta_{12} + w^2)\sqrt{a_{22}}\left[\frac{w^1}{\sqrt{a_{11}}}(\ln\sin\theta_{12})_{x^1}\right.$$

$$\left.+\frac{w^2}{\sqrt{a_{22}}}(\ln\sin\theta_{12})_{x^2}\right] - 2w^1\omega\sqrt{a_{22}}\sin\theta_{12} + |\omega|^2 r_2$$

As the boundary conditions of this equation $\tilde{s}$ is taken as zero at the inlet boundary and $\tilde{s}$ is assumed to satisfy the periodicity condition along the inlet region of cascade. On the cascade surfaces, integrating equation (10) by parts will give a relation between $\tilde{s}_{x^1}$ and $\tilde{s}_{x^2}$, which is similar to the way given by Hafez et al. (1984). For the outlet region, $\tilde{s}$ is regarded as constant along a streamline.

Numerical Method

In order to get a stable and convergent solution of the mixed type equation (8) in the transonic flow field, the artificial density in the following form is used (Hafez et al., 1978):

$$\tilde{\rho}_{i,j} = \rho_{i,j} - \begin{cases} \mu_{i,j}\ (\rho_{i,j} - \rho_{i-1,j}) \\ \mu_{i,j}\ (\rho_{i+1,j} - \rho_{i,j}) \end{cases}$$

where the artificial viscosity $\mu_{i,j} = \text{Max}\ [0,\ \bar{C}\ (M_{i,j} - 1)]$ and $\bar{C}$ is a parameter governing the strength of the artificial viscosity terms. In the present study the range of $\bar{C}$ is from 0.1 to 0.6.

The discrete algebraic equation (8) with the artificial density is solved by means of an AF2 iteration scheme (Holst, 1978). The formulas are

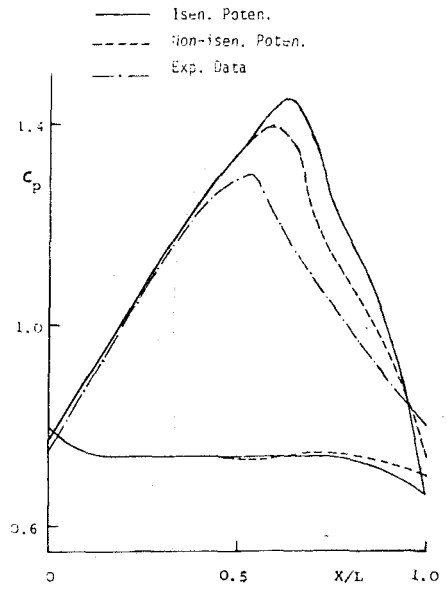

Fig. 2 Comparison of pressure coefficient on DCA 2-8-10 cascade surfaces ($M_I = 1.03$, $\beta_I = 61.8$ deg, $P_E/P_I = 1.29$)

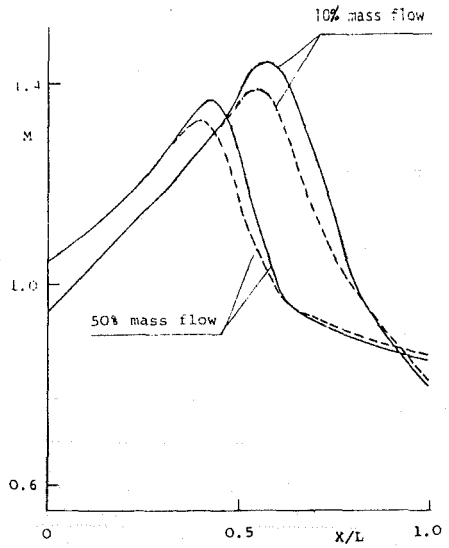

Fig. 3 Variation of Mach number for DCA 2-8-10 ($M_I = 1.03$)

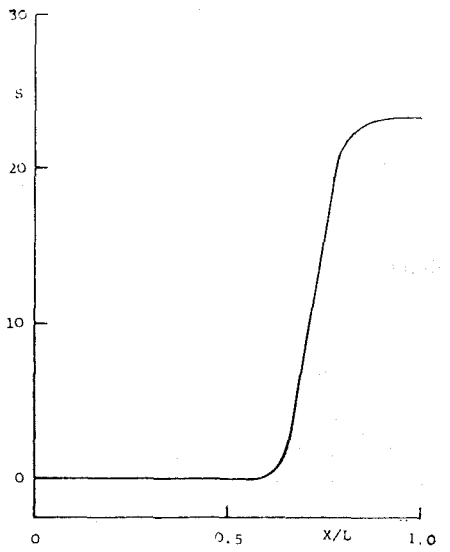

Fig. 4 Distribution of entropy on suction surface for DCA 2-8-10 ($M_I = 1.03$)

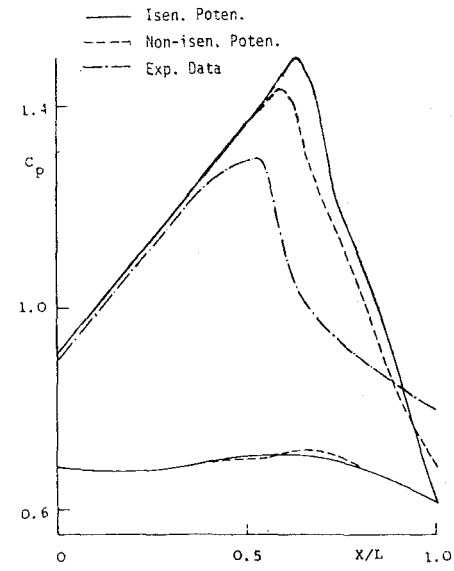

Fig. 5 Comparison of pressure coefficient on DCA 2-8-10 cascade surfaces ($M_I = 1.11$, $\beta_I = 62.5$ deg, $P_E/P_I = 1.35$)

$$[\alpha_k - \vec{\delta}_{x1}\,(D_1\rho A_1)^n_{i-1/2,j}]\,f^n_{i,j} = \alpha\sigma\, L\Phi^n_{i,j}$$

$$[\alpha_k \vec{\delta}_{x1} - \vec{\delta}_{x2}(D_2\rho B_2)^n_{i,j+1/2}\vec{\delta}_{x2}]C^n_{i,j} = f^n_{i,j}$$

where $C^n_{i,j} = \Phi^{n+1}_{i,j} - \Phi^n_{i,j}$, $f_{i,j}$ is an intermediate variable, $L\Phi_{i,j}$ is the residual of the difference equation, σ is a relaxation factor, and α is a sequence consisting of some constants, which may be expressed as

$$\alpha_k = \alpha_h\,(\alpha_1/\alpha_h)^{\frac{k-1}{m-1}} \quad (k = 1,\ldots,m)$$

In this paper the values of these constants are $\alpha_1 = 0.7 \sim 1.5$, $\alpha_h = 7 \sim 13$, and $m = 9$ separately.

The calculation procedure of the whole transonic nonisentropic potential equations consists of iterations between the solutions of equations (8), (9), and (10). At the beginning of calculation, an initial distribution of Φ may be calculated based on an estimated distribution of the velocity. Density ρ may then be computed by use of equation (9) assuming $\tilde{s}$ to be zero. Next equation (8) is solved with the line relaxation method to yield a new field of Φ and equation (10) is also solved by the line relaxation method to get a distribution of $\tilde{s}$. At this point, an improved density ρ may be obtained from equation (9), containing the influence of entropy. With this distribution of ρ and other gas variables, a new calculation cycle begins and this procedure will continue until convergence is reached. The convergence is checked when the maximum relative change of the relative velocities at all grids in the whole flow field is less than a prescribed precision, say 1×10^{-4}. It is expected that compared with the classical potential calculation, the convergence of the present nonisentropic potential calculation will be a little bit better due to the introduction of entropy, despite the fact that a calculation of entropy from the momentum equations is added.

Numerical Results and Discussion

A number of transonic cascades have been computed to

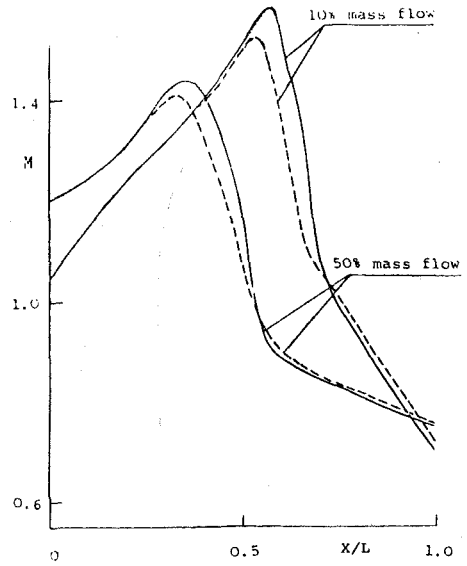

Fig. 6 Variation of Mach number for DCA 2-8-10 ($M_I = 1.11$)

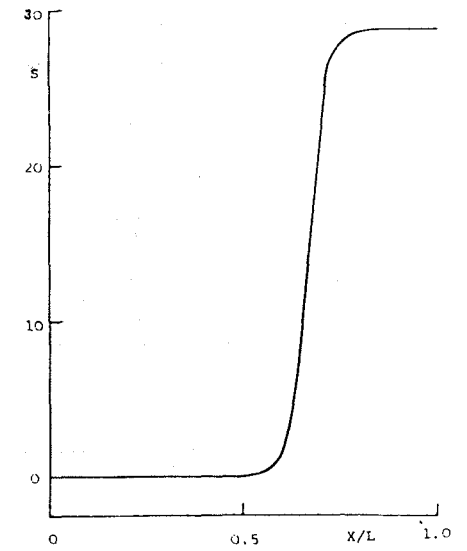

Fig. 7 Distribution of entropy on suction surface for DCA 2-8-10 ($M_I = 1.11$)

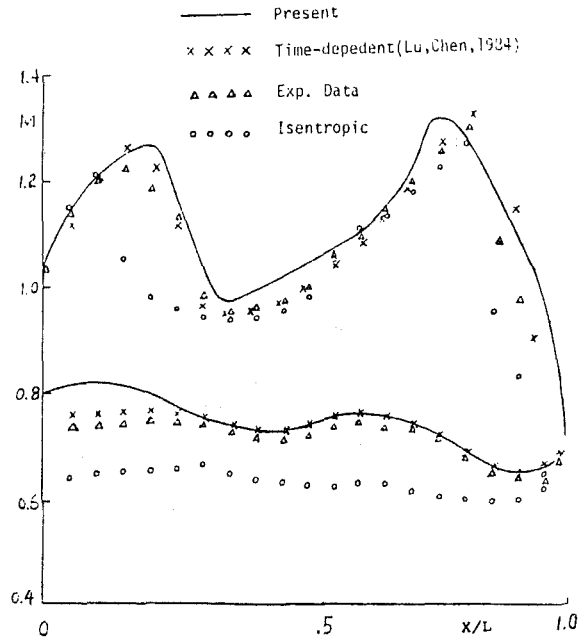

Fig. 8 Comparison of Mach number contours for $T_1 - (18A6I4b)08$ cascade

evaluate the validity of the present method. The numerical results for a DCA 2-8-10 cascade under two flow conditions and a T_1 cascade will be given below.

1 DCA 2-8-10 Cascade. The geometries of the cascade and the test results are given by Starken (1971). In the calculations a 50 × 14 grid is used.

(1) $M_I = 1.03$, $\beta_I = 61.8$ deg, $P_E/P_I = 1.29$. It is seen from the distribution of the pressure coefficient in Fig. 2 that the shock computed from the nonisentropic potential equations is positioned one mesh upstream of the isentropic shock, and the value of the pressure coefficient is less than the latter in the shock region and is closer to the experimental data. The variation of Mach number on the two streamlines (Fig. 3) shows that the location of the maximum Mach number moves one mesh upstream and its value decreases, although Mach number after the shock is almost the same or even increases slightly. So the shock is weaker and the pressure coefficient decreases, and these are in agreement with the experimental results shown in Fig. 2.

In Fig. 4, the variation of the entropy on the cascade suction surface is plotted. Its final value is greater than 23 J/K kg.

(2) $M_I = 1.11$, $\beta_I = 62.5$ deg, $P_E/P_I = 1.35$. As Mach number increases, the difference of the pressure coefficient between the nonisentropic potential and isentropic potential calculations also increases and the shock is placed 2 meshes upstream compared to the isentropic solution (Fig. 5). The curve of the pressure coefficient by the present method is closer to the experimental results, but the difference between the computed and the experimental results behind the shock in this condition is larger than in the preceding case, which may be attributed to the stronger interaction between the shock and the boundary layer.

The distributions of Mach number and the entropy on the suction surface (Figs. 6 and 7) are all similar to the former. The only change in the present case is the enhance of the shock and the increase in Mach number ahead of the shock. The entropy across the shock amounts to about 30 J/K kg. Unlike the situation on the suction surface, the position of the shock on other streamlines is shifted only one mesh forward, which may be related to the use of coarser meshes.

2 $T_1 - (18A_6I_{4b})08$ Cascade. The cascade shape is described by Savage et al. (1955). The inlet flow conditions: $M_1 = 0.832$ and $\beta_1 = 30$ deg and the outlet condition $\beta_2 = 11.6$ deg are given. The Mach number contours are shown in Fig. 8 and compared with the isentropic potential calculation, the time-dependent solution (Lu and Chen, 1984), and the experimental data. In this complicated case it is noted that the present model gives a result close to the Euler solution and agreed with the test data although this result is quite different from that of the isentropic calculation.

In order to demonstrate whether the Rankine–Hugoniot condition is satisfied in the present model, consider a normal shock in a stationary cascade first. The entropy variation is calculated from the momentum equation, which simplifies to

$$(\rho u^2)_x + P_x = 0$$

Besides, the mass and energy are conserved in the potential formulation

$$(\rho u)_x = 0$$

$$\left(C_p T + \frac{u^2}{2}\right)_x = (h_0)_x = 0$$

where x is normal to the shock.

From these three equations it is easy to obtain the Rankine–Hugoniot condition and the Prandtl relation

$$M_1^* M_2^* = 1$$

In the two-dimensional case to derive the Rankine–Hugoniot condition, the continuity equation, the energy equation, and the momentum equations along two coordinates need to be used. In this method only the continuity equation, the energy equation, one or a combination of the momentum equations, and the equation of irrotationality are considered, and the Rankine–Hugoniot condition is not satisfied in a rigorous sense. But compared to the classical potential formulation in which neither momentum equation is included, as shown by Klopfer and Nixon (1983), this model may give a result close to the Euler solution meeting the Rankine–Hugoniot condition and is much simpler than the latter in computation.

In the calculations of these examples it is found that the iteration numbers of the nonisentropic potential are 180–190 times, while those of the classical one are 185–200 times for achieving the convergence precision. The entropy is less frequently evaluated (every 10 or 15 iterations) due to its relatively small change in the computation and hence the whole computing time increases very slightly.

Concluding Remarks

In order to calculate the entropy increase across the shock, the corresponding partial differential equations and the boundary conditions are established by extracting the entropy variation from the density. The nonisentropic potential model presented in this paper is more rigorous in theory and very effective in computation. It would extend the range of application of the potential formulation.

The numerical results of the transonic cascade flows on the surface of revolution show that since the shocks are not isentropic, they are placed one or two meshes farther upstream compared to the isentropic solution. Mach numbers before the shocks decrease and those after the shocks increase slightly, so the nonisentropic shocks are weaker. The agreement with the experimental data is improved. It is also seen that the results of this method are close to Euler solution.

From a viewpoint of computation, the convergence of the present nonisentropic potential calculation is a little bit better than the isentropic one and the increase in computing time due to calculating the entropy is small.

Acknowledgments

This project was supported by the Scientific Foundation of the Chinese Academy of Sciences and by the Gas Turbine Establishment of the People's Republic of China.

References

Hafez, M. M., Murman, E. M., and South, J. C., 1978, "Artificial Compressibility Methods for Numerical Solution of Transonic Full Potential Equation," AIAA Paper No. 78-1148.

Hafez, M., Habashi, W., and Kotiuga, P., 1984, "Conservative Calculations of Non-isentropic Transonic Flows," AIAA Paper No. 84-1182.

Holst, T.L., 1978, "An Implicit Algorithm for the Conservative Transonic Full Potential Equation Using an Arbitrary Mesh," AIAA Paper No. 78-1113.

Klopfer, G. H., and Nixon, D., 1983, "Non-isentropic Potential Formulation for Transonic Flows," AIAA Paper No. 83-0375.

Osher, S., Hafez, M., and Whitlow, W., Jr., 1985, "Entropy Condition Satisfying Approximations for Full Potential Equation of Transonic Flow," *Mathematics of Computation*, Vol. 44, No. 169.

Savage, M., Felix, R., and Enery, J., 1955, "High Speed Cascade Tests of a Blade Section Designed for Typical Hub Conditions of High-Flow Transonic Rotors," NACA RM L55F07.

Starken, H., 1971, "Untersuchung der Strömung in Ebenen Uberschall-Verzogerung Gittern," DLR FB 71-99, DFVLR, Institut für Luftstrahlantriebe.

Steinhoff, J., and Jameson, A., 1982, "Multiple Solutions of the Transonic Potential Flow Equation," *AIAA J.*, Vol. 20, No. 11.

Xu, J. Z., and Ni, W. Y., 1985, "The Solution of Transonic Cascade Flow by the Combined Shock-Capturing and Fitting Method," to be published.

Zhang, J. L., and Wu, C. H., 1984, "A Fast Algorithm for Solving the Conservative Transonic S_1 Full-Potential Equation Employing Non-orthogonal Curvilinear Coordinates and Non-orthogonal Velocity Components," *Computational Methods in Turbomachinery*, IMechE, London.

Inter and Intrablade Row Laser Velocimetry Studies of Gas Turbine Compressor Flows

M. C. Williams
Project Engineer,
Pratt & Whitney Engineering Division,
East Hartford, CT 06108

Characterization of the aerodynamics of the flows within gas turbine intrablade passages requires the development of sensitive laser-Doppler velocimeters, a data acquisition system capable of efficiently and accurately handling substantial quantities of data, and appropriate methods of posttest data analysis and display to maximize the value of the recorded data. Pratt & Whitney developed a confocal LDV and data acquisition system that were first employed in the mid-1970s for gas turbine intrablade fan studies. Experience gained through use of the instruments in several aerodynamic studies has provided the basis for the development of a second generation system. The performance of the recently enhanced instrument configured as a single-component LDV has been demonstrated by a NASA-sponsored fan study in which approximately 200 million valid velocity signals were rapidly acquired. The high resolution and data rates achieved permitted detailed mappings of the flow at a variety of conditions and locations. Following this successful study, a second NASA-sponsored program was initiated to assess the feasibility of utilizing this LDV capability to perform detailed stator–rotor interaction studies in a multistage compressor. The equipment employed in these studies will be described and data typical of the findings will be presented.

Introduction

Laser-Doppler velocimetry (LDV) techniques have advanced considerably since their introduction in the late 1960s; matched with improved data acquisition systems, the LDV has become a cost-effective tool for the study of aerodynamics and hydrodynamics in many fields. Use of the LDV at Pratt & Whitney got underway in 1969 and evolved in the direction of operating in harsh gas turbine environments. Primary goals in the instrument's development included high sensitivity to accommodate relatively small windows for on-axis backscatter gas turbine studies and rapid data acquisition rates to minimize test times.

Initial studies at Pratt & Whitney were directed at jet flows and intrablade fan flows where the relatively large working distances, although presenting numerous problems, did not require the instrument to focus close to window surfaces or rotor hubs where substantial quantities of flare light originate. With the advent of commercial transit velocimeters in the 1970s, comparative studies were performed to assess the relative merits of the fringe and time-of-flight systems. The ability of the Pratt & Whitney fringe system to acquire data rapidly (an order of magnitude faster in jet flows) and to acquire data from all angular positions of the rotor, while, to date, no one has devised a practical method of examining more than one blade passage with a time of flight instrument (Binder et al., 1985) outweighed the increased sensitivity to smaller particles of the time-of-flight instruments for intrablade studies in our compressors. Consequently, development and application of fringe velocimetry in rotating machinery has remained the principal method employed.

Experience gained in LDV studies on half-scale transonic speed compressor fans run in the past decade at Pratt & Whitney (Williams, 1985) have led to refinements in the optics and data acquisition methods that were recently utilized in two NASA funded studies. The first, the NASA TS27 Transonic Fan Study, utilized a single-component version of the LDV to probe the intrablade region of the fan. Following this successful application of the instrument it was felt that the next significant flow to address was the measurement of airflow through multistage compressor rigs. Although limited studies of the dynamics of these flows have been obtained with hot wire and hot film probes, the advent of the laser-Doppler velocimeter with its nonperturbing nature is expected to develop into the preferred instrumental method.

Program

To assess the feasibility of utilizing an LDV in these flows, an exploratory program sponsored under the NASA Energy Efficient Engine Contract, NAS 220646, was recently undertaken at Pratt & Whitney. A multistage compressor rig, the Energy Efficient Engine high-pressure compressor, consisting of 6th through 15th compressor stages, was outfitted with win-

Contributed by the Gas Turbine Division of THE AMERICAN SOCIETY OF MECHANICAL ENGINEERS and presented at the 32nd International Gas Turbine Conference and Exhibit, Anaheim, California, May 31–June 4, 1987. Manuscript received at ASME Headquarters February 19, 1987. Paper No. 87-GT-235.

dows between the 6th stator–7th rotor, 9th stator–10th rotor, and 13th stator–14th rotor. The windows, extending circumferentially one stator gap wide, permitted hub-to-tip traversing midway between the stator trailing edge and the rotor leading edge both in and out of the stator vane wakes. A confocal two-color, two-component backscatter LDV system developed for use in gas turbine environs was employed to obtain detailed mappings of velocity magnitude and air angle as a function of rotor position ($\approx$1000 angular increments were resolved) at several spanwise and gapwise positions downstream of the 6th and 9th compressor stators. Although a complete mapping was not obtained, sufficient data were acquired behind the 13th stator to identify the flow's character there as well.

The equipment employed in these studies and the difficulties encountered will be described. Data typical of the findings will be presented. Unexpected modulations in the multistage compressor data have led to the application of spectral analysis techniques to identify and characterize the periodic fluctuations. Emphasis will be placed on these data analysis techniques and the insight gained from their application to the data.

Optical Instrument

Both single-color, single-component and two-color, two-component configurations of the same basic confocal backscatter Laser-Doppler Velocimeter (LDV) design have been developed at Pratt & Whitney. The unit in the two-component system configuration is shown in Fig. 1. A Spectra Physics Model 164 argon ion laser operating in "all lines mode" supplied approximately 800 mW of light to the head. Divergence of the incident laser beam was reduced in the LDV by first passing the beam through a galilean telescope type assembly to adjust the beam diameter to tailor its size to accommodate the number of fringes and fringe spacing required by the flow to be studied and to reduce the beam divergence materially from the laser to minimize the generation of false turbulence signals (better then 95 percent divergence reduction is normally achieved). This instrument incorporates path length compensation to permit laser operation without an etalon, dichroic beam splitters for color separation during beam splitting, and remotely positionable sensitivity vector beam orientation (resolvable to $\pm$0.05 deg). This assembly is coupled to a half-wave plate, which is configured to rotate at one half of the beam splitters' rate to maintain the proper light polarization for the beam splitters' coatings. The beam splitters in the two-component assembly were placed at 56 deg included angle rather than the 90 deg orientation frequently utilized, the two probe volumes' major axes are superimposed with the 0.488 μm fringes intersecting the 0.5145 μm fringes at an angle of 56 deg in the plane normal to probe volumes' major axes. Although a 90 deg orientation could have been employed, the narrower 56 deg included angle is generally employed at Pratt & Whitney since it permits the two sensitivity vectors nominally to be within 28 deg of the anticipated flow direction. This orientation substantially increases the effective swept area of the probe volume while concurrently decreasing the effect of angular fluctuations on angle bias generation. In this study although substantial velocity fluctuations were anticipated, angular fluctuations were expected to be small enough that only one orientation of the beam splitters would be needed for all testing (this proved to be the case).

Backscattered light from the instrument's probe volume was collected by a 3.158 in. (80 mm) diameter trepanned multiple element achromat, which incorporated a large, 2.125 in. (54 mm) diameter center stop for flare light control. The stop served to limit the probe volume length viewed by the collection lens. In addition this stop increased the signal-to-noise ratio by preventing scattering light from regions somewhat outside of the probe volume from entering the annular collection lens. Both the collection and projection lenses are removable and can be selected from a group of focal lengths to tailor the instrument's focal length to the working distances involved in each test program in order to maximize the instrument's light gathering efficiency. In the engine fan studies both 7.48 (19 cm) and 12.5 (318 cm) in. focal length collection optics had been used. In the smaller spans of the multistage high-pressure compressor study, hub-to-tip traversing for all three stages was accomplished with the 7.48 in. (19 cm), effective F3.8, collection lens. Light collected from the probe volume was brought to focus on a field stop whose size determined the field of view available to the photomultipliers (PMT). In the two-component system, separation of the signals from the two fringe volumes was accomplished with color separating beam splitters in the PMT housing.

As all the experience to date with the refined LDV design had been with the single-component version, the instrument was initially configured as a single-component system for the multistage study. If initial test results appeared promising with this proven system then the instrument would be reconfigured to the previously untested two-component mode. Optical performance of the new two-component system was expected to be comparable to the single-component design but this had not been established in an engine test environment. Consequently, a demonstration of the two-component head capabilities was needed before undertaking a program of this scope.

Test Vehicle and Modifications for LDV Testing

A full-scale experimental multistage compressor comprising rotors 6 thru 15, developed for the NASA Energy Efficient Engine, was powered by a 40,000 hp steam turbine for this study. To evaluate the potential difficulties associated with making LDV interrotor velocity measurements, three axial locations were selected for study.

The first window location, aft of the 6th stator and forward of the 7th rotor, was chosen to serve as a benchmark since the seed would have passed through only one rotating stage and particle migration would not be severe enough to restrict measurements significantly throughout the passage (Fig. 2).

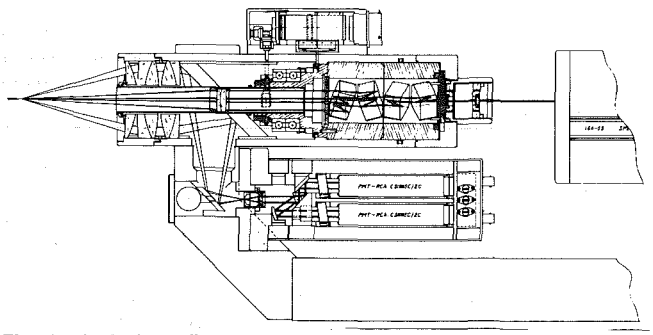

Fig. 1 Optical configuration of improved two-component confocal backscatter laser Doppler velocimeter

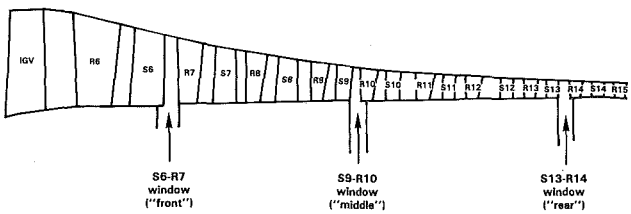

Fig. 2 Energy-efficient engine high-pressure compressor

Based on earlier transonic engine fan tests, it was anticipated that data acquisition at this location could be routinely accomplished. The window, 3 1/2 in. (89 mm) in the circumferential direction by 1 in. (25 mm) axially permitted a radial traverse from hub to tip behind the approximately 4 in. (102 mm) span stators. In the circumferential direction the window permitted probing from midway between stators (50 percent gap) through a stator wake (100 percent gap) to the corresponding location in the next passage (150 percent gap). The laser-Doppler velocimeter was moved along each of three mutually orthogonal axes, one parallel to the rig centerline, the second perpendicular to the rig centerline and passing through the centerline when the LDV was positioned at the midpoint of the window's major dimension, and the third traverse coordinate tangential and parallel to the rotor planes. Circumferential probing was, therefore, not strictly possible. The maximum deviation of the measurement plane from the rig's expected streamlines was approximately 3 deg when the LDV was positioned near the extremities of this window.

The second window, located in the 9th stator–10th rotor region, was also placed to permit hub-to-tip and 50 percent stator gap to 150 percent stator gap traversing. This location, following four rotor/stator stages, was expected to delineate any problems with seeding loss to the airfoils and walls. In addition, the passage height had shrunk to 1.85 in. (47 mm) increasing the likelihood that window and hub flare would make measurements near these surfaces difficult.

The third window, in the 13th stator/14th rotor region, was chosen to maximize the difficulties faced by the LDV, passage height was reduced to 1.05 in. (27 mm), and the seed would have to survive the passage through eight stages of compression and an air temperature rise of several hundred degrees F, which was anticipated to promote seed evaporation. Whether the material as a liquid would survive depended on the increased pressure, roughly eight times atmospheric, which might somewhat compensate for the 600 + °F (333 + °C) rise in gas temperature.

Previous experience in the engine fan testing had been with larger ≈1 m diameter rotors where installation of flat windows resulted in minimal perturbations at the rotor wall. Due to the smaller diameter of the high-pressure compressor, coupled with the need for extended circumferential traversing, it became necessary to depart from a flat window design. The inner surfaces of the windows were ground to a cylindrical contour chosen to approximate closely the curvature of the rig's outer flow path. In a window of this type, traversing the LDV vertically (circumferentially) from the normal to the rig axis results in the two incident laser beams for each LDV axis being refracted by differing amounts for all beam orientations, except when the plane of the two incident beams is parallel to the rig axis. This variability produced slight shifts in the LDV calibration constants and in the position of the probe volume. Proper choice of the outer window contour was expected to permit some control of these effects so an optical analysis was performed at Pratt & Whitney to select outer contours in an effort to control this effect.[1] Although a complex figure for the window would have permitted better control of the optical distortions, a cylindrical grind was chosen to keep fabrications costs to a reasonable value. Following polishing, the windows were antireflection coated on both surfaces.

The windows, formed of approximately 0.25 in. (6.4 mm) fused silica, were fitted into metal frames. The frames were fabricated with approximately 2 mil (0.05 mm) wide slots upstream of the inner window surface. These slots were used to conduct washing fluid via an internal channel from either of two remotely located reservoirs. During testing when data rates and (or) signal quality degraded (suggesting that the window had become fouled) either or both of the supplies would be momentarily pressurized to introduce acetone and (or) demineralized water into the airstream immediately upstream of the window. Generally a 1 or 2 s wash (approximately 1 to 2 cm^3 of the fluids) would restore system performance.

Di(2-ethylhexyl)phthalate (DOP), atomized by four Laskin nozzles, was introduced via a cruciform manifold into the ducting 100 ft upstream of the test rig. A lower vapor pressure oil, Dow Corning's DC704 diffusion pump fluid, was obtained as an alternate seed in the event that evaporation of the DOP occurred. A second backup material, nominal 1.0 μm diameter ziconium dioxide, injected by a fluidized bed seeder, was also prepared in case the DOP and DC704 were both found to be unsatisfactory.

Data Acquisition System

TSI Model 1990A counter processors were used to evaluate the incoming data stream. These devices, measuring the time relation between four and eight fringe crossings of a Doppler burst, were used to reject spurious signals and insure that the majority of measurements were from single particles traversing the probe volume. Modifications to the counters included outputting a strobe signal at the midpoint of the fringe count with the counters operating in the 4/8 mode. To obtain circumferential position measurements, a once per revolution speed signal was used to initialize a Real Time Systems Model 371 (RTS) multiplier. This device, capable of dividing the interarrival time between successive speed pulses into a prescribed number of intervals, was used to provide ≈1000 increments or "clicks" between successive once per rev signals. Angular indexing of the LDV data was achieved at the measurement location by utilizing the four-count strobe to interrogate and store in temporary memory the current click position indicated by the RTS multiplier. If after completion of the eight counts, the TSI counter indicated a valid detection had been made, the velocity component and temporarily stored rotor angle position were passed to the minicomputer, a PDP 11/34 equipped with direct memory access. Following the completion of an acquisition, typically 200,000 to 400,000 velocities were acquired in 2 to 10 min; the data were passed from magnetic disk to magnetic tape for storage and posttest analysis. The data acquisition system employed in this study is shown in Fig. 3.

No effort was made to force simultaneity between the two

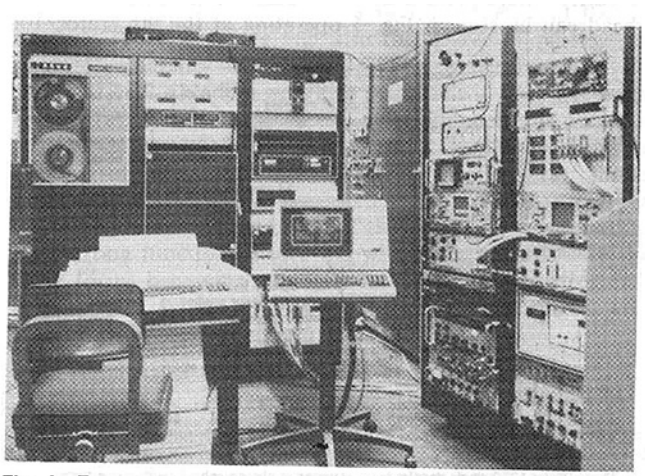

Fig. 3 Two-component laser Doppler velocimeter data acquisition system utilized in E^3 high-pressure compressor study

[1] Analysis of this aberration and window/lens designs to control the problem can be found in *International Symposium on Laser Anemometry*, FED Vol. 33, ASME Winter Annual Meeting, Nov. 17–22, 1985; see pages 293–298, "LDV Measurements in Pipe Flow Problems and Experiments," by J. Els and G. Rouve.

channels when the two-component LDV optics were employed. It was felt that considerable care is required to force simultaneity while not inadvertantly imposing constraints on the data collection, which effectively eliminates some valid data, thereby possibly biasing the data more than would have occurred with independently operating channels. As there was no a priori knowledge of the flow characteristics in the multistage rig and the study was intended to evaluate measurement feasibility, simultaneous measurements were not attempted.

Test Program

The test rig/instrument orientation was chosen such that the LDV, when centered in the window directly downstream of the stator trailing edge, placed the measuring plane of the LDV parallel to the rig centerline and tangent to the rig rotor diameters. Axial growth of the rig from static to the steady-state condition was monitored and compensated for by using the LDV to detect the fore-aft window boundaries and centering the LDV between these limits. All testing was performed with the rig stabilized at the 100 percent speed, design operating line condition. The test condition for the rig was continuously monitored and maintained such that the corrected standard day conditions varied less than 0.1 percent during the program.

Initial testing was performed in the 9th stator/10th rotor region with the single-component LDV utilized previously in a number of transonic fan studies. These efforts demonstrated the viability of getting good measurements at this location. Using these data as benchmark, the optical head was converted to the recently completed two-component configuration in order to ascertain whether the more efficient two-component mode of operation could be effectively utilized in this study. A series of repeat points was acquired that demonstrated that the two-component system performance was comparable to the single component. Consequently, all remaining data were obtained with the two-component optics. The average acquisition rate per unit test time using the two-component system in this program was approximately 160,000 velocity component measurements per minute of test. The average data rate in the previous fan test had been approximately 80,000 measurements per minute. The chronology of data rate versus acquisition time in the development and application of laser-Doppler velocimetry at Pratt & Whitney is shown in Fig. 4. Nearly circumferential traverses were made at each of five spanwise locations, 20 percent span intervals separated the traverses radially while circumferential spacing varied with the finest spacing used to define the stator wake regions; generally approximately 10 circumferentially spaced locations were probed at each spanwise location. The LDV head can be seen in Fig. 5 operating at the 9th stator/10th rotor window location, the 6th stator/7th rotor window is visible to the right. No difficulty was experienced in obtaining data at all locations probed in this region of the compressor. Seed migration effects were not found to be an obstacle to data acquisition, data were obtained everywhere that the instrument probed, and measurements were obtained as close as 0.06 in. (1.5 mm) from the rig's hub. The LDV probe volume length in this study was approximately 0.06 in. (1.5 mm). Once the five radial by ten circumferential point matrix had been completed, a similar set of traverses was performed through the upstream window. A similar matrix was then attempted at the 13th stator/14th rotor window. At this location data rates dropped to unacceptably low values due to seed loss through evaporation and window contamination. A lower vapor pressure oil, DC704 diffusion pump oil, was substituted for the DOP and testing resumed. Although an increase in data rate was obtained, the increase was not sufficient to permit a detailed mapping of this region in a reasonable time. Additional seeding experiments utilizing (1) nominal 1.0 μm zirconia suspended in DOP and dispersed via the Laskin nozzle seeder and (2) dispersing dried 1.0 μm zirconia from a fluidized bed were tried, but these attempts also met with limited success. In addition to not obtaining adequate seed at the 13th stator/14th rotor location, a significant problem was encountered in keeping the window's inner surface clear of contaminants. Fluids used to wash the upstream windows periodically during testing vaporized at this test location. The only way the windows could be cleaned was to reduce the rig operating speed (to lower gas temperature), wash the windows, reset the test condition, and try to obtain a data point before window contamination again excessively degraded the LDV signals. Despite these difficulties a few representative data sets were obtained at the 13th stator/14th rotor, which showed the flow structure at this location. At this point the program goals to obtain data wherever possible and to identify potential problems with LDV testing in multistage compressors had been met and testing was terminated. One hundred thirty-six data points had been obtained with complete mappings at the 6th stator/7th rotor and 9th stator/10th rotor locations and ≈20 percent of the matrix completed at the 13th stator/14th rotor locations.

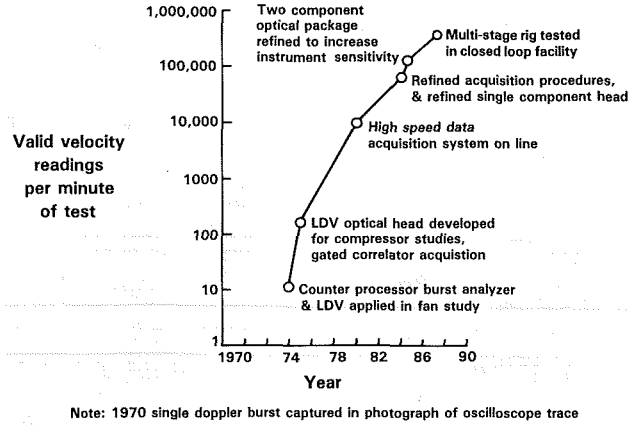

Note: 1970 single doppler burst captured in photograph of oscilloscope trace

Fig. 4 Development of LDV measurement rate in rotating rig studies

Data Reduction

Each of the data points consisted of two velocity components with 100,000 to 150,000 measurements per velocity component. During the acquisition phase, each velocity measurement had been assigned a rotor position value in-

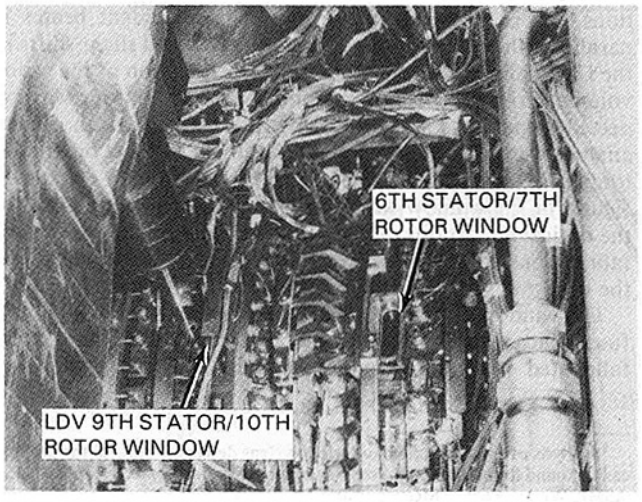

Fig. 5 Compressor-LDV test configuration, 6th stator/7th rotor and 9th stator/10th rotor windows visible

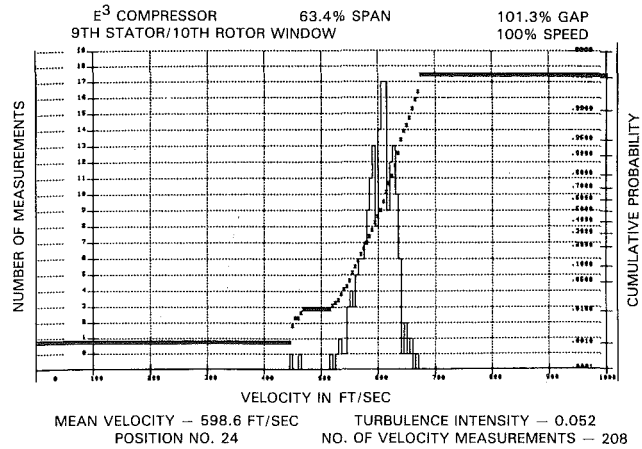

Fig. 6 Low-turbulence monomodal histogram, $\sigma/v = 0.052$

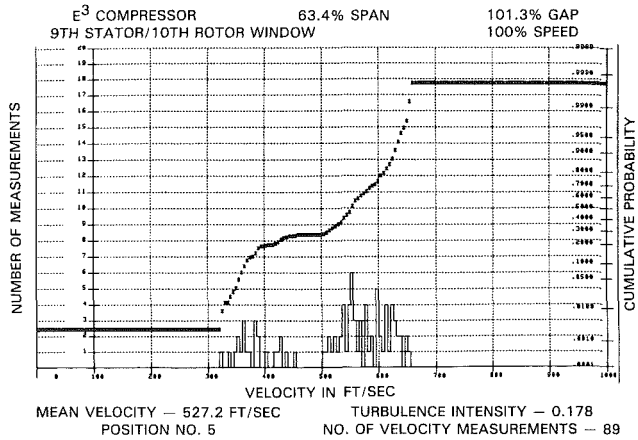

Fig. 7 High-turbulence bimodal histogram indicates presence of flow instability, $\sigma/v = 0.178$

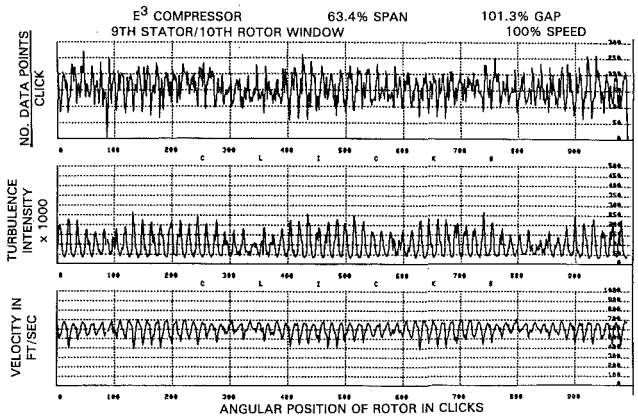

Fig. 8 One velocity component, typical multistage compressor data set showing the amount of data, turbulence, and mean velocities at approximately 1000 angular positions

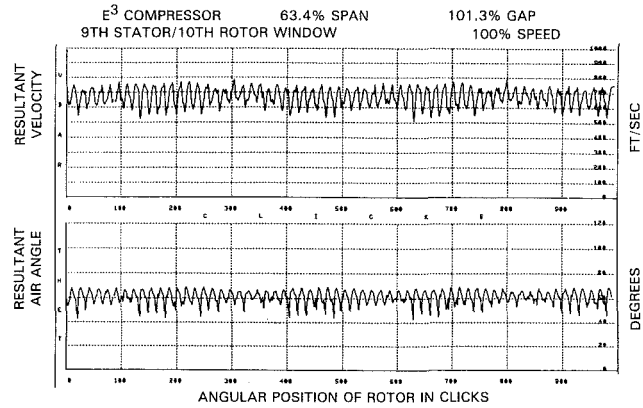

Fig. 9 Vector addition of two velocity components, multistage compressor, 9th stator/10th rotor region

dicating which of approximately 1000 angular positions of the rotor the measurement occurred in. The first step in data reduction was to order the data by angular position (hereafter referred to as click position), review the resulting histograms for possible editing,[2] and obtain the mean of each histogram. Figures 6 and 7 show typical low and high turbulence level histograms obtained. In cases where oscillatory flows are present, the histograms can become bimodal as the shifting flows cross the measuring location. To resolve the character and relative strength of multimodal flows, a cumulative velocity distribution plot is superimposed on the histogram figures. By using probability plot axes, normal distributions plot as straight lines and bimodal distributions plot as two intersecting lines with the intersection point indicating the approximate division between the two populations. Although in the examples shown the distributions can be clearly resolved by looking at the histograms, the cumulative plot becomes very useful when the distributions overlap. Figure 8 displays the results of analyzing all 1000 positions and plotting in the upper graph the number of velocity data per click, the middle graph displays the histogram's turbulence intensity per click, and the lower graph the mean velocity per click. These data were placed in a data base accessible by the Compressor Aerodynamics Group for review and analysis.[3] The data were then vectorially added to the second velocity component data similarly reduced to produce the resultant velocity vector and air data displayed in Fig. 9.

Fourier Analysis

An unusual aspect of many of the data sets obtained is the beatlike behavior found in the component velocity and resultant velocity mappings of the multistage compressor rig. In all previously run transonic fan programs, some passage-to-passage variations had been noted due to minor mechanical differences in the blading. The velocity magnitude and air angle of fan data obtained at 85 percent span and 0.26 chord within the blade row (Fig. 10) show the presence of the intrablade shock structure and also the degree of passage-to-passage variability encountered.[4] The nonuniformities introduced by the blading were also detectable in the blade wake regions (Fig. 11). In both cases no periodic patterns were apparent. Conversely a study of data from the rotor wake regions of the multistage compressor (Fig. 12) shows nonuniformities, which suggested that periodic structures might be present. The strength of these features was found to be a strong function of location within the passage with the wave forms becoming strongest in the stator wake regions; compare Fig. 9 data taken from the stator wake region with data taken in the free stream, Fig. 12.

[2]No data editing was found to be necessary for the bulk of the data. At the 13th stator/14th rotor location noise began to appear due to window contamination. All data are presented with no editing.

[3]Results of the aerodynamic analysis will be released in the NASA Contract Final Report, "E^3 High Pressure Compressor, Rig #70749-03 LDV Data Assessment."

[4]The possibility that these variations resulted from statistical uncertainties in the data or instabilities in controlling rig conditions during testing was explored by acquiring the test point on three separate occasions spanning a two-week interval; all data showed the same patterns.

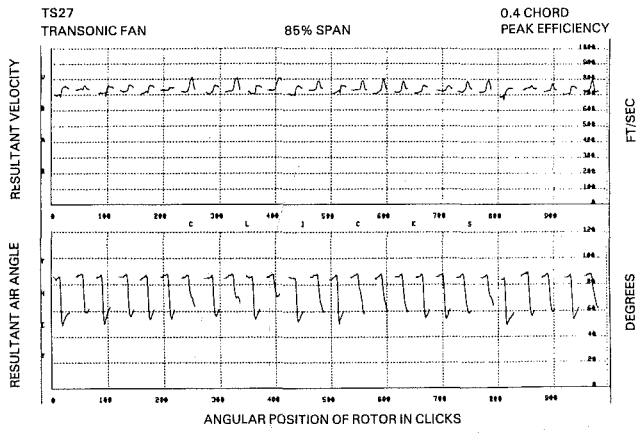

Fig. 10 Intrablade shock structure in transonic fan: Note high passage-to-passage variability

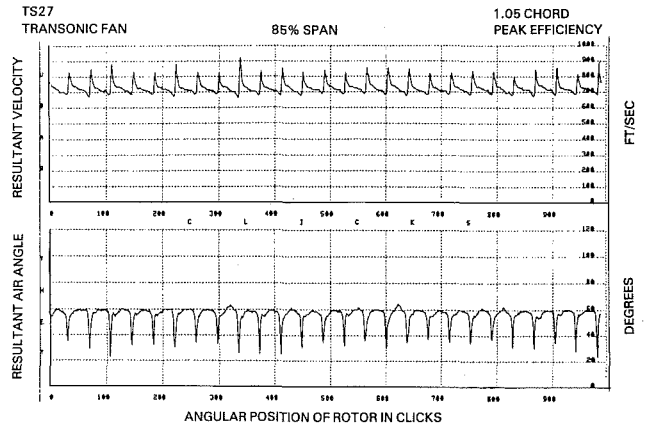

Fig. 11 Transonic fan wake data variability introduced by blading remains visible

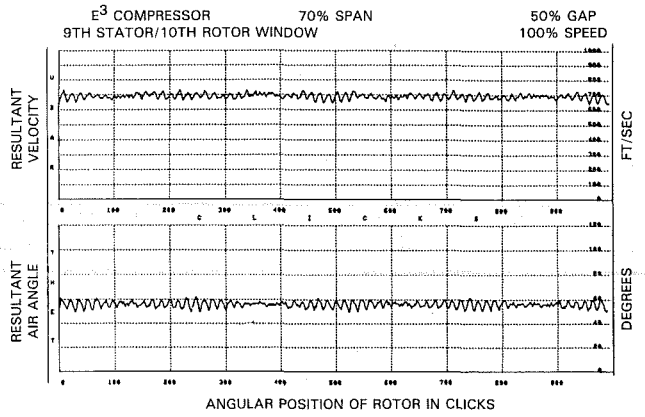

Fig. 12 Resultant multistage compressor velocity and air angle data showing periodic (4E) beat at the 9th stator/10th rotor location

Figure 12 displays a four cycle per revolution beat frequency, which was observed in the 9th stator/10 rotor location for many of the data sets. This suggested that the periodicities observed were being caused by the 66 bladed rotor 9 blade wakes interacting with the forward propagating back pressure field from rotor 10's 62 blades. Bear in mind that what is being displayed is spatially separated velocity anomalies, not temporally distinct periodicities. For example, Fig. 7 shows a distinctly bimodal distribution indicating that a periodic oscillation was probably occurring at this click location, yet the periodicity of the oscillation was not recorded in the acquisition process. The nature of the aerodynamic instability

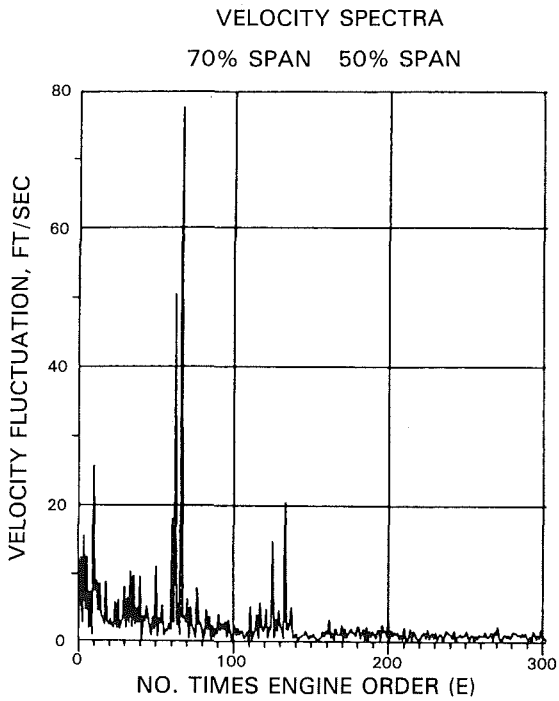

Fig. 13

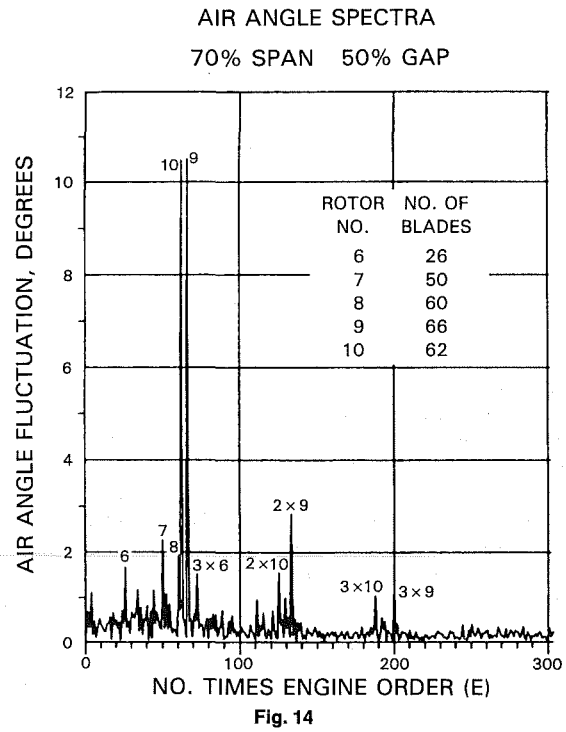

Fig. 14

Figs. 13 and 14 Fourier transforms of velocity and air angle waveforms from Fig. 9; several of the peaks from Fig. 14 are labeled by the rotor number of the source and the harmonics

that produced these bimodal distributions is not presently understood. The bimodality occurred periodically, suggesting that a rotor wake/stator wake interaction may have periodically generated a vortex street or other oscillatory flow behavior. In the following displays only the mean value of the distribution is used, i.e., all time information has been ignored. To investigate this beat phenomenon further a Fourier transform (FT) routine was developed to transform the wave form, either the velocity component wave in Fig. 8, or the resultant velocity vector or air angle curve from the spatial in-

to the frequency domain from Fig. 9 or 12. Figures 13 and 14 display the result of transforming the velocity and air angle curves of Fig. 9 with the spatially discrete periodicities that contributed to the measured waveform being clearly observable. In analyzing these results it quickly became evident that many more rotors than the immediate upstream and downstream rotors were contributing to the velocity fluctuations observed. In fact, in some data sets, periodic contributions from as far forward as rotor 6 were clearly disconcerned aft of stator 9. The fundamentals and harmonics from the various rotors are identified in Fig. 14. Although the impact of these findings is not fully understood, it appears that potentially hazardous aerodynamic excitation frequencies and magnitudes can be convected from rotors somewhat removed from the location of concern. With many of the newer compressors of a close coupled design, i.e., decreased rotor/stator spacing, there appears to be increased potential for structurally destructive aerodynamically induced interactions to occur.

Waveform Enhancement

With the contributing components' frequency and amplitude levels clearly identified, the possibility of manipulating the data to enhance wave forms of specific interest suggested itself. One approach investigated involved extracting only the wake wave form created by one rotor, ignoring all interactions with other rotors. First an FT was performed on the velocity or air angle curve, then the real and imaginary components of the fundamental and harmonics associated with the rotor of interest were extracted, and finally an inverse Fourier transform was performed on these data. Figure 15 displays velocity and air angle data from the 9th stator/10th rotor location where the 9th rotor's 66 blades wakes were severely distorted by the presence of a strong bow wave propagating forward from the 62 blades of rotor 10. The average or mean rotor 9 blade wake shown in Fig. 16 was extracted from the velocity curve of Fig. 15 in the manner described above. In a multistage compressor with windows located between every stage, this method could be employed to track the distortions introduced and decay produced by passage of a specific rotor's wake through successive stages.

A second method employed was to subtract out only the contribution of one rotor by similarly performing the FT, identifying and removing the real and imaginary terms of the wave form to be deleted, and performing an inverse Fourier transformation (IFT) on the remaining data. In this fashion, a particularly strong perturbation created by a nearby rotor can be removed allowing weaker fluctuations to be more clearly observed. The upper graph of Fig. 17 shows a portion of an air angle wave form from the 50 percent gap/50 percent span location of the 6th rotor (26 blades)/7th rotor (50 blades) data set in which the 50E (times engine order) signals from the downstream rotor clearly dominate the data. The fundamental and 2nd through 4th harmonics of rotor 7 were deleted from the transform and the IFT performed; the lower portion of the figure shows the resulting wave form with the 26E blade wakes now clearly visible.

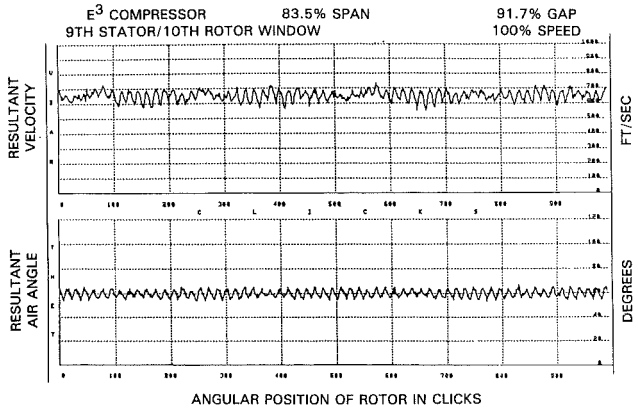

Fig. 15 Resultant waveforms in which upstream rotor wake (66E) is difficult to detect because downstream rotor (62E) bow wave dominates

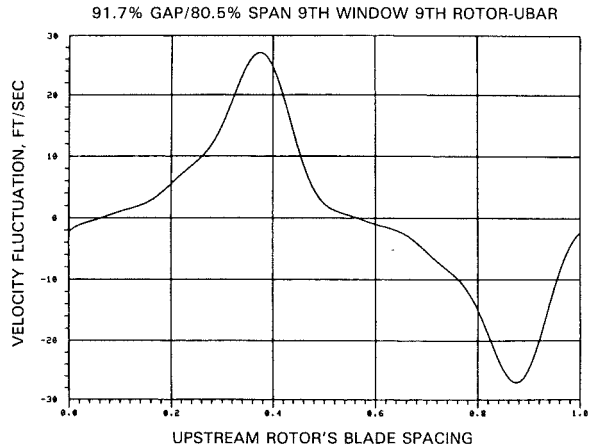

Fig. 16 Fourier transformation and inverse transformation retrieves average upstream rotor blade wake profile from resultant velocity waveform of Fig. 15

Conclusions

The initial thrust of the program, to identify the viability of using a two-component LDV to obtain nonperturbing measurements of air velocity and angle in the stator/rotor interaction region of a multistage compressor, was clearly demonstrated to be practical.

- Initial concerns with the possibility of locally unseeded regions developing after passage of the seeded flow through several stages of a compressor was not found to be a problem. No seed level degradation was observed after four stages of compression. After eight stages, seed evaporation difficulties arose but no locally unseeded regions developed.
- The additional pressure created in the higher stages of the compressor is not sufficient to offset the increasing volatility of DOP seed produced by the rising gas stream temperature.
- Turbulence introduced by rotor wakes persists in terms of identifiable velocity fluctuations for several stages before mixing reduced the rotor's contributions to unidentifiable random fluctuations.

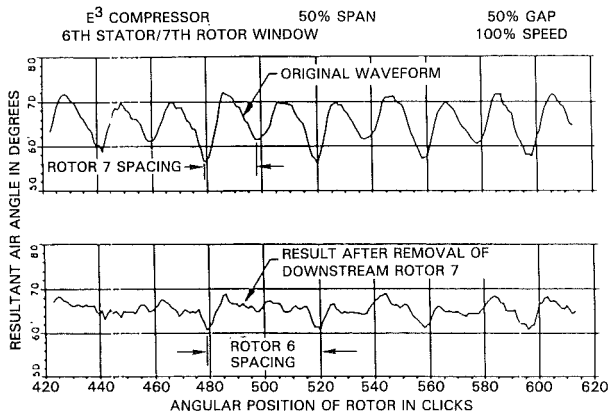

Fig. 17 Downstream rotor effects dominate air angle data; application of FT and IFT techniques removes downstream rotor contribution permitting upstream rotor wakes to be seen

• Although the data were not recorded in a fashion that preserved the temporal aspects of the measurement, Fourier transform techniques could be usefully applied to identify the relative magnitude of contributions from the various stages of the multistage compressor. The spatial wave forms obtained could also be manipulated with FT techniques to extract additional information about hardware-related periodicities present in the flow.

• In addition to improving the understanding of compressor aerodynamics, LDV data analyzed utilizing the FFT techniques described are expected to be of use in studying the structural behavior of close coupled compressor designs.

Areas to Address for Further Development

Test time/costs would benefit from improved data rates achievable by increasing seed densities beyond current levels and by accelerating the data acquisition system's various operations to increase the percent of test time during which data are actually being recorded.

Lower vapor pressure oils or solid particulates will be needed for future testing in the highest pressure/temperature regions of multistage compressors.

Either methods of cleaning windows during high-temperature rig operation will have to be developed that remain effective at the highest stages of compression or possibly methods of supplying a continuous gas purge could be developed to prevent contaminants from accumulating.

Acknowledgments

The study of interrotor flows in a high-speed multistage compressor was made possible by support from the NASA Lewis Research Center under Contract no. NAS3-20646. The author would also like to thank Randolph House, a fellow Pratt & Whitney employee, who designed and fabricated the single and two-component LDV systems and participated in their successful application in this study.

References

Binder, A., Forster, W., Kruse, H., and Rogge, H., 1985, "An Experimental Investigation Into the Effect of Wakes on the Unsteady Turbine Rotor Flow," ASME *Journal of Engineering for Gas Turbines and Power*, Vol. 107, pp. 458–466.

"Final Report, TS 27 Fan/Laser Doppler Velocimetry Program," 1990, NASA-Lewis Research Center, Contract No. NAS3-20646.

Williams, M. C., 1985, "Intrablade Velocity Mapping in Transonic Fan Passages of Gas Turbine," *International Symposium on Laser Anemometry*, FED-Vol. 33, pp. 19–26.

Laser-Doppler Velocimeter Measurement of Annulus Wall Boundary Layer Development in a Compressor Rotor

B. Lakshminarayana
Evan Pugh and Distinguished Alumni Professor,
Director of Computational Fluid Dynamics Studies.
Fellow ASME

K. N. S. Murthy
Graduate Student.

Department of Aerospace Engineering,
The Pennsylvania State University,
University Park, PA 16802

Detailed measurement of the flow field in the tip region of a compressor rotor was carried out using a laser-Doppler velocimeter (LDV). The axial and tangential components of relative velocities were measured upstream, inside the passage, and at the exit of the rotor, up to about 20 percent of the blade span from the blade tip. In addition, the relative stagnation pressures were measured from a Kiel probe; static pressures were derived from this and from the LDV measurement. The data are interpreted to understand annulus-wall boundary layer development inside the rotor, leakage flow, and losses in the tip region. The annulus wall boundary layer is well behaved at the leading edge and far downstream of the rotor. But inside the passage, complex interactions between the leakage flow and the annulus-wall boundary layer result in unconventional profiles with wide deviations from models employed for analyses.

Introduction

The boundary layers that develop on the casing of compressor stages limit pressure rise, efficiency, mechanical reliability, and mass flow through the stage. In addition, they introduce considerable three dimensionality and unsteadiness in the flow, and affect the stall and surge characteristics of the compressor. In recent years, they have also been recognized as a source of noise. Previous attempts to analyze this flow were based on simplified flow models and momentum integral techniques (Mellor and Wood, 1971; DeRuyck and Hirsch, 1981; Horlock and Perkins, 1974) that neglect the complex interactions in the endwall region of blade rows. Comparisons between the measured and predicted annulus-wall boundary layer (AWBL) growth are poor or only qualitative in nature for the rotor endwall boundary layer, but are quite good for the stator or IGV blade rows. These methods have not been tested for AWBL inside a rotor passage. One of the objectives of this paper is to provide appropriate data for validating these analyses and the computer codes now under development.

The annulus-wall boundary layer (AWBL) that develops on the casing of a turbomachinery stage is three dimensional and turbulent in nature. Furthermore, interaction between the leakage flow and blade boundary layer produces an extremely complex flow field in the tip region. This region of the AWBL remains largely unexplored experimentally, and it is beyond the scope of analytical methods. Measurements inside the rotor are complicated, since the measuring probe has to be rotated with the rotor. The measurement technique for the small clearance region is also complex, and minature probes combined with elaborate data processing procedures must be employed in acquiring data in this region. There are no data available at present for the AWBL growth inside the rotor blade and in the immediate vicinity of the trailing edge of the rotor in the downstream region.

A comprehensive program to acquire such data in the endwall region was started at The Pennsylvania State University. Some of these data were presented and interpreted by Murthy and Lakshminarayana (1986). Additional data were acquired in the tip region of a low-speed axial flow compressor using a laser-Doppler velocimeter and a Kiel probe. The flow field was measured inside the rotor passage as well as upstream and downstream of the rotor. The earlier data as well as the present data are interpreted in this paper from the point of the annulus-wall boundary layer growth, including the effect of tip clearance and losses.

Experimental Facility, Technique, and Program

The endwall flow measurements are carried out in a single-stage axial flow compressor (AFC) facility. A schematic view of the facility is shown in Fig. 1, and the detailed description of the facility is given by Lakshminarayana (1980) and Sitaram and Lakshminarayana (1983). The compressor stage consists of an inlet guide vane (IGV) blade row, a rotor, and a stator. The inlet guide vane, consisting of 43 blades, is followed by the 21-bladed rotor. The distance between the IGV trailing edge and the rotor leading edge is 24.1 cm (or

Contributed by the Gas Turbine Division of THE AMERICAN SOCIETY OF MECHANICAL ENGINEERS and presented at the 32nd International Gas Turbine Conference and Exhibit, Anaheim, California, May 31–June 4, 1987. Manuscript received at ASME Headquarters February 24, 1987. Paper No. 87-GT-251.

three chord lengths of IGV blades) at midradius. The hub/annulus-wall diameter ratio of the facility is 0.5, with the diameter of the annulus wall equal to 0.936 m. The rotor is driven by a 37 kW variable-speed motor and is followed by the stator row of 25 blades. An axial flow fan with a variable blade setting is positioned downstream of the rotor, and is used to control the pressure rise and mass flow rate through the facility. Overall performance of the rotor is shown by Sitaram and Lakshminarayana (1983). Good peak efficiencies are exhibited by the rotor. Operating conditions for the data reported herein are as follows: inlet velocity ($V_{z\infty}$) of 29.5 m/s; flow coefficient based on tip speed of 0.56; stage loading coefficient based on tip speed of 0.4864; rotor speed of 1080 rpm; tip clearance between 2.5 and 3.5 mm. The blade element data at the tip of the rotor are as follows: chord 15.41 cm; spacing 14.12 cm; maximum thickness 5.10 percent of chord; stagger angle of 45.0 deg; maximum camber height 8 percent of the chord. The rotor blades are of the NACA 65 series with the design lift coefficient varying along the blade span. Blade element details for the IGV and rotor are given by Sitaram and Lakshminarayana (1983).

The facility is equipped with a traversing mechanism to traverse the probe circumferentially while the rotor is in motion. The main feature of the rotating-probe traverse gear mechanism is a SLO-SYN motor of 0.007 Nm torque driving a 3.8×10^{-2} m diameter shaft through a planetary reduction gear train. The gear train steps down circumferential step size from a 1.8 deg/step to a 0.0166 deg/step. This arrangement enables comprehensive measurement of the stagnation pressure field. The probe holder and stepping motor are mounted inside the rotating hub of the experimental facility. The motor is powered and controlled by a stationary indexing device through an eight-channel brush slip-ring unit. An electrical signal from a probe or from a transducer is transmitted to the instruments through a mercury slip-ring unit. The traverse unit and the probe are locked except when indexed. Only the probe holder traverses along the slots in the rotating hub.

A single-component LDV system was used to measure the flow field inside the rotor passage. Details of the LDV system and data acquisition procedure are described by Murthy and Lakshminarayana (1986). A single channel, dual-beam laser anemometer with on-axis backscatter light collection (TSI

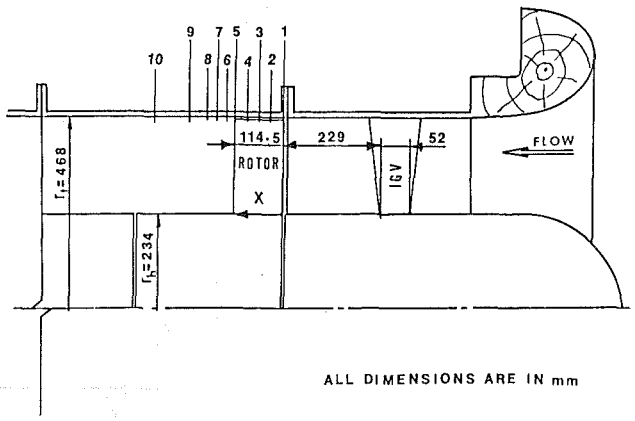

Fig. 1 Schematic of the AFC facility and the LDV measuring stations

Model 9100-6) was used to make measurements in the endwall region behind the rotor blade. The system operated with a Lexel 4W argon-ion laser tuned for the green line (514.5 mm). The transmitting optics consisted of a beamsplitter, a $3.75\times$ beam expander, and a 152-mm-dia front lens with a focal length of 762 mm. The half-angle of the intersecting beams was measured as 3.12 deg and provided a probe volume diameter of 0.133 mm and a probe volume length of 2.50 mm, based on the $1/e^2$ intensity points. The receiving optics consisted of the 152 mm front lens, a field-stop unit, and a receiving assembly with a photomultiplier tube. The entire system moved on a three-axis traverse table, which also has the facility to tilt the assembly so that the beams are projected radially to the rotor. A counter-type signal processor (TSI Model 1995) interfaced with HP 2100S computer provided an on-line data processing capability. An ensemble-averaging technique was used to average the velocity information. The flow was seeded with an atomized spray of mineral oil and was injected into the flow 200 mm upstream of the rotor.

The description of the endwall flow field is incomplete without the total pressure and loss distributions inside and at the exit of the rotor. The LDV measurement, although very useful in describing the velocity field, cannot yield information regarding the pressure field. To derive the static pressure and aerodynamic losses associated with endwall flows, a

Nomenclature

C = chord length
C_R = axial chord of rotor at tip
C_L = lift coefficient normalized by $\rho W_1^2/2$
K = fraction of lift retained in tip clearance region
C_p = static pressure coefficient $=(P-P_a)/(\rho U_t^2/2)$
P_R = relative stagnation pressure normalized by $\rho U_t^2/2$
PS = pressure surface
P = static pressure
R = radius normalized by tip radius ($r_t=0.468$ m)
SS = suction surface
T_x, T_θ = turbulent intensities in axial and tangential directions, respectively
U = blade speed
V_θ = absolute tangential velocity
W_x, W_θ = axial and tangential relative velocity components normalized by blade tip speed (53 m/s)
X = axial distance from rotor leading edge normalized by axial chord at tip (10.9 cm)
Y = tangential distance measured from suction surface normalized by blade local spacing ($Y=0$ on the SS and $Y=1$ on PS)
ρ = air density
τ = clearance height
$\bar{\phi}$ = mass-averaged flow coefficient (normalized by blade tip speed)
$\bar{\psi}$ = mass-averaged pressure rise coefficient (normalized by $1/2\ \rho U_t^2$)
ψ_{loss} = relative stagnation pressure loss coefficient $=(P_{R1}-P_{Rl})/(\rho U_t^2/2)$

Subscripts

1, 2 = rotor inlet and exit
a = atmosphere
l = local
h, t = hub, tip

Superscripts

— = blade-to-blade mass average

rotating Kiel probe was used. The relative total pressure distribution inside and at the exit of the rotor passage was measured using a miniature Kiel probe (United sensor type KAA). The probe had a head size of 1.65 mm, which introduced negligible aerodynamic interference. Errors due to shear gradient and blockage were insignificant due to the small head size. The probe was insensitive to yaw and pitch angles of ±50 deg and to Reynolds number variation well within the present operating range. Turbulence-induced error was extremely small. Severe turbulence, especially encountered near the tip region, may have decreased the yaw and the pitch ranges slightly.

Static pressures were derived from the stagnation pressure measured from the Kiel probe and the velocity components measured from LDV system. In deriving the static pressure, it is assumed that the radial velocities are small (say less than 10 percent of the free-stream velocity), and thus the derived data for C_p are subject to a small error.

The LDV and Kiel probe measurements were taken at $X=0$ (leading edge), 0.25, 0.5, 0.75, 1.0 (trailing edge), 1.04, 1.17, 1.41, 2.0, and 3.0. These are designated as stations 1, 2, . . . , 10, respectively, in Fig. 1. The LDV measurements were taken at about 25 radial locations, from $R=0.913$ to 0.989. Kiel probe data was acquired at 9–14 radial stations in the same interval.

Experimental Results

In the blade-to-blade data presented in this section, the tangential distance Y is normalized by the local blade spacing. Inside the rotor passage, $Y=0$ corresponds to suction surface, and $Y=1.0$ corresponds to pressure surface. The inlet flow at $X=-0.35$ was circumferentially uniform. The radial distribution of the inlet flow at $X=-0.35$, acquired with a conventional probe, is shown in Fig. 2. The relative stagnation pressure distribution in the tip region at inlet ($X=0$) is shown in Fig. 3.

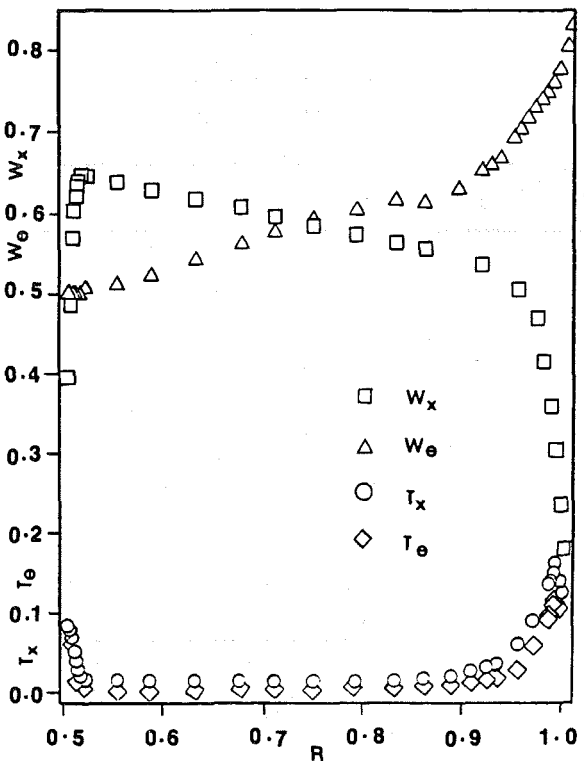

Fig. 2 Axial and tangential velocity profiles at inlet at $X=-0.35$

At every axial location, nearly 25 radial surveys were conducted to map velocity distribution inside the rotor passage. The radial station nearest the casing wall is at $R=0.98$ (very close to the blade tip and 5 mm from the wall); the station farthest from the casing wall is at $R=0.902$. Data from the Kiel probe are used to derive losses in the endwall region. Some of the loss data and comparison with the correlations available are given by Lakshminarayana et al. (1986).

Static Pressure Distribution. The static pressure coefficients at various axial, chordwise, and tangential locations were derived from the stagnation pressures measured from a Kiel probe and the velocities measured by LDV. The distribution of C_p at $x=0.25$, 0.5, 0.75, 1.0 (trailing edge), and 2.0 are shown in Figs. 4–8.

At $X=0.25$ in Fig. 4, a low static pressure region is observed very near the blade tip near $Y=0.1$, close to the blade suction surface. This indicates the presence of leakage flow. The region affected by the leakage flow is very small, and the radial extent of the region is less than 5 percent of span from the blade tip. Outside this region, the usual inviscid effect (with low pressures near the suction side and high pressures near the pressure side) can be seen clearly.

At midchord ($X=0.5$, Fig. 5), nearly half the blade passage is affected by the leakage flow, and its influence is confined to about 5 to 8 percent of the span from the blade tip. The peak suction pressures are about the same as those observed at $X=0.25$.

The presence of a core, where the pressures are very low, indicates that the leakage flow has rolled to form a vortex. The formation of a leakage vortex may be in the inception stage at this location since the extent of the core region is still small, even though C_p values are affected in the entire passage in the tip region. The static pressure distribution in the inviscid region (away from the tip) is very similar to that observed at $X=0.25$.

The influence of leakage flow is more severe at $X=0.75$ (Fig. 6) than that observed at $X=0.25$ and 0.5; the leakage jet seems to have penetrated much farther into the passage. The core is located at $Y=0.5$ (near midpassage) and the influence of the leakage flow extends to more than half the passage width and about 12 percent of the span from the tip. A comparison of C_p distribution plotted in Figs. 4, 5, and 6 indicates that the suction peak associated with the leakage flow moves toward the pressure surface as the flow progresses from

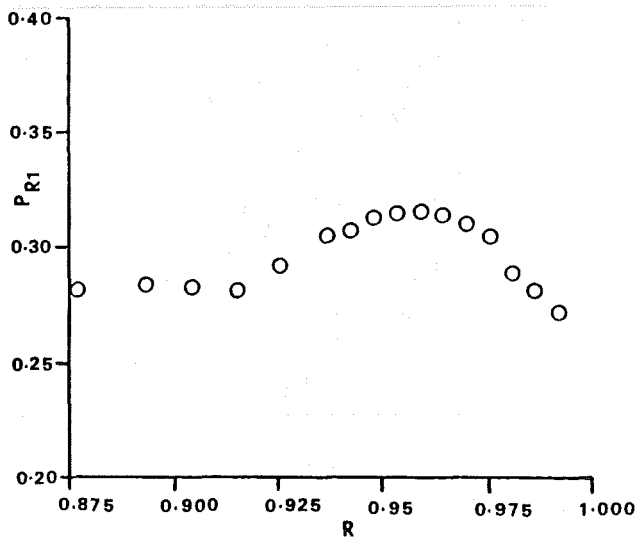

Fig. 3 Stagnation pressure (P_{R1}) distribution near the tip region at inlet

$X=0.25$ to 0.75. The peak value of C_p is located near $Y=0.1$ at $X=0.25$, and near $Y=0.55$ at $X=0.75$. At $X=0.75$, the inviscid pressure gradient has decreased substantially from that observed at $X=0.5$. Unlike other regions ($X\leq 0.75$), a distinct core seems to indicate the presence of a leakage vortex.

The C_p distribution at $X=1.0$ shows a well-developed leakage vortex region, with the core of the leakage vortex located from the midpassage to the pressure surface. The radial extent of this region extends to about 12 percent of the span from the tip. The inviscid region shows a very small pressure gradient in the blade-to-blade direction. As the flow progresses downstream, a distinct vortex region of nearly circular shape seems to develop ($X=2.0$, Fig. 8). Peak suction pressures, as well as suction pressure outside the core, decrease substantially as the flow progresses downstream from $X=1.0$ to $X=2.0$. This indicates the diffusion and dissipation of the leakage flow and the vortex by molecular viscosity and turbulence. The presence of rotor wake can also be seen clearly at the location $X=2.0$.

Annulus-Wall Boundary Layer Development Inside and at the Exit of the Rotor Passage. The annulus-wall boundary layer (AWBL) developing inside a rotor blade passage is skewed, three dimensional, turbulent, and highly complex, and develops under a streamwise pressure gradient. A complex velocity profile results from the interaction of the leakage flow with the AWBL. The profile consists of a wall layer, leakage jet layer, free shear layer, and inviscid region. The characterization of the flow field is extremely difficult. The AWBL inside the rotor passage is presented at five axial stations inside the rotor and at five tangential locations.

The axial and relative tangential velocity profiles at $X=0.25$ at five tangential locations are shown in Fig. 9. The axial velocity profile seems to indicate that the boundary layer is fairly well-developed near the suction surface ($Y=0.05$) and the pressure surface ($Y=0.95$), and the boundary layer near the midpassage ($Y=0.5$ and 0.75) indicates some unusual behavior. The flow near $Y=0.5$ and 0.75 at this location seems to be dominated by inviscid effects, as indicated by both the axial and tangential velocity profiles. The tangential velocity profile at $Y=0.25$ shows several unusual trends. The dip in the W_θ profile away from the blade tip ($R_T-R=0.0125$) may be the result of the leakage jet turning back to move toward the suction side (Fig. 10). Such a phenomenon will result in flow overturning (large V_θ, small W_θ) observed at this location. The tangential velocity profile at $Y=0.95$, close to the pressure surface, indicates large flow underturning. This again is consistent with the leakage flow, which tends to decrease the flow turning and hence increase the relative tangential velocity close to the wall. The velocity profile at $X=0.25$ is very similar to that measured at the leading edge $X=0.0$ (not shown in the paper).

A schematic of the nature of the leakage flow is given in Fig. 10. The leakage jet tends to move away from the suction surface and then roll back. The distance it travels depends upon the magnitude of the leakage velocity, which in turn depends on the chordwise location. Near the leading edge ($X=0.25$), the leakage flow has just emerged and has not had a chance to penetrate into the passage. Hence, it rolls back quickly, resulting in a dip in the relative tangential velocity profile shown at $Y=0.25$ at $X=0.25$. No measurements are available in locations such as A in Fig. 10. This location should have a jet type of W_θ profile, as the flow is underturned in this region. The measurements shown in Fig. 9 are at locations such as B in Fig. 10. The rollback of the leakage flow tends to provide a lower relative tangential velocity or higher absolute tangential velocity.

The axial and tangential velocity profiles at the midchord ($X=0.5$) are shown in Fig. 11. This location shows well-developed boundary layers all the way from the suction to the

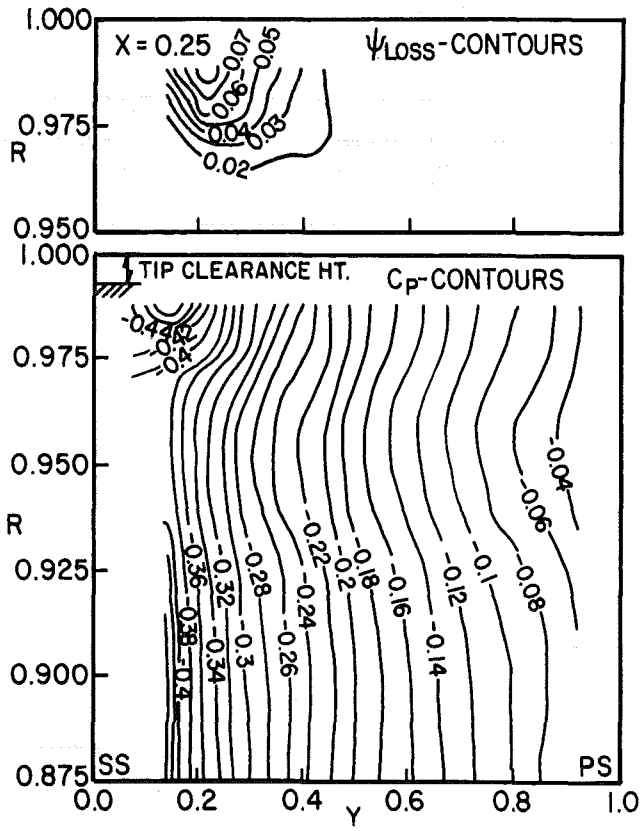

Fig. 4 C_p and ψ_{loss} contours in the blade tip region at $X=0.25$

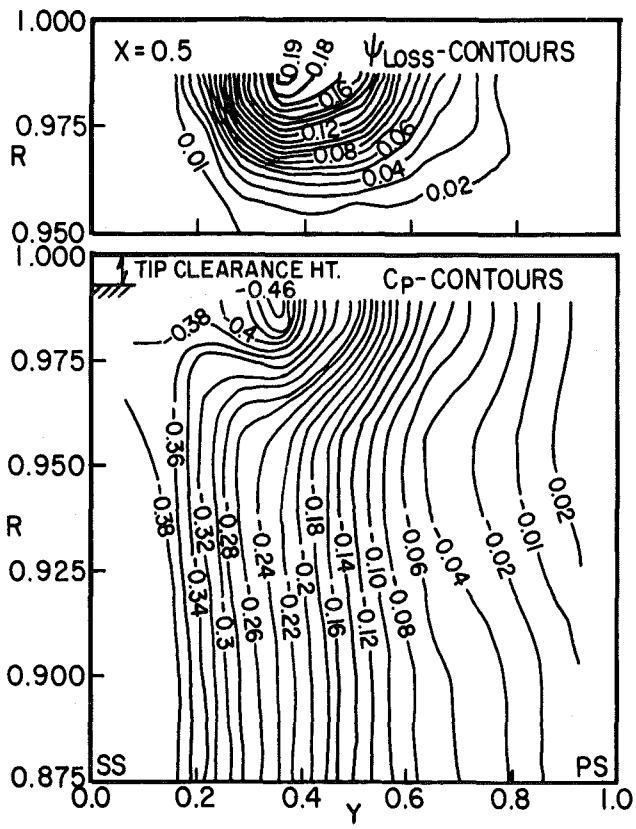

Fig. 5 C_p and ψ_{loss} contours in the blade tip region at $X=0.5$

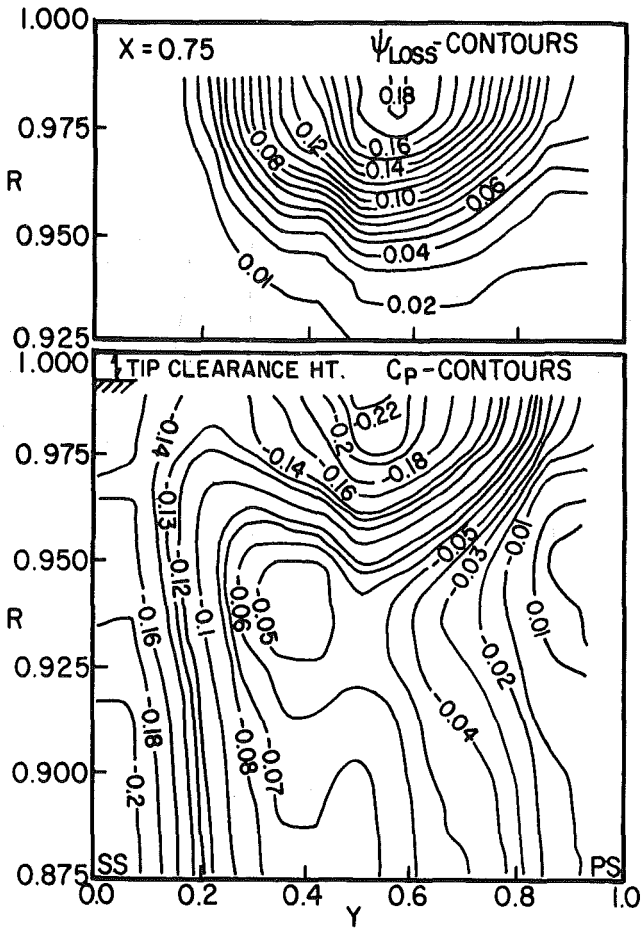

Fig. 6 C_p and ψ_{loss} contours in the blade tip region at $X = 0.75$

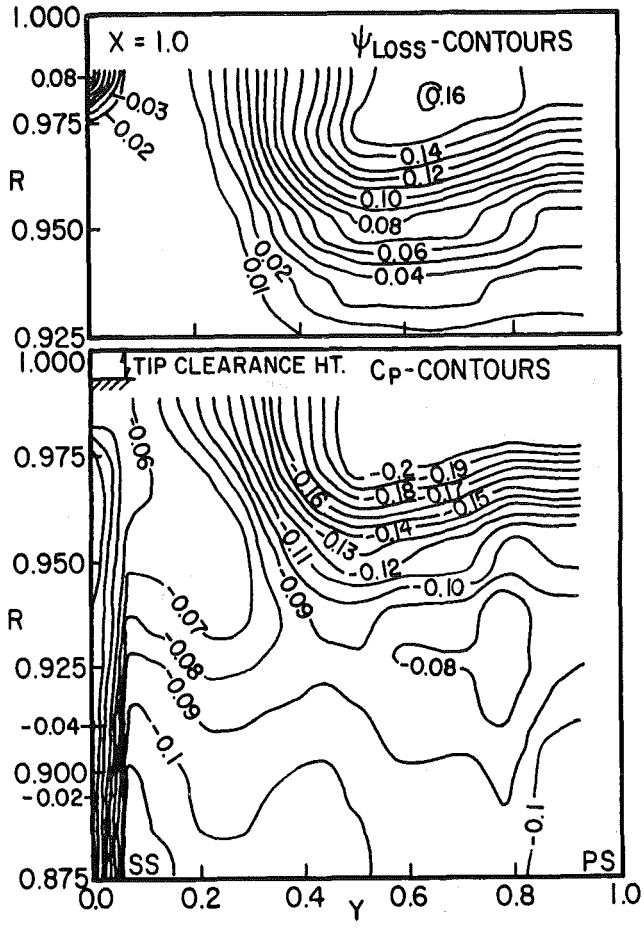

Fig. 7 C_p and ψ_{loss} contours in the blade tip region at $X = 1.0$

pressure surface. Large boundary layer growth occurs very close to the suction surface. The boundary layer has grown substantially from $X = 0.25$ to 0.5, and the boundary layer is highly skewed with large transverse components as shown in Fig. 11. The tangential velocity profiles at $Y = 0.05$, 0.25, and 0.50 again exhibit a very complex structure. The effect of leakage flow is dominant, as expected. The phenomena indicated in Fig. 10 can be seen clearly in this figure. The dip in relative tangential velocity occurs at locations $Y = 0.25$ through $Y = 0.75$, which represents roughly the middle half of the passage. The severity of leakage flow is thus evident, indicating that the leakage flow has penetrated deeper into the passage; this rolls back toward the suction surface. Furthermore, the boundary layer closest to the suction side shows a tendency toward separation; this is expected from the streamwise pressure gradient that exists in this region. There is a substantial difference in the boundary layer profile and the growth between $X = 0.25$ and $X = 0.5$. This is the region where leakage flow, streamwise pressure gradient, seems to have a major effect on the velocity distribution and the boundary layer growth. Some of these observations are consistent with the C_p distribution at this location (Fig. 5). Maximum suction pressures are observed close to $Y = 0.35$ and the W_θ profile shows the dominant influence of leakage flow between $Y = 0.25$ and 0.5. It is interesting to note that near the annulus wall, close to the pressure and suction surfaces, the relative tangential velocities are high. This indicates that boundary layers are highly skewed at these locations. A similar trend was observed by Hunter and Cumpsty (1982) for an isolated compressor rotor.

The relative tangential velocity distribution at $X = 0.5$ exhibits a jet-wake type profile. The velocity distribution is unconventional, and it is clear that none of the assumptions made for velocity profiles in the analysis of AWBL would be valid in this region. The annulus-wall boundary layer is highly three dimensional, with unconventional velocity profiles and a substantial variation along the tangential direction. The variation seems to indicate that the analysis based on passage-averaged values are not valid for the prediction of the annulus-wall boundary layer growth in a rotor.

The axial and tangential velocity profiles at $X = 0.75$ are shown in Fig. 12. The velocity profiles show a substantial change between $X = 0.5$ and $X = 0.75$. The boundary layers are thicker near the suction surface and thinner near the pressure surface. The leakage flow, which had a major influence on the velocity profiles at $X = 0.5$, seems to have diffused and mixed with the mainstream at this location. The trend toward separation observed at $Y = 0.05$ and 0.25 at $X = 0.5$ appears to have disappeared at this location. The magnitude of the dip in the relative tangential velocity profile (near the blade tip) is reduced, indicating that the influence of leakage flow is somewhat diffused even though the radial extent of the influence has increased from $X = 0.5$ to 0.75. This is consistent with the C_p distribution observed at $X = 0.5$ and $X = 0.75$. The pressure distribution and the velocity profiles shown in Figs. 6 and 12 show the spreading of the leakage flow; the minimum pressure has also decreased substantially between the two locations. Hence, the core of the vortex is not as strong as it was at $X = 0.5$. The boundary layers are still thick but variation between the suction surface and the pressure surface is not as pronounced as that observed at $X = 0.5$ (Fig. 11).

The velocity profiles at $X=1.0$, shown in Fig. 13, indicate the influence of mixing between the leakage and the mainstream flows. The sharp relative tangential velocity gradient close to the wall observed earlier is reduced substantially due to diffusion of the leakage jet or vortex. The boundary layer behavior shows a tendency toward uniformity from the pressure to the suction surface. The dips in the relative tangential velocity profiles (even though smaller than those observed for $X<1.0$) still persist, indicating that the strength of the leakage vortex and leakage flow is still appreciable. This effect persists for the most part near the middle of the passage at $Y=0.5$ and 0.75. This indicates a tendency for the leakage vortex to move away from the suction surface and toward the pressure surface; this is consistent with the C_p distribution shown at this location in Fig. 7. Most of the vortex influence is confined between $Y=0.5$ and $Y=1$ as is evident from data given in Figs. 7 and 13. The intensity of the leakage vortex seems to have decreased, and even though the vortex is larger it is not as strong at the core as it has been at other locations.

The velocity profile at one axial chord downstream of the trailing edge, shown in Fig. 14, indicates that the boundary layer velocity profiles have become nearly uniform. Even though the wake regions close to $Y=0.05$ and 0.95 seem to indicate that the three dimensionality of the boundary layer still exists at these locations, the influence of the leakage flow and vortex seems to be substantially lower. There is an indication that the leakage vortex is weak at this location and has spread out considerably. This is confirmed by the C_p contours shown in Fig. 8.

Passage-Averaged AWBL Profiles. The annulus-wall boundary layer development based on the passage-averaged mean velocities is shown in Fig. 15. This information is very important since most of the calculation techniques (Mellor and Wood, 1971; DeRuyck and Hirsch, 1981; Horlock and Perkins, 1974) are based on pitch-averaged velocity profiles. It is clear from the data that the irregularities that eixt in the profiles at various locations inside the passage (caused by the tip leakage flow and vortex) have been reduced or eliminated in the averaging process. The AWBL (based on mean axial velocity) grows fairly rapidly from $X=0$ to $X=0.5$. The AWBL based on the mean tangential velocity shows a similar trend. Cross flows are large from the blade leading edge to downstream of the trailing edge.

No attempt has been made to derive momentum thickness based on the mean local velocity profile. It is extremely difficult to distinguish where the inviscid velocity will end and the

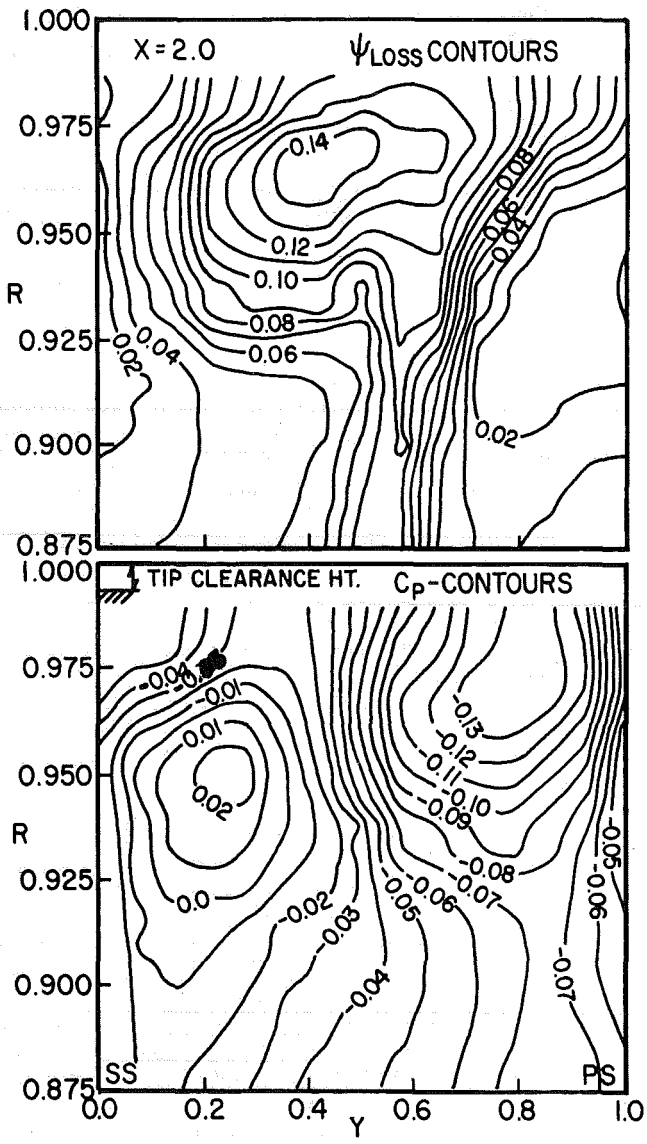

Fig. 8 C_p and ψ_{loss} contours in the blade tip region at $X=2.0$

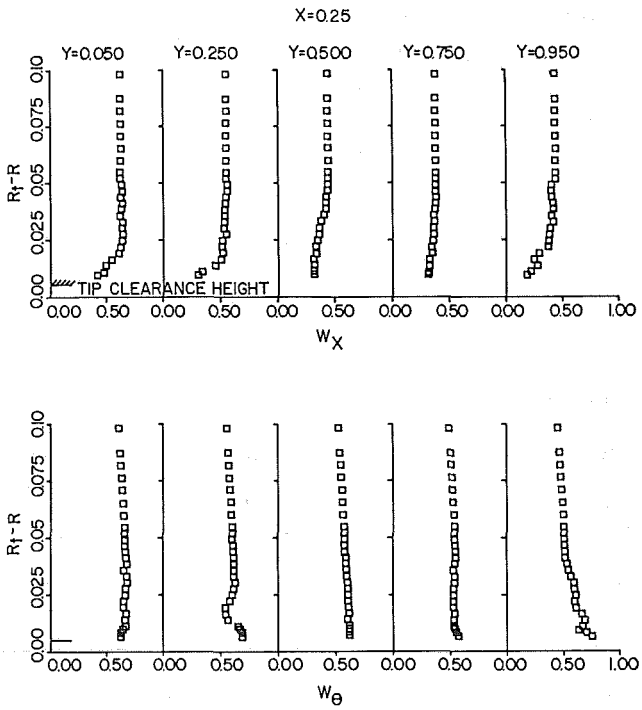

Fig. 9 Axial and relative tangential velocity profiles in the AWBL at $X=0.25$

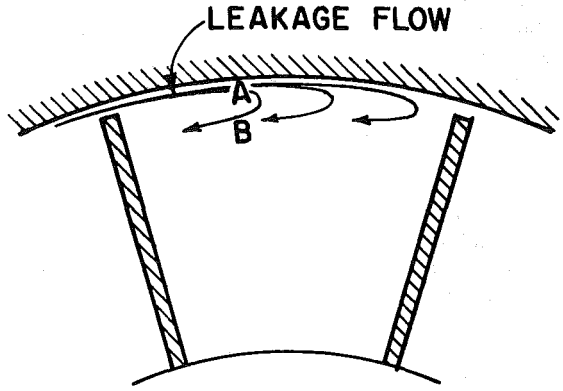

Fig. 10 Nature of leakage flow in the tip region

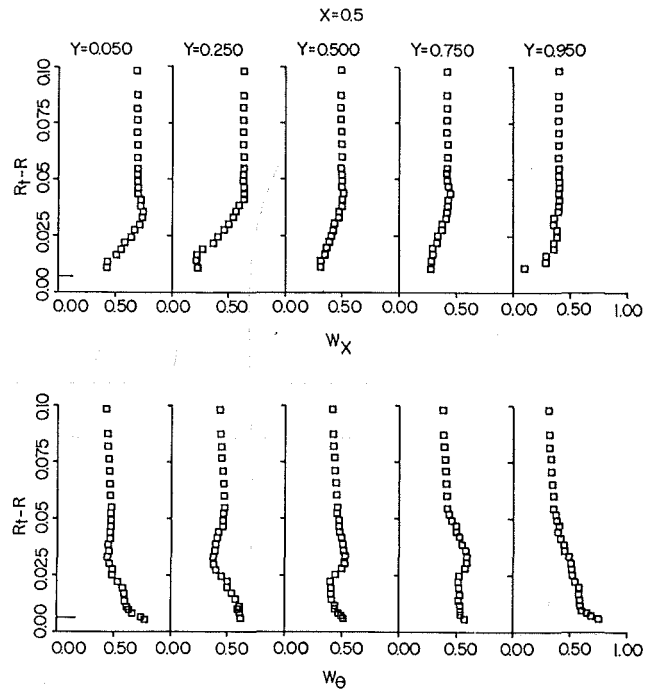

Fig. 11 Axial and relative tangential velocity profiles in the AWBL at $X = 0.5$

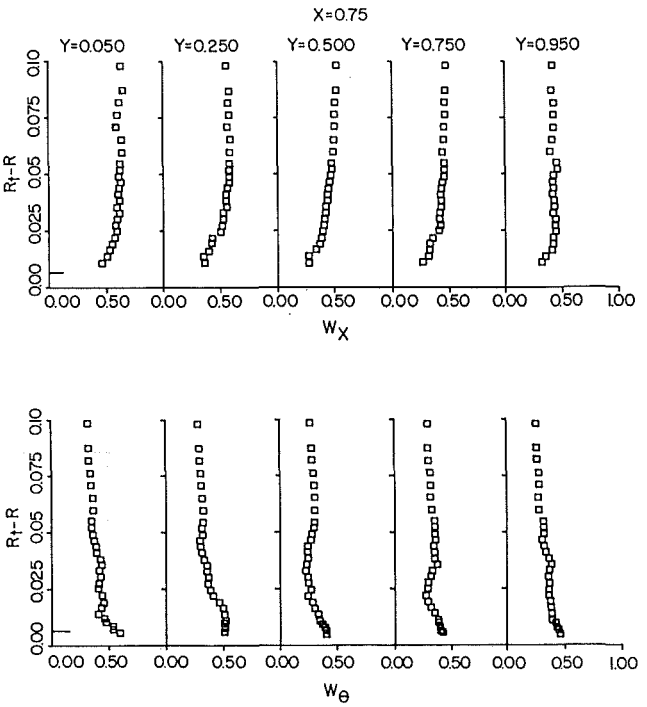

Fig. 12 Axial and relative tangential velocity profiles in the AWBL at $X = 0.75$

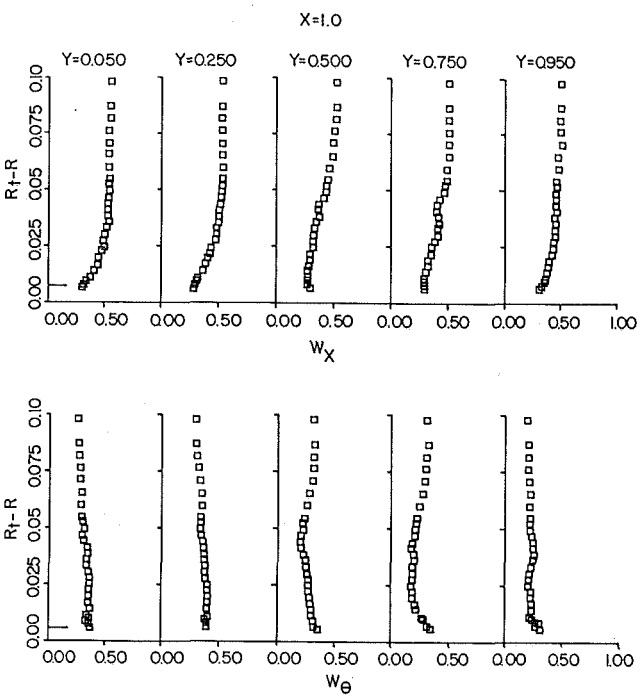

Fig. 13 Axial and relative tangential velocity profiles in the AWBL at $X = 1.0$

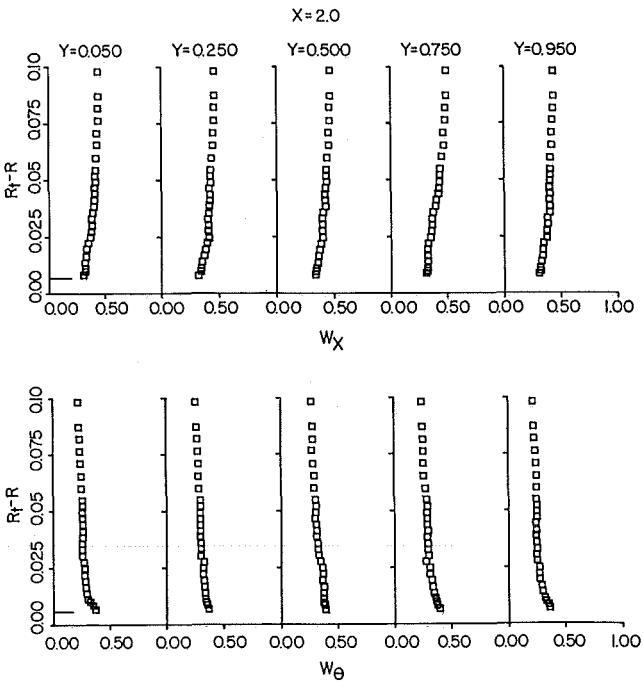

Fig. 14 Axial and relative tangential velocity profiles in the AWBL at $X = 2.0$

boundary layer begin. Furthermore, the profiles near the wall in the tip clearance region could not be obtained by the LDV system. Hence, any calculation of the momentum thickness should involve extrapolation of the data, thus introducing considerable inaccuracy. Some of the data on the momentum thickness variation upstream and downstream of the rotor, based on the five-hole probe measurement and comparison with the prediction, are given by Lakshminarayana et al. (1983). The thrust of the present paper is to present AWBL profiles derived from the LDV measurement within the passage and to interpret the data.

Spanwise Variation of Lift Coefficient. One of the assumptions made in analysis of the leakage flow, based on the lifting line theory, is that part of the lift is retained at the tip (Lakshminarayana, 1970). Thus, the tip vortex associated with the leakage flow is viewed as circulation shedding caused by partial unloading of the blade tip. It is interesting to study the variation of lift along the blade span. The lift coefficient was computed by integrating the static pressure coefficient along the blade surface at a radial location. The static pressure was derived from the total pressure and the velocity measurements, using a Kiel probe and LDV, respectively. Static pressure closest to the blade surface is assumed to be

static pressure on the blade surface. Lift coefficient based on the blade element theory was computed using the equation

$$C_L = 2\frac{S}{C}(\tan\beta_1 - \tan\beta_2)\frac{\cos^2\beta_1}{\cos\beta_m} \quad (1)$$

where β_1, β_2, and β_m are relative inlet, outlet, and mean angles, respectively, and S is the blade spacing. The fraction of lift retained k is the ratio of lift calculated from the derived blade pressure distribution and the lift calculated from the blade element theory. The value of k at various radial locations is plotted in Fig. 16. Also shown is the value of k derived from the direct measurement of blade pressure distribution (Sitaram and Lakshminarayana, 1983).

Even though there is some disagreement between the two sets of data, the plot shows that the blade is partially unloaded from tip to about 5 percent of the span from the tip.

Stagnation Pressure Losses in the Annulus-Wall Region. Subsequent to the investigations reported by Lakshinarayana et al. (1986), a more systematic approach was taken and stagnation pressures were measured at a large number of axial, radial, and tangential stations. The data given in this paper are more comprehensive that those presented by Lakshminarayana et al. (1986). The loss contours (ψ_{loss}) are shown in Figs. 4–8 for $X=0.25$, 0.5, 0.75, 1.0, and 2.0, respectively. The loss contours are reported in the same figure as the C_p contours, and this provides a logical comparison between the two.

The losses are small at $X=0.25$ (Fig. 4). This is confined to a very small region close to the blade tip near the pressure surface. The losses increase as the flow travels from $X=0.25$ to $X=0.5$, where the loss region has spread to nearly half the blade passage, up to about 8 to 9 percent of the blade span from the tip. The loss coefficient in the core region is quite high and its value is about 0.19. This region, where a leakage vortex seems to have formed, has the appearance of a combined vortex. The losses increase as the flow travels from $X=0.5$ to $X=0.75$ even though the peak losses remain about the same as at the earlier station. This indicates that the extent of the tip vortex region has increased, even though the properties of the core have not changed significantly. Here again the C_p contours and ψ_{loss} contours are very consistent. At $X=1.0$ (Fig. 7), the loss contours have spread across the entire passage and up to 15 percent of the span from the blade tip. The peak loss coefficient of 0.16 observed at this station is not significantly different from the observed values at earlier stations, but the passage-averaged losses are higher; this will be discussed later. As the flow travels to $X=2.0$, core losses tend to decrease and the leakage vortex to spread out (see Fig. 8). This plot clearly shows the interaction between the leakage flow the wake. The effect of leakage flow is to displace the wake, which is originally in the radial direction at the trailing edge. The losses now have spread to about 15 percent of the span and across the entire passage. Here again there is a close correlation between C_p contours and the loss contours.

The mass-averaged loss coefficient (averaged across the entire passage) is shown in Fig. 17 at various axial locations. The losses at $X=0.25$ are negligible and are confined to 5 to 6 percent of the span from the blade tip. From $X=0.25$ to $X=0.5$, there is substantial change in the loss coefficient distribution, both in magnitude and extent. The losses extend up to about 7–8 percent of the span from the tip of the blade. Beyond this region peak losses do not increase significantly, but losses at other spanwise locations show some substantial increases at $X=0.75$. The increase in losses between $X=0.75$ to 1.0 is negligible, but beyond this region the increase in loss is substantial, indicating an interesting phenomenon. Most of the leakage formation/vortex losses seem to occur from one-quarter chord to three-quarters chord, and the peak losses occur slightly away from the blade tip. This is probably the location of the core of the tip vortex. It seems to indicate that the leakage vortex formation is nearly complete at $X=0.75$. Downstream of the trailing edge, there is a large mixing of the leakage flow with the wake resulting in an increase in the losses from $X=1.0$ to 1.41. Major redistribution of the flow

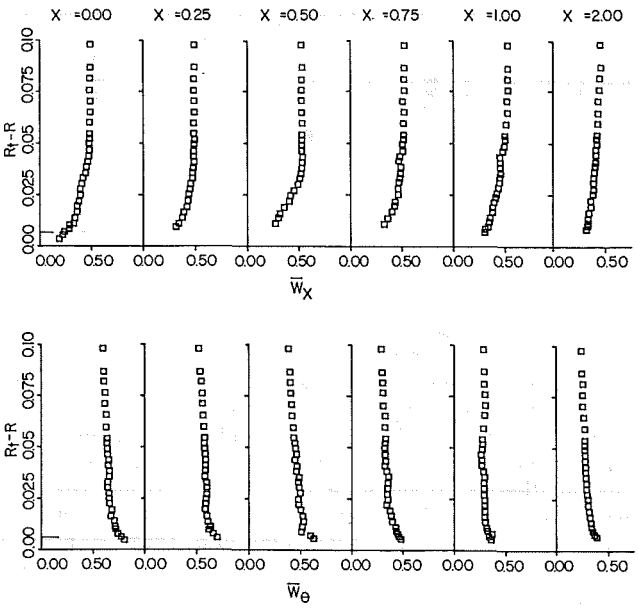

Fig. 15 AWBL profiles based on passage-averaged mean velocities

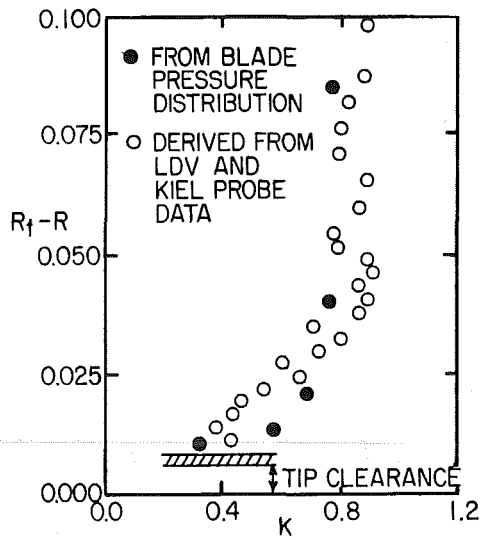

Fig. 16 Radial distribution of k, the fraction of the retained lift

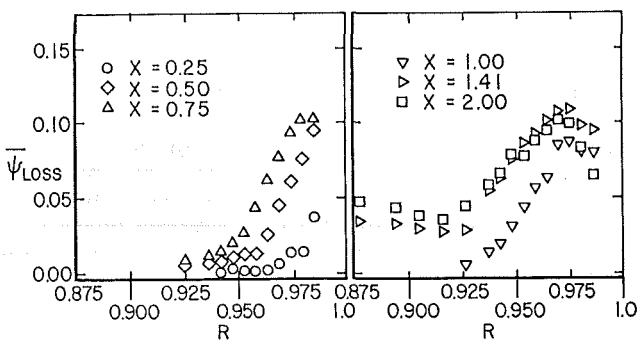

Fig. 17 Radial distribution of mass averaged loss coefficient

field occurs beyond the trailing edge, and maximum losses occur at less than a half-chord from the trailing edge, beyond which the losses remain substantially the same.

Conclusions

1 It is evident from the data presented in this paper that the annulus wall boundary layer growth inside the rotor passage is complex and is modified greatly by the leakage flow and pressure gradient.

2 The velocity distribution inside the rotor passage was unconventional, with considerable three dimensionality and skewness in the profiles.

3 The axial velocity profiles at midchord, where the leakage flow influence was intense, showed a tendency toward separation.

4 The annulus-wall boundary layer profiles were modified considerably by the leakage flow. The tangential velocity distribution shows the influence of the leakage flow, resulting in "jet" and "wake" type profiles inside the AWBL.

5 The influence of leakage flow on AWBL decreases considerably as the flow progresses downstream of the trailing edge.

6 The boundary layers are generally thicker on the suction side, and thinner on the pressure side. The boundary layer profiles and thicknesses vary considerably from blade to blade, and show a tendency toward axisymmetric boundary layer far downstream of the trailing edge.

7 The velocity distribution inside the rotor passage suggests that none of the known velocity models can possibly fit the measured distribution.

8 The pressure coefficient derived from the Kiel probe data and LDV data indicate the presence of a leakage vortex whose strength is significant beyond midchord. This data also shows that the core of the vortex moves toward the pressure surface.

9 The data on the mass-averaged loss coefficient indicate that most of the losses occur from one-quarter to three-quarter chord. Large mixing between the wake and the leakage flow results in increased losses from the trailing edge to about a half-chord downstream.

Acknowledgments

This work was supported by the National Aeronautics and Space Administration through Grant NSG 3212, with Dr. P. Sockol as the grant monitor.

References

DeRuyck, J., and Hirsch, C., 1981, "Investigations of an Axial Compressor End Wall Boundary Layer Prediction Method," ASME *Journal of Engineering for Power*, Vol. 103, pp. 20–33.

Horlock, J. H., and Perkins, H. J., 1974, "Annulus Wall Boundary Layers in Turbomachines," AGARD AG 185.

Hunter, I. H., and Cumpsty, N. A., 1982, "Casing Wall Boundary Layer Through an Isolated Compressor Rotor," ASME *Journal of Engineering for Power*, Vol. 104, p. 805.

Lakshminarayana, B., 1970, "Method of Predicting the Tip Clearance Effects in Axial Flow Turbomachinery," ASME *Journal of Basic Engineering*, Vol. 92, No. 3, pp. 467–481.

Lakshminarayana, B., 1980, "An Axial Flow Compressor Facility Designed for Flow Measurements in a Rotor Passage," ASME *Journal of Fluids Engineering*, Vol. 102, No. 4, pp. 402–411.

Lakshminarayana, B., Pouagare, M., and Davino, R., 1982, "Wall Boundary Layer Development Near the Tip Region of an IGV of an Axial Flow Compressor Rotor Passage," Parts I and II, ASME *Journal of Engineering for Power*, Vol. 104, pp. 760–781.

Lakshminarayana, B., et al., 1983, "Annulus Wall Boundary Layer Development in a Compressor Stage, Including the Effects of Tip Clearance," AGARD CP 351.

Lakshminarayana, B., Sitaram, N., and Zhang, J., 1986, "End Wall and Profile Losses in a Low Speed Axial Flow Compressor," ASME *Journal of Engineering for Gas Turbines and Power*, Vol. 108, pp. 22–31.

Mellor, G. L., and Wood, G. M., 1971, "An Axial Compressor End Wall Boundary Layer Theory, ASME *Journal of Basic Engineering*, Vol. 93, pp. 300–316.

Murthy, K. N. S., and Lakshminarayana, B., 1986, "Laser Doppler Velocimeter Measurements in the Tip Region of a Compressor Rotor," *AIAA Journal*, Vol. 24, No. 5, pp. 807–814.

Sitaram, N., and Lakshninarayana, B., 1983, "End Wall Flow Characteristics and Overall Performance of an Axial Flow Compressor Stage," NASA CR 3671.

Characterization of Shock Wave-Endwall Boundary Layer Interactions in a Transonic Compressor Rotor

D. C. Rabe

A. J. Wennerstrom

Aero Propulsion Laboratory,
Air Force Wright Aeronautical Laboratories,
Wright-Patterson Air Force Base, OH 45433

W. F. O'Brien

Mechanical Engineering Department,
Virginia Polytechnic Institute
and State University,
Blacksburg, VA 24061

The passage shock wave-endwall boundary layer interaction in a transonic compressor was investigated with a laser transit anemometer. The transonic compressor used in this investigation was developed by the General Electric Company under contract to the Air Force. The compressor testing was conducted in the Compressor Research Facility at Wright-Patterson Air Force Base, OH. Laser measurements were made in two blade passages at seven axial locations from 10 percent of the axial blade chord in front of the leading edge to 30 percent of the axial blade chord into the blade passage. At three of these axial locations, laser traverses were taken at different radial immersions. A total of 27 different locations were traversed circumferentially. The measurements reveal that the endwall boundary layer in this region is separated from the core flow by what appears to be a shear layer where the passage shock wave and all ordered flow seem to end abruptly.

Introduction

Continued advances in transonic axial-flow compressor designs require an increased understanding of the actual flow field behavior. With advances in laser anemometry, detailed nonintrusive measurements can now be made within complex compressor flow fields. Through a comparison with these detailed compressor flow field measurements, analytical models may be improved to the level where they can predict the complete compressor flow field behavior. This capability will enable designers to improve transonic compressor designs.

From a design standpoint, compressor performance improvement usually means a reduction of losses, which will result in increased efficiency. Three categories of losses in a transonic compressor without part-span shrouds have been identified [1]: (1) losses due to the blade profile and wake, (2) endwall, boundary layer, and clearance losses, and (3) shock losses. Shock losses are defined to include only the losses due to shock waves in the primary flow field. Losses resulting from the intersection of a shock wave with the blade and endwall boundary layers are included in the blade profile and endwall losses, respectively. The characterization of the passage shock wave-endwall boundary layer interaction reported here helps to improve the understanding of shock losses and the tip endwall boundary layer development in a transonic flow compressor.

Contributed by the Gas Turbine Division of THE AMERICAN SOCIETY OF MECHANICAL ENGINEERS and presented at the 32nd International Gas Turbine Conference and Exhibit, Anaheim, California, May 31–June 4, 1987. Manuscript recieved at ASME Headquarters February 17, 1987. Paper No. 87-GT-166.

Background

Many experimental studies on axial flow compressors have been performed to investigate the flow behavior within a rotor passage. These studies have incorporated gas fluorescence techniques [2], hot wire probes [3], holographic techniques [4–6], and laser Doppler [7–13] and laser transit [14–18] anemometer measurements. Generally, these studies have been directed at an understanding of the complete compressor flow field. Most investigators [4–8, 10–13, 16–18] have enhanced the measurement technique or used the measurement technique to investigate the details of the compressor flow field. Some of the other studies [2, 9, 14, 15] have been mainly directed at comparing the detailed flow field measurements with computational results.

Two related papers [3, 10] were studies of the detailed flow field behavior near the tip of a low-speed compressor rotor. The present study investigates this region in a state-of-the-art low-aspect-ratio transonic compressor. This region of the flow is important because it can contribute significantly to the overall losses of the rotor. Using established prediction guidelines [1], the efficiency loss associated with the tip endwall flow can be estimated. For an entrance boundary layer displacement thickness of about 8.6 mm, the compressor studied in this work would have an estimated 3 percent efficiency loss due to the tip endwall boundary layer losses. Therefore, this region of the flow field can contribute significantly to the losses in a compressor.

Experimental Hardware

The test compressor used in the investigation is a two-stage transonic compressor that incorporates low-aspect-ratio

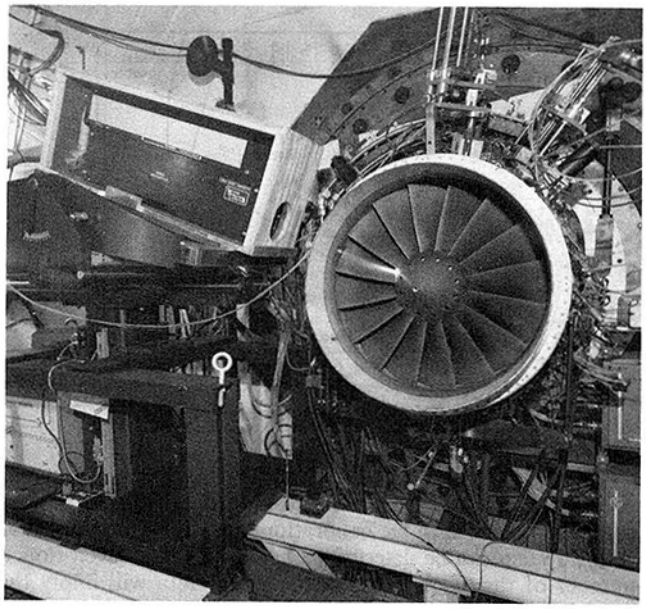

Fig. 1 LTA compressor measurement setup

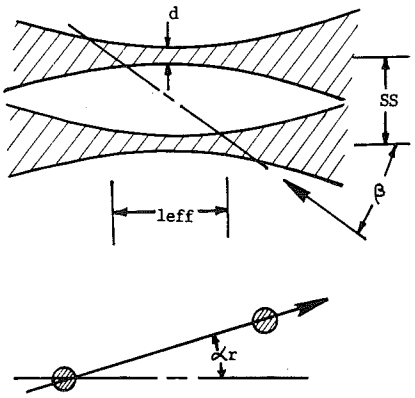

Fig. 2 LTA probe volume geometry

blading. It is configured without inlet guide vanes. The flow field measurements were performed in the first-stage rotor, which has 16 blades. The blade aspect ratio of this stage is 1.00, based on the average span divided by the root axial chord. The inlet hub-to-tip ratio of the first stage is 0.29, and the tip clearance near the peak efficiency speed was measured to be 0.22 percent of the radius of the compressor. Figure 1 shows the overall experimental configuration in the Compressor Research Facility. With the inlet ducting and bellmouth removed from the compressor, the first-stage rotor is completely visible.

Laser System. The optical head of the laser transit anemometer (LTA) used in the investigation is shown to the left of the compressor in Fig. 1. The LTA system was manufactured by Spectron Development Laboratories, Incorporated. References [16] and [19] describe the principles of operation of the LTA. A description of the correlex used to process the LTA signal has been presented by Mayo and Smart [20]. The LTA optical system produces two parallel beams of light from a single input laser beam with an optical power of approximately 0.7 W. The two parallel beams are then focused in the flow field to form two small spots separated by a distance SS (see Fig. 2). Back-scattered light from dust or artificially induced seed particles is detected by two photomultiplier tubes, one viewing each spot. The term dust is used here to signify any natural particles in the atmosphere that will scatter the incident laser light. Since the plane containing the two spots can be rotated, the two spots can be aligned to the velocity vector in the plane perpendicular to the optical axis. The scattered light from particles passing through the two spots can then be cross correlated to yield a histogram of particle transit times. This cross correlation is performed by the correlex mentioned above. The correlex used in this investigation was capable of performing up to 64 different correlations simultaneously. If the dust or artificial seed particles follow the flow, the transit time histogram, along with the spot separation, can yield the absolute flow velocity in the plane perpendicular to the optical axis. From the spot rotation, α_r, the flow angle can be determined.

The probe volume dimensions for the LTA were determined experimentally [21]. The spot separation SS and beam diameter d were determined by measuring the linear beam power distribution at the focal point. A knife edge was translated across the two beams and the transmitted power was recorded as a function of the knife edge position. The beam diameter was considered to be the width of the beam passing 95.5 percent of the beam power and was found to be 0.016 mm. With an output power per spot of approximately 120 mW, the power density at each focal point was approximately 600 W/mm^2. The spot separation measured using the knife edge was 0.279 mm. Therefore, neglecting turbulence effects with this beam diameter-to-spot separation ratio, a particle will theoretically only pass through both spots if the spot rotation angle α_r is within ± 3.3 deg of the absolute flow velocity vector direction projected in the plane of the measurement. This compares favorably with the useful range of about ± 3 deg observed during the experiment.

The effective length of the probe volume was determined using a free jet positioned at different angles to the optical axis in the plane of the two spots. The minimum angle β_{min} between the optical axis and the jet axis, for which velocity measurements could be made, is dependent on the effective length l_{eff}, and spot separation SS. Knowing the minimum angle, the effective length can be calculated from

$$l_{eff} = \frac{SS}{\tan \beta_{min}}$$

With a minimum angle of 33 deg, the effective length was calculated to be 0.430 mm. Again neglecting turbulence effects, the dimensions for the LTA probe geometry would permit measurement of the component of the absolute velocity vector in the plane perpendicular to the optical axis if the following two conditions are met. First, the absolute flow velocity vector must be within ± 57 deg of the measurement plane. Second, the spot rotation must be aligned to within

Nomenclature

d = spot diameter
l_{eff} = effective probe volume length along the optical axis
LTA = laser transit anemometer
S = measurement length along the line of measurement
SS = spot separation distance
Xw = maximum deceleration distance
α_r = spot rotation angle
β = angle between optical axis and flow velocity vector
γ = angle between the shock wave and the normal to the line of measurement

±3.0 deg of the absolute flow velocity component direction in the measurement plane. Therefore, the absolute flow velocity vector can have a significant component in the optical axis direction, and the LTA can still measure its component in the measurement plane.

The LTA, or any laser anemometer, can only measure the behavior of particles carried in the flow that scatter the incident laser light. If the particles do not behave like the flow, then the LTA will not measure the flow behavior. During the compressor testing, polystyrene latex spheres of 0.5 μm diameter were introduced through a probe located approximately 2.0 m upstream of the blade row. This is about three times farther upstream than what was successfully used in a similar configuration [8]. The probe could be translated in the radial direction, and through rotation, the seed could be introduced at different circumferential locations. However, during the experiment, the seed injection location and flow rate had no effect on the observed data rate of the LTA signal. Therefore, all of the compressor measurements reported here are considered to have been made using the natural particles in the atmosphere. The inlet flow to the compressor was filtered to 5.0 μm, so the particles used to measure the flow behavior were less than this diameter. Generally, the use of particles with diameters of 1.0 μm or less is desirable [8, 22]. In normal atmospheric air, the amount of particles with diameters between 1.0 μm and 5.0 μm is 0.01 percent of the number of particles with diameters between 0.1 μm and 5.0 μm, according to the data provided in the FRANK chart [23]. The minimum diameter of 0.1 μm is essentially the smallest seed diameter the LTA is able to utilize for flow measurements. From the distribution of natural particles in the atmosphere, it is felt that the measurement uncertainty based on particle dynamics would be no larger than that reported by Strazisar and Powell [8].

Measurement Errors. Particle dynamics is just one of the many sources of measurement error in laser anemometry. Since the LTA system must be physically moved with respect to the compressor, there are positioning errors. In the measurement of the flow within a rotor, errors are introduced by the timing of the measurement within the blade passage. Statistical errors are introduced by computing the flow velocity from a finite number of particles. Finally, there are bias and precision errors associated with the electronics used to measure the particle transit time. These bias and precision errors are transmitted to the mathematical data reduction algorithms and affect the outcome of the calculation of velocity.

The positioning of the LTA during the experiment was performed using a TSI model 9500 traverse, which is shown in Fig. 1. This traverse has a measurement resolution specification of 2 μm. The timing of the interblade measurement location was performed using a 5 MHz clock. With the compressor rotating at approximately 11,000 rpm, the timing would introduce an uncertainty in circumferential positioning of ±0.013 deg.

The number of measurements required to obtain a 95 percent confidence level that the measured mean velocity is within a certain accuracy is presented by Strazisar [13]. For a turbulence level of 5 percent or less and a desired uncertainty of 2 percent, 25 measurements are required. If only four measurements are used at this turbulence level, the uncertainty will increase to 5 percent. Generally more than 25 measurements were made at each location in the flow field; however, data were only excluded if fewer than 10 measurements were made. Therefore, the statistical accuracy of the data presented is generally better than 2 percent but may be closer to 5 percent in some cases.

The bias and precision errors for the LTA system can be investigated experimentally. Employing a calibration technique previously reported [21], the electronic and calculation bias error can be reduced to the calibration bias. The precision error of the system can be determined by measuring a given flow a number of times, and the scatter in the data will imply the precision error. From an experiment of this type, the standard deviation of the velocity measurement was found to be 0.15 percent of the measured velocity. Therefore, an uncertainty of ±0.3 percent with a confidence level of 95 percent is indicated for the precision error of the velocity measurement.

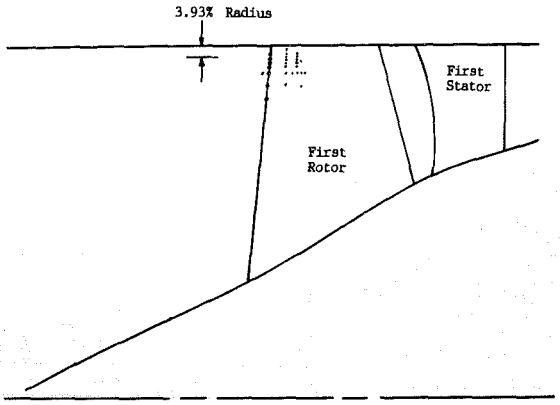

Fig. 3 LTA measurement locations

Test Results and Discussion

The axial and radial locations measured in the transonic compressor are shown in Fig. 3. Measurements were made in the fifth and the seventh blade passages of the first-stage rotor. These passages are counted clockwise from the zero blade passage, which is illuminated by the laser light in Fig. 1.

The circumferential distance was usually divided by the timing network into 17 circumferential locations per blade passage. This resulted in each data collection window being about 5.5 percent of the blade-to-blade distance. Particle transits measured anywhere along this measurement length are considered to represent the velocity at the middle of this window. Data were collected based on a time limit of 3–5 min per angle. Generally five angles in 2-deg increments were used to measure the flow on the upstream side of the shock wave while six angles in 3-deg increments were used to measure the flow on the downstream side of the shock wave.

The laser measurements were made near the peak efficiency point of the compressor. During the 50 h of compressor operation, the standard deviations in the pressure ratio, corrected speed, mass flow, and efficiency were 1.14, 0.14, 0.75, and 0.85 percent, respectively. To take the LTA data, the compressor was set to the desired corrected speed and then held at the respective mechanical speed during a laser measurement scan. While the LTA data were being reduced and stored, the compressor speed was adjusted, if necessary, to the desired corrected speed.

The inlet absolute velocity profiles for five of the radial locations measured at the leading edge of the blade are shown in Fig. 4. The absolute velocity is presented as a percent of an average blade-to-blade absolute velocity within the blade row. The velocity is plotted from the suction side (0 percent blade passage) to the pressure side. The next suction side is at 100 percent blade passage in the figure. Figure 4 shows that the inlet velocity profile has a sinuous form across the passage near the endwall. The absolute velocity is generally higher nearer the suction surface than the pressure surface. As the measurements are made closer to the tip endwall, the overall magnitude decays as would be expected. A significant change

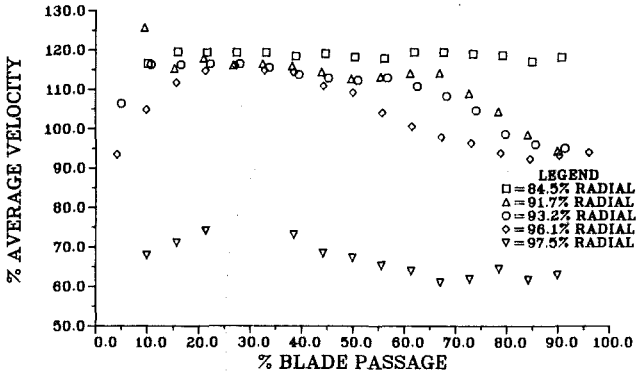

Fig. 4 Absolute velocity profile, 0 percent chord

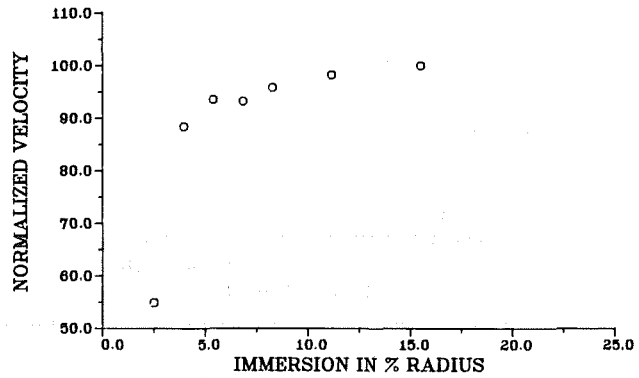

Fig. 5 Inlet endwall boundary layer profile

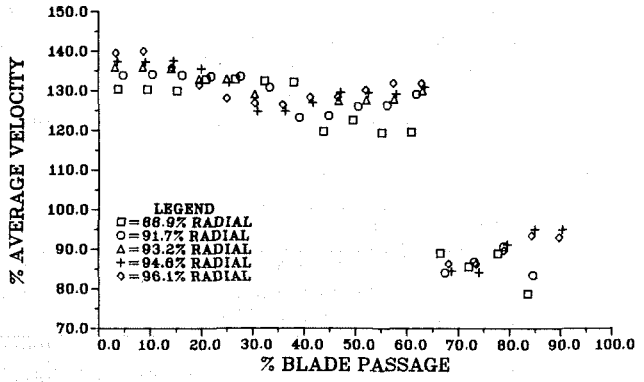

Fig. 6 Relative velocity profile, 12 percent chord

in magnitude is observed between 96.1 and 97.5 percent of the radius. The decay in the velocity from suction side to pressure side, as well as the sinuous behavior, appear to be the result of the precompression waves emanating from the suction surface of the blading in the first 20 percent of the axial chord. A flow pattern with precompression waves has been previously reported [5].

An inlet boundary layer profile composite using the average absolute velocity for each radial location measurement made at the leading edge is presented in Fig. 5. The decay in the velocity as the wall is approached is expected. However, the boundary layer thickness is larger than expected. This is thought to be due to the extra 1.5 m extension of constant area ducting upstream of the compressor inlet leading to the bellmouth.

Results for five of the radial locations measured at the 12 percent axial chord location are shown in Fig. 6. In this figure, the relative velocity is presented as a percentage of the average

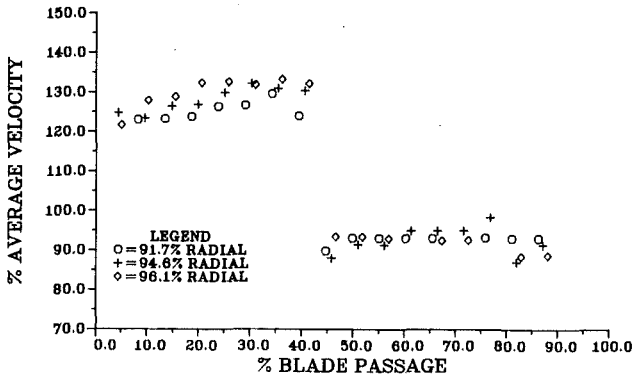

Fig. 7 Relative velocity profile, 22 percent chord

blade-to-blade relative velocity within the blade row. The passage shock wave, located at 64 percent of the blade passage, is observed to be at a constant position within the passage for all radial locations presented. Some scatter in the level of measured velocity exists on the upstream side of the passage shock wave. A closer look at this region reveals that at different depths the behavior changes. At a depth of 88.9 percent a change in velocity at 42 percent of the blade passage is sudden and discrete. As the measurement location moves toward the endwall, the velocity changes more gradually and approaches a sinuous behavior similar to that observed at the leading edge. The variations in relative velocity between the suction surface and the middle of the passage are again attributed to precompression waves emanating from the suction surface of the blade within the passage. The precompression waves tend to spread out across the passage as the tip endwall is approached.

When a measurement was attempted at 96.8 percent radius, only three measurements were obtained from the 17 locations across the blade passage. These measurements were observed at 10, 67, and 73 percent of the blade passage. The magnitude of the three velocity measurements obtained at these circumferential locations is consistent with measurements at 96.1 percent of the radius. The measurements made at 96.1 percent of the radius showed no unusual behavior. Turbulence level was indicated to be essentially the same as at other radial locations (less than 5 percent). Even though only three velocity values are reported at the 96.8 percent radial location, particle transit times were observed at the other locations by the LTA system. These particle transits, however, were uncorrelated. The angle of velocity search was widened and eventually included purely circumferential flow, but still no additional correlated signals were observed. Measurements were attempted closer to the endwall, but no correlated signals were observed. Three possible reasons are offered as to why a correlated signal was not observed at more locations beyond 96.1 percent of the radius. First, the absolute velocity vector direction could be outside the region of acceptable angles for the LTA spot orientation as stated earlier. Second, the turbulence level could be greater than 20–30 percent where the LTA cannot make measurements because of its probe volume geometry. Third, the flow could be much slower than the expected velocity. In any event, the change in the flow field behavior occurred abruptly over a distance of only 0.7 percent of the radius. This abrupt change indicates that there is a shear layer between the well-ordered core flow region and the endwall boundary layer region. A previous study by McDonald et al. [14] presents LTA measurements at a percent of span that would correspond to the 96.1 percent radial location in the compressor studies here. However, there is no report in this reference of measurements closer than this to the endwall.

Relative velocity measurements at three of the radial loca-

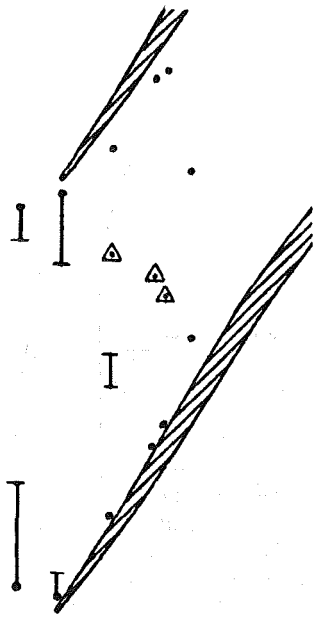

Fig. 8 Flow field behavior at 91.7 percent radius

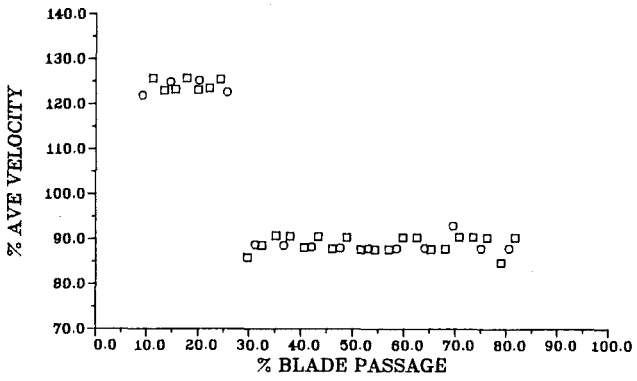

Fig. 9 Relative velocity profile: 25 percent chord; 91.74 percent radius

tions measured at 22 percent of the axial chord location are shown in Fig. 7. Relative velocity is again nondimensionalized by the average velocity used at the previous location. Measurements at all of the radial locations show essentially the same behavior. The passage shock wave is again located at the same position within the blade passage for all radial locations presented. At this location, there is no evidence of the precompression waves observed at the previous two locations. However, the flow field was measured at only two locations at 96.8 percent radius. These measurements were observed at 15 and 80 percent of the blade passage similar to the measurements at 12 percent of the axial chord. Again, the magnitude of measured velocity at these two locations is consistent with the measurements made at 96.1 percent radius at this axial station.

At 12 and 22 percent of the axial chord, the flow became essentially unmeasurable between 96.1 and 96.8 percent of the radius even though measurements at 97.5 percent of the radius were made at the leading edge of the blade (see Fig. 4). This layer between measurable and unmeasurable flow was not only constant in radial position from 12 percent of the axial chord to 22 percent of the axial chord, but it was also at the same depth across the blade passage from the suction surface to the pressure surface. This was not a result of a low data rate in this region, but instead the particle transit times measured in this region were uncorrelated for the transit time range sampled. An attempt was made to measure closer than 96.8 percent of the radius to the endwall. Similar results were observed until the probe volume was so close to window surface (99.0 percent radius) that the reflected light scattered from the window interface prevented any transit measurements.

A composite of all the measurements made at 91.7 percent radius is presented in Fig. 8. The triangles represent discrete jumps in the relative flow velocity and a shock wave similar to that observed in Fig. 7. The bands along the circumferential measurement lines indicate gradual changes in the flow velocity as shown in Figs. 5 and 6 due to the leading edge expansion fan and precompression waves. From Fig. 8, the passage shock wave is estimated to be at an angle of 20 deg to the axial direction at 22 percent of the axial chord. The points near the blade surfaces indicate the maximum extent of the LTA measurements in the circumferential direction.

The observed passage shock wave pattern compares favorably with other transonic compressor rotor studies at peak efficiency. References [4, 6, 9, 11, 14] all present data near or at the peak efficiency. The passage shock wave is reported to be axial [9, 11, 14]. Reference [4] reports a shock wave angle of 20 deg, similar to that seen in Fig. 8, for 90 percent speed and part flow, which would be near the peak efficiency point. The data presented by Moore et al. [6] show that the angle of the shock wave can vary along the 90 percent speed line from axial to 35 deg. Numerous references [4, 6, 9, 11, 14] show that the shock turns toward the suction surface as shown in Fig. 8.

Holographic studies [4, 6] indicate that a leakage vortex develops in the leading edge region of the rotor passage. No evidence of this vortex was observed in the present study, unless it occurred beyond 96.1 percent of the radius where measurements were uncorrelated. For a low-speed compressor, Hah [24] shows in his numerical study of the endwall and tip clearance flows that there would be no effect of the leakage at 95 percent of the radius. Only very near the tip at 99.4 percent of the radius is the tip clearance effect noticed. Similar results for the inlet region of the passage in a low-speed compressor were previously measured [10].

Estimated Particle Size

The size of the particles measured by the laser anemometer can be estimated if the particle deceleration distance behind the shock wave can be determined. The particle deceleration distance perpendicular to the shock wave can be estimated from the measured compressor flow field shown in Fig. 9. This figure presents two sets of measurements made within the same blade passage. The distance used to make a measurement in one case is 5.5 percent of the blade passage, and in the other case, the distance for a measurement is 2.7 percent of the blade passage. With the longer distance, the change in velocity is observed to jump from the velocity before the shock to the velocity after the shock between two adjacent measurement locations. When the distance was 2.7 percent of the blade passage, the velocity changed over *two* measurement locations. This behavior was observed in measurement made in both blade passages. If the deceleration distance of the measured particles is the only factor influencing this result, then a range of deceleration distance can be calculated. Referring to Fig. 10, the maximum deceleration distance Xw perpendicular to the shock wave can be calculated from

$$Xw = \Delta S \cos \gamma$$

In this relationship, ΔS is the measurement length along the line of measurements used to make one velocity measurement, and γ is the angle between the shock wave and the normal to the line of measurements. As noted above, a discrete change in velocity was obtained with a measurement length of 5.5 per-

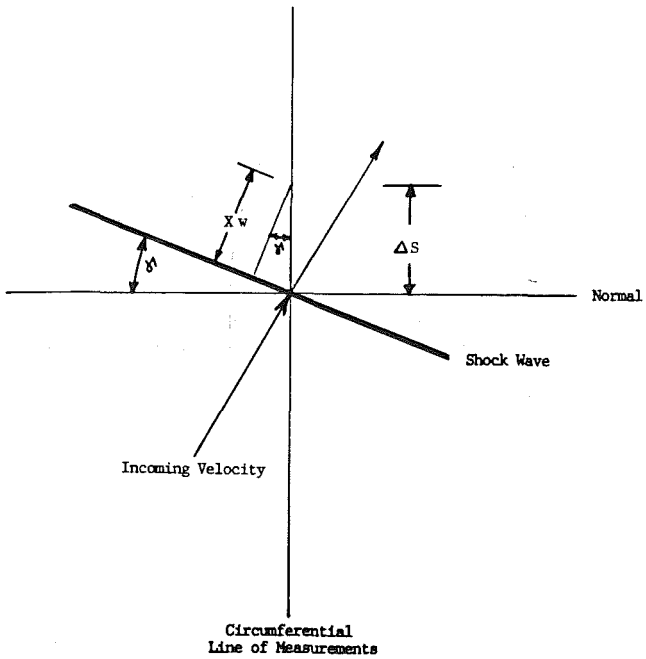

Fig. 10 LTA measurement orientation to passage shock wave

cent of the blade passage but not with 2.7 percent of the blade passage. Therefore, the particle deceleration distance must be between the maximum deceleration distances calculated using these two measurement lengths. For the results obtained in Figs. 8 and 9, the particle deceleration distance would be between 2.9 mm and 5.9 mm. From these distances and the data presented by Melling [22], the particles being measured are considered to be on the order of 0.4 μm to 0.6 μm. This agrees favorably with the expected diameters based on natural dust particles.

This calculation ignores any movements in the shock location that could also cause the loss of data in the finer step measurements. If the shock wave did move, as reported by Strazisar [11], the resolution of the shock location would indicate that the diameter of the measured particles would be even smaller than the range given above. The range of 2.9 mm to 5.9 mm is essentially half of the deceleration distance reported by Strazisar [8], who estimated the seed diameter to be about 1.3 μm.

Summary and Conclusions

An LTA measurement system was successfully used to measure the flow behavior within a transonic compressor. Measurements to investigate the passage shock wave were made at different radial positions at three axial locations near the tip endwall of the compressor. The well-ordered core flow was found to be separated from the endwall boundary layer by what appears to be a shear layer where the flow behavior changes abruptly. The shear layer appears to be at a constant depth between 96.1 and 96.8 percent of the radius from 12 to 22 percent of the axial chord. At the leading edge, no evidence of this flow discontinuity was found in the data taken at the 97.5 percent radial location. However, this radial location is definitely within the endwall boundary layer at the leading edge. The flow discontinuity within the passage also appears to be at a constant depth across the blade passage at 12 and 22 percent of the axial chord. Because of the importance of the losses in the endwall boundary layer, more detailed studies are being planned to investigate this region in subsequent transonic flow compressor tests.

The precompression waves produced by the compressor rotor were also studied. The behavior of the precompression waves in the entrance region and at 12 percent of the axial chord changed with the radial location. Between the 88.9 and 96.1 percent radial locations at 12 percent of the axial chord, the precompression waves went from what appears to be a coalescent shock wave to a series of weak shock waves across 50 percent of the passage. The behavior of a series of weak shock waves was also observed at the blade leading edge. As the endwall was approached at the blade leading edge, the precompression wave is thought to have caused the observed sinuous velocity profile.

A method to estimate the seed diameter from the actual LTA measurements is presented. By varying the measurement length, the measured particle deceleration distance can be estimated. If the shock wave is measured discretely, then the deceleration distance of the measured particles must be less than the maximum deceleration distance for that measurement length. The largest particle diameter would be predicted if the measurement length was considered as the maximum deceleration distance. It was estimated in this manner that the diameters of the natural particles in the atmosphere measured in this experiment were on the order of 0.4 μm to 0.6 μm.

Acknowledgments

The test program described within this report was conducted by the Technology Branch of the Turbine Engine Division at the Aero Propulsion Laboratory. The authors wish to acknowledge the contributions of all of those co-workers whose participation made the testing and subsequent data analysis possible. The authors also wish to acknowledge the employees of the General Electric Company who developed the compressor test vehicle.

References

1 Koch, C. C., and Smith, L. H., Jr., "Loss Sources and Magnitudes in Axial-Flow Compressors," ASME *Journal of Engineering for Power*, Vol. 98, 1976, pp. 411-424.

2 Epstein, A. H., Kerrebrock, J. L., and Thompkins, W. T., Jr., "Shock Structure in Transonic Compressor Rotors," *AIAA Journal*, Vol. 17, No. 4, 1979.

3 Lakshminarayana, B., Pouagare, M., and Davino, R., "Three-Dimensional Flow Field in the Tip Region of a Compressor Rotor Passage—Part I: Mean Velocity Profiles and Annulus Wall Boundary Layer," ASME *Journal of Engineering for Power*, Vol. 104, 1982, pp. 760-771.

4 Wuerker, R. F., Kobayashi, R. J., Heflinger, L. O., and Ware, T. C., "Application of Holography to Flow Visualization Within Rotating Compressor Blade Row," NASA CR 121264, Feb. 1974.

5 Benser, W. A., Bailey, E. E., and Gelder, T. F., "Holographic Studies of Shock Waves Within Transonic Fan Rotors," ASME *Journal of Engineering for Power*, Vol. 97, 1975, pp. 75-84.

6 Moore, C. J., Jones, D. G., Haxell, C. F., Bryanston-Cross, P. J., and Parker, R. J., "Optical Methods of Flow Diagnostics in Turbomachinery," *ICIASF '81 Record*, Sept. 1981.

7 Wisler, D. C., "Shock Wave and Flow Velocity Measurements in a High Speed Fan Rotor Using the Laser Velocimeter," ASME *Journal of Engineering for Power*, Vol. 99, 1977, pp. 181-186.

8 Strazisar, A. J., and Powell, J. A., "Laser Anemometer Measurements in a Transonic Axial Flow Compressor Rotor," ASME *Journal of Engineering for Power*, Vol. 103, 1981, pp. 430-437.

9 Pierzga, M. J., and Wood, J. R., "Investigation of the Three-Dimensional Flow Field Within a Transonic Fan Rotor: Experiment and Analysis," ASME *Journal of Engineering for Gas Turbines and Power*, Vol. 107, 1985, pp. 437-449.

10 Murthy, K. N. S., and Lakshminarayana, B., "Laser Doppler Velocimeter Measurements in the Tip Region of a Compressor Rotor," *AIAA Journal*, Vol. 24, No. 5, 1986, pp. 807-814.

11 Strazisar, A. J., "Investigation of Flow Phenomena in a Transonic Fan Rotor Using Laser Anemometry," ASME *Journal of Engineering for Gas Turbines and Power*, Vol. 107, 1985, pp. 427-435.

12 Williams, M. C., "Laser Velocimetry Study of Stator/Rotor Interaction in a Multi-stage Gas Turbine Compressor," *Advanced Instrumentation for Aero Engine Components*, AGARD CP-399, 1986.

13 Strazisar, A. J., "Laser Fringe Anemometry for Aero Engine Components," *Advanced Instrumentation for Aero Engine Components*, AGARD CP-399, 1986.

14 McDonald, P. W., Bolt, C. R., Dunker, R. J., and Weyer, H. B., "A

Comparison Between Measured and Computed Flow Fields in a Transonic Compressor Rotor," ASME *Journal of Engineering for Power*, Vol. 102, 1980, pp. 883–891.

15 Dunker, R. J., Strinning, P. E., and Weyer, A. B., "Experimental Study of the Flow Field Within a Transonic Axial Compressor Rotor by Laser Velocimetry and Comparison With Through-Flow Calculations," ASME *Journal of Engineering for Power*, Vol. 100, 1978, pp. 279–286.

16 Smart, A. E., Wisler, D. C., and Mayo, W. T., Jr., "Optical Advances in Laser Transit Anemometry," ASME *Journal of Engineering for Power*, Vol. 103, 1981, pp. 438–444.

17 Schodl, R., "A Laser Two Focus (L2F) Velocimeter for Automatic Flow Vector Measurements in the Rotating Components of Turbomachines," *Measurement Methods in Rotating Components of Turbomachinery*, ASME, New York, 1980.

18 Schodl, R., "Laser Two Focus Velocimetry," *Advanced Instrumentation for Aero Engine Components*, AGARD CP-399, 1986.

19 Mayo, W. T., Jr., Smart, A. E., and Hunt, T. E., "Laser Transit Anemometer With Microcomputer and Special Digital Electronics; Measurements in Supersonic Flows," 8th ICIASF, Naval Post Graduate School, Monterey, CA, Sept. 24–26, 1979.

20 Mayo, W. T., Jr., and Smart, A. E., "Photon Correlation: A Fast New Digital Processor for Optical Measurements," Poster Paper, CLEO 1982, Phoenix, AZ.

21 Rabe, D. C., and Dancey, C. L., "Comparison of Laser Transit and Laser Doppler Anemometer Measurements in Fundamental Flows," presented at the AIAA/ASME/SAE/ASEE 22nd Joint Propulsion Conference, June 16–18, 1986, paper No. AIAA-86-1650.

22 Melling, A., "Seeding Gas Flows for Laser Anemometry," *Advanced Instrumentation for Aero Engine Components*, AGARD CP-399, 1986.

23 *Air Pollution Engineering Manual*, 2nd ed., Environmental Protection Agency, Research Triangle Park, NC, 1973.

24 Hah, C., "A Numerical Modeling of Endwall and Tip-Clearance Flow of an Isolated Compressor Rotor," ASME *Journal of Engineering for Gas Turbines and Power*, Vol. 108, 1986, pp. 15–21.

The Use of Holographic Interferometry for Turbomachinery Fan Evaluation During Rotating Tests

R. J. Parker

D. G. Jones

Advanced Research Laboratory,
Rolls-Royce plc,
Derby, United Kingdom

Holography has been developed by Rolls-Royce as a technique for routine use in the evaluation of fan designs for aeroengines. It is used to investigate both aerodynamic and mechanical behavior of the rotating fan. Holographic flow visualization provides clear, three-dimensional images of the transonic flow region between the fan blades. Flow features such as shocks, shock/boundary layer interaction, and over-tip leakage vortices can be observed and measured. Holograms taken through an optical derotator allow vibration modes of the rotating fan to be mapped during resonance or flutter. Examples are given of the use of both techniques at rotational speeds up to and in excess of 10,000 rpm. Holography has provided valuable information used to verify and improve numerical modeling of the fan behavior and has been successful in evaluating the achievement of design intent.

Introduction

In the modern, high-bypass aeroengine the fan provides the vast majority of the thrust from the engine. The optimization of fan design is thus paramount for the achievement of the high efficiency and low fuel consumption that the customer demands. Computer-aided design (CAD) plays a key and increasing role in the achievement of this goal. Finite element modeling is used extensively to predict the mechanical behavior of the fan and three-dimensional, time-marching flow prediction is used to assess aerodynamic performance. These advanced computational techniques require a measurement data base for their verification and improvement.

Holography is one of several advanced measurement techniques capable of providing this measurement data base. It is now routinely employed by Rolls-Royce. The purpose of this paper is to review the way in which holographic interferometry has contributed to the understanding of both the mechanical and aerodynamic behavior of the fan through its use on rotating fans in aerodynamic test facilities.

The aeroengine fans investigated by holography were either the traditional shrouded (clappered) fan or the new, wide-chord fan (Fig. 1). In both designs the gas flow field has been investigated. The vibrational behavior of the two fan types is very different, the clappered fan being more prone to coupled blade-and-disk modes of vibration than its newer replacement.

Contributed by the Gas Turbine Division of THE AMERICAN SOCIETY OF MECHANICAL ENGINEERS and presented at the 32nd International Gas Turbine Conference and Exhibit, Anaheim, California, May 31–June 4, 1987. Awarded the Aircraft Gas Turbine Committee's Jim Kamman Best paper Award. Manuscript received at ASME headquarters February 19, 1987. Paper No. 87-GT-236.

Holographic Interferometry

Holography is a photographic technique that, through the use of coherent illumination from a laser, records three-dimensional images of objects. It achieves this by recording and reproducing both the phase and the amplitude of the light scattered from the object. If two or more images are recorded on a single hologram, an interference pattern is formed that

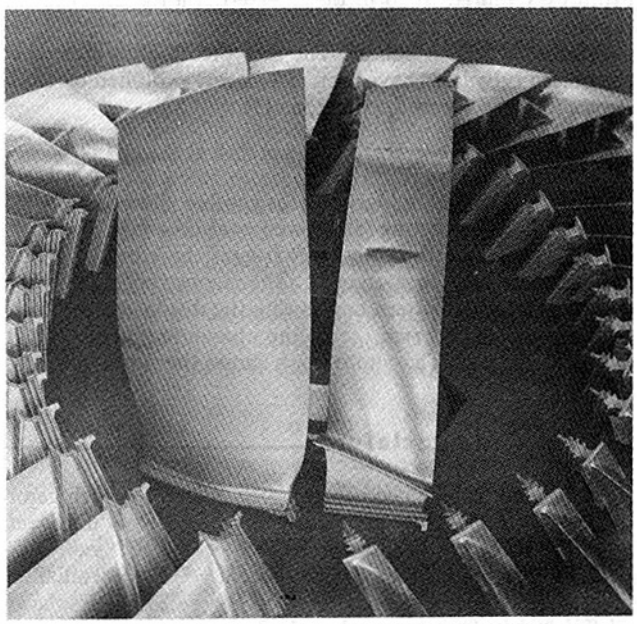

Fig. 1 Comparison of two types of fan blade used by Rolls-Royce: right, clappered (shrouded) blade and left, new wide-chord blade

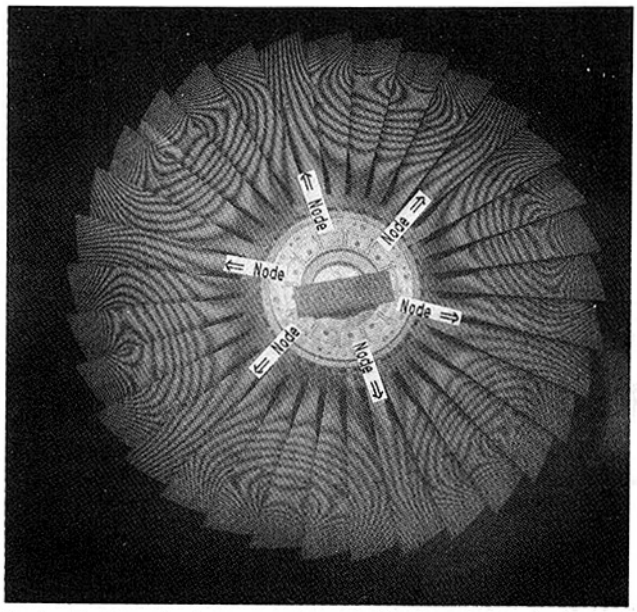

Fig. 2 Double-pulse hologram of nonrotating fan vibrating in the 2F3D mode

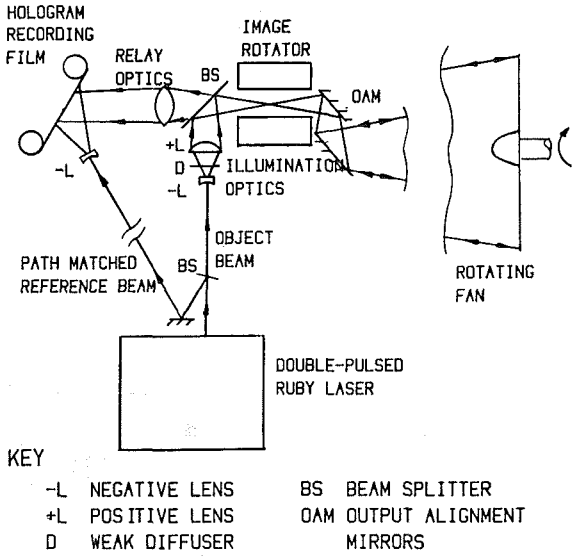

Fig. 3 Schematic representation of the holographic system with optical derotator

contours any change in the scattered wavefronts with a pattern of light and dark interference fringes. These fringe patterns contain information about the change in shape of the object between exposures or the change in refractive index (and density) of the fluid around the object. There are many excellent accounts in the literature of the recording process and the many applications of holographic interferometry [1–4]. There is not space in this paper for a more detailed description of holography.

One major limitation on the use of holography is the extreme stability required during the recording of a hologram. When small, continuous-wave lasers are used, both object and holographic camera must be mounted on a vibration-isolated table in a controlled, laboratory environment. This requirement has been overcome with the development of reliable, high-energy, pulsed ruby lasers. Their very short pulse length (typically 30 ns) allows holograms to be recorded away from the laboratory in hostile environments. The double exposure required to form the interferogram is produced by rapid double-pulsing of the laser. This gives time intervals selectable from 1 to 800 μs. The new possibilities created by the pulsed ruby laser have been extensively exploited by Rolls-Royce in a variety of applications [5].

Holography for Flutter Studies

The use of pulsed holography for routine vibration analysis of nonrotating, vibrating fans is well established [6]. The rapid double pulse from the ruby laser freezes the vibrating fan at two points in the vibration cycle. The reconstructed hologram produces a fringe pattern contouring the displacement during this short time interval, revealing the mode shape of the vibration (Fig. 2). The photograph shows the fan vibrating in a 2F3D mode of vibration. (N.B.: This notation implies that the vibration mode is in the second family, i.e., there is one turning point in the radial distribution of axial displacement, and that there are three diametral repeat cycles: The visible pattern repeats six times around the fan, but adjacent groups of blades are moving in antiphase so that the vibration pattern repeats only three times.)

The fringe map provides information on displacment between the two laser pulses. For each point on the fan, the fringe order (contour level) $N(R, \theta)$ is given by

$$N(R, \theta) = \frac{n}{\lambda} 2(\Delta d \cdot \hat{r}) \tag{1}$$

assuming colinear illumination and observation. For small pulse intervals relative to the period of vibration, the holographic fringe pattern may be treated as an instantaneous map of velocity.

Flutter is a complicated aeroelastic phenomenon in which mechanical vibrations give rise to unsteady aerodynamic forces, which can couple further energy into the vibration. This phenomenon can only be adequately studied and measured in rotating tests on fans under typical centrifugal and aerodynamic loading. Pulsed holography may be used on rotating fans to produce similar fringe maps to those observed in the laboratory. If the vibration amplitude is large so that the pulse interval can be kept very short, the fringes will be clearly visible. As the amplitude decreases, the pulse interval must be increased until a point is reached where significant rotation of the fan has occurred between the two pulses. The limits to this regime were considered by Storey [7]. Once outside these limits, an optical derotator must be employed to hold the image of the fan steady while the two holographic exposures are made [8].

Nomenclature

C = Gladstone-Dale constant $= 2.25 \times 10^{-4}$ m^3/kg for air at 288 K and $\lambda = 694$ nm
n = refractive index of transparent medium
$\hat{n}$ = unit vector normal to the local shock surface
N = fringe order number
$\hat{r}$ = unit vector along the viewing ray
R = radial coordinate on fan
Δd = displacement of point (R, θ) on fan in time interval Δt
Δt = time between laser pulses
$\Delta\rho$ = density change across the shock or flow feature
θ = circumferential coordinate on fan
λ = laser wavelength (ruby = 694 nm)
ω = angular speed of rotation

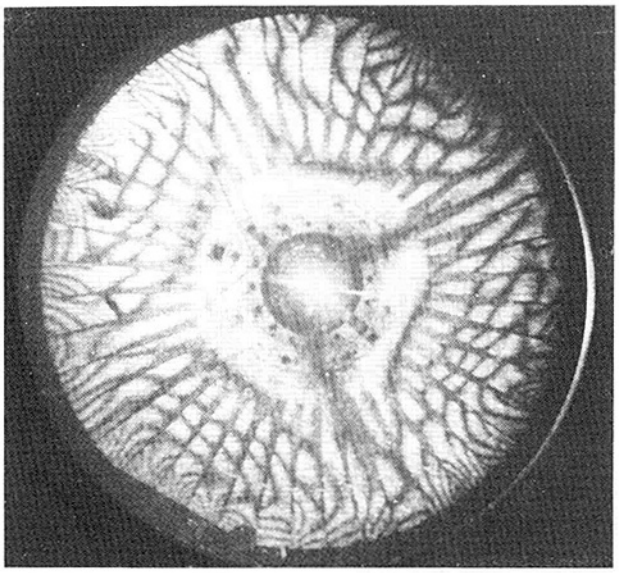

Fig. 4 Hologram of rotating laboratory fan 0.56 m (22 in.) in diameter vibrating in the 2F2D mode, obtained at 4125 rpm

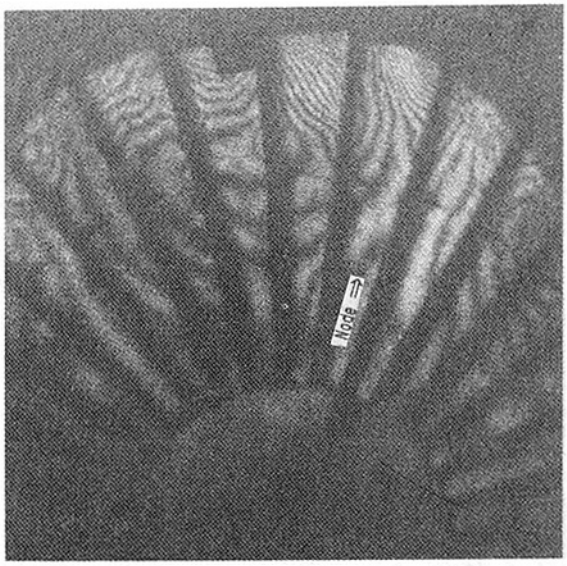

Fig. 6 Hologram of a fluttering fan 0.86 m (34 in.) in diameter rotating at 9890 rpm

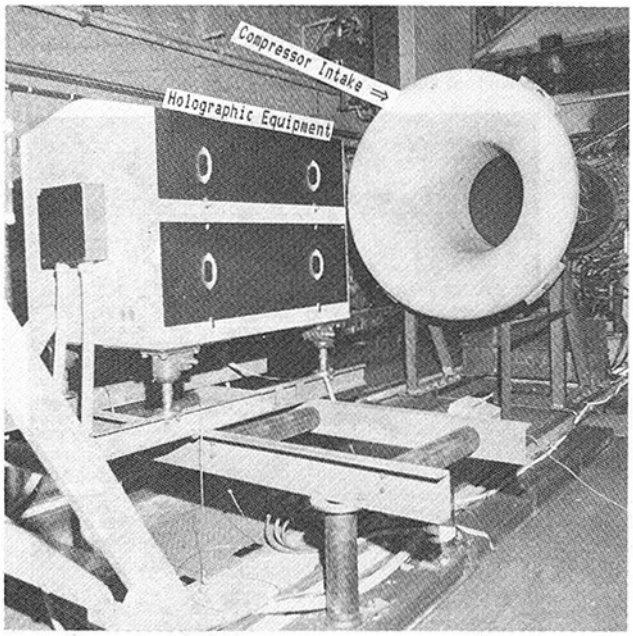

Fig. 5 Photograph showing holographic equipment installed on the compressor test facility

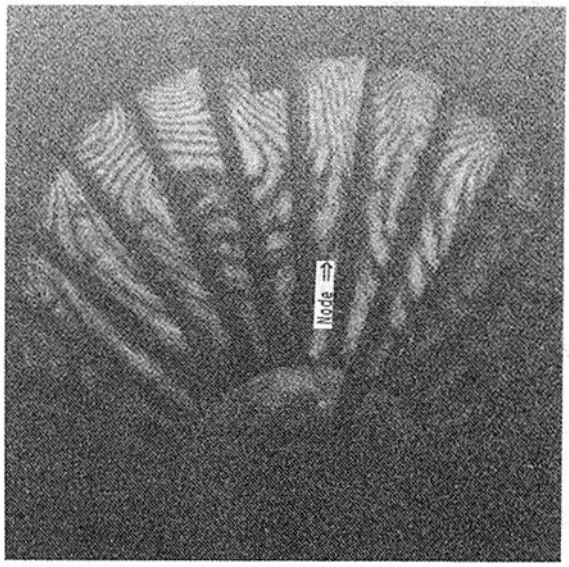

Fig. 7 Similar hologram to Fig. 6 showing the traveling-wave nature of the flutter vibration; speed 9888 rpm

Holographic Apparatus

The holographic system employed is shown schematically in Fig. 3. The derotator used was of a mirror-Abbé design [9] and had an effective f/No. of 7. The speed of the derotator is electronically matched to that of the fan by phase-locked circuitry and shaft encoders on the fan and the derotator motor. It is important that the rotational axes of the derotator and the fan are aligned to a high degree of accuracy (< 1 mm in 6 m). The alignment procedure uses a continuous HeNe laser to define the axis of the derotator [9].

The fan must be painted with a retro-reflective paint (3M 7210 silver Reflective Liquid) to increase the amount of laser light returned to the optical system. During laboratory testing on a small fan in vacuum, using piezo-electric excitation, holograms similar to that shown in Fig. 4 were achieved. This shows a 0.56 m (22 in.) clappered fan vibrating predominantly in a 2F2D mode while rotating at 4125 rpm.

The system has been used to study clappered fan models 0.86 m (34 in.) in diameter on an aerodynamic test facility. Figure 5 shows the holographic equipment installed on the facility. The distance from the holographic unit to the fan was 6 m. This distance is determined by the acceptance cone (F/No.) of the derotator. Other derotator designs would allow much closer positioning of the instrument and the fan [10].

Results

Using this system it was possible to observe only a sector of the 0.86 m fan because of the light loss in the optical system [9]. It was nonetheless possible to observe a fan in supersonic unstalled flutter and in particular to show the traveling-wave nature of the flutter vibration mode. Figures 6 and 7 show two interferograms recorded in flutter. The fan speed was 9890 and 9888 rpm for the two pictures, respectively. The fan is shown to be vibrating in a 2F3D mode. The orientation of the

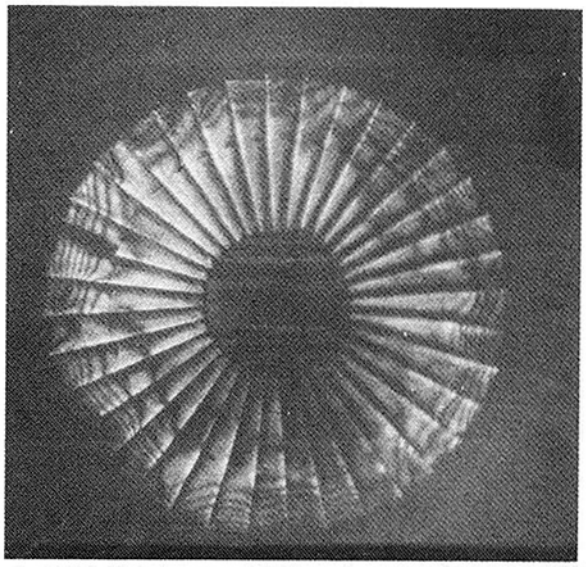

Fig. 8 Full-field hologram of 0.86 m fan excited by engine-order resonance at 5900 rpm

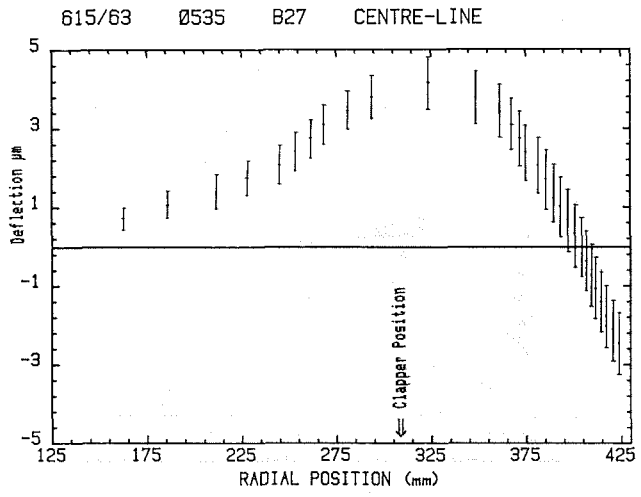

Fig. 9 Measured axial displacement along the centerline of a blade derived from a hologram taken in flutter

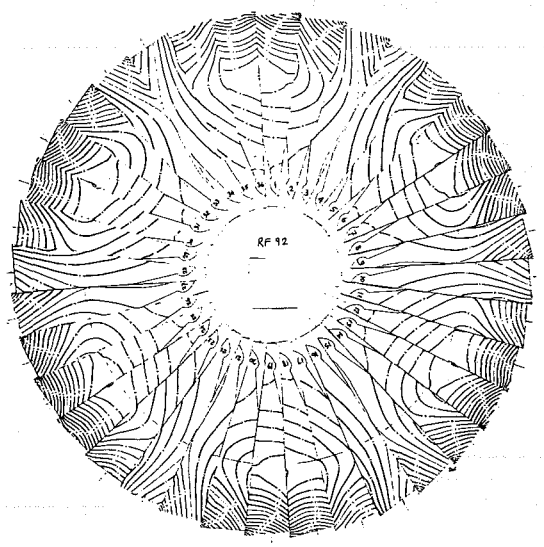

Fig. 10 2F3D vibration mode of a model fan predicted by finite-element analysis

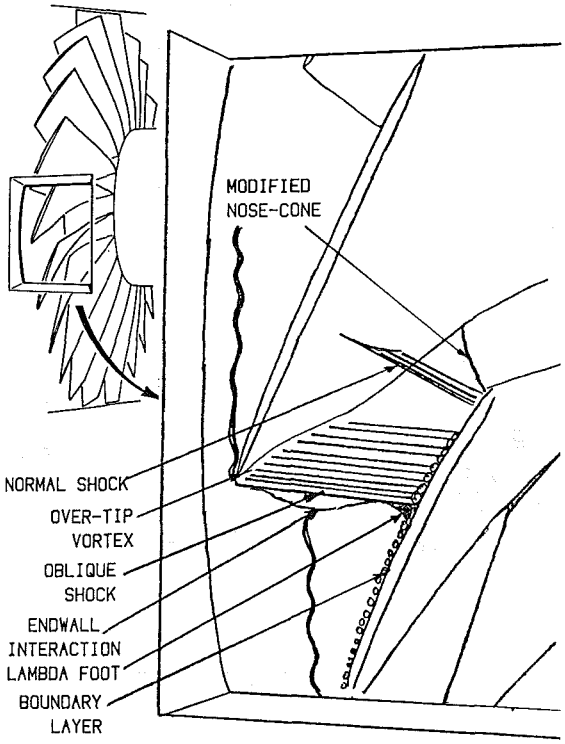

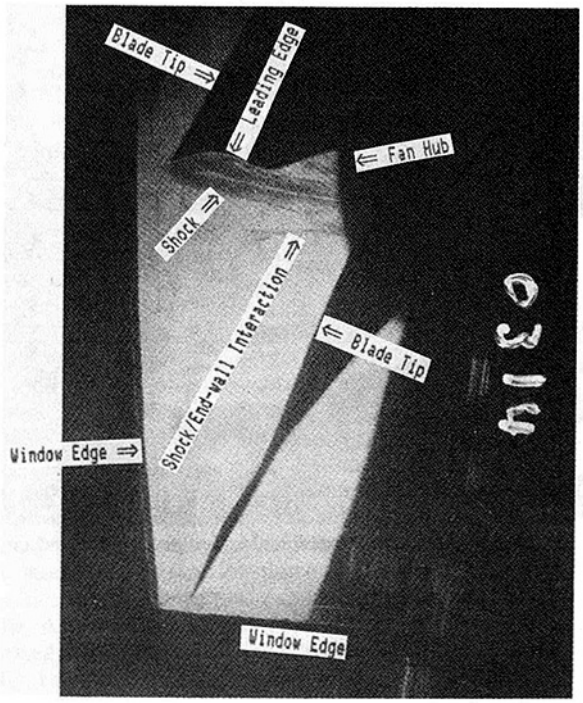

Fig. 11 Sketch showing fan flow features visualized by holography (not all features can be seen in a single hologram). The lower photograph shows a hologram taken at 1 μs pulse separation showing oblique shock with blade geometry indicated.

fan was the same in the two figures, but the phase of the flutter cycle on which the laser was triggered has changed. The progression of the flutter mode relative to the marked blade (black square at leading edge) can clearly be seen.

Further recent advances in this technique have increased the optical efficiency of the holographic system so that a complete instantaneous picture of the 0.86 m diameter fluttering fan can be formed. Recent tests have further studied behavior of fans in supersonic unstalled flutter at 11,000 rpm and have also

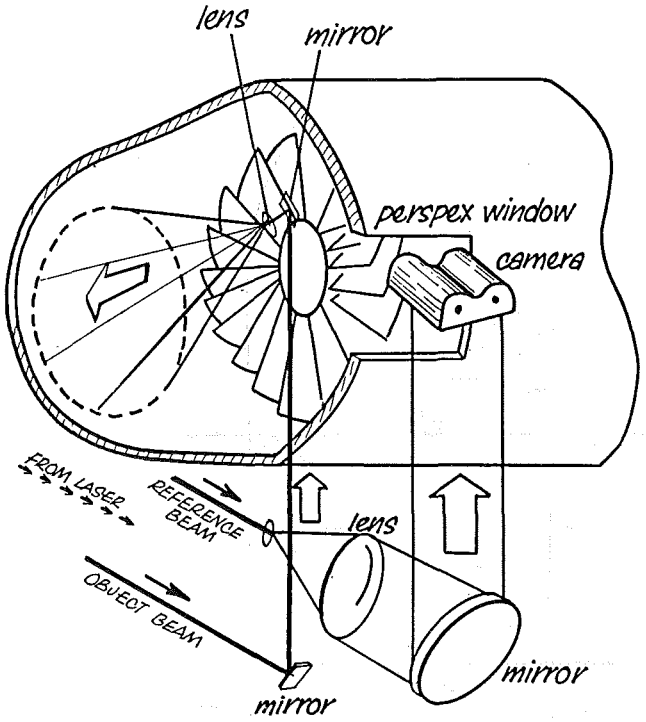

Fig. 12 Diagram showing holographic apparatus for flow visualization

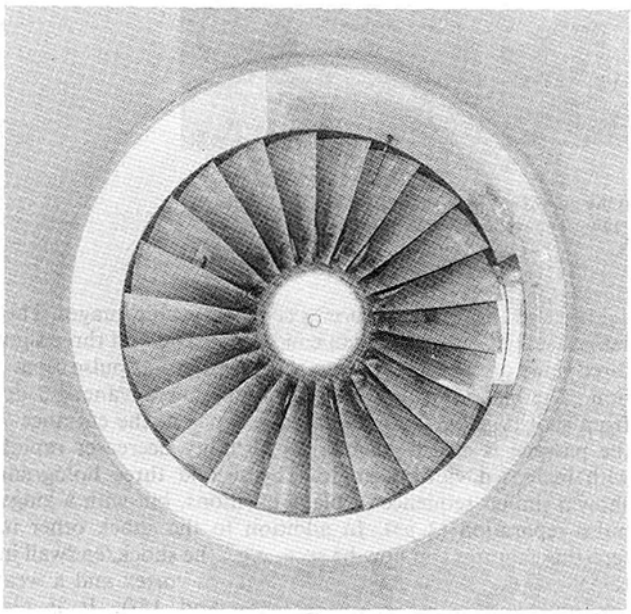

Fig. 13 Photograph of the compressor test facility showing laser input window (top right), viewing window (center right), and painted casing (left)

studied the engine-order resonance response of the fan at lower speeds: Fig. 8 shows the fan vibrating predominantly in a 1F3D mode at 5900 rpm.

Analysis

Analysis of the holograms allows deflection maps of individual blades to be produced. Figure 9 shows the measured axial displacement of a blade with minimal torsion at the tip. Of particular interest are the positions of the turning point and the zero-crossing points relative to the clapper. These data together with extracted data on the axial displacement and torsion of each blade around the structure can be compared with

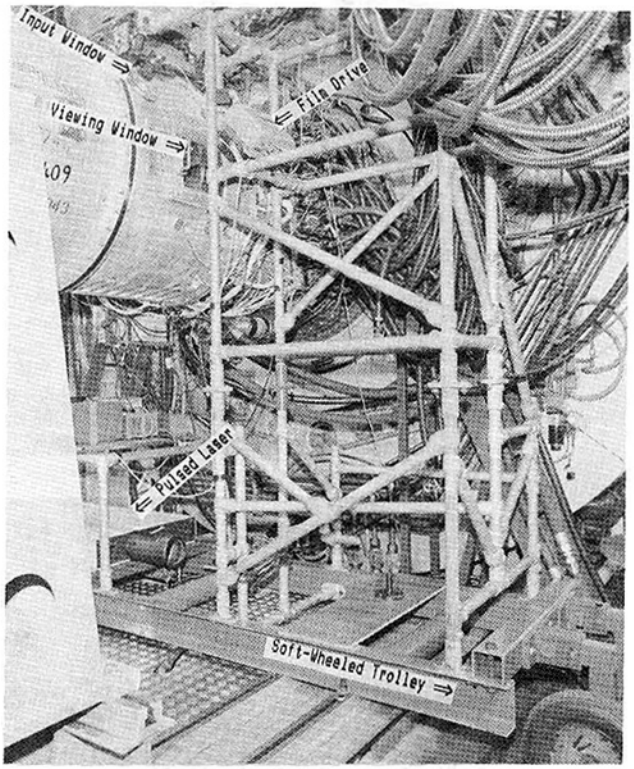

Fig. 14 Pulsed laser and holographic equipment installed in the compressor test facility

predicted behavior in finite-element models. Alternatively, the finite element model has been used to produce a displacement map for direct comparison with the holographic fringe pattern (Fig. 10).

Holographic Flow Visualization in Rotating Fans

In vibration analysis holographic interferometry has been used to contour the displacement of the vibrating fan occurring during a short pulse interval. In holographic flow visualization, a hologram is recorded of the nonrotating casing of the compressor test rig as seen through the rotating blades [11]. The optical interference contours the change in density of the flow field between the two exposures. The change in density seen in the hologram is produced by the rotation of the flow features through the field of view. The fringe order N, observed in the hologram at a particular radial height R, is given by

$$N(R) = \frac{C}{\lambda} \Delta\rho R\omega\Delta t(\hat{r}\cdot\hat{n})^{-1} \tag{2}$$

When viewed in the reconstructed hologram the effect is to produce a three-dimensional image of the shock or other flow feature. The flow features that have been studied by holography in this way are shown schematically in Fig. 11.

Holographic Flow Visualization Apparatus

Figure 12 shows a sketch of the holographic equipment. The main requirements affecting rig design are the provision of a large window over the fan-blade tips and a smaller window, upstream of the fan, for illumination of the casing. The casing must be painted white to provide an adequate, diffuse reflector for the laser light. These features can be seen in the photograph in Fig. 13, which shows the view from inside the rig. The installation of the equipment in the test facility is shown in Fig. 14. The use of rigid constructions holding all the

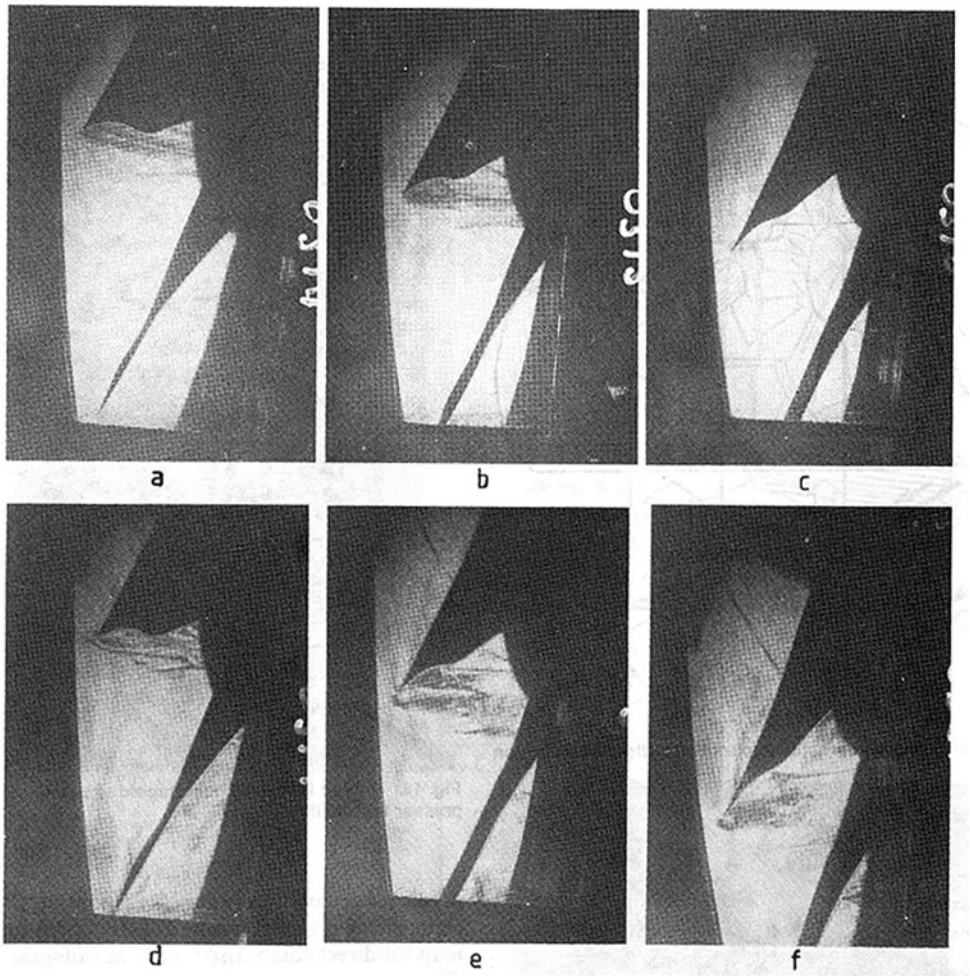

Fig. 15 Sequence of six holograms at the same flow condition: (*a, b, c*) 1 μs pulse separation; (*d, e, f*) 3 μs pulse separation; 3 deg rotation between successive shots

optical equipment and mounted on wheels facilitates installation and greatly reduces the occupancy time in these expensive facilities.

The use of a diffuse background is far preferable to the direct illumination approach as used by Wuerker et al. [12], despite the former system's more wasteful use of the available laser light. The two systems were compared in a previous paper [13]. The system described here provides a much greater range of three-dimensional views of the flow field from each hologram, facilitating interpretation of the images and giving greater accuracy in quantitative measurements of shock position. The difficulties experienced by Decker [14] in digitizing shock positions due to poor localization of fringes are removed by this approach.

Pulse Separation and Pulse Timing

The two important parameters under the control of the laser operator when recording holograms are the pulse interval and the time at which the laser is fired. The pulse interval determines the magnitude of the density gradient in the flow visualized in the hologram [11]. At very short (typically 1 μs) intervals only the sharpest gradients are seen, i.e., shocks, but at longer intervals (3-10 μs) other flow features—wakes, over-tip leakage, and boundary layer effects—may be observed. The triggering position of the laser pulses, which is determined using once per revolution and once per blade signals from the fan, controls the position of the blades in the window and the particular blade passage captured in the hologram.

Figure 15 shows a sequence of six holographic images. They were all taken at identical fan conditions. The first three show three views of the same passage taken with a 1 μs pulse separation. The blade position in the window has advanced 3 deg from shot to shot. Only the oblique shock at the entrance to the passage is clearly visible. Its visibility decreases rapidly with increased viewing angle. The second three holograms show a similar sequence of blade positions, but with a longer pulse separation (3 μs). In addition to the shock other interesting features can now be seen, e.g., the shock/endwall interaction (Fig. 15*d*), the over-tip leakage vortex and a weak bow shock at part-span (Figs. 15*e* and 15*f*). It is also noticeable that the shock remains visible over a larger range of viewing angles.

Holographic Investigation of Fan Performance

The holograms can be used to study a large number of important features of the fan's performance. By repeating holograms at the same condition and with the same blade passage, variations of the flow field in time may be observed. By taking holograms of different passages at the same fan condition, it is possible to observe the passage-to-passage variations of the flow field caused by blade-to-blade stagger angle and camber variations within the engineering tolerances [13].

The most important data provided by the holograms for computer model verification have been the nature of the shock system and its development with the changes in operating con-

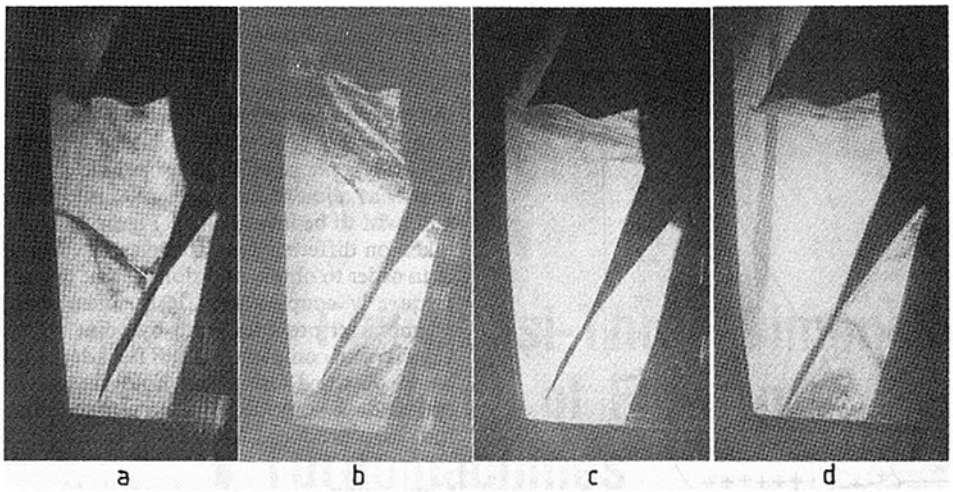

Fig. 16 Development of forward shock with increasing fan speed: (*a*) 70 percent, (*b*) 90 percent, (*c*) 100 percent, (*d*) 110 percent as a percentage of the design speed

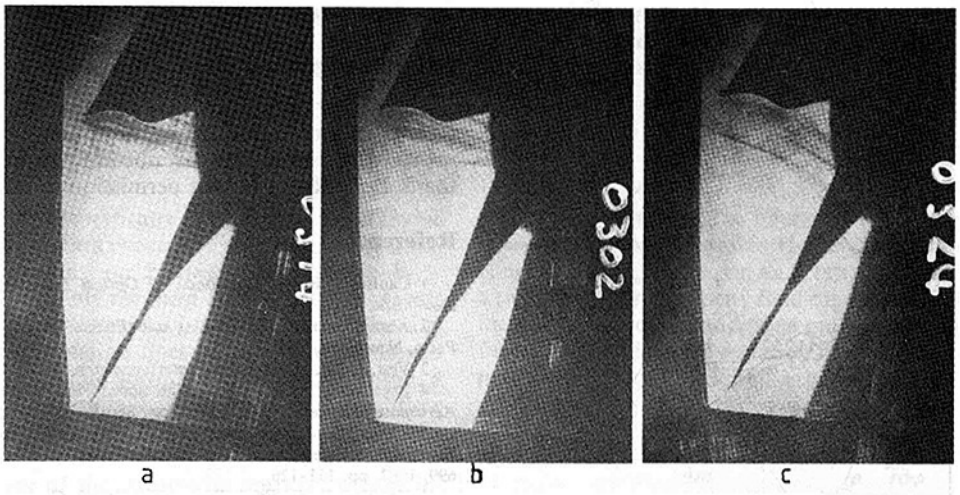

Fig. 17 Variation of shock position with throttle setting at constant speed: (*a*) maximum flow, (*b*) working line, (*c*) near surge

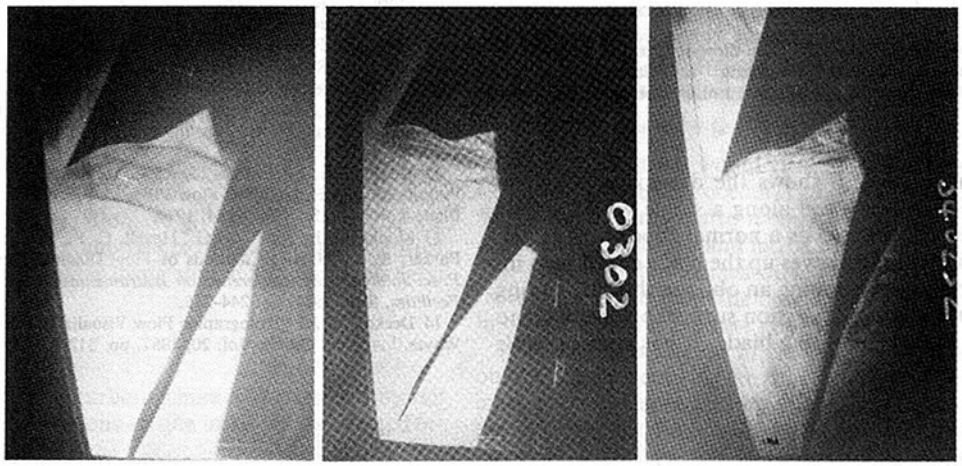

Fig. 18 Three holograms showing the effect of subtle changes in blade twist and camber on shock position; all taken at equivalent conditions

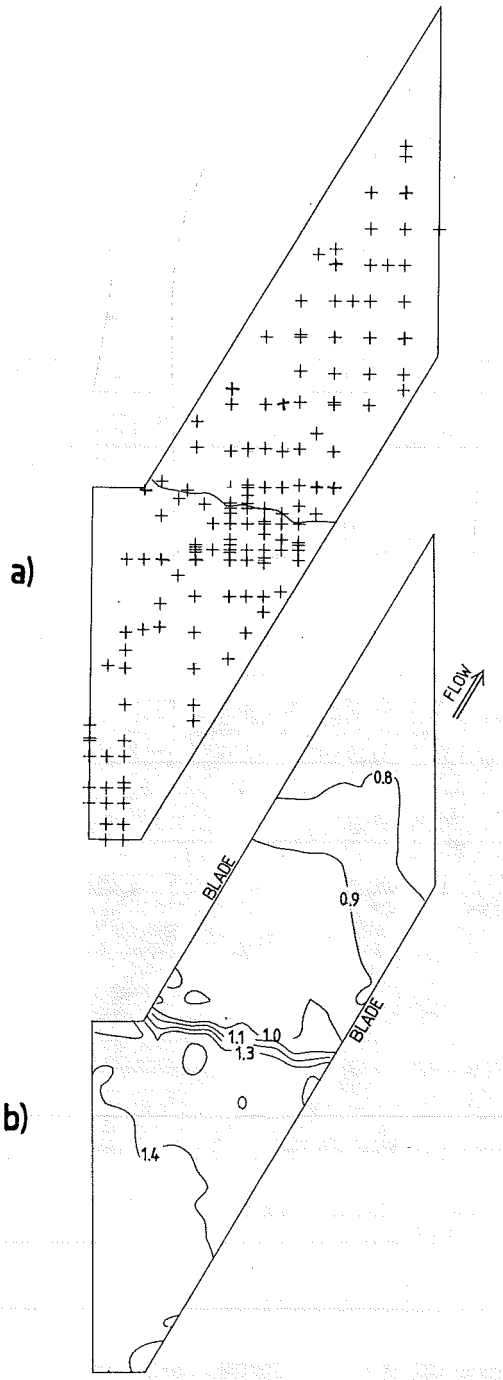

Fig. 19 Laser anemometry produces two-dimensional maps of flow velocity that complement the holograms: (a) data points for anemometry, (b) velocity magnitude (Mach number) contour map

dition of the fan. Figure 16 shows the development of the shock with increasing fan speed along a single working line. The shock begins at low speed as a normal shock on the suction surface of the blade. It moves up the blade chord with increasing speed, eventually forming an oblique shock spanning the passage entrance from the suction surface of one blade to the leading edge of the succeeding blade. It has been possible to correlate the shock configuration with the overall efficiency of the fan and thus establish design goals.

Figure 17 shows the variation of the shock system effected by throttle changes at a single fan speed. At maximum flow the shock is drawn back into the passage. As the surge margin is approached, the shock becomes more expelled.

The experience built up using holography over a number of years has allowed the result of subtle changes in fan camber and twist to be investigated. Figure 18 shows three holograms taken on different fans at the same running condition.

In order to obtain additional data, the holographic testing is frequently coupled with laser anemometry [13]. The laser anemometer provides point-by-point measurement of the gas velocity and complements full field data on shock position and angle obtained using the holography. Figure 19 shows a typical data-point distribution at one radial height and a contour map produced from laser anemometry data.

Conclusion

This paper demonstrates the versatility of holography as an optical diagnostic technique. In the study of rotating aeroengine fans it allows both the mechanical and aerodynamic behavior to be investigated. Holography has provided useful data for the verification of finite-element models of the vibration of rotating fans and for three-dimensional time-marching models of the flow field.

Acknowledgments

The authors gratefully acknowledge the financial support received from the U.K. Ministry of Defence for the development of the techniques described in this paper. The authors thank Rolls-Royce plc for permission to publish this work.

References

1 Caulfield, H. J., *Handbook of Optical Holography*, Academic Press, New York, 1979.

2 Abramson, N., *The Making and Evaluation of Holograms*, Academic Press, New York, 1981.

3 Vest, C. M., *Holographic Interferometry*, Wiley, New York, 1979.

4 Bryanston-Cross, P. J., "High Speed Flow Visualization," *Progress in Aerospace Sciences*, Vol. 23, 1986, pp. 85–104.

5 Parker, R. J., and Jones, D. G., "Industrial Holography—the Rolls-Royce Experience," *Laser and Optoelectronic Technology in Industry*, SPIE 699, 1987, pp. 111–126.

6 Hockley, B. S., Ford, R. A., and Foord, C. A., "Measurement of Fan Vibration Using Double Pulse Holography," ASME *Journal of Engineering for Power*, Vol. 100, 1978, pp. 655–663.

7 Storey, P. A., "Holographic Interferometry of Rotating Components," SPIE 599, 1986.

8 Storey, P. A., "A Study of Aero-engine Fan Flutter at High Rotational Speeds Using Holographic Interferometry," PhD Thesis, University of Loughborough, United Kingdom, 1983.

9 Storey, P. A., "Holographic Vibration Analysis of a Rotating Fluttering Fan," *AIAA Journal*, Vol. 22, No. 2, 1984, pp. 234–241.

10 Fagan, W. F., Beeck, M. A., and Kreitlow, H., "The Holographic Vibration Analysis of Rotating Objects Using a Reflective Image Derotator," *Optics and Lasers in Engineering*, Vol. 2, Apr.–June 1981, pp. 21–32.

11 Parker, R. J., and Jones, D. G., "Holographic Flow Visualization in Rotating Transonic Flows," *Institute of Physics Conference Series*, No. 77, 1985, pp. 141–146.

12 Wuerker, R. F., Kobayashi, R. J., Heflinger, L. D., and Ware, T. C., "Application of Holographic Flow Visualization Within Rotating Compressor Blade Row," NASA CR121264, 1974.

13 Moore, C. J., Jones, D. G., Haxell, C. F., Bryanston-Cross, P. J., and Parker, R. J., "Optical Methods of Flow Diagnostics in Turbomachinery," *Proc. International Conference on Instrumentation in Aerospace Simulation Facilities*, Sept. 1981, pp. 244–255.

14 Decker, A. J., "Holographic Flow Visualization of Time-Varying Shock Waves," *Applied Optics*, Vol. 20, 1981, pp. 3120–3126.

A Full Quasi-Three-Dimensional Calculation of Flow in Turbomachines

M. Ribaut

Brown Boveri Ltd., Switzerland

The problem of calculating a three-dimensional flow with three families of two-dimensional solutions is considered. From a throughflow solution and several blade-to-blade solutions the boundary values of a set of transverse solutions are obtained. The resulting overdetermined boundary condition problem is solved by means of a compatibility function defining the divergence of the transverse velocity field. The influence of the latter on the blade-to-blade solution is formulated in two different ways and compared with the experiment. The new method should considerably improve the prediction of three-dimensional cascade flow presenting a large amount of streamwise vorticity in the meridional direction.

Introduction

Considering not the theoretically possible but the effective performance of a calculation procedure, the methods iterating two-dimensional solutions on blade-to-blade and hub-to-shroud surfaces are certainly the most efficient, at the present time. However, they have a serious inconvenience: The vorticity lying on the intersection lines of the abovementioned surfaces cannot be taken into account. For this very reason, a quasi-three-dimensional method using only a throughflow solution (e.g., [1]) may be more effective than a so-called "fully three-dimensional" method (e.g., [2]), since at least the peripheral component of the streamwise vorticity will be involved in the calculation of the meridional velocity field. It is important to see that although the streamwise vorticity can easily be derived from the calculated two-dimensional velocity fields, it cannot influence the solution without some extraneous consideration. This was well understood in [3], where a third family of two-dimensional solutions, in surfaces perpendicular to the mainstream, was calculated for properly defining the rotational flow in a curved duct.

In the present contribution, it will be shown how a full quasi-three-dimensional approach, involving three families of two-dimensional solutions, can improve the solution to the flow through the cascade of a turbomachine. Let us remark that the designation "fully three-dimensional" should only refer to methods solving simultaneously the three components of the momentum equation (e.g., [4]) or considering simultaneously the two components of the boundary vortex vector as unknown, if one is using source and vortex integral equations [5].

Basic Considerations

The velocity field of a turbomachine is determined by the local and boundary conditions arising in all points situated inside or respectively at the boundary of the three-dimensional space wetted by the fluid. However, considering only two components, c_m and c_φ on an arbitrary surface of revolution, a two-dimensional velocity field can be defined by formulating local and boundary conditions only at the points of this surface. Using an integral equation method, the local conditions may be introduced by defining the value of the divergence and curl [5, 6]:

$$\nabla \cdot c_{m\varphi} = -c_m \frac{1}{\rho}\frac{\partial \rho}{\partial m} - (c_\varphi - r\omega)\frac{1}{\rho}\frac{\partial \rho}{r\partial \varphi} - \frac{1}{r\rho}\frac{\partial (r\rho c_n)}{\partial n} \tag{1}$$

$$\nabla \times c_{m\varphi} = 0 \tag{2}$$

where the first two terms on the right-hand side of equation (1) account for the fluid compressibility; the last term expresses the fact that the stream surfaces are neither identical with nor equidistant from the surface of revolution considered. For the purpose of convenience, no diffusion of the boundary vorticity was assumed, the strength of the latter being always defined by the boundary condition:

$$c_m \cos \alpha_m + (c_\varphi - r\omega)\cos \alpha_\varphi = -c_n \cos \alpha_n \tag{3}$$

This set of equations would yield the true blade-to-blade solution if, by a magic procedure, the true value of c_n and of its derivative with respect to n could be known at the surface of revolution considered and introduced in equations (1) and (3). The aim of any quasi-three-dimensional calculation is therefore to determine the best possible approximation of c_n in order to obtain the best possible solution.

A first approximation to the velocity component c_n can be obtained by calculating an axisymmetric flow in the meridional plane (or another hub-to-shroud surface). In this way, the channel curvature, the variation of the channel height and blade thickness, and the influence of the peripherial component of the vorticity can be introduced in the blade-to-blade solution through the last source term of equation (1). If

Contributed by the Gas Turbine Division for publication in the JOURNAL OF TURBOMACHINERY. Manuscript received at ASME Headquarters May 26, 1987.

several hub-to-shroud solutions are involved, this term will become dependent on φ. However, this expansive improvement risks to produce disappointing results, since a larger part of the streamwise vorticity will, in general, be neglected. The only way really to improve the solution is to calculate a transverse solution on a number of cross-passage surfaces.

Transverse Solution

Let us consider a quasi-three-dimensional method calculating the meridional velocity of an axisymmetric flow (e.g., [1, 7]) and a number of blade-to-blade solutions on given surfaces of revolution. In this case, only the meridional component of the vortex vector lying on these surfaces cannot be taken into account. Therefore, we want to calculate the velocity in sections perpendicular to the meridional plane and to the surfaces of revolution considered. As the peripheral velocity component, resulting from the blade-to-blade solutions, is not of particular interest, we concentrate on the velocity induced by the component $\bar{\gamma}_m$ of the boundary vorticity. The strength of this vortex component may be derived from a flux balance of the vortex vector at the blade surface

$$\bar{\gamma}_m = \frac{\partial}{\partial n}\left(\int_0^s \bar{\gamma}_n ds\right) \cdot \sin\beta \tag{4}$$

The abscissa s of a point at the blade surface has its origin at the leading edge and the vortex strength $\bar{\gamma}_n$ results from the blade-to-blade solutions.

The problem to solve may then be defined in the following way. Given a vortex strength $\bar{\gamma}_m$ on two arcs BC and DA of a closed contour (see Fig. 1), find a vector field v satisfying the local conditions

$$\nabla \cdot v = q + q' \tag{5}$$

$$\nabla \times v = \gamma_m \tag{6}$$

and the boundary conditions

$$b \times v = \frac{1}{2}\,\bar{\gamma}_m \tag{7}$$

where b is the unit normal vector oriented inward on the boundary. Assuming that the transverse section can be approximated by a surface of revolution, the velocity field v can by transformed on a radial plane and calculated in the same way as the blade-to-blade solution (see [6]). If the transverse section is nearly planar, the following identity may be used [8]:

$$v = \frac{1}{2\pi}\left[-\int_{\partial\Omega} \nabla \times (\bar{\gamma}_m LnD)\,ds + \iint_\Omega q' \nabla LnD\, dxdy\right] \tag{8}$$

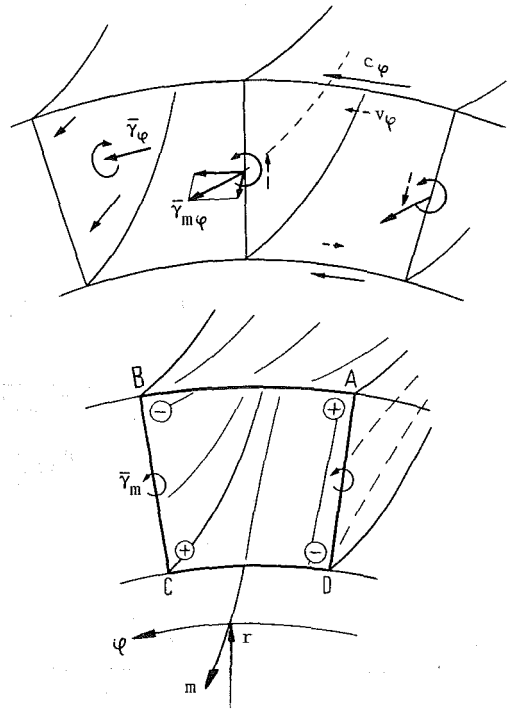

Fig. 1 Geometry and flow definitions

neglecting the effects of compressibility ($q = 0$) and the diffusion of the boundary vorticity ($\gamma_m = 0$).

To solve the overdetermined boundary value problem described above, a compatibility function must be introduced [8], in the form of a distribution of divergence between the blade sides bearing the given vortex strength $\bar{\gamma}_m$

$$q'(\varphi, n) = g(\varphi)q_1'(n) + (1 - g(\varphi))q_2'(n) \tag{9}$$

$g(\varphi)$ is a distribution function taking the value 1 on AD and 0 on BC. The boundary values q_1' and q_2' of the compatibility function are the unknowns that compensate for the lack of degrees of freedom on the arcs AD and BC resulting from the overspecification of the vortex strength $\bar{\gamma}_m$. Thus, by application of the collocation method to equations (7)–(9), a system of linear equations can be obtained, the solution of which yields the boundary values q_1' and q_2' of the compatibility function and the vortex strength $\bar{\gamma}_m$ on the arcs AB and CD.

The physical interpretation of the compatibility function is the following. The velocity induced by the vortex component

Nomenclature

c = fluid velocity
D = distance between the point at which c is calculated and the current point of the integrals
g = distribution function
h = blade height
q = source density
q' = compatibility function
$q'_{1,2}$ = boundary values of the compatibility function
r = radius of a surface of revolution
s = curvilinear abscissa on the boundary
t = peripheral channel width
v = transverse solution
$\bar{v}$ = pitch-averaged value of v
α = angle between normal to the blade surface and curvilinear coordinates
β = angle between velocity and peripheral direction
γ = vortex density
$\bar{\gamma}$ = vortex strength (jump of velocity)
$\partial\Omega$ = boundary of the transverse section
ϵ = angle between the meridional trace m and the axial direction
ρ = fluid density
ω = angular cascade velocity
Ω = interior domain of the transverse section

Subscripts

m, φ, n = relative to the local orthogonal coordinates defined by the meridional and peripheral traces of a surface of revolution

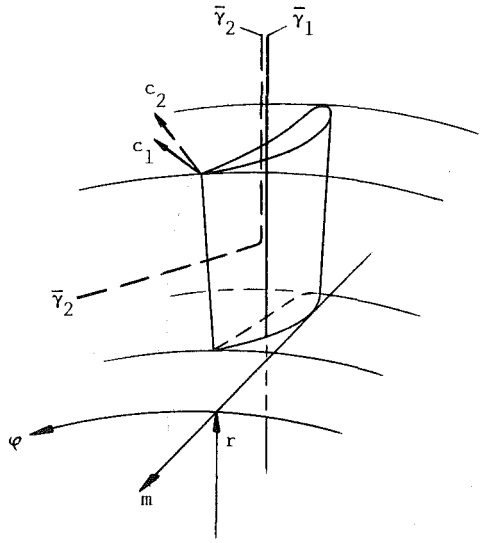

Fig. 2 Downwash induced by the streamwise vorticity

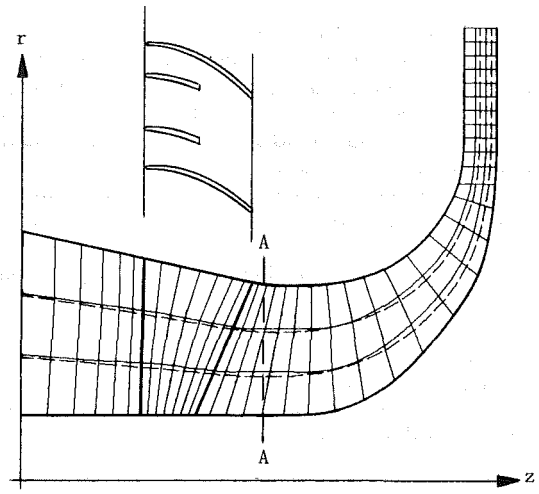

Fig. 3 Calculated prewhirl cascade

$\bar{\gamma}_m$ moves the streamlines of the main flow toward corners B and D and away from corners A and C (Fig. 1). As a consequence, the mainstream accelerates or decelerates in these regions, thus producing in the transverse section a divergence

$$\nabla \cdot v = -\frac{\partial c'_m}{\partial m} \tag{10}$$

the existence of which is revealed to the transverse solution by the overdetermined character of the boundary conditions. The exact nature of the compatibility function could be determined with equation (10), by calculating the velocity c'_m arising in the blade-to-blade surface from the influence of the transverse solution. However, in a first approximation, we will assume the distribution function $g(x)$ to be linear.

Influence on the Blade-to-Blade Solution

The influence of the transverse solution on the axisymmetric through-flow may be neglected (it vanishes for a symmetric cross section and infinitesimal blades). The influence on the blade-to-blade flow results from the introduction of the transverse velocity component v_n and its gradient in equations (1) and (3). However, as will be seen in the next section, this procedure yields rather disappointing results. This may be a consequence of the fact that an important part of c_n, induced by $\bar{\gamma}_\varphi$, is still independent of φ since it results from the axisymmetric solution. Therefore, we will try to introduce directly the velocity component v_φ (Fig. 1) induced by the vortex strength $\bar{\gamma}_m$ in the blade-to-blade solution.

Let us assume that the transverse solution is calculated in a number of sections evenly distributed from the inlet to the outlet of a blade row. On each blade-to-blade surface, a velocity field can then be superposed on the unperturbed flow, the peripheral component $\bar{v}_\varphi$ of which is obtained by averaging v_φ over the cascade pitch; the meridional component results from the condition of a rotation-free flow

$$\bar{v}_\varphi = \frac{1}{t}\int_0^t v_\varphi r d\varphi \tag{11}$$

$$v_m = \left(\bar{v}_\varphi \sin\epsilon + r\frac{\partial \bar{v}_\varphi}{\partial m}\right)(\varphi - \varphi_0(m)) \tag{12}$$

$\varphi_0(m)$ refers to the midline of the blade channel.

The above method may be justified by the following considerations. Looking at the two vortex lines $\bar{\gamma}_1$ and $\bar{\gamma}_2$ illustrated in Fig. 2, we see that the velocity induced at the blade surface by the vortex line flowing downstream is larger. Since this vortex line is more efficient, its strength $\bar{\gamma}_2$, determined by the boundary conditions, will be inferior to $\bar{\gamma}_1$. Now, the blade-to-blade solution only knows straight vortex lines and the calculated vortex distribution could only agree with the real one if the velocity difference $c_2 - c_1$ at the blade surface would be introduced in an extraneous way, at the level of the "unperturbed" flow. This is exactly what the velocity field defined by equations (11) and (12) is supposed to do. As the pitch-averaged value of the over-velocity induced by the real vortex configuration equals zero, this velocity must vanish outside of the cascade. In this way, both the meridional and the peripheral component of the blade-to-blade flow are modified by an axisymmetric part arising from the through-flow or the transverse flow solution.

A third possibility to account for the meridional component of the streamwise vorticity would be to calculate the velocity induced at the profile surface either by numerical integration or analytically, as was suggested in [7] for the axial turbomachine. However, first attempts to follow this way were disappointing and would probably be successful only in the framework of a full-three-dimensional solution like the one proposed in [5].

Application

The present method was applied to flow through the prewhirl cascade of a radial compressor, illustrated in Fig. 3. The flow direction at the outlet of the cascade (section A-A) was measured with a contactless laser-velocimeter [9, 10]. It appeared that the meridional flow to the cascade was deflected by about 15 deg at the blade root and 35 deg at the top of the blade where the circulation was about eight times larger, thus producing a huge amount of nearly meridional streamwise vorticity flowing downstream at the trailing edge. The interest of this experiment was first demonstrated by Melling [10], which obtained surprisingly bad results with the classical quasi-three-dimensional method described in [7].

By applying the present method, the transverse solution was calculated at each third of the meridional blade length, the conical sections being projected axially on a radial plane. Making use of equation (8), the boundary conditions were formulated at the midpoint of ten equivalent intervals distributed on each of the boundary arcs. The compatibility function was interpolated linearly from ten unknown values distributed along each blade side at the abovementioned midpoints. Due to the low Mach number, the three-dimensional solution con-

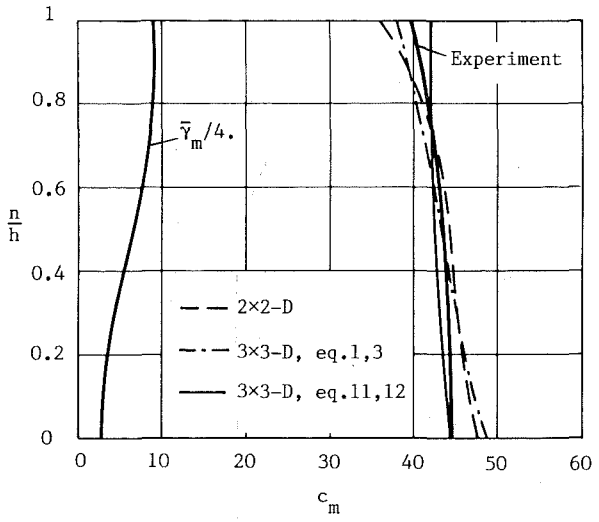

Fig. 4 Distribution of meridional vorticity and velocity over the blade height

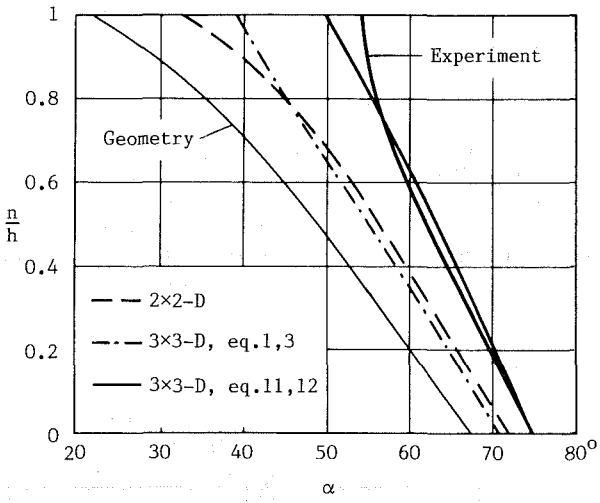

Fig. 5 Comparison between calculated and measured flow outlet angles

verged to 0.1 percent in eight iterations, each iteration including a throughflow solution, three transverse solutions, and four blade-to-blade solutions. The computation time was about 90 s on an IBM-3081 machine.

The calculated meridional velocity and the flow angle at the cascade outlet are compared in Figs. 4 and 5 with the experiment [10]. It will be seen that the classical method involving only two two-dimensional solutions (dashed lines) predicts a nearly 20 deg false outlet angle at the shroud. The inclusion of a transverse solution providing better values of c_n in equations (1) and (3) improved this result only a little (dashed-dotted lines). Reasonable agreement with the experiment could only be achieved by accounting for the peripheral velocity induced by the meridional vorticity with equations (11) and (12) (solid lines). The resulting transverse velocity field at the outlet of the cascade is illustrated in Fig. 6, whereas the vorticity at its origin is reported in Fig. 4.

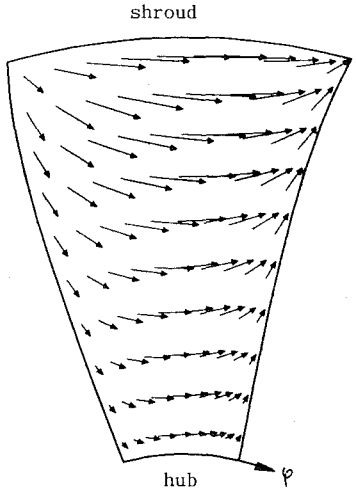

Fig. 6 Calculated transverse velocity field in the outlet section

Conclusions

The usual practice of calculating three-dimensional flows with two families of two-dimensional solutions results in a loss of information, which can be avoided by including a third family of transverse solutions. The calculation of the transverse velocity field is rendered possible by a compatibility function accounting for the overdetermined character of its boundary conditions. However, the proper introduction of this additional information in the blade-to-blade solution has been shown to be disappointing. Nevertheless, by superposing in a straightforward way the pitch-averaged peripheral velocity provided by the transverse solution to the blade-to-blade velocity field, a considerable improvement of the solution could be achieved for a cascade flow presenting nearly 100 percent spanwise variation of its blade circulation. These results give evidence of the necessity to further deepen the insight into quasi-three-dimensional flow calculation.

References

1 Jennions, I. K., and Stow, P., "A Quasi-Three-Dimensional Turbomachinery Blade Design System: Part 1—Throughflow Analysis," ASME *Journal of Engineering for Gas Turbines and Power*, Vol. 107, 1985, pp. 301–307.

2 Wang, Q., Zhu, G., and Wu, C. H., "Quasi-Three-Dimensional and Full Three-Dimensional Rotational Flow Calculations in Turbomachines," ASME *Journal of Engineering for Gas Turbines and Power*, Vol. 107, 1985, pp. 277–285.

3 Abdallah, S., and Hamed, A., "The Elliptic Solution of the Secondary Flow Problem," ASME *Journal of Engineering for Power*, Vol. 105, 1983, pp. 530–535.

4 Bosman, C., and Highton, J., "A Calculation Procedure for 3-D, Time-Dependent, Inviscid, Compressible Flow Through Turbomachine Blades of Any Geometry," *Journal of Mech. Eng. Science*, Vol. 21, 1979, pp. 39–79.

5 Ribaut, M., "Three-Dimensional Calculation of Flow in Turbomachines With the Aid of Singularities," ASME *Journal of Engineering for Power*, Vol. 90, 1968, pp. 258–264.

6 Ribaut, M., and Vainio, R., "On the Calculation of 2-D Subsonic and Schock-Free Transonic Flow," ASME *Journal of Engineering for Power*, Vol. 97, 1975, pp. 603–609.

7 Ribaut, M., "On the Calculation of 3-D Divergent and Rotational Flow in Turbomachines," ASME *Journal of Fluids Eng.*, Vol. 99, 1977, pp. 187–196.

8 Ribaut, M., "A Solution to Boundary Value Problems With Over-Specified Boundary Conditions," *ZAMP*, Vol. 36, 1985, pp. 629–634.

9 Melling, A., "Instrumentation for LDA Signal Processing," VKI Lecture Series 1981-3, *Laser Velocimetry*, 1981.

10 Melling, A., "Strömungsfeldmessungen am Windkanal," T. B. HTX-VB3722, 1982, unpublished.

M. A. Habib

A. E. Attya

Mechanical Engineering Department,
Cairo University,
Cairo, Egypt

D. M. McEligot

Westinghouse Electric Corporation
(formerly Gould Ocean Systems Division),
Middletown, RI;
Mechanical Engineering and Applied
Mechanics Department,
University of Rhode Island,
Kingston, RI
Fellow ASME

Calculation of Turbulent Flow and Heat Transfer in Channels With Streamwise-Periodic Flow

A computational method for the calculation of the flow and heat transfer in a channel, with elements of various heights inducing a streamwise-periodic flow, is presented and evaluated. The time-averaged conservation equations of mass, momentum, and energy were solved together using a finite-control-volume method. Reynolds stresses were obtained using a two-equation model, which solves the time-averaged equations of the turbulence kinetic energy and its dissipation rate. The calculated flow field is shown to be in satisfactory agreement with the experimental data. The results indicate that the local and overall heat loss parameters increase with increasing Reynolds and Prandtl numbers and element height and with decreasing spacing.

1 Introduction

Streamwise-periodic flow is expected to occur when the geometry of the walls bounding a flow becomes periodic in the main flow direction. The term implies that repeating units or cells formed by the walls eventually cause the flow pattern to repeat in this direction so that, at corresponding points in successive cells, the velocity components, turbulence quantities, and pressure and temperature differences have identical values.

In applications to gas turbine engines and power plants such conditions can be anticipated over a wide range of scales, ranging from large flow obstructions to small ribs. Segmental baffles may be employed in shell-and-tube heat exchangers used as coolers in large-scale, high-pressure, power plant installations (Berner et al., 1984). Fins in compact heat exchangers used as regenerative heat exchangers or in gas-cooled solar collectors may have components perpendicular to the main flow direction. Labyrinth seals provide a minimum leakage flow for cooling hot spots (Rhode et al., 1986). Corrugated walls, with or without fins, may be used as passages in heat exchangers for the purpose of heat transfer augmentation (Amano et al., 1987). Periodic roughness elements were proposed for the surface of the nuclear fuel rods in high-temperature gas-cooled reactors (HTGR) serving as the energy supply in gas turbine power plants (Short, 1978). Small ribs are employed in the internal cooling passages of gas turbine blades for high-temperature service (Han et al., 1988).

The mathematical problem presents a substantial challenge to those wishing to predict the flow field and related heat or mass transfer. In application, only the geometry, the mass or volume flow rates, and an estimate of the gas transport properties are known. The periodicity condition implies that inlet profiles are results that must be calculated, rather than being specified boundary conditions as in most numerical prediction codes. A further computational difficulty in numerical techniques that use upwind differencing for convective terms, or a variant thereof (Gosman and Pun, 1973), is that, at outlets where the velocity is high, the interior points become uncoupled from the adjacent boundary; this confuses the application of the appropriate boundary condition for periodicity of the gradients.

Numerical analyses for streamwise-periodic flows have been mostly for laminar conditions. Patankar et al. (1977) presented a technique for flow around a series of staggered plates perpendicular to the main flow (as tubes in some crossflow heat exchangers) and were able to use central differencing for the convective terms. Short (1978) extended the TEACH code of Gosman and Pun (1973) to handle the coupling of conduction in stainless-steel cladding and ribs to convection of high-pressure helium for HTGR fuel rods and cooling passages (sometimes called conjugate heat transfer). Faas (1980) and Faas and McEligot (1979) extended Short's study and applied it to channels with corrugated walls representing geothermal cracks. Heinrich and Yu (Berner et al., 1984) treated flow around segmental baffles with a transient approach and Kelkar and Patankar (1987) applied the technique of Patankar et al. to the same problem. Webb and Ramadhyani (1985) addressed conjugate heat transfer for staggered ribs. Faghri (1987) reports success on the triply periodic version for application to flow through fibrous filters and for arrays of electronic modules on printed wiring boards (Asako and Faghri, 1987). To the authors' knowledge, the only treatments considering streamwise-periodic, *turbulent* flow have been by Amano (1985) for the corrugated wall and Rhode et al. (1986) for labyrinth seals, plus an early approximation for large periodic roughness elements by Gosman et al. (1977) that did not employ periodic boundary conditions.

Heat transfer predictions depend strongly on the velocity field employed. To date the availability of turbulent flow field

Contributed by the Gas Turbine Division and presented at the ASME Winter Annual Meeting, Boston, Massachusetts, December 13–18, 1987. Manuscript received by the Gas Turbine Division, June 1987.

measurements to test the validity of the numerical predictions has been limited. For a number of years, Logan and his colleagues have measured developing and downstream flows in channels with short ribbed roughness elements (Logan and Islam, 1976; Logan and Siuru, 1977; Schofield and Logan, 1987). Ichimiya (1987) presents a few velocity and turbulence profiles for the throughflow region above a series of fins. At The University of Arizona Berner et al. (1984) and Habib et al. (1984) obtained mean velocity and turbulence distributions in flow around segmental baffles. These latter data form the basis of the present predictions. Founti et al. (1985) measured the flow on the shell side of a model disk-and-doughnut heat exchanger, a nominally axisymmetric case of streamwise-periodic flow complicated by a few axial supporting rods.

The *objective* of the present paper is to predict heat transfer to and from the walls between staggered, periodic obstructions, which are adiabatic, as shown in Fig. 1 (in the following discussion the terms obstruction, element, baffle, and rib will be used interchangeably). It is believed to be the first numerical treatment of turbulent flow between staggered elements. This situation is the appropriate problem when one is interested in predicting heat losses from a heat exchanger provided the elements have poor fin effectiveness or when the elements are far apart.

The approach is semi-empirical. The flow problem is solved by combining the experimental measurements with numerical prediction techniques. Specifically, the data are applied to estimate the streamwise boundary conditions and the interior field is solved numerically. Then the results are used in the numerical solution of the thermal energy problem. Calculations are conducted for water with a Prandtl number of about seven and for common gases (Pr = 0.7).

Both the flow and heat transfer in such channels are affected by a number of geometric factors as well as the flow rate and physical properties of the fluid. The nondimensional geometric factors are the spacing between each two consecutive elements S/D and element height H/D or the distance or opening between the tip of the element and the opposite wall (called "window cut" in heat exchangers) C/D, where D is the channel height.

In this paper the flow field and local and overall heat transfer coefficients are presented, discussed, and appraised. The mean flow is assumed to be steady, turbulent, and two dimensional with constant transport properties. The calculation procedure was first developed and tested with the measurements of turbulent flow fields between baffles by Berner et al. (1984) and Habib et al. (1984). The governing equations and boundary conditions are described in the following section, which is ended by a description of the solution procedure. The results are then presented and discussed. The paper ends with a few concluding remarks.

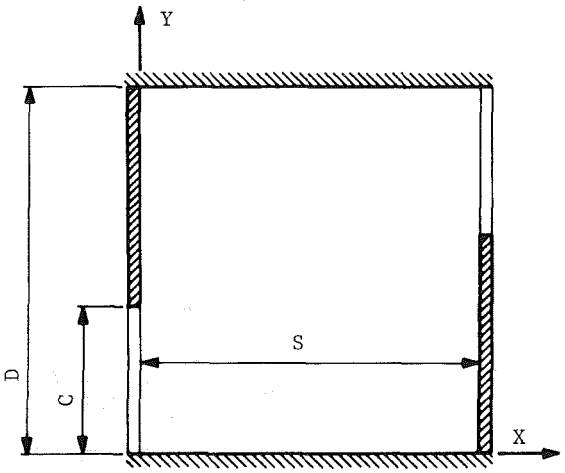

Fig. 1 Computational domain and geometric parameters

2 Mathematical Formulation

Equations representing the conservation of mass, energy, turbulence kinetic energy, and its dissipation rate, plus the momentum equations in the directions perpendicular and parallel to the elements, were solved in Cartesian coordinates. The equations were elliptic in form and were solved with a modified version of the TEACH computer program (Gosman and Pun, 1973; Habib and Whitelaw, 1980; Habib and McEligot, 1982) to give predictions of the flow and heat transfer in a channel with alternating periodic elements. The governing equations, turbulence model, and solution procedure are presented in the following subsections.

2.1 Governing Equations. With terms involving density fluctuations assumed to be negligible, the time-averaged conservation equations for mass and momentum may be expressed in the following compact tensor form:

$$\frac{\partial}{\partial x_j}(\rho \bar{U}_i) = 0 \tag{1}$$

$$\frac{\partial}{\partial x_j}(\rho \bar{U}_i \bar{U}_j + \rho \overline{u_i u_j}) = -\frac{\partial P}{\partial x_i} \tag{2}$$

where $\bar{U}_i$ and u_i are the time-averaged and fluctuating velocity components in the coordinate directions x_i, ρ is the fluid den-

Nomenclature

C_f = skin friction coefficient
C = window cut in heat exchangers
D = channel height
G = rate of generation of turbulent kinetic energy
H = element height = $D - C$; enthalpy
h = convective heat transfer coefficient = $q_w/(T_w - T_b)$
K = turbulent kinetic energy
k = thermal conductivity
l = length scale of energy containing eddies
Nu = Nusselt number; Nu_o, for smooth channel with laminar flow
P = pressure
Pr = Prandtl number
q_w = wall heat flux
Re = Reynolds number = $\rho \bar{U}_c C/\mu_l$; Re_s, based on spacing = $\rho \bar{V}_b S/\mu_l$
S = spacing between elements
T = temperature; T_b, bulk temperature
U, U_i = streamwise velocitiy component
V, V_i = vertical velocity component
X, x_i = streamwise coordinate
Y, y_i = vertical coordinate
ϵ = dissipation rate for turbulent kinetic energy
κ = constant in turbulence model
μ = dynamic viscosity
ρ = density
ψ = dimensionless stream function

Subscripts

av = average
b = bulk
eff = effective
l = molecular
t = turbulent

sity, P is the local pressure and the terms $-\rho\overline{u_i u_j}$ are the Reynolds stresses.

In a similar manner, the time-averaged conservation equation for the thermal energy may be expressed as

$$\frac{\partial}{\partial x_j}(\rho \bar{U}_j \bar{H}) = \frac{\partial}{\partial x_j}\left(\Gamma_H \frac{\partial \bar{H}}{\partial x_j}\right) - \frac{\partial}{\partial x_j}(\rho \overline{u_j H}) \tag{3}$$

where $\Gamma_H = \mu_l/\mathrm{Pr}$ is the laminar diffusion coefficient, Pr is the Prandtl number, and the terms $-\rho\overline{u_j H}$ are the turbulent heat fluxes.

2.2 Turbulence Model. The present work incorporates a two-equation turbulence model, which involves the solution of the conservation equations for the kinetic energy of turbulence, $K = \overline{u_i u_j}/2$, and its rate of dissipation (Launder and Spalding, 1972). The K–ϵ model relates the Reynolds stresses and turbulent heat fluxes to the gradients of the mean velocities and temperatures, respectively, via exchange coefficients in the following manner:

$$-\rho\overline{u_i u_j} = \mu_t\left(\frac{\partial \bar{U}_i}{\partial x_j} + \frac{\partial \bar{U}_j}{\partial x_i}\right) - \frac{2}{3}\rho K \delta_{ij} \tag{4}$$

$$-\overline{\rho u_j H} = \Gamma_t \frac{\partial \bar{H}}{\partial x_j} \tag{5}$$

where μ_t is the turbulent viscosity, $\Gamma_t = \mu_t/\mathrm{Pr}_t$ is the turbulent thermal diffusion coefficient, and Pr_t is the turbulent Prandtl number, with $\delta_{ij} = 0$ if $i \neq j$ and $\delta_{ij} = 1$ if $i = j$.

The turbulent viscosity is modeled as (Launder and Spalding, 1972)

$$\mu_t = C_\mu \rho K^2/\epsilon \tag{6}$$

The turbulent viscosity is thus obtained from the solution of the transport equations for K and ϵ, which can be expressed as

$$\frac{\partial}{\partial x_j}(\rho \bar{U}_j K) = \frac{\partial}{\partial x_j}\left(\frac{\mu_{eff}}{\sigma_K}\frac{\partial K}{\partial x_j}\right) + G - \rho\epsilon \tag{7}$$

$$\frac{\partial}{\partial x_j}(\rho \bar{U}_j \epsilon) = \frac{\partial}{\partial x_j}\left(\frac{\mu_{eff}}{\sigma_\epsilon}\frac{\partial \epsilon}{\partial x_j}\right) + C_1\frac{\epsilon}{K}G - C_2\rho\frac{\epsilon^2}{K} \tag{8}$$

where $\mu_{eff} = \mu_l + \mu_t$ and G is the generation rate of turbulence kinetic energy given by $G = -\rho\overline{u_i u_j}\,\partial U_i/\partial x_j$. The quantities σ_K, σ_ϵ, C_μ, C_1, and C_2 are the turbulence model constants discussed extensively by many workers (Jones and Launder, 1972; Rodi, 1980). Their standard values, which are used in the present work, are given in Table 1.

In streamwise-periodic flow the inlet and outlet velocities and their gradients are not known in advance but are results of the solution procedure. In this paper the main interest is the heat transfer to or from the walls between the elements. Therefore, a semi-empirical treatment is presented where inlet and outlet velocity profiles are prescribed through the interpolation of available flow data (Berner et al., 1984; Habib et al., 1984) and fully developed channel flow. The inlet and outlet profiles of the dissipation rate were determined from its model

$$\epsilon = C_\mu K^{3/2}/l \tag{9}$$

where l is the length scale that characterizes the energy containing eddies, taken as $l = 0.03D$.

All velocity components were presumed zero along the wall. The wall temperature was presumed constant along the top and bottom walls and the elements were taken to be adiabatic. The wall functions (Launder and Spalding, 1972) corresponding to the dependent variables were taken as

$$\tau_w = \mu_l \frac{\bar{U}_p}{y_p}\frac{y_p^+}{\bar{U}_p^+} \tag{10}$$

and

Table 1 Constants in conservation equations

Constant	C_μ	σ_k	σ_ϵ	C_1	C_2	C_f	κ	E
Value	0.09	1.0	1.22	1.45	1.9	9.24	0.42	9.8

$$q_w = \mu_l \frac{(\bar{H}_w - \bar{H}_p)}{y_p}\frac{y_p^+}{\bar{U}_p^+ + P_f}$$

where

$$\bar{U}_p^+ = \frac{1}{\kappa}\ln E y_p^+ \quad \text{and} \quad y_p^+ = C_\mu^{1/4} K_p^{1/2} y_p/\nu_l$$

with

$$P_f = C_f\left(\frac{\mathrm{Pr}}{\mathrm{Pr}_t} - 1\right)\left(\frac{\mathrm{Pr}_t}{\mathrm{Pr}}\right)^{1/4}$$

The subscript p refers to the node nearest the wall. These relations and equation (8) are for high-Reynolds-number conditions.

The value of the turbulence kinetic energy near the wall, K_p, is calculated from the transport equation for K with its flux to the solid wall set to zero. The corresponding value of ϵ was calculated from equation (9) with $l = C\,\mu^{1/4}\,\kappa\,y_p$. The wall function quantities E, κ, and C_f are constants given in Table 1.

2.3 Solution Procedure. The above conservation equations were first integrated over a typical volume, which was formed by division of the flow field into a number of finite volumes to yield the finite difference equations. These equations were solved together using the solution procedure described by Patankar and Spalding (1972). An estimate of the velocity field at the first iteration was obtained by solving the momentum equations with presumed values of the pressure distribution. Moreover, there is no guarantee that the resultant velocity field will satisfy the continuity equation; therefore, after each calculation over the solution domain, adjustments were made to the pressure and velocity fields to satisfy continuity. The procedure is repeated until convergence is obtained. The energy equation is then solved assuming constant fluid transport properties, and the temperature field is obtained.

Most of the computations were made with a grid of 18 × 20 nodes with more nodes concentrated near the walls and in regions of separation and high velocity gradients. The computations were made using a VAX 11/780. A grid independence test was conducted; it showed that an increase in the number of nodes from 10 × 20 to 18 × 20 affects the predicted velocity significantly only in the region of reversed flow and near the maximum velocity and the velocities were modified by less than 5 percent. Since the major velocity gradients are in the x direction, grid spacing was varied only in this direction; 20 nodes were used for the y direction for all cases. The results are considered to be numerically converged in the present solution procedure when the maxima of the mass flux and momentum flux residuals summed at all nodes are less than 0.6 percent of the inlet flux. For the temperature calculations the solution was considered to be converged when the sum of the energy flux residuals at all nodes is less than 0.1 percent of the inlet energy flux. To achieve these two conditions the solution procedure required 150 iterations each for the flow field and the temperature field.

In presenting the numerical results, the Reynolds number ($\mathrm{Re} = \rho\,\bar{U}_b C/\mu_l = \mathrm{Re}_s C/D$)) and the local Nusselt number ($\mathrm{Nu} = hL/k$) are used, where $h = q_w/(T_w - T_b)$ is the heat transfer coefficient; T_w is the wall temperature, and T_b is the bulk temperature given by Karlekar and Desmond (1977)

$$T_b = \int_0^D \bar{U}\,T\,dy \Big/ \int_0^D \bar{U}\,dy \tag{11}$$

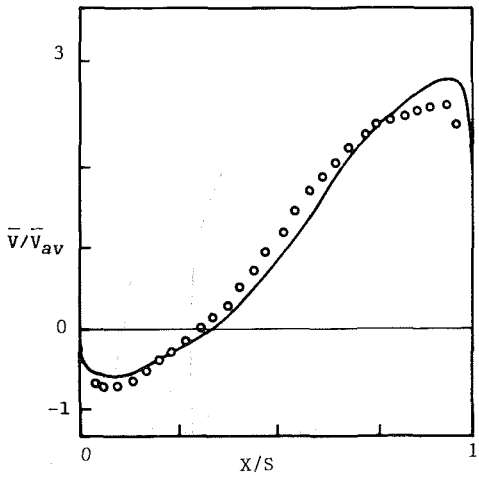

Fig. 2 Predicted vertical velocity distribution at midplane compared to data of Habib et al. (1984)

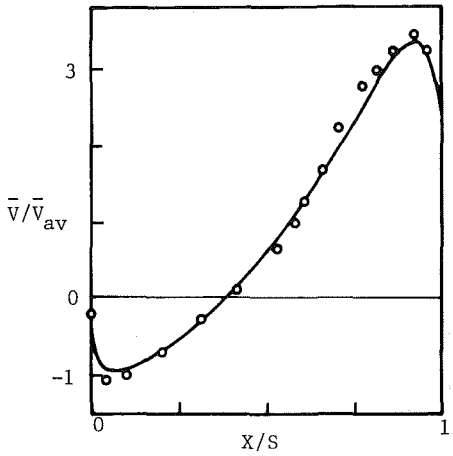

Fig. 4 Predicted vertical velocity distribution at midplane compared to data of Berner et al. (1984)

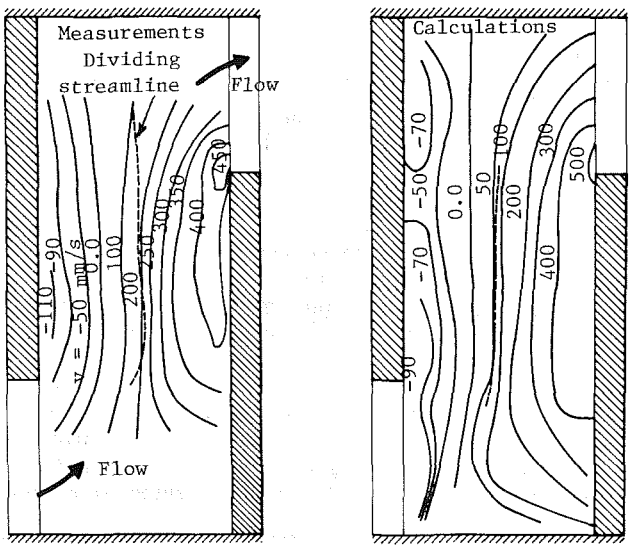

Fig. 3 Predicted vertical velocity contours compared to measurements of Habib et al. (1984)

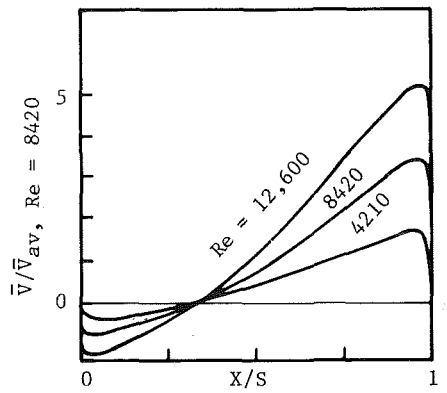

Fig. 5 Calculated velocity profiles at different Reynolds numbers (Y/D = 0.5, S/D = 0.4, C/D = 0.3)

q_w is the wall heat flux, k is the fluid thermal conductivity, L is a characteristic length taken as $L = 2D$, $\bar{U}_b$ is the bulk velocity, and $\bar{U}$ and T are the local time-mean velocity and temperature, respectively.

The average Nusselt number for a single wall in the typical cell is given by

$$\overline{\mathrm{Nu}} = \bar{h}\, L/k \tag{12}$$

where $\bar{h} = (\int_0^S h\, dx)/S$. For the overall Nusselt number the heat transfer with both walls is taken into account.

The velocity field is presented by the dimensionless stream function ψ, defined as given by Webb and Ramadhyani (1985)

$$\psi_{x,y} = \left\{\int_0^y \bar{U}\, dy - \int_0^x \bar{V}\, dx\right\} / \int_0^D \bar{U}\, dy \tag{13}$$

with $\psi_{0,0} = 0$.

3 Results and Discussion

In order to evaluate the computational procedure, the results are first compared to data of Berner et al. (1984) and Habib et al. (1984). Then, the predictions of the flow field and heat transfer in the flow around baffle-type elements are presented.

3.1 Comparison to Experimental Data. The data of Habib et al. (1984) were obtained in the streamwise-periodic flow in the cell formed between two consecutive baffles. The geometric parameters of the cell are $C/D = 0.3$, $S/D = 0.37$, and the baffle overlap, being the distance from the centerplane to the baffle tip, is $0.2D$. The Reynolds number based on the spacing between baffles is $\mathrm{Re}_s = (D/C)\mathrm{Re} = 6000$.

Figure 2 shows the comparison between the calculated and measured mean vertical velocity profiles at the middle of the cell. Figure 3 allows a comparison of the contours of the isovels inside the cell. The comparison indicates that the agreement is generally satisfactory. The width of the reversed flow region is approximately predicted but the absolute values of the mean velocity in the reversed flow region are underpredicted. The maximum velocity at the right baffle is overpredicted by 10 percent. The comparison between the contours in Fig. 3 indicates that the location of the dividing streamline at the boundary of the recirculating flow is predicted reasonably well.

The discrepancy between the calculations and the experiment may be attributed partly to the numerical accuracy in the calculation procedure. Increasing the number of grid points to reduce effects of the numerical diffusion leads to a slight improvement in the predictions. However, as noted earlier, an increase in the number of nodes from 10 × 20 to 18 × 20 gives a change of less than 5 percent and only inside the recirculation zone and at the highest mean velocity location.

At a higher Reynolds number the present calculations were compared to the measurements of Berner et al. (1984). These data were taken at geometric parameters of $C/D = 0.3$, S/D

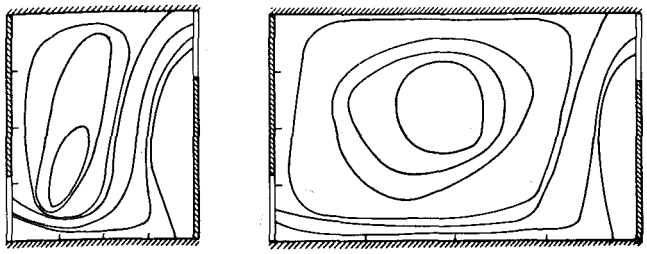

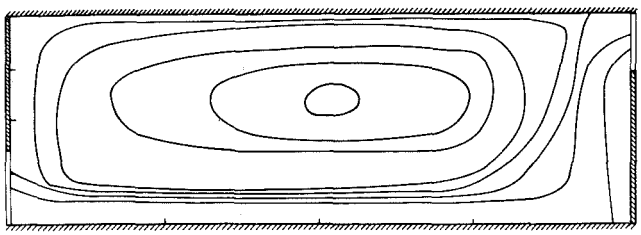

Fig. 6 Streamlines for different element spacings

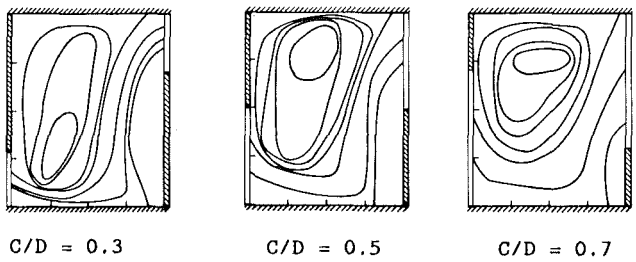

Fig. 7 Streamlines for different element heights (*S/D* = 0.4)

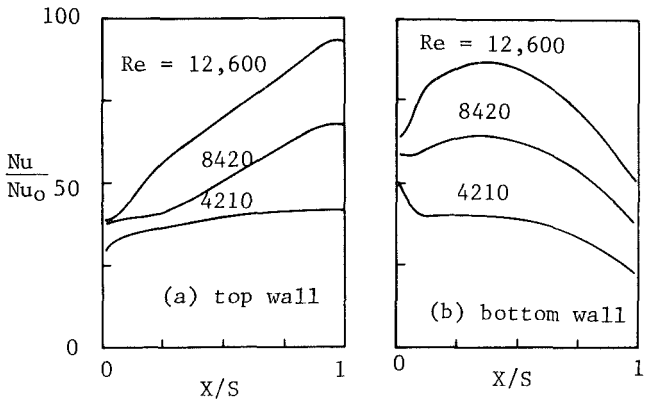

Fig. 8 Predicted variation of local heat transfer parameters (*C/D* = 0.3, *S/D* = 0.4, Pr = 0.7)

= 0.4, and Re_s = 10,200. The calculated velocity in the middle plane of the cell is compared to the data in Fig. 4. Apart from the region of reverse flow where the absolute value of the velocity is slightly underpredicted, the mean velocity values are predicted reasonably well.

3.2 Flow Field Predictions. The field as described in Fig. 3 is a turbulent shear flow, which is characterized by a large recirculation zone downstream of the left baffle with flow downward near the left baffle and upward near the right baffle. The flow is deflected due to the presence of baffles and impinges on the top and bottom walls and on the upstream face of the baffles at different angles.

The predicted effect of the Reynolds number on the velocity distribution at the central plane of the cell is shown in Fig. 5. The size of the reversed flow region increases slightly with the Reynolds number. The strength of the reversed flow region is greatly increased as the Reynolds number is increased.

The effect of baffle spacing on the flow field is presented in Fig. 6 for S/D = 0.4, 0.8, and 1.6 (with the horizontal scale exaggerated by a factor of two). The flow field is presented in terms of the two-dimensional stream function given by equation (13). The influence of the window cut on the flow field is given in Fig. 7. The curvature of the streamlines is shown to increase significantly as the window cut is decreased with high absolute values found in the reversed flow region. The center of the recirculating flow region is shifted upward as the window cut is increased.

3.3 Heat Transfer Predictions. Predicted local and overall Nusselt numbers along the channel walls are presented in this section to investigate the local and overall heat transfer characteristics as affected by the geometric parameters, Reynolds number and fluid properties. The heat transfer coefficients are presented in terms of the ratio of the value in a baffled channel to the one for a smooth channel, Nu/Nu_o, where Nu_o is the value of the smooth channel for laminar flow, a convenient and common reference (Holman, 1981).

There are apparently no heat or mass transfer data available corresponding to the conditions of these calculations. Therefore this work presents true predictions for the thermal field rather than the "postdiction" usually encountered. With shorter elements the data of Han et al. (1988) should provide appropriate tests for further studies.

The effect of the Reynolds number on the local heat transfer over the top and bottom walls is shown in Fig. 8. On the bottom wall the figure indicates a maximum value of the Nusselt number near X/S = 0.37. As shown by the streamlines of Fig. 6 the flow first impinges at the bottom wall and thus induces a maximum value of the heat transfer coefficient there. Then the flow gradually moves away from the bottom wall causing lower values of the heat transfer coefficients at the right side of the cell as shown in Fig. 8. The above phenomena appear for all Reynolds numbers except that the maximum of the Nusselt number on the bottom wall is not well defined at the lowest Reynolds number. A small local maximum can also be noticed near X/S = 1.0 in Fig. 8(*b*). This is caused by a small recirculation region near the right corner of the cell. These two maxima at the bottom wall were also presented by the numerical results of Kelkar and Patankar (1987) for laminar flow at Re = 500.

On the top wall the local Nusselt number increases with X, reaching its maximum value near $X = S$. As shown in Fig. 6, the top wall is covered by the recirculating eddy and the throughflow impinges on the top wall near $X = S$. This observation explains the behavior of the Nusselt number distribution.

The influence of the Reynolds number on the overall heat transfer is shown in Fig. 9 for two different values of Prandtl number. The figure indicates the dependence of the heat transfer on the Reynolds and Prandtl numbers. The figure also presents the effect of the Reynolds number and Prandtl number on the heat transfer of the smooth channel as given by Faggiani and Gori (1982) and Petukhov and Roizen (1965) and, thus, exhibits the significant augmentation of heat transfer caused by insertion of baffles. The dependence of the Nusselt number on the Prandtl number is given in Fig. 10.

The effect of baffle spacing on the local heat transfer over the top and bottom walls is shown in Fig. 11. On the bottom wall the increase in the spacing, S/D, from 0.4 to 0.8 leads to

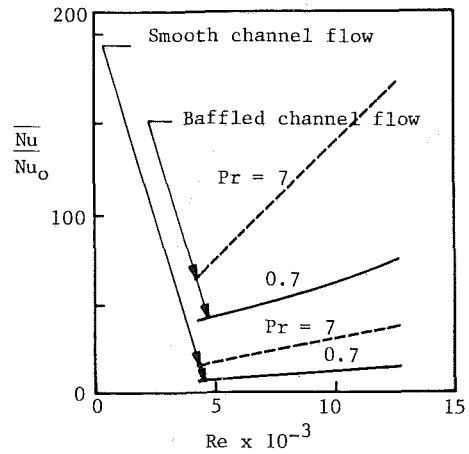

Fig. 9 Effect of Reynolds number on overall heat transfer (*S/D* = 0.4, *C/D* = 0.3)

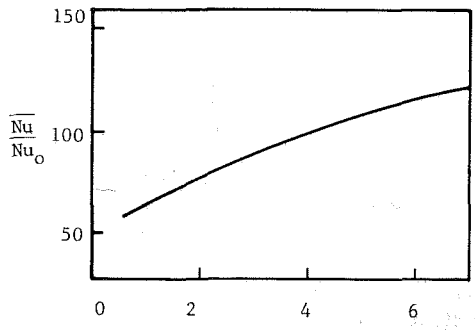

Fig. 10 Effect of Prandtl number on overall heat transfer (*S/D* = 0.4, *C/D* = 0.3, Re = 8420)

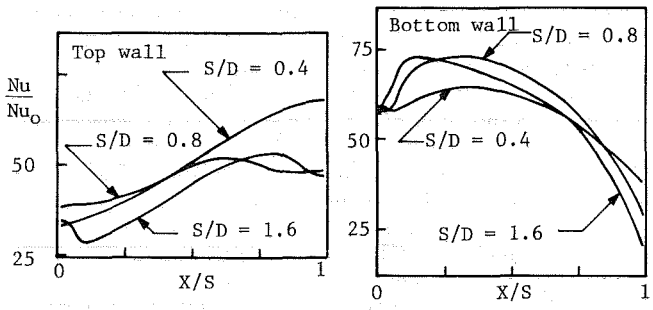

Fig. 11 Effect of element spacing on local heat transfer (*C/D* = 0.3, Re = 8420, Pr = 0.7)

an increase in the Nusselt number over most of the bottom surface. Further increase in the spacing to $S/D = 1.6$ causes a decrease in the Nusselt number. On the bottom wall the normalized location of the maximum Nusselt number is shifted toward the left side of the cell as the spacing is increased. On the top wall the Nusselt number is generally decreased by increasing the baffle spacing, Fig. 11.

The change of the overall heat transfer over top and bottom walls with the baffle spacing at two Prandtl numbers is shown in Fig. 12. A maximum value for the Nusselt number over the bottom wall is indicated near $S/D = 1.1$. The same phenomenon was also observed by Webb and Ramadhyani (1985) at $S/D = 1.0$ for laminar flow. The combined overall heat transfer on both walls decreases with the baffle spacing at the two Prandtl numbers as shown in Fig. 12. This consequence is similar to the calculations for laminar flow by Kelkar and Patankar (1987). The results of Webb and

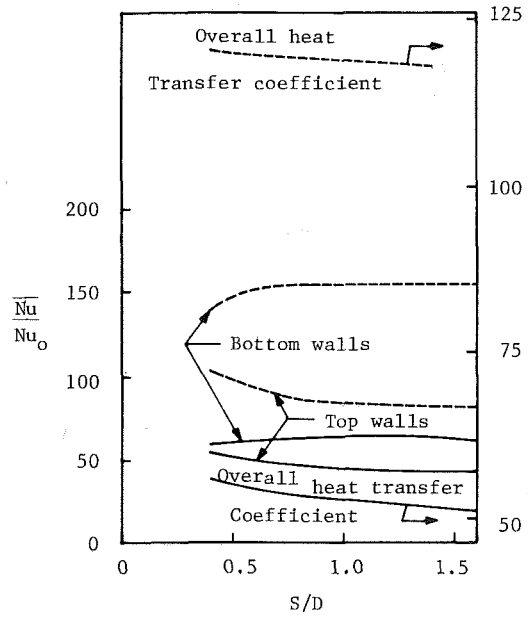

Fig. 12 Effect of baffle spacing on average heat transfer parameters; ·····, Pr = 7; ————, Pr = 0.7 (*C/D* = 0.3, Re = 8420)

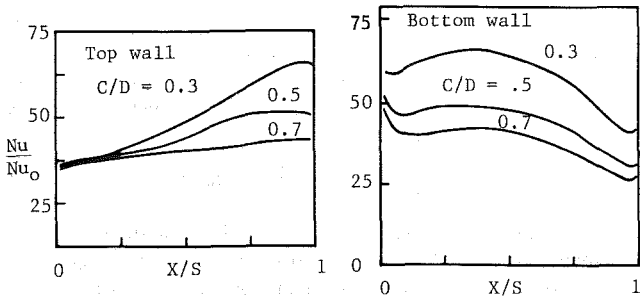

Fig. 13 Effect of element height on local heat transfer parameters (*S/D* = 0.4, Re = 8420, Pr = 0.7)

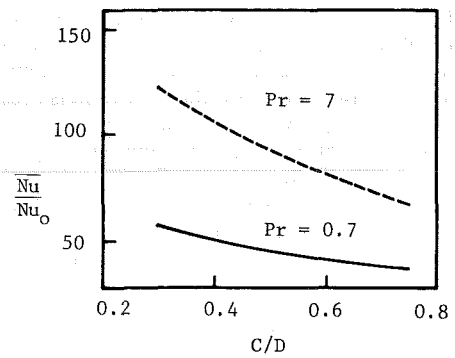

Fig. 14 Effect of element length on overall heat transfer parameters (*S/D* = 0.4, Re = 8420)

Ramadhyani (1985) for laminar flow also indicate a decrease of Nu below $S/D = 1.0$. For this flow in particular, it was noticed that the recirculation region covered all the regions between the baffles. This is not shown by the present calculations nor by Kelkar and Patankar and it is expected to be caused by the short baffle height used by Webb and Ramadhyani.

The effects of the opening on the local heat transfer on the top and bottom walls and on the overall heat transfer are shown in Figs. 13 and 14, respectively. The effect of the baffle

height is shown to be similar to the effect of the Reynolds number (Fig. 9). As can be deduced from the flow field of Fig. 7, the velocity of the throughflow increases with the baffle height (since the total flow rate is kept constant in these calculations as C/D is varied) and, therefore, the heat transfer is increased with increasing baffle height.

4 Concluding Remarks

Numerical predictions were made for the turbulent flow and heat transfer in channels with streamwise-periodic flow. The flow is characterized by a large recirculation zone behind the obstructions and by regions of large velocity gradients. Results are representative of standard numerical approaches using the simple, popular version of the k–ϵ turbulence model and wall functions for high Reynolds numbers with the constant shear layer approximation near the wall.

The parameters affecting the flow and heat transfer were the element spacing and length and Reynolds and Prandtl numbers. The calculations were shown to be in reasonable agreement with the measured flow fields, which provided the boundary conditions. Augmentation of heat transfer was obtained with increase in the Reynolds number and element height and with decrease in the baffle spacing. Substantial increases in the heat transfer were observed for high Prandtl number fluids.

Acknowledgments

Portions of this study were supported by National Science Foundation Grant ENG 79-07806, The University of Arizona, Cairo University, and Gould, Inc., to whom we are most grateful. By acceptance of this article for publication, the publisher recognizes the U.S. Government's (license) rights in any copyright and the Government and its authorized representatives have unrestricted right to reproduce in whole or in part said article under any copyright secured by the publisher.

References

Amano, R. S., 1985, "A Numerical Study of Laminar and Turbulent Heat Transfer in a Periodically Corrugated Wall Channel," ASME *Journal of Heat Transfer*, Vol. 107, pp. 564–569.

Amano, R. S., Bagherlee, A., Smith, R. J., and Niess, T. G., 1987, "Turbulent Heat Transfer in Corrugated-Wall Channels With and Without Fins," ASME *Journal of Heat Transfer*, Vol. 109, pp. 62–67.

Asako, Y., and Faghri, M., 1987, "Three-Dimensional Heat Transfer and Fluid Flow Analysis of Arrays of Rectangular Blocks Encountered in Electronic Equipment," National Heat Transfer Conference, Pittsburgh, PA, ASME Paper No. 87-HT-73.

Berner, C., Durst, F., and McEligot, D. M., 1984, "Flow Around Baffles," ASME *Journal of Heat Transfer*, Vol. 106, p. 743.

Faas, S. E., 1980, "Numerical Prediction of Flows in Two-Dimensional Ducts With Repeating Surface Geometries," M.S.E. report, Aero. Mech. Engr., Univ. Arizona; available from NTIS as AD-A094 249/0.

Faas, S. E., and McEligot, D. M., 1979, "Flow in a Corrugated Duct," APS Fluid Dynamics Meeting, Notre Dame, IN.

Faggiani, S., and Gori, F., 1982, "Remarks of the Heat Transfer to Gases in Turbulent Flow Between Parallel Plates," *Proc., 7th Int. Heat Transfer Conf.*, Munich, Vol. 3, p. 33.

Faghri, M., 1987, Personal communication, Mech. Engr. Dept., Univ. Rhode Island, Kingston, RI.

Founti, M. A., Vifidis, C., and Whitelaw, J. H., 1985, "Shell-Side Flow in a Model Disc-and-Doughnut Heat Exchanger," *J. Experiments in Fluids*, Vol. 3, pp. 293–300.

Gosman, A. D., Khalil, E. E., and Whitelaw, J. H., 1979, "The Calculation of Two-Dimensional Turbulent Recirculating Flows," *Turbulent Shear Flows I*, F. Durst et al., eds., Springer, pp. 237–255.

Gosman, A. D., and Pun, W. M., 1973, Lecture Notes for Course Entitled "Calculation of Recirculating Flows," Report HTS/74/2, Mech. Eng. Dept., Imperial College, CA.

Habib, M. A., and McEligot, D. M., 1982, "Turbulent Heat Transfer in a Swirl Flow Downstream of an Abrupt Pipe Expansion," *Proc., 7th Int. Heat Transfer Conf.*, Munich, Vol. 3, p. 159.

Habib, M. A., Durst, F., and McEligot, D. M., 1984, "Streamwise-Periodic Flow Around Baffles," *Proc. 2nd Int. Conference on Applications of Laser Anemometry to Fluid Mechanics*, Lisbon, Portugal.

Habib, M. A., and Whitelaw, J. H., 1980, "Velocity Characteristics of a Confined Coaxial Jet With and Without Swirl," ASME *Journal of Fluids Engineering*, Vol. 102, p. 47.

Han, J. C., Chandra, P. R., and Lau, S. C., 1988, "Local Heat/Mass Transfer Distributions Around Sharp 180 deg Turn in Two-Pass Smooth and Rib-Roughened Channels," ASME *Journal of Heat Transfer*, Vol. 110, pp. 91–98.

Holman, J. P., 1981, *Heat Transfer*, McGraw-Hill, New York.

Ichimiya, K., 1987, "Effects of Several Roughness Elements on an Insulated Wall for Heat Transfer From the Opposite Smooth Heated Surface in a Parallel Plate Duct," ASME *Journal of Heat Transfer*, Vol. 109, pp. 68–73.

Jones, W. P., and Launder, B. E., 1972, "The Prediction of Laminarization With a Two-Equation Turbulence Model," *Int. J. Heat Mass Transfer*, Vol. 15, p. 301.

Karlekar, B. V., and Desmond, R. M., 1977, *Engineering Heat Transfer*, West Publishing Company, New York.

Kelkar, K. M., and Patankar, S. V., 1987, "Numerical Prediction of Flow and Heat Transfer in a Parallel Plate Channel With Staggered Fins," ASME *Journal of Heat Transfer*, Vol. 109, pp. 25–30.

Launder, B. E., and Spalding, D. B., 1972, *Mathematical Models of Turbulence*, Academic Press, New York.

Logan, E., and Islam, O., 1976, "Channel Flow Over a Smooth-to-Rough Surface Discontinuity With Zero Pressure Gradient," ASME *Journal of Fluids Engineering*, Vol. 98, pp. 626–634.

Logan, E., and Siuru, W. D., 1977, "Response of a Turbulent Pipe Flow to a Change in Roughness," ASME *Journal of Fluids Engineering*, Vol. 99, pp. 548–555.

Patankar, S. V., and Spalding, D. B., 1972, "A Calculation Procedure for Heat, Mass and Momentum Transfer in Three-Dimensional Parabolic Flows," *Int. J. Heat Mass Transfer*, Vol. 15, p. 1787.

Patankar, S. V., Liu, L. H., and Sparrow, E. M., 1977, "Fully Developed Flow and Heat Transfer in Ducts Having Periodic Variations of the Cross-Sectional Area," ASME *Journal of Heat Transfer*, Vol. 99, pp. 180–186.

Petukov, B. S., and Roizen, L. I., 1965, "Heat Exchange and Friction Resistance in Pipes and Channels of Various Geometrical Shapes," *Heat Mass Transfer*, I. Nauka i Technika, Minsk, USSR.

Rhode, D. L., Demko, J. A., Traegner, U. K., Morrison, G. L., and Sobolik, S. R., 1986, "Prediction of Incompressible Flow in Labyrinth Seals," ASME *Journal of Fluids Engineering*, Vol. 108, pp. 19–25.

Rodi, W., 1980, *Turbulence Models and Their Application in Hydraulics*, Int. Assn. Hydraul. Res., Delft, Netherlands.

Schofield, W. H., and Logan, E., 1987, "Viscous Flow Around Wall-Mounted Obstacles," Aero. Propulsion Rpt. 172, Aero. Research Lab., Australia.

Short, B. E., Jr., 1978, "Numerical Prediction of Heated Flow Between Rib Rough Surfaces," M.S.E. report, Aero. Mech. Engr., Univ. Arizona, Tucson, AZ.

Webb, B. W., and Ramadhyani, S., 1985, "Conjugate Heat Transfer in a Channel With Staggered Ribs," *Int. J. Heat Mass Transfer*, Vol. 28, No. 9, p. 1679.

Influence of Upstream Flow Conditions on the Heat Transfer to Nozzle Guide Vanes

V. Krishnamoorthy

B. R. Pai

Propulsion Division,
National Aeronautical Laboratory,
Bangalore—560 017, India

S. P. Sukhatme

Department of Mechanical Engineering,
Indian Institute of Technology,
Powai, Bombay—400076, India

The influence of a combustor located just upstream of a nozzle guide vane cascade on the heat flux distribution to the nozzle guide vane was experimentally investigated. The surface temperature distribution around the convectively cooled vane of the cascade was obtained by locating the cascade, firstly in a low-turbulence uniform hot gas stream, secondly in a high-turbulence, uniform hot gas stream, and thirdly in a high-turbulence, nonuniform hot gas stream present just downstream of the combustor exit. The results indicate that the increased blade surface temperatures observed for the cascade placed just downstream of the combustor can be accounted for by the prevailing turbulence level measured at cascade inlet in cold-flow conditions and the average gas temperature at the cascade inlet.

1 Introduction

Modern gas turbines require an accurate estimation of the distribution of heat transfer coefficients around turbine blade surfaces for optimum design of cooling configurations. Considerable difficulties exist in the estimation of external heat transfer coefficients around the blade surfaces as they are influenced by a large number of interacting parameters, such as flow turbulence, blade surface-to-gas temperature ratio, pressure gradients, curvature, etc. (Krishnamoorthy, 1986). Model investigations carried out under laboratory conditions have been useful for identifying the various boundary layer regimes over the blade surface. However, relating data generated under laboratory conditions to engine environment presents considerable difficulties. This has been mainly due to the difficulty in the characterization of flow in the engine environment and simulation of the same in the laboratory.

With a view to identifying the effects of flow conditions prevailing at the combustor exit on the heat flux distribution over a nozzle guide vane, experiments were conducted in a hot gas cascade tunnel using a convectively cooled vane cascade. The surface temperature distribution around the cooled vane was measured in order to assess the sensitivity of the heat flux distribution around the vane to upstream conditions. To identify the individual effects of free-stream turbulence and the temperature nonuniformity at the combustor exit, experiments were done with the cascade located, firstly in a low-turbulence uniform hot gas stream, secondly in a high-turbulence uniform hot gas stream, and thirdly in a high-turbulence nonuniform hot gas stream prevailing close to the exit of the combustor. The gas temperature distribution and the turbulence intensity at cascade inlet were measured. Experiments were conducted at a nominal gas temperature of 533 K and at a Reynolds number $Re_c = 3.54 \times 10^5$, based on the blade chord and the exit conditions.

2 Details of Test Blade and Cascade

The profile, location, and size of cooling holes and the cascade parameters for the nozzle guide vane used in the experiment are shown in Fig. 1. The experimentally obtained surface velocity distribution is shown in Fig. 2. A five-vane cascade was used, with the instrumented blade located in the middle. The blade span was restricted to 80 mm, equal to the width of the annular passage at the combustor exit.

Air at room temperature was used as the coolant. The mass flow of coolant through each cooling hole in the central vane was controlled and metered through a rotameter. The coolant was supplied to the remaining vanes from a common manifold. In order to ensure fully developed flow through the cooling holes, 0.4-m-long stainless steel tubes were soldered at the blade inlet. The coolant temperature at inlet and outlet was measured. The temperature of the coolant in the midspan region was assumed to be the average of the inlet and outlet temperatures. The measured coolant mass flow rate was used for estimating the Reynolds number and the coolant heat transfer coefficient at midspan was estimated using the relation for fully developed turbulent flow through circular pipes (Kreith, 1965).

The surface temperature distribution in the midspan region was obtained by means of 1-mm-dia sheathed chromel alumel thermocouples, located just beneath the blade surface. The thermocouples were located in slots provided on the blade surfaces and were silver-soldered over the slot length. The profile

Contributed by the Gas Turbine Division for publication in the JOURNAL OF TURBOMACHINERY. Manuscript received at ASME Headquarters February 1988.

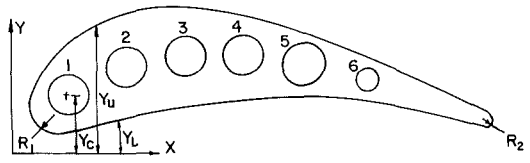

COOLING HOLE

HOLE	1	2	3	4	5	6
DIA	6·2	6·2	6·2	6·2	6·2	3·175
X	5·9	14·6	23·34	32·09	40·85	50·87
Y_c	9·45	13·79	15·26	15·23	13·9	11·56

PROFILE

X	68·8	65·8	62·8	59·8	56·8	53·1	50·1	47·1	44·1
Y_u	6·5	8·0	9·4	10·8	12·1	13·8	15·0	16·3	17·5
Y_L	4·6	5·2	6·1	6·7	7·3	8·0	8·5	8·7	9·0

X	41·1	38·1	35·1	32·0	29·0	26·0	23·0	20·0	17·0
Y_u	18·7	19·7	20·7	21·5	22·1	22·5	22·7	22·7	22·3
Y_L	9·1	9·1	8·9	8·7	8·4	8·1	7·6	7·1	6·4

X	13·9	11·0	9·5	6·5	3·5	2·0
Y_u	21·6	20·5	19·8	17·8	15·2	13·2
Y_L	5·8	5·2	4·9	4·1	3·7	4·1

X	4·25
Y	7·8
R_1	4·25

X	68·15
Y	5·7
R_2	1·15

ALL DIMENSIONS ARE IN MM

CASCADE DATA

CHORD = 69·5 mm
SPAN = 140 mm
PITCH = 45·5 mm

STAGGER ANGLE = 41°

TURNING ANGLE = 60°

Fig. 1 Coordinates of nozzle guide vane

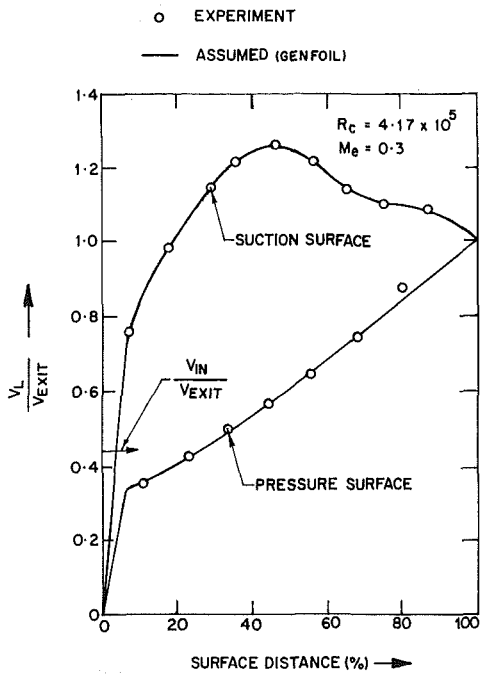

Fig. 2 Nondimensional velocity distribution

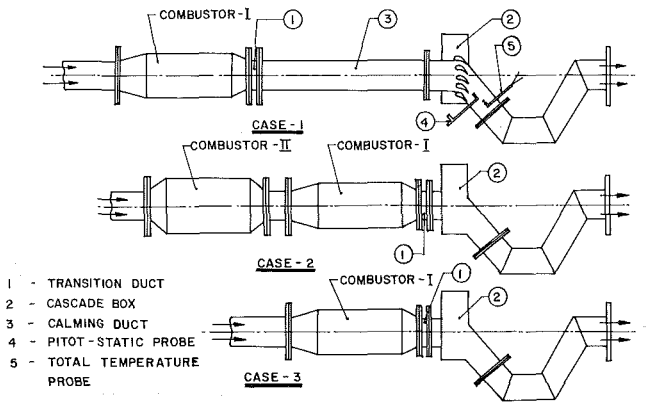

Fig. 3 Layouts of tunnel

was hand-finished after soldering. In all, 21 thermocouples were used, 12 covering the suction surface and 9 covering the pressure surface. The error in measured temperature due to thermocouple installation was estimated to be small (less than 1°C) and was neglected (Watson, 1964). The thermocouple outputs were fed to a data-logger for direct temperature measurement.

3 Experimental Setup and Procedure

The experiments were conducted at a nominal gas temperature of 533 K. The layout of the three arrangements used in the investigation is shown in Fig. 3. A gas turbine combustor (combustor I) was used as the gas generator with aviation kerosene as the fuel. A short transition duct of length 0.06 m, connected to the exit of combustor I, provided transition from a 0.08-m-wide annular sector to a 0.08 m × 0.182 m rectangular section.

In the first series of experiments (Case 1), the cascade was located at the end of a 1-m-long calming duct, which was connected to the short transition duct with a stainless steel wire mesh (pitch 4 mm × 4 mm and wire diameter 1 mm) in between. In the second series of tests (Case 2) the calming duct was deleted, and an additional combustor (combustor II) was connected upstream and fired. Combustor I was still kept in the circuit, but in an unfired condition. In the third series of experiments (Case 3), combustor I was fired, with the cascade located at the end of the short transition duct, without the calming duct in circuit.

The required Mach and Reynolds numbers were set by monitoring the total and static pressure one chord downstream of the cascade exit in the midpassage region. The stagnation temperature along the exit duct axis was measured two chords distance downstream of the cascade exit. During the experiments, the coolant flow rate was initially set and the required external flow conditions corresponding to the re-

Nomenclature

C = chord length of vane
h_c = coolant-passage heat transfer coefficient
$\dot{m}_c$ = total coolant mass flow rate
M_e = Mach number at cascade exit
Re_c = flow Reynolds number
T_c = coolant temperature
T_{og} = free-stream gas total temperature
T_w = vane surface temperature
U_L = local free-stream velocity
$<u'^2>_i$ = root mean square of fluctuating velocity in mean flow direction at inlet
ϵ = local free-stream turbulence intensity
ϵ_i = free-stream turbulence intensity at cascade inlet
η = cooling effectiveness = $(T_{og} - T_w)/(T_{og} - T_c)$
λ = a measure of the length of transition region

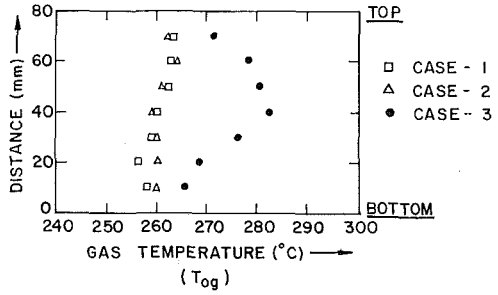

Fig. 4(a) Gas temperature distribution at cascade inlet (spanwise direction)

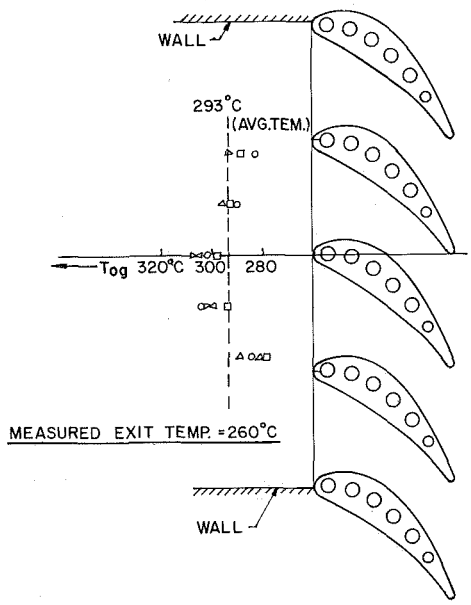

Fig. 4(b) Gas temperature distribution at cascade inlet (pitchwise direction): Case 3

quired Re_c, M_e, and T_{og} were set by controlling the air and fuel mass flows. The surface temperatures were recorded after reaching steady-state conditions. The variations in the set air mass flows and gas temperatures were around ± 2 percent and the error in the temperature measurement was ± 1°C.

4 Results and Discussion

In order to characterize the flow at the cascade inlet, the turbulence intensity (in the cold flow condition) and the gas temperature distribution were measured. The turbulence levels were 2.6 percent for Case 1 and 13.0 percent for the Case 2 and Case 3 arrangements, for a flow velocity of 62 m/s. This corresponded to the mass flow of air required at the combustor inlet for setting the flow Reynolds number Re_c of 3.54 × 10^5 with a nominal gas temperature 533 K. The gas temperature distribution at the cascade inlet in the spanwise direction is shown in Fig. 4(*a*) when the measured exit temperature was 533 K. The temperature distributions for the Case 1 and Case 2 arrangements were fairly uniform and the values were close to the measured temperature at the exit of the cascade. In the Case 3 arrangement, the temperature distribution was nonuniform and was similar to that observed at the exit of the combustor. The peak value was higher than the value measured at the exit of the cascade. The temperature distribution in the pitchwise direction for the Case 1 arrangement was also found to be uniform and the value was close to the exit value. The Case 2 arrangement also exhibited a similar

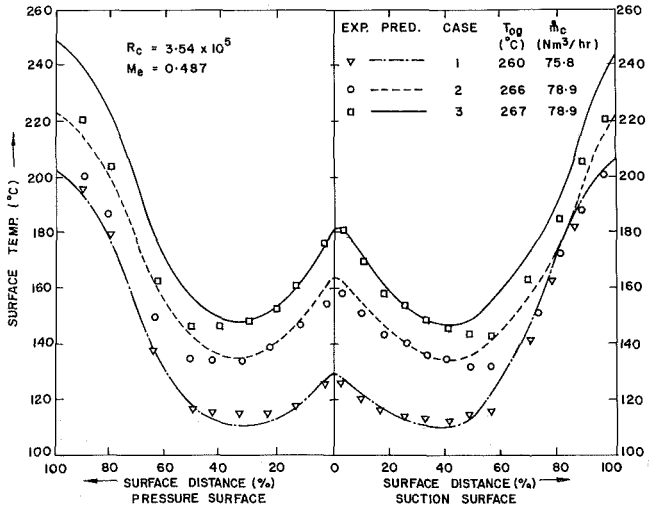

Fig. 5 Temperature distribution around N.G.V.: comparison between Case 1, Case 2, and Case 3

behavior. The measured temperature distribution over 1 pitch distance on either side of the center blade is shown in Fig. 4(*b*), for the Case 3 arrangement. The estimated pitchwise averaged temperature was higher than the measured exit temperature by about 33°C.

4.1 Effect of Combustor Flow Conditions. The symbols in Fig. 5 represent measured temperature distributions around the vane obtained for the three arrangements (Case 1, Case 2, and Case 3) used in the experiments. The flow Reynolds number (Re_c), the coolant flow conditions, and the free-stream gas temperature were maintained approximately the same to enable the comparison of the data. The effect of free-stream turbulence and the gas temperature nonuniformity on the vane surface temperature can be clearly identified. A qualitative estimate of the effect of the free-stream turbulence and the temperature nonuniformity present at the combustor exit on the cooling effectiveness (η) can be obtained, for example, by comparing the data on the suction surface in the mid-chord region. The cooling effectivenesses for the Case 1, Case 2, and Case 3 arrangements are 0.63, 0.57, and 0.51, respectively. The effect of turbulence and temperature nonuniformity is to reduce the cooling effectiveness by 10 and 21 percent, respectively, compared to the uniform flow case. An attempt to explain these results on the basis of available prediction procedures now follows.

4.2 Baseline Data. In theory, it is possible to obtain the external heat transfer coefficient distribution from the measured surface temperatures and specified coolant heat fluxes through a numerical solution of the steady two-dimensional conduction equation (Turner, 1969; Hylton et al., 1983). Such an exercise was attempted by a finite element analysis using 1702 triangular elements. However, the scatter in the derived *h* distribution was found to be unacceptably large (Krishnamoorthy, 1986). Hence, the temperature distribution around the cooled vane was estimated using a finite element heat conduction program (Krishnamoorthy, 1986) for a prescribed heat transfer coefficient distribution around the vane corresponding to the test flow conditions, and was compared with the measured distribution to obtain an indirect estimate of the heat flux distribution. The heat transfer coefficient distribution was calculated using the GENFOIL program (Krishnamoorthy, 1986). The extent of different boundary layer regimes over the vane suction and pressure surface was identified from experiments with an identical cascade having an electrically heated vane under constant-heat-flux boundary conditions. The heat transfer coefficient distribution

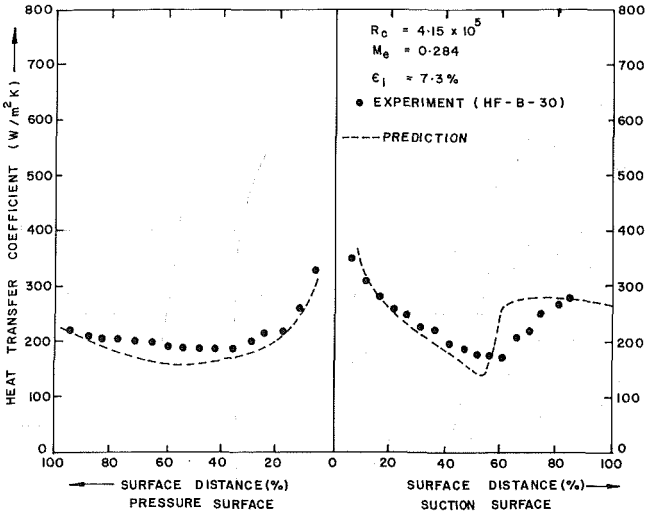

Fig. 6 Comparison of experimental and predicted heat transfer coefficient distribution (constant heat flux boundary condition)

estimated using the GENFOIL program was subsequently modified for the effect of free-stream turbulence prevailing at the cascade inlet using the following correlations for the effect of free-stream turbulence on the local heat transfer coefficient in different boundary layer regimes:

Laminar and Transitional Boundary Layer

$$h_\epsilon = h_{\epsilon=0} * (1 + 0.04\epsilon) \text{ for } \epsilon \leq 2 \quad (1)$$

$$h_\epsilon = h_{\epsilon=0} * (1 + 0.44\epsilon^{0.5})/1.502 \text{ for } \epsilon > 2$$

Turbulent Boundary Layer

$$h_\epsilon = h_{\epsilon=0} * (1 + 0.0235\epsilon) \quad (2)$$

where ϵ = local turbulence intensity = $<u'^2> \times 100/U_L$. These correlations were derived from experimental data obtained for a turbine rotor blade using a novel active turbulence generator (Krishnamoorthy, 1982, 1987). They have been validated against the experimental data obtained for nozzle guide vane profiles under uniform heat flux boundary condition and have been found to be independent of the Reynolds number of the flow (Krishnamoorthy, 1987).

The symbols in Fig. 6 represent measured values of the heat transfer coefficient around the vane with a constant-heat-flux boundary condition at a Reynolds number Re_c of 4.15 × 10^5, exit Mach number M_e of 0.284, and inlet turbulence level ϵ_i of 7.3 percent. In the same figure, the predicted heat transfer coefficient distribution using the GENFOIL program, modified to include the effects of free-stream turbulence as explained above, is also shown. The GENFOIL program is a numerical solution procedure based on the Patankar-Spalding method for calculation of boundary layers (Patankar and Spalding, 1970). The free-stream velocity distribution used in the boundary layer calculation is shown in Fig. 2. The laminar boundary layer calculation for the suction surface indicated laminar separation in the adverse pressure gradient region. Hence, based on the experimental heat transfer coefficient distribution obtained at low turbulence levels, the boundary layer on the suction surface was assumed to be laminar up to 53 percent surface distance, just upstream of the predicted laminar separation point, and turbulent over the remaining distance with a sharp transition. The comparison of the predicted and experimental heat transfer data for the pressure surface indicated that the boundary layer was laminar up to 64 percent of the surface distance. The gradual increase in the local heat transfer coefficient observed over the remaining distance indicated that the boundary layer was transitional. The calculations in the turbulent boundary layer region were done using Van Driest's eddy viscosity relation and the calculations in the transitional region were done using the universal intermittency distribution suggested by Dhawan and Narasimha (1958) with $\lambda = 0.24$ times the length of the pressure surface. This value of λ was found to give good predictions for a different nozzle guide vane studied earlier with a similar free-stream velocity distribution (Krishnamoorthy, 1986). It can be observed that the predicted values are in satisfactory agreement with the measured values. This confirmed the accuracy of the prediction procedure.

The surface temperature distribution around the vane surface for the Case 1 arrangement at $Re_c = 3.54 \times 10^5$ and $T_{og} = 533$ K was estimated using the heat transfer coefficient distribution corresponding to the measured inlet free-stream turbulence level and for a constant surface temperature, corresponding to a mean blade temperature of 423 K and free-stream gas temperature of 533 K. The heat transfer coefficient at the stagnation point was estimated using the correlation of Lowery and Vachon (1975). A comparison of the computed surface temperature distribution with the measured value is also shown in Fig. 5. The satisfactory agreement between the measurement and the prediction confirms the accuracy of the prescribed heat flux distribution. This study also confirmed the usefulness of the GENFOIL program for calculating the heat transfer coefficient distribution for the case where $(T_w/T_{og}) < 1$, with the inputs indicated.

4.3 Effects of Free-Stream Turbulence. The series of experiments conducted in the Case 2 arrangement indicated the effects of free-stream turbulence. A comparison of the predicted surface temperature obtained with the heat transfer coefficient distribution corresponding to 13 percent turbulence level with the experimental value is shown in Fig. 5. It may be noted that this was the turbulence level measured in cold flow conditions at the inlet to the cascade. It can be observed again that the prediction is in satisfactory agreement with the experiment. This suggests that the turbulence level at the combustor exit is mainly determined by the complex flow path in the combustion chamber. It appears that the effect of free-stream turbulence on the heat transfer coefficient distribution on a nozzle guide vane due to the turbulence level at the exit of the combustor can be estimated using the turbulence level measured under cold flow conditions.

4.4 Influence of Combustor. The significant nonuniformity in the measured gas temperature distribution in the pitchwise direction at the cascade inlet (Fig. 4*b*) suggested that the area average of the measured inlet gas temperature would be an appropriate value for estimating the heat flux distribution around the vane. Hence in the prediction program for the surface temperature distribution the heat flux distribution was obtained using the heat transfer coefficient distribution corresponding to the inlet free-stream turbulence level, $\epsilon_i = 13$ percent, and the pitchwise area average of the measured gas temperature distribution at cascade inlet. The predicted surface temperature distribution is compared with the experimental data in Fig. 5. It can be observed that the predictions are in satisfactory agreement with the experimental data.

5 Concluding Remarks

Results of the experimental investigations carried out to identify the effects of flow conditions at the combustor exit on the heat flux distribution over a nozzle guide vane cascade are presented. The experiments conducted by locating the vane cascade in a low-turbulence, uniform hot gas stream (Case 1), high-turbulence uniform hot gas stream (Case 2), and in the combustor exhaust hot gas stream (Case 3) indicate that the heat flux distribution can be estimated with a knowledge of the different boundary layer regimes over the vane surface and the correlation available from Krishnamoorthy and Sukhatme

(1987) for the effect of the free-stream turbulence on the local heat transfer coefficient. The observed decrease in the cooling effectiveness η over the blade surface due to the effects of the combustor is of the order of 21 percent. The heat flux distribution around the vane located close to the exit of the combustor can be estimated with satisfactory accuracy using the heat transfer coefficient corresponding to the measured cold flow turbulence level and the gas temperatures averaged in the pitchwise direction at cascade inlet.

Acknowledgments

The authors wish to thank the Aeronautical Research and Development Board, India for the financial support provided for this investigation.

References

Dhawan, S., and Narasimha, R., 1958, "Some Properties of Boundary Layer Flow During Transition From Laminar to Turbulent Motion," *Journal of Fluid Mechanics*, Vol. 3, No. 4, pp. 418–436.

Kreith, F., 1965, *Principles of Heat Transfer*, 2nd ed., International Text Book Co., New York.

Hylton, L. D., Mihlec, M. S., Turner, E. R., Nealy, D. A., and York, R. E., 1983, "Analytical and Experimental Evaluation of the Heat Transfer Distribution Over the Surfaces of the Turbine Vanes," NASA CR-168015.

Krishnamoorthy, V., 1982, "Effect of Turbulence on the Heat Transfer in a Laminar and Turbulent Boundary Layer Over a Gas Turbine Blade," ASME Paper No. 82-GT-146.

Krishnamoorthy, V., 1986, "Effect of Free Stream Turbulence on the Convective Heat Transfer to Gas Turbine Blades," Ph.D. Thesis, Mech. Engg. Dept., I. I. T., Bombay, India.

Krishnamoorthy, V., and Sukhatme, S. P., "The Effect of Free Stream Turbulence on Gas Turbine Blade Heat Transfer," National Aeronautical Laboratory Technical Memorandum, NAL TM PR 8707.

Lowery, G. W., and Vachon, R. I., 1975, "The Effect of Turbulence on Heat Transfer From Heated Cylinders," *International Journal of Heat and Mass Transfer*, Vol. 18, pp. 1229–1242.

Patankar, S. V., and Spalding, D. B., 1970, *Heat and Mass Transfer in Boundary Layers*, 2nd ed., Intertext, London, United Kingdom.

Turner, A. B., 1969, "Local Heat Transfer Measurement on a Gas Turbine Blade," University of Sussex, 69/ME/15, Sussex, United Kingdom.

Watson, G. G., 1964, "A Survey of Techniques for Measuring Surface Temperature," NEL REP No. 153.

Journal of Turbomachinery Technical Briefs

The Effect of Hub Radius on the Flow Due to a Rotating Disk

John W. Chew[1]

1 Introduction

In gas turbine engine design, an understanding of the flow entrainment and windage of rotating compressor and turbine disks is required. von Karman's (1921) integral solution for turbulent flow on a disk rotating in a quiescent infinite environment (called a free disk below) is often used to give quick estimates of these quantities. In the present contribution, von Karman's method is applied to the case of a disk with a nonzero inner radius. The solution given is a correction to that of Metzger et al. (1979).

The validity of von Karman's free disk solution has been demonstrated by comparison with measurements of the disk moment coefficient (see, for example, Dorfman, 1963, and Cham and Head, 1969). Measurements of the flow entrainment of a free rotating disk are also in agreement with von Karman's prediction. Newman (1983) shows a comparison between von Karman's flow entrainment prediction and the measurements of Case (1966) and Cham and Head (1969). Good agreement between theory and experiment is shown for the rotational Reynolds number, $\mathrm{Re} > 8 \times 10^5$; at lower values of Re the influence of the laminar region near the center of the disk may be important. Here Re is defined as $\Omega b^2/\nu$ were Ω, b, and ν denote angular velocity, outer disk radius, and kinematic viscosity, respectively.

In von Karman's original analysis, 1/7th power laws were assumed for the tangential and radial velocity profiles. A solution of the integral momentum equations was then deduced in which the radial velocity (u) and the tangential velocity (v) were directly proportional to radius (r) and the boundary layer thickness (δ) varied with $r^{0.6}$. With this form of the solution, the r dependency may be eliminated from the integral momentum equations and the solution obtained algebraically. Applying von Karman's method to a disk with a nonzero inner radius, Metzer et al. assumed a solution in which u varied with $r-a$, where a is the inner radius, v varied with r, and δ varied with $(r-a)^{0.6}$. Manipulation of the integral equations then yielded algebraic expressions for the unknown constants of proportionality for u and δ. The resulting "constants of proportionality" turn out to be dependent on r, indicating that the assumed form of the solution is inappropriate and that Metzger et al.'s result does not represent a solution of the momentum integral equations. If u and δ are allowed to vary with r in a general manner, the integral momentum equations give two simultaneous differential equations. These equations and their solution using numerical methods are discussed below.

2 Integral Momentum Equations

A cylindrical coordinate system (r, ϕ, z) is used with the disk face at $z=0$ and the axis of rotation at $r=0$. The velocity in this system is denoted (u, v, w) and the angular velocity of rotation is Ω. Assuming steady, axisymmetric flow with $u=v=0$ and pressure $p=$const outside the disk boundary layer, the radial and tangential momentum equations reduce to

$$\frac{1}{r}\frac{\partial}{\partial r}(\rho r u^2)+\frac{\partial}{\partial z}(\rho u w)=\rho\frac{v^2}{r}+\frac{\partial \tau_r}{\partial z} \tag{1}$$

$$\frac{1}{r}\frac{\partial}{\partial r}(\rho r u v)+\frac{\partial}{\partial z}(\rho v w)=-\rho\frac{uv}{r}+\frac{\partial \tau_\phi}{\partial z} \tag{2}$$

where ρ, τ_r, and τ_ϕ denote density, radial shear stress, and tangential shear stress, respectively.

Following von Karman (1921), radial and tangential velocity profiles are assumed as follows:

$$u=u_1\Omega r f(\eta), \quad v=\Omega r g(\eta) \tag{3}$$

where

$$\eta=\frac{z}{\delta}, \quad f(\eta)=\eta^{1/n}(1-\eta), \quad g(\eta)=1-\eta^{1/n} \tag{4}$$

and, for the present, n is an arbitrary constant. Shear stresses on the disk, denoted by the subscript w, are given by Blasius' law as applied by von Karman

$$\tau_{\phi,w}=-\rho k_n\left(\frac{\nu}{\delta}\right)^{2/(n+1)}(\Omega r)^{2n/(n+1)}(1+u_1^2)^{(n-1)/2(n+1)} \tag{5}$$

$$\tau_{r,w}=-u_1\tau_{\phi,w} \tag{6}$$

where k_n is a constant depending on the choice of n and ν is the kinematic viscosity. Integrating equations (1) and (2) across the boundary layer with relations (4) to (6) gives, with a little algebraic manipulation

$$I_{ff}\frac{1}{x^3}\frac{d}{dx}(x^4u_1^2\delta_1)-I_{gg}\delta_1+I_{fg}\frac{u_1}{x^4}\frac{d}{dx}(x^5u_1\delta_1)=0 \tag{7}$$

$$I_{fg}\frac{1}{x^4}\frac{d}{dx}(x^5u_1\delta_1)=k_n\left(\frac{1}{\delta_1 x^2}\right)^{2/(n+1)}(1+u_1^2)^{(n-1)/2(n+1)} \tag{8}$$

where

$$I_{ff}=\int_0^1 f^2(\eta)\,d\eta, \quad I_{gg}=\int_0^1 g(\eta)\,d\eta,$$

$$I_{fg}=\int_0^1 f(\eta)g(\eta)\,d\eta, \quad \delta_1=\frac{\delta}{r}\mathrm{Re}^{2/(n+3)},$$

$$x=\frac{r}{b}, \quad \mathrm{Re}=\frac{\Omega b^2}{\nu} \tag{9}$$

[1]Theoretical Science Group, Rolls-Royce plc, Derby, United Kingdom.

Contributed by the Gas Turbine Division for publication in the JOURNAL OF TURBOMACHINERY. Manuscript received by the Gas Turbine Division August 22, 1986.

and b is the outer radius of the disk. In deriving equations (7) and (8), density variations have been neglected.

For the present case, the problem is closed by specifying δ_1 and u_1 at the inner radius $x=a/b$. Consideration of the integral equations (7) and (8) then shows that, for particular values of n and k_n, u_1 and δ_1 are functions of a/b and x only. The mass flow $\dot{m}_b$ entrained by the disk, and the moment M on one side of the disk, are obtained by integrating across the boundary layer at $x=1$ to find the flux of mass and angular momentum. This gives

$$C_w = 2\pi (u_1\delta_1)_{x=1} I_f \, \mathrm{Re}^{(n+1)/(n+3)} \tag{10}$$

$$C_m = 4\pi (u_1\delta_1)_{x=1} I_{fg} \, \mathrm{Re}^{-2/(n+3)} = 2\,\frac{I_{fg} C_w}{I_f \, \mathrm{Re}} \tag{11}$$

where

$$I_f = \int_0^1 f(\eta)\, d\eta, \quad C_w = \frac{\dot{m}_b}{\rho \nu b}, \quad C_m = \frac{2M}{\rho \Omega^2 b^5} \tag{12}$$

Note that the mass flow and moment coefficients, C_w and C_m, are functions of Re and a/b only.

3 Results and Discussion

Equations (7) and (8) were solved using standard numerical techniques. The computer program used employs a library routine based on Gear's (1971) method for the solution of two simultaneous first-order differential equations obtained from (7) and (8).

This program was originally developed for Ekman layer flow, and works with variables nondimensionalized using the "linear turbulent Ekman layer solution"; details are given by Chew and Rogers (1987). In effect, the present solution assumes $\delta_1 = \dot{m} = 0$ at $r=a$. u_1 will have a finite value at $r=a$, but numerical results indicate that the solution is insensitive to the choice of this value.

Results for the case $n=7$ are shown in Fig. 1. From equations (10) and (11) above we see that $C_w/C_{w,0}$ and $C_m/C_{m,0}$, where the subscript 0 denotes the value for $a=0$, are equal and are functions of a/b only. Figure 1 shows this function as given by the numerical solution and $C_w/C_{w,0}$ as given by Metzger et al. (1979). Also shown on this graph is the equation

$$\frac{C_w}{C_{w,0}} = 1 - \left(\frac{a}{b}\right)^5 \tag{13}$$

This relationship was found to give a good approximation for the present results and is suitable for use in quick engineering calculations. It is apparent from these results that Metzger et al.'s solution differs considerably from the present solution.

Values of $C_w/C_{w,0}$ were also calculated for the cases $n=8$, 9, and 10, with k_n taking the values recommended by Schlichting (1979). For all these cases, the results were very close to those given in Fig. 1 for $n=7$, and use of equation (13) is again recommended. The "whole face" values for the mass flow and moment coefficients can be found from Newman's (1983) generalization of von Karman's solution, and are summarized below.

$$\begin{aligned}
&n=7, \quad C_{w,0} = 0.219\ \mathrm{Re}^{0.8}, && C_{m,0} = 0.0729\ \mathrm{Re}^{-0.2};\\
&n=8, \quad C_{w,0} = 0.187\ \mathrm{Re}^{9/11}, && C_{m,0} = 0.0561\ \mathrm{Re}^{-2/11};\\
&n=9, \quad C_{w,0} = 0.164\ \mathrm{Re}^{5/6}, && C_{m,0} = 0.0448\ \mathrm{Re}^{-1/6};\\
&n=10, \quad C_{w,0} = 0.146\ \mathrm{Re}^{11/13}, && C_{m,0} = 0.0365\ \mathrm{Re}^{-2/13}.
\end{aligned} \tag{14}$$

The results for $a=0$, $n=7$ agree with experiment for $8\times10^5 \le \mathrm{Re} \le 2\times10^6$. At higher Reynolds numbers, higher values of n are expected to be more appropriate. According to Newman $n=8$, 9, and 10 are appropriate for $\mathrm{Re} > 1.6\times10^7$, 3.3×10^7, and 7.2×10^7, respectively.

Obviously, as equation (13) has not been directly verified by experiment, some caution is required in applying this result. However the design engineer often has to make estimates of flow rate and windage in situations for which experimental data are not available, and in this context equation (13) is recommended for engineering use. Some support for the present results is given by comparing the influence of nonzero hub radius with the influence of the laminar flow region at the center of a whole disk. Transition to turbulent flow occurs when $\mathrm{Re}(r/b)^2 \simeq 2\times10^5$. As measurements of flow entrainment agree with fully turbulent theory for $\mathrm{Re} > 8\times10^5$, it follows that the influence of the laminar region is small for $r_t/b < 0.5$ where r_t is the transition radius. From this result it might be expected that the effect of hub radius will be small if the radius ratio $a/b < 0.5$; Fig. 1 does indeed confirm this behavior.

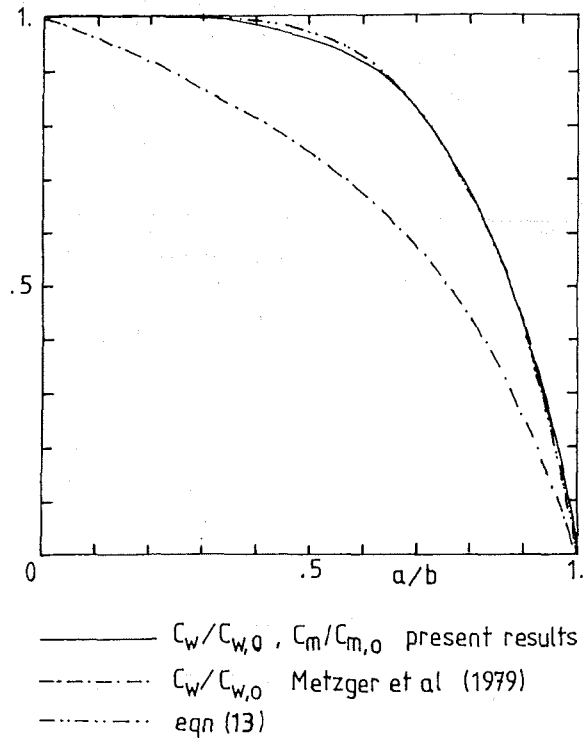

Fig. 1 Effect of hub radius on disk pumping and windage

References

Case, P., 1966, "Measurements of Entrainment by a Free Rotating Disc," *J. Roy. Aero Soc.*, Vol. 71, pp. 124–126.

Cham, T.-S., and Head, M. R., 1969, "Turbulent Boundary Layer Flow on a Rotating Disc," *J. Fluid Mech.*, Vol. 37, pp. 129–147.

Chew, J. W., and Rogers, R. H., 1987, "An Integral Method for Calculation of Turbulent Forced Convection in a Rotating Cavity with Radial Outflow," *Int. J. Heat and Fluid Flow*, in press.

Dorfman, L. A., 1963, *Hydrodynamic Resistance and the Heat Loss of Rotating Solids*, Oliver and Boyd, Edinburgh, pp. 56–58.

Gear, C. W., 1971, *Numerical Initial Value Problems in Ordinary Differential Equations*, Prentice-Hall, Englewood Cliffs, NJ.

Karman, T. von, 1921, "Uber Laminare und Turbulente Reibung," *Z. Angew, Math. Mech.*, Vol. 1, pp. 233–252.

Metzger, D. E., Mathis, W. J., and Grochowsky, L. D., 1979, "Jet Cooling at the Rim of a Rotating Disc," ASME *Journal of Engineering for Power*, Vol. 101, pp. 68–72.

Newman, B. G., 1983, "Flow and Heat Transfer on a Disc Rotating Beneath a Forced Vortex," *AIAA Journal*, Vol. 21, pp. 1066–1070.

Schlichting, H., 1979, *Boundary-Layer Theory*, 7th ed., McGraw-Hill, New York, pp. 596–612.